DOT/FAA/TC-14/25

Federal Aviation Administration
William J. Hughes Technical Center
Aviation Research Division
Atlantic City International Airport
New Jersey 08405

Full-Scale Testing of an Advanced Stitched Efficient Unitized Structural Concept Panel

January 2015

Final Report

This document is available to the U.S. public through the National Technical Information Services (NTIS), Springfield, Virginia 22161.

This document is also available from the Federal Aviation Administration William J. Hughes Technical Center at actlibrary.tc.faa.gov.

U.S. Department of Transportation
Federal Aviation Administration

NOTICE

This document is disseminated under the sponsorship of the U.S. Department of Transportation in the interest of information exchange. The U.S. Government assumes no liability for the contents or use thereof. The U.S. Government does not endorse products or manufacturers. Trade or manufacturers' names appear herein solely because they are considered essential to the objective of this report. The findings and conclusions in this report are those of the author(s) and do not necessarily represent the views of the funding agency. This document does not constitute FAA policy. Consult the FAA sponsoring organization listed on the Technical Documentation page as to its use.

This report is available at the Federal Aviation Administration William J. Hughes Technical Center's Full-Text Technical Reports page: actlibrary.tc.faa.gov in Adobe Acrobat portable document format (PDF).

Technical Report Documentation Page

1. Report No.	2. Government Accession No.	3. Recipient's Catalog No.
DOT/FAA/TC-14/25		

4. Title and Subtitle	5. Report Date
FULL-SCALE TESTING OF AN ADVANCED STITCHED EFFICIENT UNITIZED STRUCTURAL CONCEPT PANEL	January 2015
	6. Performing Organization Code
7. Author(s)	8. Performing Organization Report No.
Andrew Bergan and John G. Bakuckas Jr.	
9. Performing Organization Name and Address	10. Work Unit No. (TRAIS)
William J. Hughes Technical Center Aviation Research Division Atlantic City International Airport, NJ 08405	11. Contract or Grant No.
12. Sponsoring Agency Name and Address	13. Type of Report and Period Covered
U.S. Department of Transportation Federal Aviation Administration William J. Hughes Technical Center Aviation Research Division Materials and Structures Section ANG-E281 Atlantic City International Airport, NJ 08405	Final Report
	14. Sponsoring Agency Code ANM-115

15. Supplementary Notes

The Federal Aviation Administration William J. Hughes Technical Center Aviation Research Division COR was Dr. John G. Bakuckas, Jr.

16. Abstract

Integrally stitched composite technology is an area that shows promise in enhancing structural integrity of aircraft and aerospace structures. The most recent generation of this technology is the Pultruded Rod Stitched Efficient Unitized Structure (PRSEUS) concept developed by Boeing Research and Technology and the National Aeronautics and Space Administration. A joint test program on the assessment of damage-containment capabilities of the PRSEUS concept for curved fuselage structures was recently conducted at the Federal Aviation Administration William J. Hughes Technical Center using the Full-Scale Aircraft Structural Test, Evaluation, and Research facility.

This report summarizes the test results for the PRSEUS fuselage panel, which was subjected to axial tension, internal pressure, and combined axial tension and internal pressure loads. The test results showed excellent performance of the PRSEUS concept. No growth of barely visible impact damage was observed after ultimate loads were applied. With a two-bay notch severing the central stringer, damage was contained within the two-bay region well above the required limit load conditions. Catastrophic failure was well above the ultimate load level. Detailed post-test examinations using nondestructive inspection (NDI) techniques and destructive teardown evaluations were conducted in stable damage growth regions to identify dominant failure mechanisms for use in future progressive failure analysis. These examinations showed (1) extensive delaminations developed ahead of the notch tip, (2) the extent and location of damage detected by NDI was verified by teardown evaluations, (3) typical composite damage mechanisms, including delamination, fiber fracture, fiber-matrix interface failure, and matrix cracking, and (4) the role of stitching and warp knitting in the failure mechanisms.

17. Key Words	18. Distribution Statement
Damage containment, Residual strength test, Full-scale test, Notched, Structural test, Polymer matrix composite, PRESEUS	This document is available to the U.S. public through the National Technical Information Service (NTIS), Springfield, Virginia 22161. This document is also available from the Federal Aviation Administration William J. Hughes Technical Center at actlibrary.tc.faa.gov.

19. Security Classif. (of this report)	20. Security Classif. (of this page)	21. No. of Pages	22. Price
Unclassified	Unclassified	280	

Form DOT F 1700.7 (8-72) Reproduction of completed page authorized

ACKNOWLEDGEMENTS

This report summarizes a team effort consisting of representatives from several organizations, including the Federal Aviation Administration (FAA), The Boeing Company, The National Aeronautics and Space Administration, Sandia National Labs, and Drexel University.

The FAA authors wish to acknowledge Yongzhe Tian, Jeff Panco, and Patrick Sheehan for their diligent efforts during the Full-Scale Aircraft Structural Test, Evaluation, and Research (FASTER) modifications and testing at the FAA William J. Hughes Technical Center. Thanks also to Dave Galella and Paul Swindell for providing nondestructive inspection support and to Curtis Davies for providing digital image correlation equipment and post-test inspection guidance.

Many thanks to Kim Linton from Boeing for the planning, design, and execution of the test. His efforts were instrumental to the successful completion of the test program. Thanks also to Albert Neal for the development and validation of the finite element model and Gregory Korkosz (Boeing retiree) for the design of the modification of the FASTER facility for this test-program support throughout the entire test program.

From NASA, many thanks to Dawn Jegley and Andrew Lovejoy for their many efforts during the test program and to Patrick Johnston, who performed several ultrasonic examinations of the panel.

From Sandia National Labs, acknowledgement is due to Michael Bode, Michael Holle, Randy Duvall, Cigi Nelson, and Kyle Thompson for planning and performing the post-test ultrasonic and computed tomography inspections.

Many thanks are also due to the Drexel University Centralized Research Facility and Dr. Edward Basgall for making the scanning electron microscope examinations possible; Reewanshu Chadha and Amey Khanolkar for their efforts performing the acoustic emission study; Justine Malandra for her work on strain gage data reduction; and Jonathan Awerbuch and Tien-Min Tan for their input and guidance in all aspects of the test program.

TABLE OF CONTENTS

		Page
EXECUTIVE SUMMARY		xiii
1.	INTRODUCTION	1
2.	BACKGROUND ON COMPOSITE STRUCTURAL CERTIFICATION	2
3.	TEST PANEL DESIGN AND PREPARATION	4
3.1	Geometry	4
3.2	Test Load Introduction Reinforcements	6
3.3	Materials and Layup	7
3.4	Fabrication and Inspection	8
3.5	Panel Preparation and Attachment to Fixture	8
4.	FASTER FIXTURE MODIFICATIONS	9
4.1	Frame Loader Slide System	11
4.2	Axial Load Mechanism	11
5.	EXPERIMENTAL PROCEDURE	12
5.1	Test Phases and Load History	12
5.1.1	Phase I: Pristine Case	13
5.1.2	Phase II: BVID Case	13
5.1.3	Phase III: Two-Bay Notch Damage Case	16
5.2	Inspection and Monitoring Methods	18
5.2.1	Visual Inspection	18
5.2.2	Strain and Displacement	18
5.2.3	Pulse-Echo Ultrasound	20
5.2.4	Flash Thermography	21
5.2.5	The AE Method	22
5.2.6	Post-Test NDI	23
5.2.7	Fracture Surface Morphology	26
5.2.8	Ply-by-Ply Teardown	27
6.	ANALYTICAL PROCEDURE	28
7.	RESULTS AND DISCUSSION	29
7.1	Pre-Test Analytical Predictions	29
7.2	Phase I Testing	31

7.3 Phase II Testing, Effect of BVID 37

7.3.1 Introduction of BVID 37
7.3.2 Strain and Displacement 42

7.4 Phase III Testing, Effect of Through-the-Thickness Notch 45

7.4.1 Observations During Each Load Step 46
7.4.2 The AE Results 64

7.5 Post-Test NDI Observations 65

7.5.1 Visual Inspection 66
7.5.2 Pulse-Echo Ultrasound 69
7.5.3 Through-Transmission Ultrasound 70
7.5.4 Flash Thermography 71
7.5.5 X-Radiographic Computed Tomography 72

7.6 Teardown Observations 73

7.6.1 Global Observations 73
7.6.2 Ply-by-Ply Teardown 75
7.6.3 Fractography 76

8. SUMMARY 82

9. FUTURE WORK 83

10. REFERENCES 83

APPENDICES

A—Panel Engineering Drawings
B—Locations of Strain Gages and Linear Variable Differential Transformers
C—Digital Image Correlation and Visual Monitoring Setup
D—Notch Machining
E—Loader, Strain, and Displacement Data
F—Digital Image Correlation Data
G—Visual Monitoring Results

LIST OF FIGURES

Figure		Page
1	Increasing Damage Severity Requires Lower Sustained Loads	4
2	Overall Panel Geometry Showing the Interior Surface and Substructure: Test Panel Interior Surface, Frame Cross Section A-A, and Stringer Cross Section B-B	5
3	Load Introduction Doublers and Radius Blocks	6
4	Detail of Skin/Stringer Doubler Interleaving	7
5	One End of the Panel With Clevises and Seal Attached	9
6	Comparison of Existing FASTER Fixture and Modified FASTER Fixture	10
7	Frame-Loader Slide System	11
8	The Axial Loading Mechanism Assembly, Cross Beam With Seven Load Trains, and Single Load Train Subassembly	12
9	Phase II BVID Location and Test Setup: BVID Location, Cross Section A-A BVID Location Detail, and BVID Setup Photo	15
10	The Two-Bay Notch: Notch Location, Dimensions, Exterior Photograph, and Interior Photograph	17
11	Photograph of the Visual Monitoring Setup	18
12	Exterior Strain Gage and LVDT Locations	19
13	Interior Strain Gage Locations	20
14	Pulse-Echo Linear Phased-Array Ultrasound Setup	21
15	The FASTER Lab Flash Thermography System: Heat Source and Camera and Sample Result	21
16	Test Panel Showing the Location of the AE Sensors Mounted Along 24-Inch and 28-Inch Concentric Circles	23
17	The MAUS V Ultrasound System	24
18	Through-Transmission Ultrasound System: Tank and Gantry and Specimen Fixture in Tank Prior to Scan	25
19	Sandia National Labs Flash Thermography System: Camera and Hood Unit and Data Acquisition	25

20	X-Radiographic Computed Tomography System	26
21	Locations of Post-Test Inspections	27
22	Typical FEM Mesh Rendered With Profiles and Thickness Showing the Panel Modeled as Shell Elements and FASTER Fixture Loaders Modeled as Stiff Bar Elements: Interior, Axial Load Application, Hoop Load Application, and Frame Load Application	29
23	Typical 50% Limit Load Strain Results for Each of the Three Loading Functions Applied, Showing Good Repeatability and Agreement With the FEM: Axial Load: Strain Gage 38, Pressure Load: Strain Gage 45, Combined Load: Strain Gage 38, and Combined Load: LVDT 1	32
24	Typical Combined Limit Load Strain Results for Selected Strain Gage Locations: Top View of Gage Locations, Side View of Gage Locations, Exterior, and Interior	33
25	Combined Limit Load Axial Bending Strain: Top View of Gage Locations, Side View of Gage Locations, Mid-Bay, Between F-2 and F-3, and Near F-4	34
26	Combined Limit-Load Axial-Displacement Measurements	35
27	Hoop Strain Field in the Test Section: Pressure: 1.0 P and Combined: 1.0 P + 100% DLL	36
28	Photographs of the BVID Region, as Seen From the Exterior and Interior, Before and After Impact: Before Impact, After First Impact, After Second Impact, and Detail View	38
29	Location and Size of Post-Impact NDI Region	39
30	Pulse-Echo Ultrasound (a) Before Impact and (b) After Impact	40
31	Flash Thermography (a) Before Impact and (b) After Impact	41
32	The BVID Had No Effect on Global Strain and Displacement Distributions: Strain Gage Locations, Side View of Gage Locations, Mid-Bay Strain, and Axial Displacement	42
33	Axial Strain Field in the Test Section, Under Axial Ultimate Axial Load: DIC Axial Strain Fringe Plot and Axial Strain Along Section A-A	44
34	Phase III Load History With Key Damage Progression Observations, Letters A–H: Phase III Load History and Zoomed View of LS5	46
35	Axial Strain in the Vicinity of the Notch Tip Recorded via DIC and Strain Gage: DIC Axial Strain Fringe Plot, Axial Strain Along Section A-A, and Axial Strain History at SG7 Location	47

36 The Axial Strain Distribution at Notch Tip A for 1.0 P + 70% DLL and Section Plots Showing Normal Strain Along 0°, 45°, and 90° Sections: DIC Axial Strain Fringe Plot and Normal Strain Along Sections 48

37 Photographs of Notch Tip A Exterior Surface Damage Showing Crack Progression During LS-2: Panel Test Section Schematic, 1P + 70% DLL, 1P + 88% DLL, and 1P + 100% DLL 49

38 Photographs of Notch Tip A Interior Surface Damage Showing Crack Progression During LS-2: Panel Test Section Schematic, 1P + 54% DLL, 1P + 67% DLL, and 1P + 100% DLL 50

39 Photographs of Notch Tip Damage Showing Crack Progression During LS-2: Interior Schematic, Cross-Section Schematic, Stringer Flange Axial Strain, and Mid-Bay Interior Skin Axial Strain 51

40 Photographs of the Interior Surface Showing Damage Progression From Notch Tip B During Load LS-3: Before Damage Event and After Damage Event 52

41 Strain in and Around the Two-Bay Region During LS-3: Interior Schematic, Cross-Section Schematic, Mid-Bay Axial Strains, and Stringer Flange Axial Strain 53

42 Exterior Surface Crack Progression During LS-5, Showing the Crack Arrest Behavior of the Stitched Rows 55

43 Sequential Frames Captured Using High-Speed Camera Showing Crack Progression Beyond the Two-Bay Region 56

44 The Visually Observed Damage Accumulation in the Interior Surface: 1P + 100% DLL, 1P + 138% DLL, and 1P + 140% DLL 57

45 Crack Progression up to Point G, Figure 35, Showing Constant Crack Growth Rate 58

46 Selected Strain Gage and LVDT Locations: Interior Schematic and Cross-Section A-A Schematic 59

47 Overall Axial Extension 60

48 Exterior Skin Axial Strain 60

49 Interior Skin Axial Strain 61

50 Frame-Stringer Intersection Strain 62

51 Stringer Flange Axial Strain 63

52 Stringer Axial Strain 63

53 Load History Showing Accumulation of Three-Hit Events Recorded by the R15I Sensors and Corresponding First-Hit Amplitudes 64

54 Planar Location Scatter Plots for Three-Hit Events With Amplitude >90 dB for R15I Sensors at Four Load Levels: 70% DLL, 100% DLL, 148% DLL, and 184% DLL 65

55 Post-Failure Photographs of the Panel Showing a Single Meandering Crack on the Exterior and Massive Damage on the Interior, Including Numerous Matrix Cracks and Skin/Stringer and Skin/Frame Disbonding: Exterior and Interior 66

56 Detailed Photographs of Select Areas Critical to Catastrophic Failure: Locations of Detail Failure Photographs, Failure at Keyholes, and Stringer Ends 68

57 Photographs of Select Disbonded Stringers: 5-5 Disbond and S-7 Disbond 69

58 Pulse-Echo C-Scans of the Notch Tip B Region Showing Significant Delamination at the Notch Tip and Partial Frame/Stringer Disbonding: Amplitude C-Scan and Time-of-Flight C-Scan 70

59 The TTU Results 71

60 Flash Thermography Results 72

61 The CT Image of Skin/Stringer Cross Section View Near the Notch Tip 73

62 Visual Inspection of Tear-Down Segments of the S-5 Skin Stringer Disbond: Skin, Stringer Flange, Warp-Knitting, and Stitch Failures 74

63 Significant Failure Extent, Ply-By-Ply 75

64 Fracture Surface Morphology Across the Skin Thickness and Along a Crack Emanating From the Notch Tip: Plies at Notch Tip and Fiber/Matrix Interfacial Failure 77

65 Fracture Surface of a Delaminated Region Ahead of the Notch Tip Showing Failed Warp-Knit Fibers: Warp-Knit Resin-Rich Areas and Warp-Knit Detail 78

66 Fracture Surface of a Delaminated Region Ahead of the Notch Tip Showing Fibers Clean of Matrix 79

67 Fracture Surface Morphology of the Resin-Rich Disbond Region Ahead of the Notch Tip: Disbond Surface and Matrix Serrations 80

68 Characteristic Failures of Stitches Located in the First Stitched Row of S-5, Immediately Ahead of the Notch Tip: Protruding Stitch and Stitch Hole 81

LIST OF TABLES

Table		Page
1	Laminate Definitions	7
2	Test Sequence	13
3	Phase III Load Steps	16
4	Deformation and Maximum Principal Strain Fringe Plots for Six Loading Cases	30
5	Margin of Safety Summary	31
6	Measured Stringer Rod Pull Out Distance	67

LIST OF ACRONYMS

AC	Advisory Circular
ACT	Advanced Composites Technology
AE	Acoustic emission
AST	Advanced Subsonic Technology
BVID	Barely visible impact damage
CDT	Critical damage threshold
CFR	Code of Federal Regulations
CT	Computed tomography
DIC	Digital image correlation
DLL	Design limit load
DSD	Discrete source damage
FAA	Federal Aviation Administration
FASTER	Full-Scale Aircraft Structural Test, Evaluation, and Research
FEM	Finite element model
LS	Load step
LVDT	Linear variable differential transformer
MAUS	Mobile Automated Ultrasonic Scanner
NASA	National Aeronautics and Space Administration
NDI	Nondestructive inspection
PRSEUS	Pultruded Rod Stitched Efficient Unitized Structure
RCCM	Remote-Controlled Crack Monitoring
SEM	Scanning electron microscope
TTU	Through-Transmission Ultrasound
USAF	United States Air Force
VID	Visible impact damage

EXECUTIVE SUMMARY

Integrally stitched composite technology is an area that shows promise in enhancing structural integrity of aircraft and aerospace structures. The most recent generation of this technology is the Pultruded Rod Stitched Efficient Unitized Structure (PRSEUS) concept developed by Boeing Research and Technology and the National Aeronautics and Space Administration. A joint test program on the assessment of damage-containment capabilities of the PRSEUS concept for curved fuselage structures was recently conducted at the Federal Aviation Administration William J. Hughes Technical Center using the Full-Scale Aircraft Structural Test, Evaluation, and Research facility.

This report summarizes the test results for the PRSEUS fuselage panel, which was subjected to axial tension, internal pressure, and combined axial tension and internal pressure loads. The test results showed excellent performance of the PRSEUS concept. No growth of barely visible impact damage was observed after ultimate loads were applied. With a two-bay notch severing the central stringer, damage was contained within the two-bay region well above the required limit load conditions. Catastrophic failure was well above the ultimate load level. Detailed post-test examinations using nondestructive inspection (NDI) techniques and destructive teardown evaluations were conducted in stable damage growth regions to identify dominant failure mechanisms for use in future progressive failure analysis. These examinations showed (1) extensive delaminations developed ahead of the notch tip, (2) the extent and location of damage detected by NDI was verified by teardown evaluations, (3) typical composite damage mechanisms, including delamination, fiber fracture, fiber-matrix interface failure, and matrix cracking, and (4) the role of stitching and warp knitting in the failure mechanisms.

1. INTRODUCTION.

Integrally stitched composite technology is an area that shows promise in enhancing structural integrity of aircraft and aerospace composite structures [1 and 2]. The National Aeronautics and Space Administration (NASA), the United States Air Force (USAF), and The Boeing Company have a history of developing stitched composite structures and successfully demonstrated this advanced structural concept in several applications, such as the C-17 main landing gear doors. Compared to conventional stiffened composite panels with co-cured or bonded interfaces, stitched composite technology offers superior out-of-plane load and damage-containment capabilities [3 and 4]. This report introduces and provides a general overview of this joint research program and describes the development of the Pultruded Rod Stitched Efficient Unitized Structure (PRSEUS).

Stitched composite technology has been studied extensively over the past two decades [1–8]. Many coupon- and element-level experimental studies sponsored by NASA's Advanced Composites Technology (ACT) program investigated the effects of stitching on fracture toughness, in-plane mechanical properties, damage tolerance, fatigue response, and impact response [5]. A large amount of this mechanical property data generated by previous testing was critically reviewed to summarize the effects of stitching on stiffness, strength, and failure mechanisms [6]. Building on the ACT program, the Advanced Subsonic Technology (AST) program culminated in a full-scale test of a stitched composite wing [7]. Stitched composite technology developed during the ACT and AST programs was successfully applied to C-17 production parts in the lightly loaded large aircraft infrared countermeasure fairing, which first flew in 2003, and the multirib-stiffened, moderately loaded main landing gear doors, which first flew in 2007. These applications demonstrated the manufacturing and structural advantages of stitched composites [8].

After the successful production of secondary structures, Boeing's composite structure development focus shifted to large primary structures. The most recent generation of primary structure, stitched composite technology, is the PRSEUS concept, developed to reduce the weight and cost penalty of mechanical fasteners required to sustain out-of-plane loads in a primary fuselage structure. Of the several goals of the PRSEUS concept [9], the goal most relevant to this test program is to provide damage arrestment capability for composite structures while reducing overall structural weight. A key feature of the PRSEUS concept is through-the-thickness stitching, which suppresses out-of-plane damage and creates a damage-arresting behavior. This advantage over conventional composite structures allows it to operate at higher strain levels, directly translating into weight savings for structure sized by damage and residual strength requirements.

The development of the PRSEUS concept to date includes testing and analysis by NASA, the USAF, and Boeing. The damage arrestment capability of the PRSEUS concept was demonstrated using a flat panel containing three stringers and two frames with a two-bay saw cut severing the central stringer and the adjacent skin [10]. The results from this tension test revealed that the PRSEUS concept was successful in containing the damage within a two-bay damage zone and was able to sustain 130% of the design limit load (DLL). Additional, subcomponent-level tests of damage arrestment in a minimum-gauge axial tension test panel

[10], out-of-plane loading of a minimum-gauge panel [11], and buckling of a large span [12] were conducted to further validate the PRSEUS concept. Also, a pressure cube was tested to investigate the assembly joints required for application of the PRSEUS concept to large structures [12]. However, additional research is still needed to validate the damage arrestment capabilities of the PRSEUS concept. Of particular interest is the application of the PRSEUS concept to a fuselage structure under combined internal pressure and axial tension loading.

In the current program, NASA, the Federal Aviation Administration (FAA), and Boeing have partnered in an effort to assess the damage-containment features of a full-scale curved PRSEUS panel using the FAA Full-Scale Aircraft Structural Test, Evaluation, and Research (FASTER) facility. The objectives of this joint program were to (1) demonstrate that a curved PRSEUS panel meets the strength and deformation (§305) and damage tolerance (§571) requirements of Title 14 Code of Federal Regulations (CFR) Part 25 [13] and (2) characterize the damage progression of a curved PRSEUS panel. The criteria for evaluating the performance of the panel were sustaining (1) limit loads with no permanent damage and no growth of barely visible impact damage (BVID), (2) ultimate loads without failure, and (3) limit loads with a two-bay notch. The criteria were based on Boeing engineering practice, guidance from FAA Advisory Circulars (AC) 20-107B [14] and 25.571-1D [15], and satisfying the requirements of 14 CFR Part 25, noted above. The PRSEUS fuselage panel was designed and fabricated by Boeing and NASA and tested using the FAA FASTER facility [16]. The fixture was modified to accommodate the PRSEUS panel. The test program included loading and inspections of the panel (1) as-built, (2) with BVID and visible impact damage (VID), and (3) with discrete source damage (DSD) in the form of a two-bay saw cut. During the test, various mature and developmental nondestructive inspection (NDI) methods were used to monitor and record the extent of damage, including high-resolution visual, digital image correlation (DIC), acoustic emission (AE), thermography, and ultrasound. Detailed post-test examinations using NDI techniques and destructive teardown evaluations were conducted in stable damage growth regions to identify dominant failure mechanisms for use in future progressive failure analysis.

2. BACKGROUND ON COMPOSITE STRUCTURAL CERTIFICATION.

Composite structure certification is based on the strength, deformation, and damage tolerance requirements of 14 CFR 25. Guidance for an acceptable means of showing compliance with airworthiness certification requirements for composite aircraft structures is available in FAA AC 20-107B.

Damage tolerance evaluation must show that catastrophic failure due to fatigue, environmental effects, manufacturing defects, or accidental damage will be avoided throughout the operational life of the aircraft. The damage tolerance design requirements are addressed with design requirements for load levels, where increasing damage severity requires a lower sustained load, as depicted in figure 1. The damage tolerance and design load requirements are used to define the allowable damage limit and the critical damage threshold (CDT). The structure may have allowable (undetectable) damage provided the design ultimate loads are sustained. The CDT defines damage that is easily detected and must be repaired immediately after flight.

Because of the large number of possible damage scenarios, AC 20-107B recommends conducting a damage threat assessment and suggests classifying damage into the following five categories:

- Category 1 damage: Allowable damage that may go undetected. The structure must sustain ultimate loads with Category 1 damage. Some examples of Category 1 damage include BVID and allowable manufacturing defects. Substantiation data must show ultimate load capability is retained for the life of the aircraft structure.

- Category 2 damage: Reliably detectable damage. The structure must sustain loads above limit load, with exact residual strength requirement dependent on inspection method and interval. Some examples of Category 2 damage include VID, detectable delamination or debonding, and visibly significant local heat or environmental degradation.

- Category 3 damage: Reliably detectable by untrained personnel. The damage must be in a location such that it is obvious by clearly visible evidence. Structural substantiation requires reliable and quick damage detection while retaining limit or near-limit load capability. Some examples of Category 3 damage include large VID or other obvious damage that will be noticed during walk-around inspection.

- Category 4 damage: The DSD from a known incident. Structural substantiation requires that the structure retain damage-tolerant load capability. Some examples of Category 4 damage include rotor burst, bird strikes, tire bursts, and severe in-flight hail.

- Category 5 damage: Severe damage created by anomalous ground or flight events that are not covered by design criteria or structural substantiation procedures.

In this study, the load requirements to sustain categories 1, 2, and 4 damage severity, shown in figure 1, will be demonstrated.

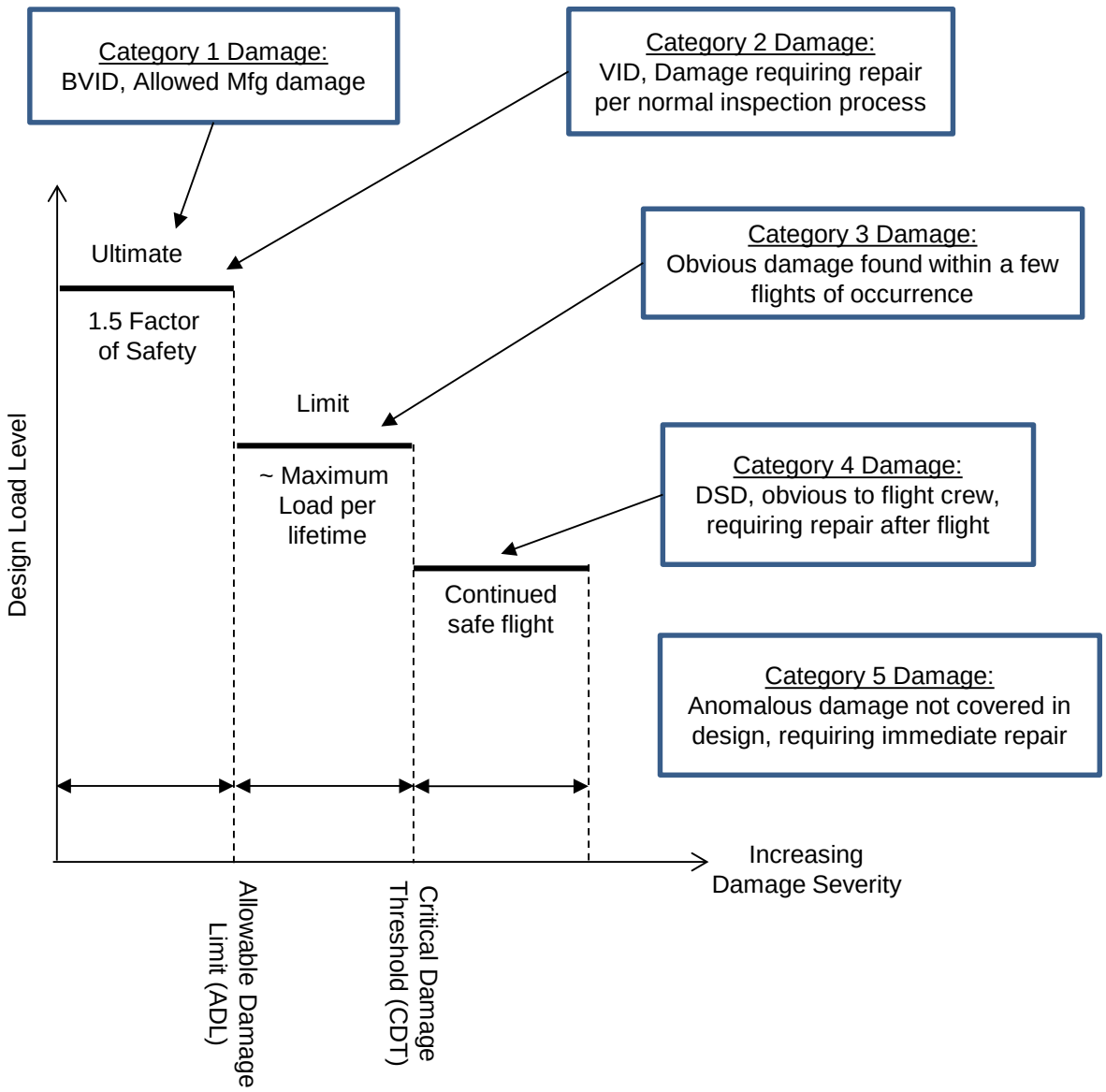

Figure 1. Increasing Damage Severity Requires Lower Sustained Loads

3. TEST PANEL DESIGN AND PREPARATION.

The test panel geometry, materials and layup, load introduction reinforcements, and the fabrication process are highlighted in the subsections below. Complete details are available in reference 17.

3.1 GEOMETRY.

The fuselage test panel has a 90-inch radius, 127-inch length, and 75-inch width with seven full-length rod-stiffened stringers and five frames, as shown in figure 2(a). The stringer spacing was 7.8 in. and the frame spacing was 24 in. The section region, highlighted in blue in figure 2(a) and enclosed by stringers S-1 and S-7 and frame F-2 and F-3, represented a section of an

aircraft fuselage. The nominal skin thickness in the test section was 0.052 inch, which is a minimum-gauge thickness for a 55 ksi operating stress level.

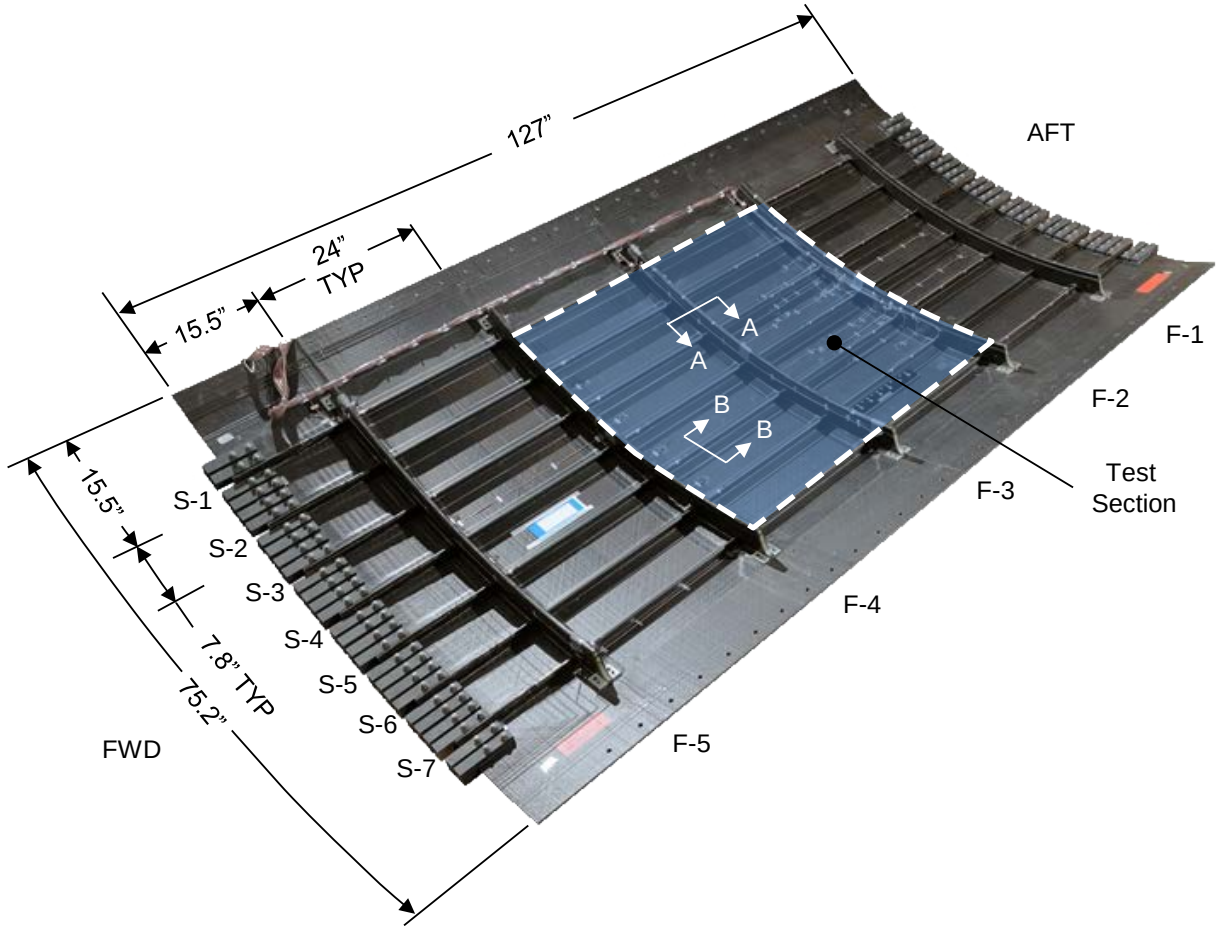

(a)

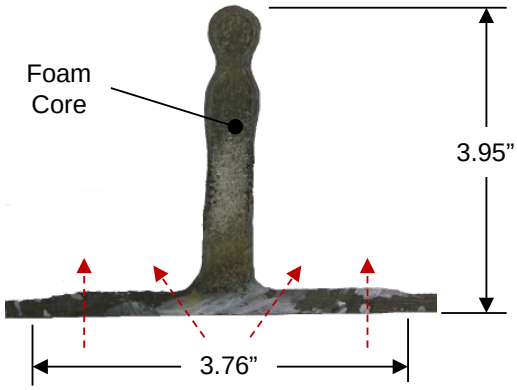

(b)

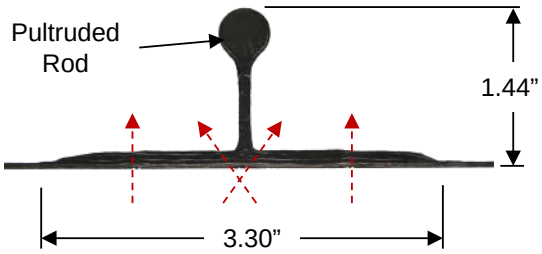

(c)

Figure 2. Overall Panel Geometry Showing the Interior Surface and Substructure (a) Test Panel Interior Surface, (b) Frame Cross Section A-A, and (c) Stringer Cross Section B-B

All areas outside of the test section contained additional plies for load introduction purposes. The skin was assembled in three pieces with splices under the second and fourth frames, F-2 and F-4, respectively. The splices were stitched using a two-sided stitching process with Vectran® thread.

The panel substructure comprises integrally stitched frames and stringers, as shown in figures 2(b) and 2(c). The frames were formed around a 0.5-inch-thick foam core support with a 3.8-inch-wide tear strap at the base. The top of the frame was reinforced with a frame cap. The detailed frame cross-section geometry, including the single-sided frame stitching attaching the frame flange to the skin, is shown in figure 2(a). The stringers are formed with a pultruded rod for high structural efficiency. The detailed stringer cross-section geometry, including the single-sided stringer stitching attaching the stringer flange to the skin, is shown in figure 2(b). Complete engineering drawings of the panel are available in appendix A.

3.2 TEST LOAD INTRODUCTION REINFORCEMENTS.

Doublers were co-cured with the panel to reinforce the load introduction areas at the axial and hoop edges as well as the frame and stringer terminations, as shown in figure 3. Transitions between the doubler regions and the test section were tapered to maintain a constant neutral axis from the load introduction region to the test section. Doublers were also added to the frame ends. Because high peel stresses were anticipated in this region because of the test setup, bolted radius blocks were also added locally at each frame end to tie the frame flange to the skin, as shown in figure 3. The axial edge skin doublers were interleaved, as shown in figure 4, with four stringer doublers to aid in transferring load into the pultruded rod.

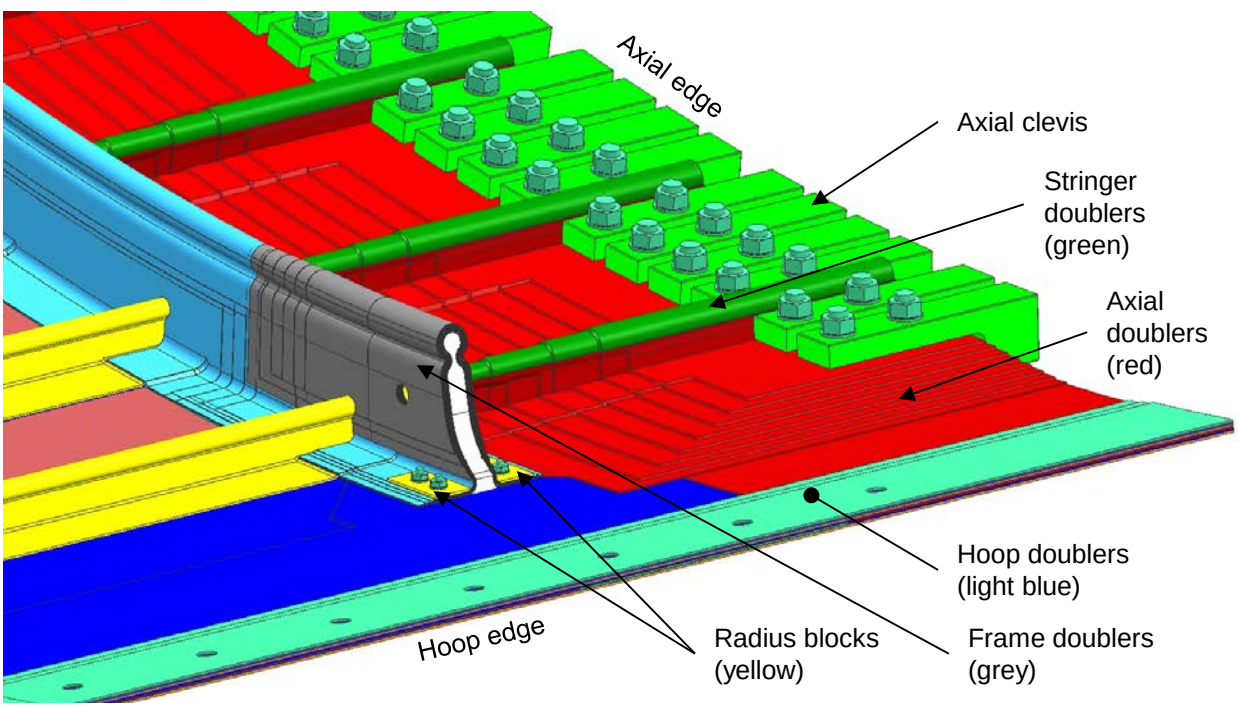

Figure 3. Load Introduction Doublers and Radius Blocks

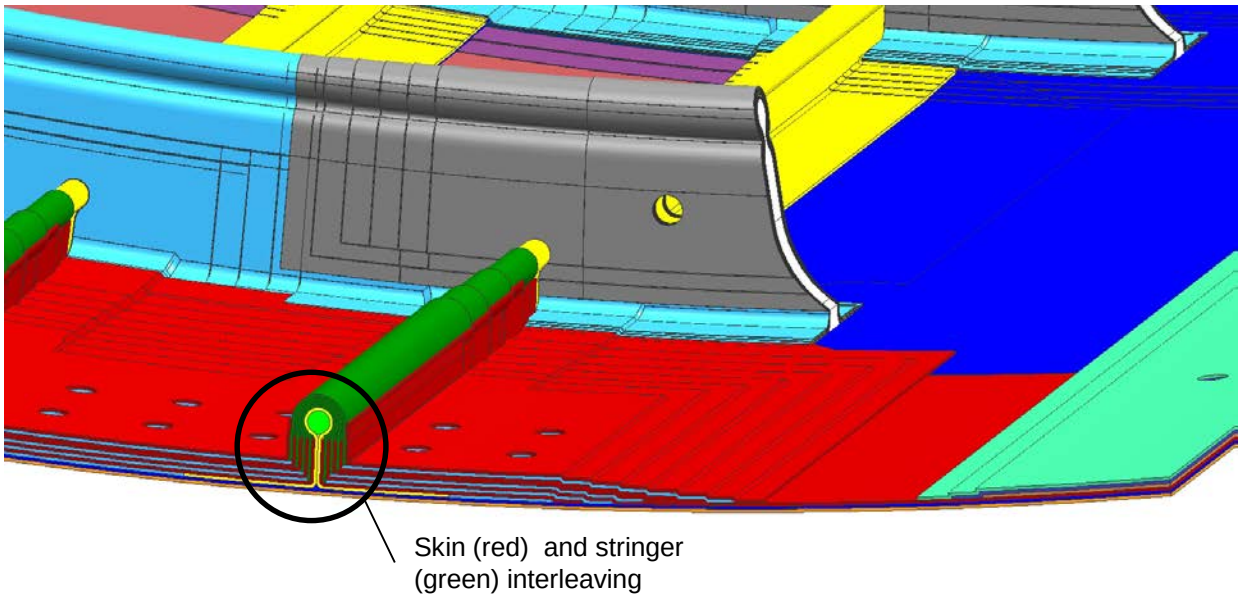

Figure 4. Detail of Skin/Stringer Doubler Interleaving

3.3 MATERIALS AND LAYUP.

The test panel dry preform was fabricated using multiaxial, warp-knit, dry carbon fiber fabric. The fibers used in forming the warp-knit fabric were standard modulus AS4 carbon fiber. The layups used in the test section of the panel are summarized in table 1 for each region, with the layups given in terms of the global coordinate system where the 0° direction is aligned with the stringers. The foam core in the frames was made of Rohacell 110 WF. The stringer rods were made of a pre-cured Toray T800/3900-2B fiber/resin. A 0.0054-inch-thick, 0/90 plain weave fiberglass ply was used on the exterior surface of the skin as a galvanic corrosion barrier. The frame flanges, frame tear straps, stringer flanges, and stringer tear straps were stitched to the skin using a one-sided 3D modified lock-stitched stitching technique with 1,200-denier Vectran thread at five penetrations per inch. The stringer web and skin splices were stitched using a conventional two-sided stitching technique with the same thread.

Table 1. Laminate Definitions

Laminate	Layup % (0/45/90)	Thickness (in.)
Skin	12/43/45	0.052
Stringer Wrap	45/43/12	0.052
Stringer Tear Strap	45/43/12	0.052
Frame Web	0/100/0	0.031
Frame Tear Strap	12/43/45	0.052
Frame Cap	33/33/33	0.094

3.4 FABRICATION AND INSPECTION.

The panel was fabricated in the Marvin B. Dow Stitched Composites Development Center at the Boeing facility in Huntington Beach, California, using existing tooling from a prior PRSEUS project [17]. The panel fabrication began with preassembly of the frames and stringers and was followed by preform assembly. With final assembly completed, the preform was then placed in the mold tool. The preform was infused with Hexflow VRM-34 epoxy resin and cured, using a Boeing proprietary process called controlled atmospheric pressure resin infusion [18], which is an out-of-autoclave, low-pressure process that results in higher fiber volume fractions than the conventional vacuum-assisted resin transfer molding process [9]. The load attachment holes were drilled around the perimeter of the panel and through the frame ends.

The skin, frame and stringer flanges, and edge-doubler regions of the panel were then inspected by Boeing using through-transmission ultrasound (TTU) at 5.0 MHz. No defects were identified. The mean average dB levels were consistent over the entire panel, with actual deviation at any one location within the acceptable ±6 dB allowed variation.

3.5 PANEL PREPARATION AND ATTACHMENT TO FIXTURE.

The axial load whiffle trees attached the panels via clevises at 28 points on each of the panels. The clevises were shimmed to align the load introduction whiffle trees with the neutral axis of the panels to minimize bending of the panels. All load attachment points were bolted connections with bushings used at the frame attachment points.

The exterior and interior surfaces enclosed by the outermost stringers and frames were painted white so that damage would be more visually evident because of the contrast between the white paint and black carbon fiber.

A modular seal that included four molded corners, 14 molded stringer pieces, and several straight pieces was assembled and bonded to the panel using PR-1422 Class B fuel tank sealant. The molded stringer pieces made of polyurethane and the straight pieces were made of ethylene propylene diene monomer rubber. All bonded joints used a fiberglass scrim to maintain uniform adhesive thickness. The panel with seal and clevises attached, ready for installation on the fixture, is shown in figure 5.

Figure 5. One End of the Panel With Clevises and Seal Attached

4. FASTER FIXTURE MODIFICATIONS.

The FASTER fixture was originally designed for accelerated fatigue studies of metallic fuselage structures [16]. The fixture can apply combined internal pressure and axial load with appropriate hoop reactions to narrow- and wide-body fuselage panels. For the purpose of conducting the PRSEUS panel test, the FASTER fixture was modified to accommodate a PRSEUS panel, including the enhanced axial load capacity required to apply catastrophic failure loads. The modified axial loading mechanism operated using hydraulic jacks with a standalone hydraulic system, controlled by the existing computer control system. The modified FASTER fixture used two sets of seven axial loaders aligned with the stringers at each end of the panel, two sets of seven hoop loaders along each straight edge of the panel, and two sets of five frame loaders connected directly to the frame ends to apply load. Complete details can be found in Bergan et al. [19]. A brief description of the modification is provided below.

The FASTER fixture modifications include accommodations for a larger panel radius, a modular seal for full-length stringers, a frame loader slide system for large axial displacements, and an increased axial load capacity. A comparison of the existing fixture and modified fixture is shown in figure 6, highlighting the new axial load mechanism. The axial loading features of the modification are discussed in the following subsections.

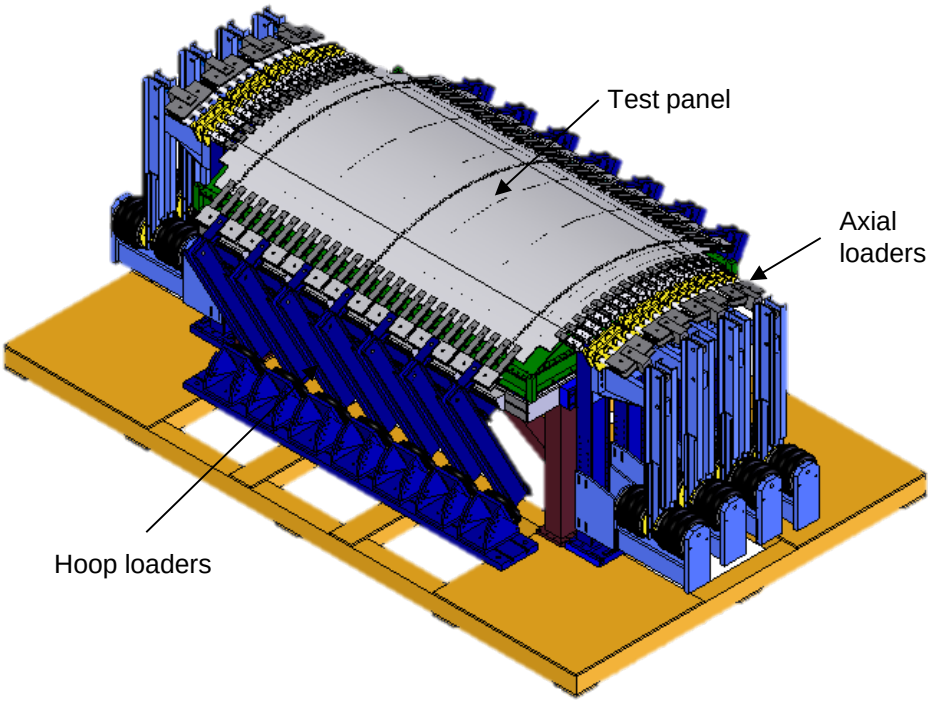

(a)

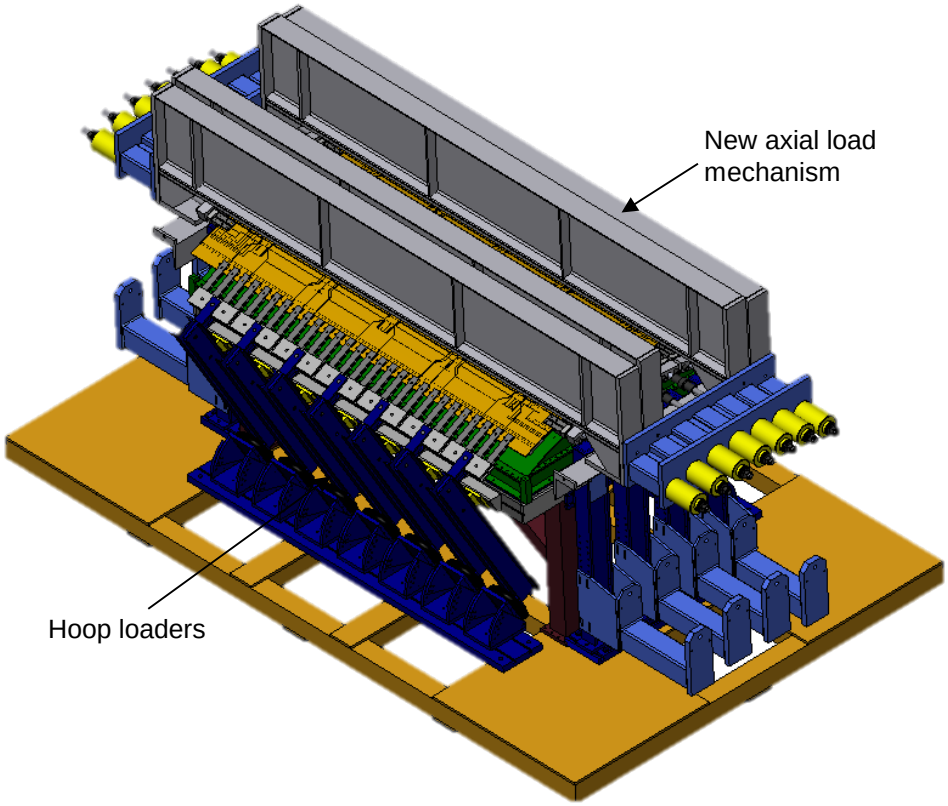

(b)

Figure 6. Comparison of (a) Existing FASTER Fixture and (b) Modified FASTER Fixture

4.1 FRAME LOADER SLIDE SYSTEM.

Initial test predictions showed an overall axial displacement of up to 0.25 inch between the outer frames (F-1 and F-5). In the original FASTER fixture configuration, this displacement would have induced large reaction forces into the frames due to the rigid frame loader design, which are not characteristic of flight loads. A frame-loader slide system was designed that allows the frame loaders to move freely in the axial direction, avoiding nonflight loads, as shown in figure 7.

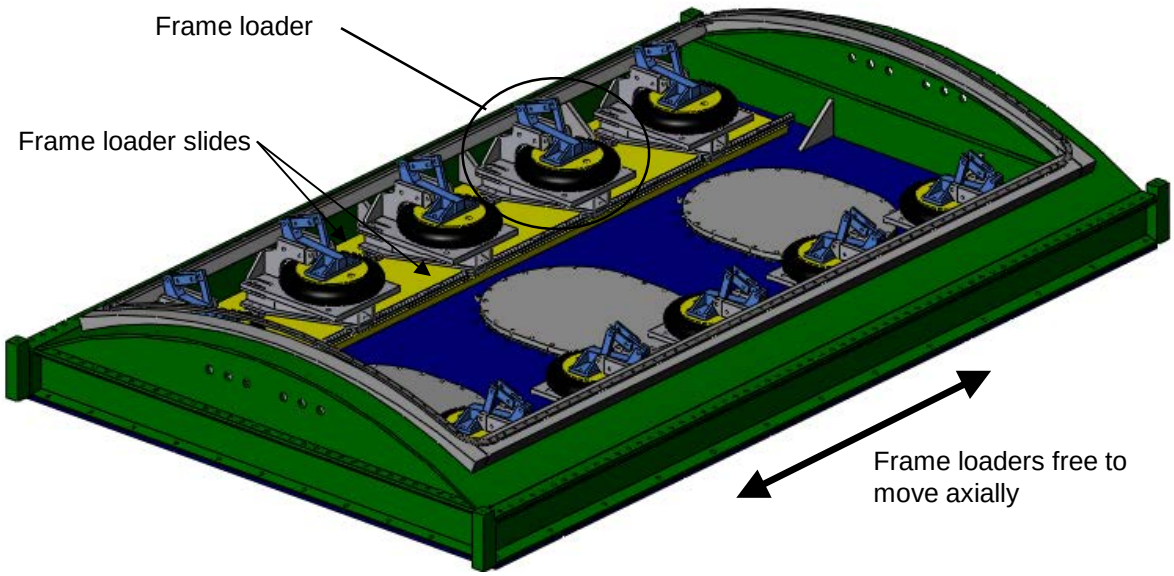

Figure 7. Frame-Loader Slide System

4.2 AXIAL LOAD MECHANISM.

Failure loads for the PRSEUS panel were predicted to exceed the original FASTER fixture axial load capacity of 100 kips. A new axial load mechanism was designed with a capacity of 840 kips to catastrophically fail the PRSEUS test panel, based on results from other PRSEUS tests [17]. The significant increase in axial load capacity was accomplished using fourteen 60-ton hydraulic jacks connected to each end of the panel, each with a whiffle tree assembly, as shown in figure 8(a and b). The axial load is reacted by four built-up beam columns, which measure 178 inches long and 24 inches tall, each weighing approximately one ton. A detailed view of a single axial load whiffle tree assembly is shown in figure 8(c).

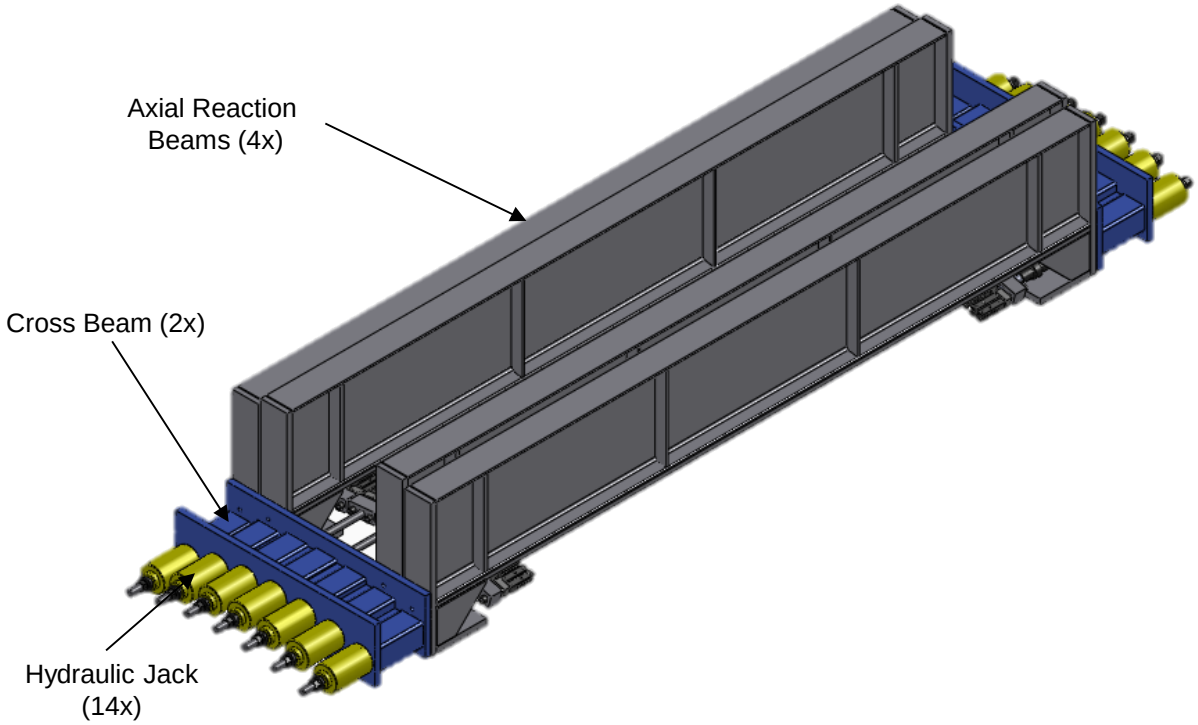

(a)

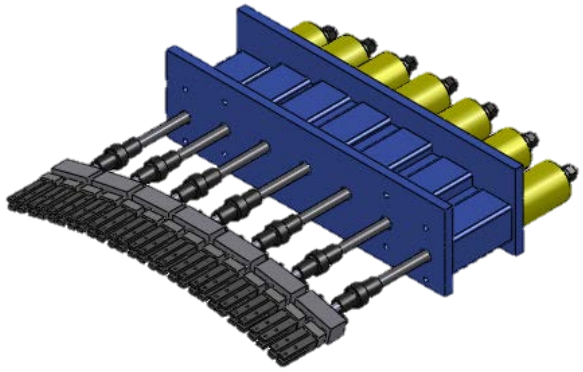

(b)

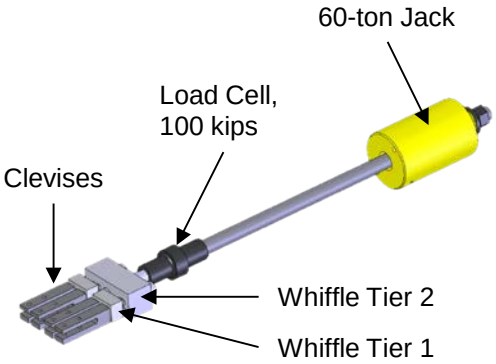

(c)

Figure 8. The (a) Axial Loading Mechanism Assembly, (b) Cross Beam With Seven Load Trains, and (c) Single Load Train Subassembly

5. EXPERIMENTAL PROCEDURE.

5.1 TEST PHASES AND LOAD HISTORY.

The tests were conducted in three separate phases, each having its own goal and loading sequence, as described below. In each phase, three load cases were applied, namely: (1) axial load, (2) internal pressure, and (3) combine loading (axial and pressure), as summarized in table 2. The load conditions applied during each phase were to demonstrate compliance with the

strength, deformation, and damage-tolerance requirements of Title 14 CFR Part 25. Pressure loads were based on an operating pressure of 9.2 psi, designated as 1.0 P, and the axial loads were based on a DLL of 227 kips. Three different pressure levels were applied: 1.0 P, 1.33 P, and 2.0 P, simulating internal cabin pressure differentials of operating pressure, cabin pressure, and ultimate cabin pressure, respectively. Loading was monotonic for all tests, applied under constant loading and pressure rates of 50 kip/min and 3 psi/min, respectively. In all combined load cases, the pressure load was applied and stabilized first before applying the axial load. This sequence was reversed upon unloading.

Table 2. Test Sequence

	Load Condition	Relative Applied Loads*	
		Axial (% DLL)	Pressure (% P)
Phase I	Axial	100	-
	Combined	100	100
	Pressure	-	133
Phase II	Axial	100	-
	Pressure	-	133
	Combined	100	100
	Pressure	-	200
	Axial	150	-
	Combined	150	150
Phase III	Pressure	-	115
	Combined	100	100
	Axial	100	0
	Failure	184	100

*Loads relative to limit load magnitude.

5.1.1 Phase I: Pristine Case.

Phase I test results provided a baseline by applying (1) 50% limit load levels for each of the three load cases (not shown in table 2) to verify proper load introduction and repeatability by examining strain and displacement results and (2) three limit load conditions: limit pressure of 12.2 psi (1.33P), axial DLL of 227 kip, and combined 1P pressure and axial DLL to demonstrate compliance with the limit strength and deformation requirement of 14 CFR 25.305. For the combined load case, pressure load was applied and stabilized, then axial load was applied to the target load; this sequence was reversed for unloading.

5.1.2 Phase II: BVID Case.

The purpose of phase II tests was to demonstrate that the panel with BVID met the ultimate strength and deformation requirement of 14 CFR 25.305 and guidance of AC 20-107B. The

damage was created using a drop-weight impactor with a 25-lb weight and 1-inch-diameter hemispherical tup impactor. The location of the BVID was over the central stringer, S-4, between frames F-2 and F-3, as shown in figure 9. An impact, with 40-ft-lb impact energy, was applied to a location between the central-stringer flange edge and the outer-stitch row, as shown in figure 9(b and c). A padded paddle was used to catch the tup after recoiling to prevent secondary impacts.

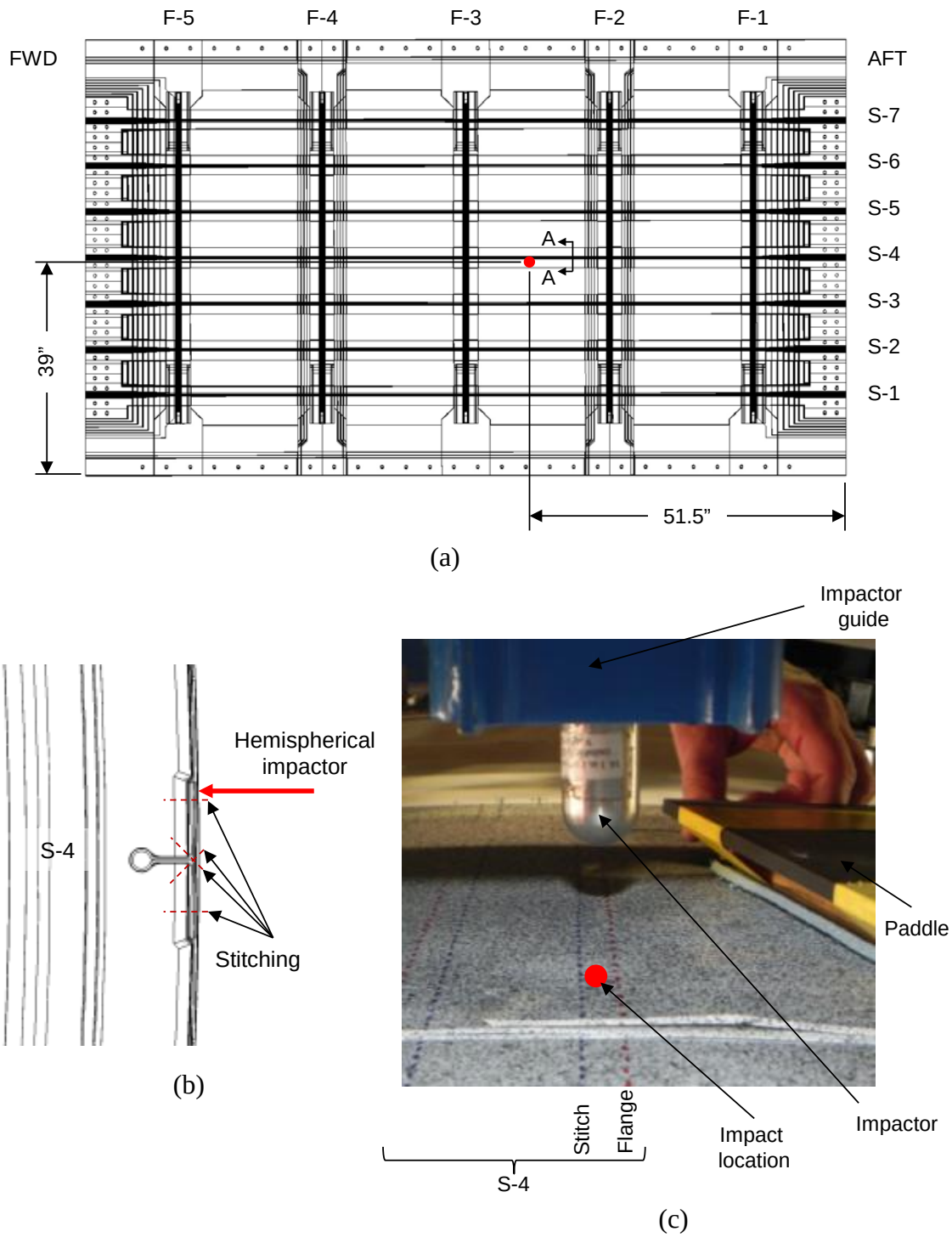

Figure 9. Phase II BVID Location and Test Setup: (a) BVID Location, (b) Cross Section A-A BVID Location Detail, and (c) BVID Setup Photo

5.1.3 Phase III: Two-Bay Notch Damage Case.

The purpose of phase III was to demonstrate compliance with 14 CFR 25.571 by showing that the panel could support limit loads with a two-bay notch severing the central stringer, and then to monitor the failure process while increasing the axial load until catastrophic failure occurred. The notch was machined over the BVID at the location shown in figure 10(a) using a 5/16-inch router bit and a machining template. The impact damage site was partially removed during the notch machining to minimize the effects on phase III results, as shown in figure 4(b). The notch was 7.8-inch long by 0.31-inch wide and was placed symmetrically across stringer S-4, as shown in figure 10(b). The notch was through the thickness and severed both the skin and the central stringer, as shown in figure 10(c and d), respectively. Complete details of the notch machining are provided in appendix D.

After the notch was machined, the panel was subjected to limit load conditions, followed by combined 1P pressure while increasing axial tension load to catastrophic failure. The final load sequence to failure incorporated a complex load history, so all target load conditions were achieved without completely unloading the panel, to eliminate concerns of additional damage formation during unloading. The load history included five load steps (LS), which are summarized in table 3. The panel was subjected to the three limit load conditions in the order of increasing severity, as predicted by the pretest analytical model [17]: pressure (1.15P), combined pressure and axial (1P + DLL), and axial (DLL) load conditions; this was followed by maintaining pressure (1P) and increasing axial load to catastrophic failure.

Table 3. Phase III Load Steps

Load Step	Load Levels		Load Changes
	Axial (% DLL)	Pressure (% P)	
1	--	115	Pressure increased to 1.15P
2	100	100	Pressure reduced to 1P then axial load increased to DLL
3	100	--	Axial reaction to pressure removed, then pressure removed
4	100	100	Pressure increased to 1P
5	184	100	Axial load increased to catastrophic failure

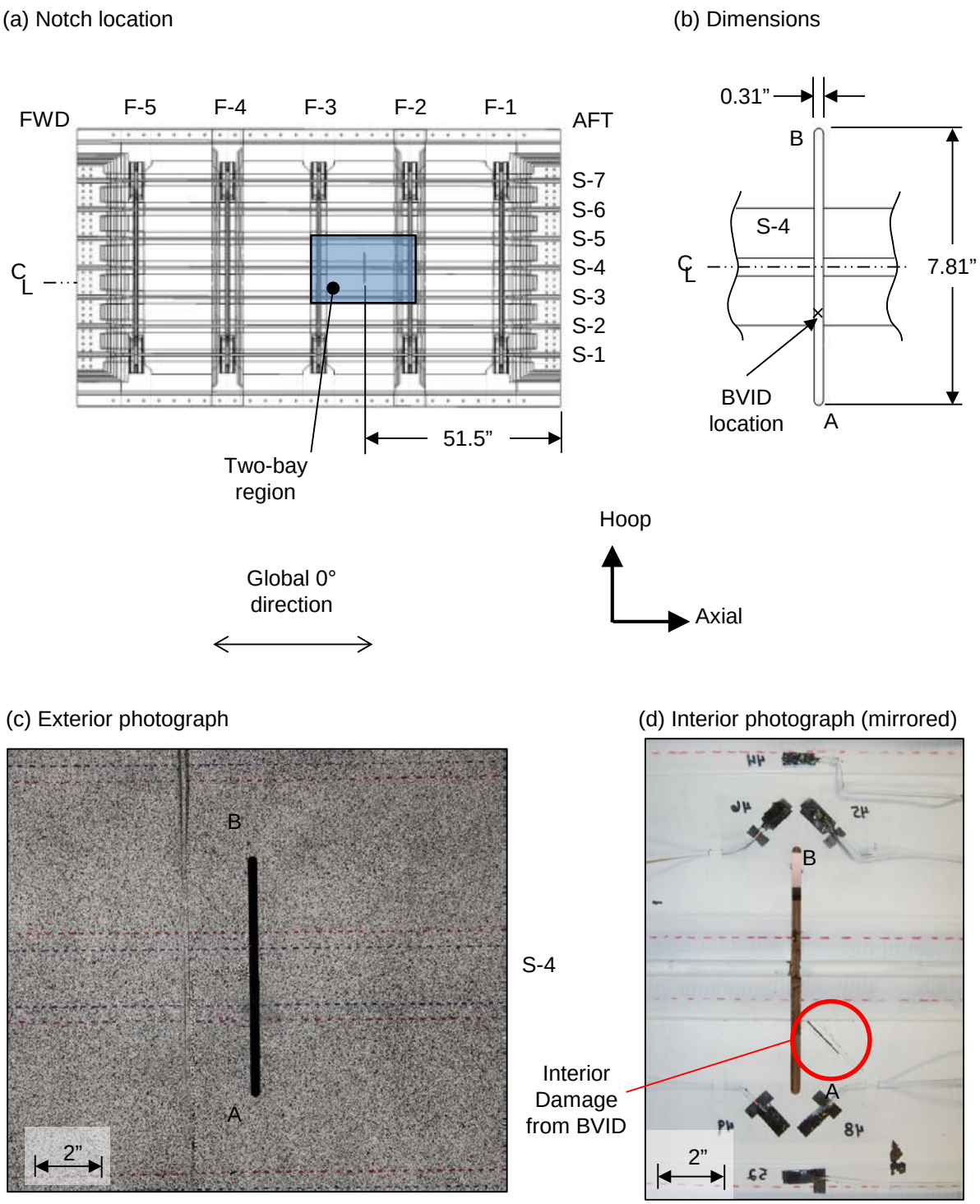

Figure 10. The Two-Bay Notch: (a) Notch Location, (b) Dimensions, (c) Exterior Photograph, and (d) Interior Photograph (mirrored)

5.2 INSPECTION AND MONITORING METHODS.

Deformation and damage were monitored throughout the three phases of the test program, employing several nondestructive examination techniques.

5.2.1 Visual Inspection.

Visual inspection tools were used for monitoring panel behavior during the test and included interior and exterior video cameras, a high-resolution exterior still camera, and two high-speed video cameras, as shown in figure 11. The two high-speed cameras were used only during Phase III to record the rapid crack progression. Complete details of the camera setup can be found in appendix C.

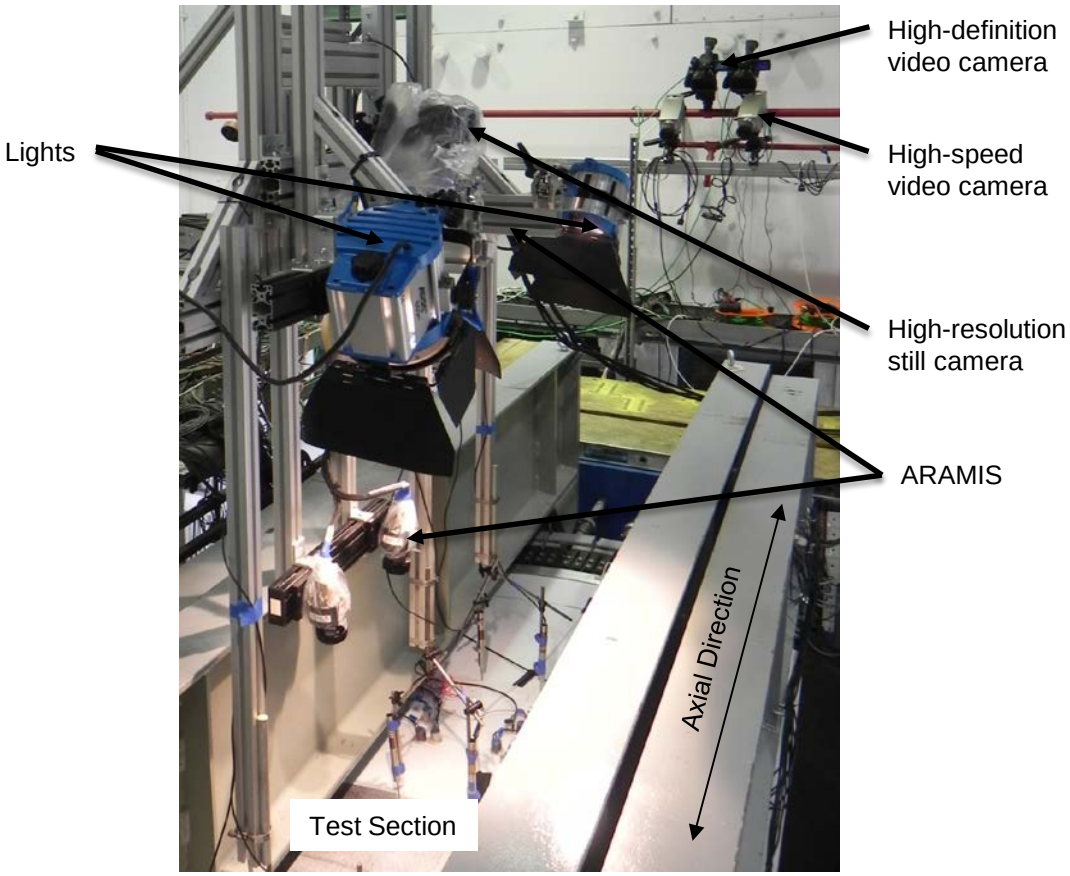

Figure 11. Photograph of the Visual Monitoring Setup

5.2.2 Strain and Displacement.

Eighty strain gages, 11 linear variable differential transformers (LVDTs), and two ARAMIS™ [20] DIC systems were used to record strain, displacement, and deformation data. Complete details can be found in appendix B. The test panel was instrumented with strain gages in the axial, hoop, and 45° directions to monitor real-time strain distribution, ensure proper load introduction from the load-application points, and monitor strains in critical regions. The strain gage locations and orientations on the exterior and interior surfaces are shown in

figures 12 and 13, respectively. Several strain gages were installed in a back-to-back configuration to monitor the bending response of the panel. Interior strain gages were coated with PR-1422 class B fuel tank sealant to operate underwater because water is the pressurization medium used in the FASTER fixture. The maximum limit of the strain gages was 3%.

The LVDTs measured the axial and radial displacements and are shown on the exterior of the panel in figure 12. The LVDT 1 was mounted on a frame so that it measured the displacement between the two points shown, whereas all other LVDTs measured displacements relative to ground. Measurements from LVDT 1 and LVDT 2 were used to eliminate axial rigid-body motion from the results. During the test, all strain and displacement data were recorded at a rate of 10 Hz.

Each of the two DIC systems had two 4-megapixel cameras and were capable of accurately measuring full-field strain within 50με. The global measurements provided means for validating the finite-element-based predictions, and the local strain fields, ahead of the notch tips, provided an indication of incipient damage and damage progression. The DIC recording was terminated in phase III when damage initiated because water was seeping out of the pressure chamber as a result of membrane failure.

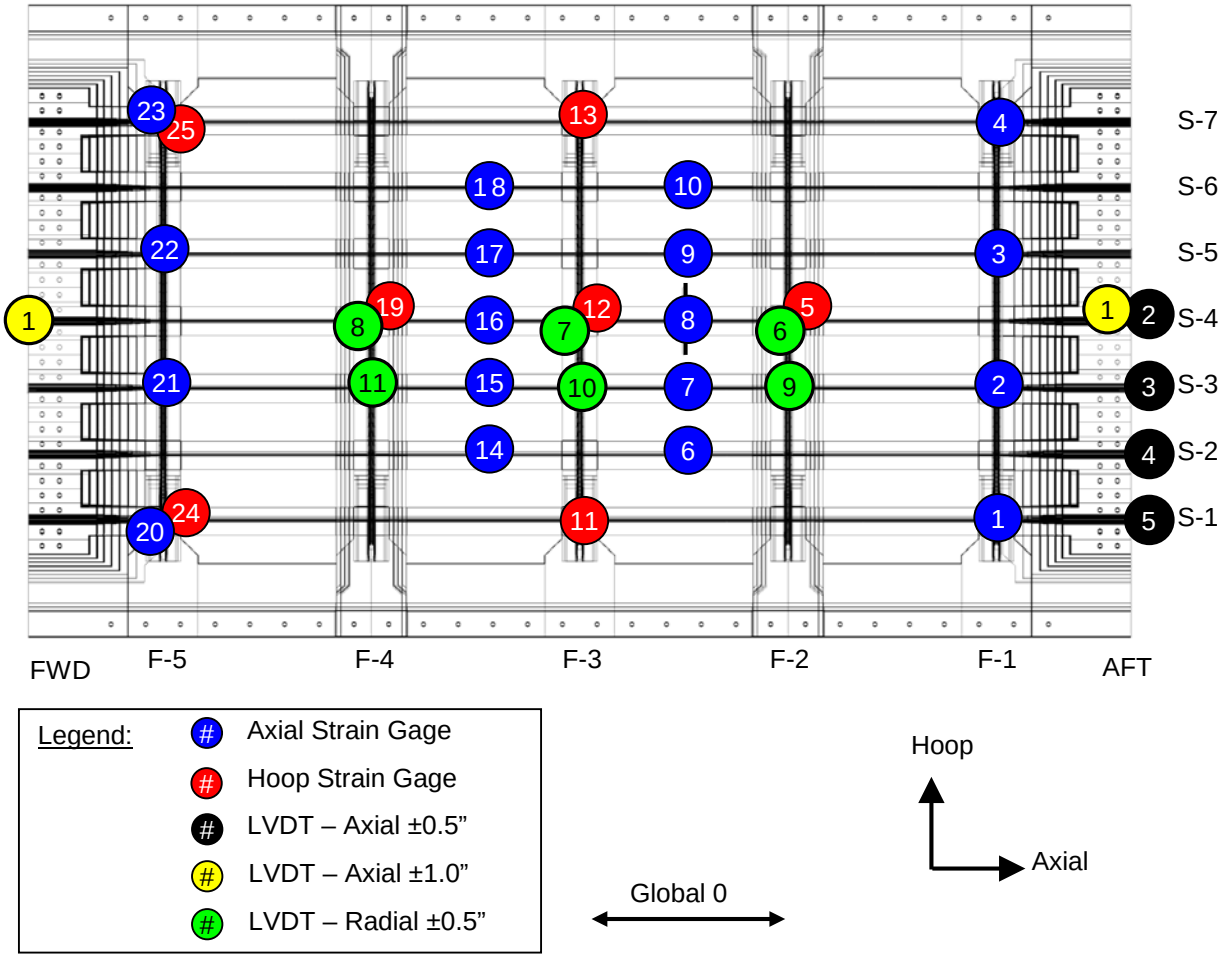

Figure 12. Exterior Strain Gage and LVDT Locations

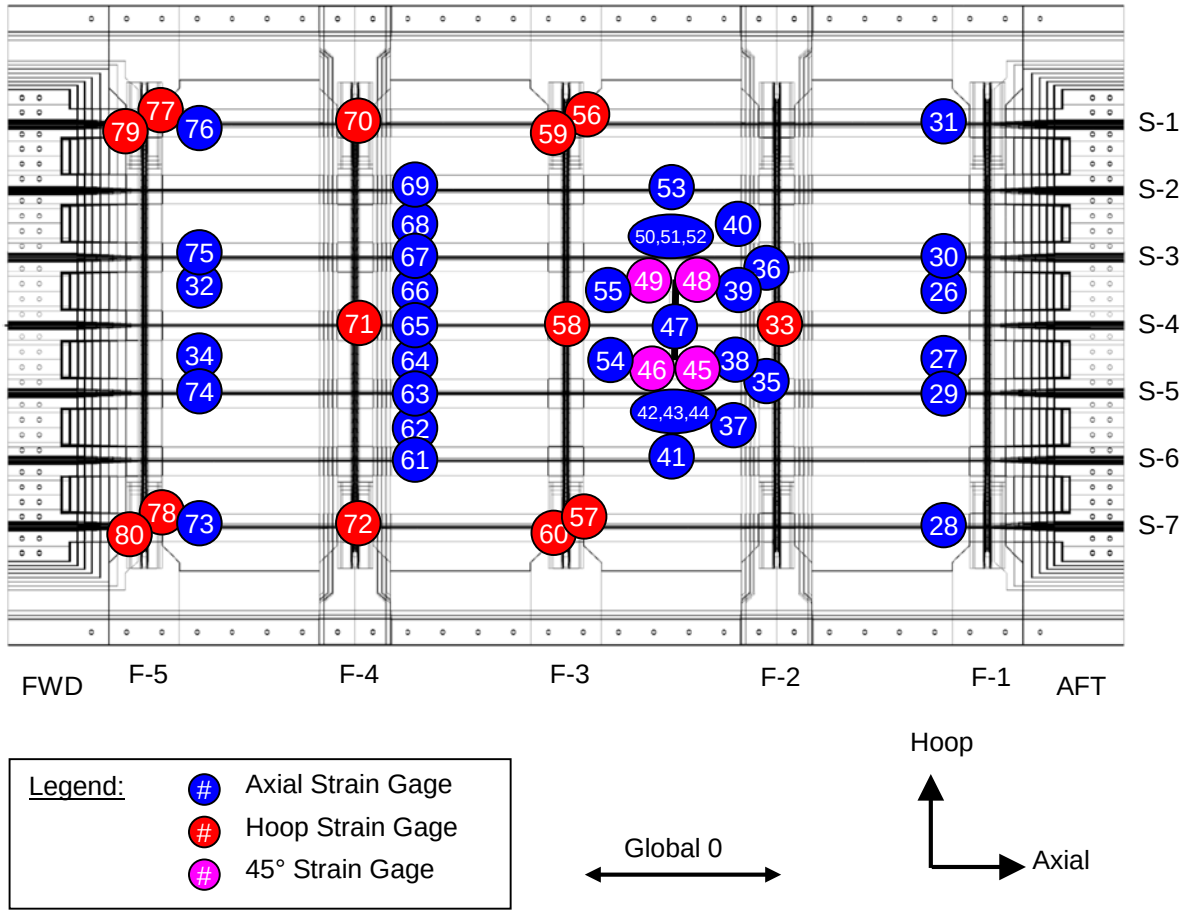

Figure 13. Interior Strain Gage Locations

5.2.3 Pulse-Echo Ultrasound.

Pulse-echo ultrasonic scans were taken using a linear phased array at 10 MHz for the purpose of determining the extent of nonvisible damage due to the BVID and potential damage accumulation in subsequent loading. The Olympus OmniScan MX2 with PA16/128 module was used in conjunction with a 10L64-I1 sensor in a NASA-captured water column mounting, as shown in figure 14. Scans were performed using a Sonix 18-in. x 18-in. manual scanner positioned with the index axis in the axial direction, so the scan axis was in the hoop direction of the panel. Scans were taken after the completion of phase 1, after impact, and after application of each load condition in phase II.

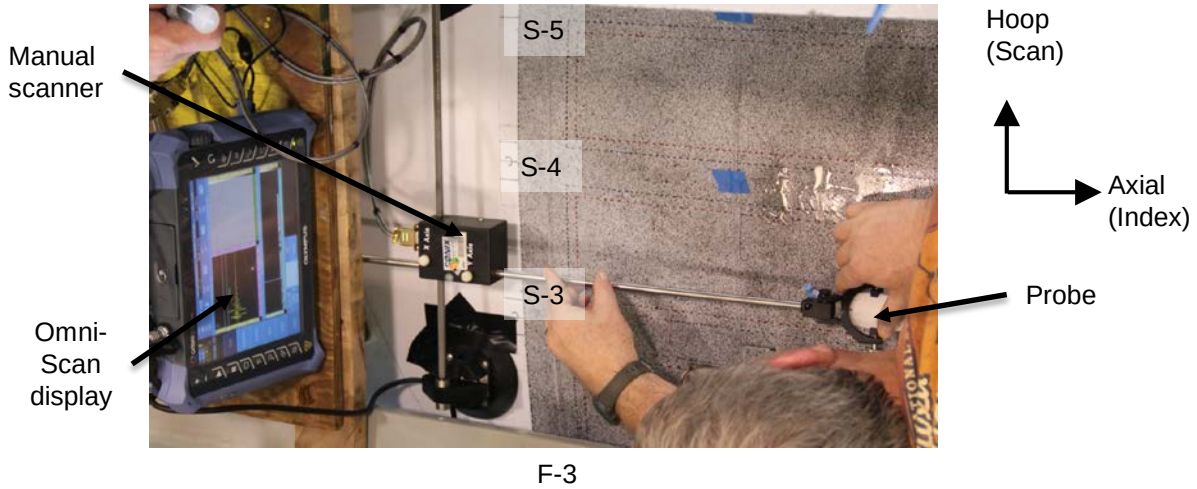

Figure 14. Pulse-Echo Linear Phased-Array Ultrasound Setup

5.2.4 Flash Thermography.

A flash-thermography system was used to inspect the test section for nonvisual damage, as shown in figure 15. The system consists of a computer that contains data-acquisition hardware and software connected to a flash lamp heat source and thermal infrared camera. A baseline scan of the panel was taken prior to phases I, II, and III. During phase II, scans were taken after each load condition. After catastrophic failure, a scan was taken of the entire width of the panel between frames F-2 and F-3.

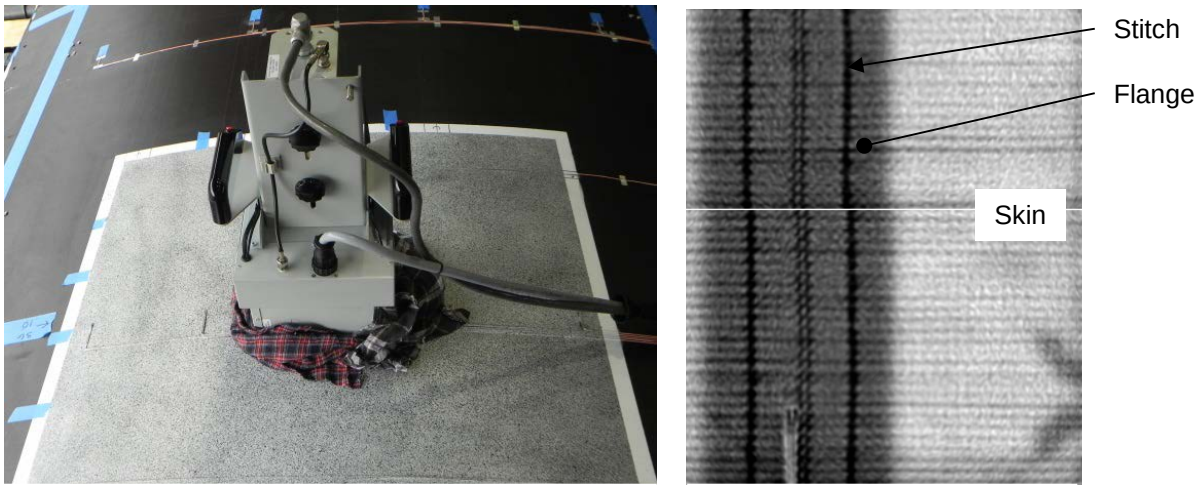

(a) (b)

Figure 15. The FASTER Lab Flash Thermography System: (a) Heat Source and Camera and (b) Sample Result

5.2.5 The AE Method.

The AE method is a passive, real-time nondestructive evaluation method, which uses a system of sensors to monitor internal stress waves resulting from damage formation and propagation within a material.

The AE was monitored using a 16-channel Physical Acoustics Corporation system, with two eight-sensor sets (resonant R15I and wideband WDI) mounted on the panel along a 610 mm and 710 mm diameter circle centered on the notch, as shown in figure 16. The AE was monitored throughout phase III of testing. Sensor placement was dictated by the panel substructure and space availability to provide adequate clearance for other inspection methods during the test. The sensors were mounted using hot glue and calibrated using pencil-lead break tests with a wave speed of 5100 m/s. The AE data acquisition was conducted using a hit-based approach with a 40 dB threshold. A hit-definition time of 0.5 ms and hit-lockout time of 0.5 ms were used throughout the test. Waveform data were collected at a maximum sampling rate of 3 Mhz. Maximum waveform duration was set at 100 ms, with pre-trigger of 0.2 ms. An analog filter of 20 kHz low pass and 400 kHz high pass was used during data acquisition.

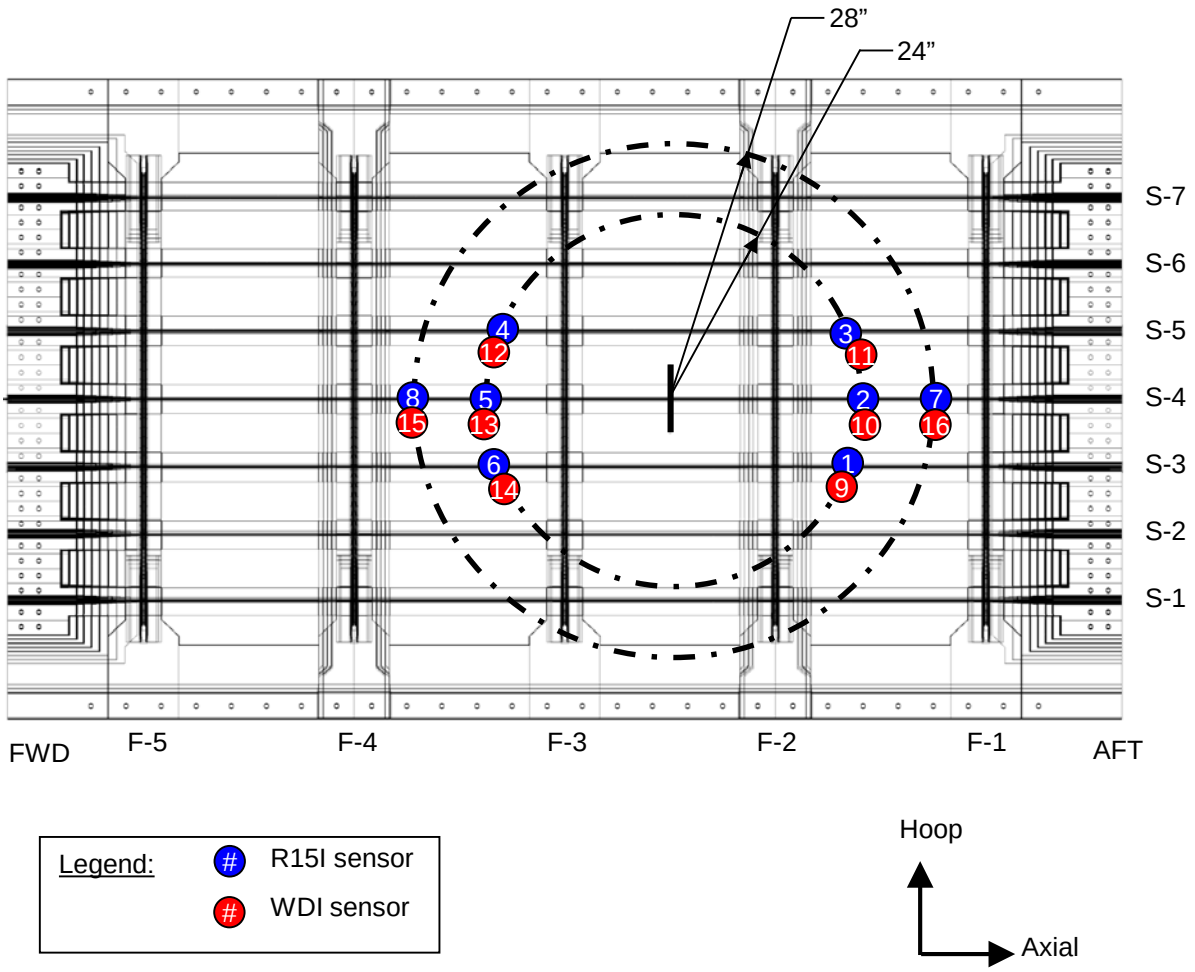

Figure 16. Test Panel Showing the Location of the AE Sensors Mounted Along 24-Inch and 28-Inch Concentric Circles

The location of the events is determined by the AE system, using the standard triangulation algorithm. However, in full-scale tests of composite structures, the excessively large number of hits obscures the emission of interest generated by the local damage formed ahead of the notch tips. Feature-based filtering of the data based on ranges of amplitude, duration, counts, or energy content has been used often; however, the rationale for selection of the proper intensity ranges remains unclear and dependent on the user’s experience. Redundant measurements of the planar source location, known as the n-hit event approach, provide a promising alternative. This procedure is superior because primarily high intensity AE signals are retained because of the redundancy, thus offering more confidence in the accuracy of the source location [21].

5.2.6 Post-Test NDI.

A variety of NDI techniques, including pulse-echo, resonant and through-transmission ultrasound, thermography, and computed tomography (CT), were used to identify and characterize the location, size, and extent of the damage in selected segments of the panel between stringer S-4 and S-7. These inspections were performed at Sandia National

Laboratories in Albuquerque, New Mexico. The purpose of these inspections was specifically to determine the size and location of delamination near the notch tip and along the stringer and frames. The 24-in. x 16-in. inspected region included frames F-2 to F-3 in the axial direction and the notch tip to stringer S-6 in the hoop direction. These inspections included:

- Pulse Echo Ultrasound, using a Mobile Automated Ultrasonic Scanner (MAUS) V system, as shown in figure 17: The pulse-echo inspection provided amplitude and time-of-flight results. The pulse-echo scan was performed at 5 MHz using a 0.25 inch diameter, delay-line probe, which is a common choice for composite based on typical flaw size. The MAUS V system was programmed to increment 0.06 inch in the axial direction after each pass in the hoop direction.

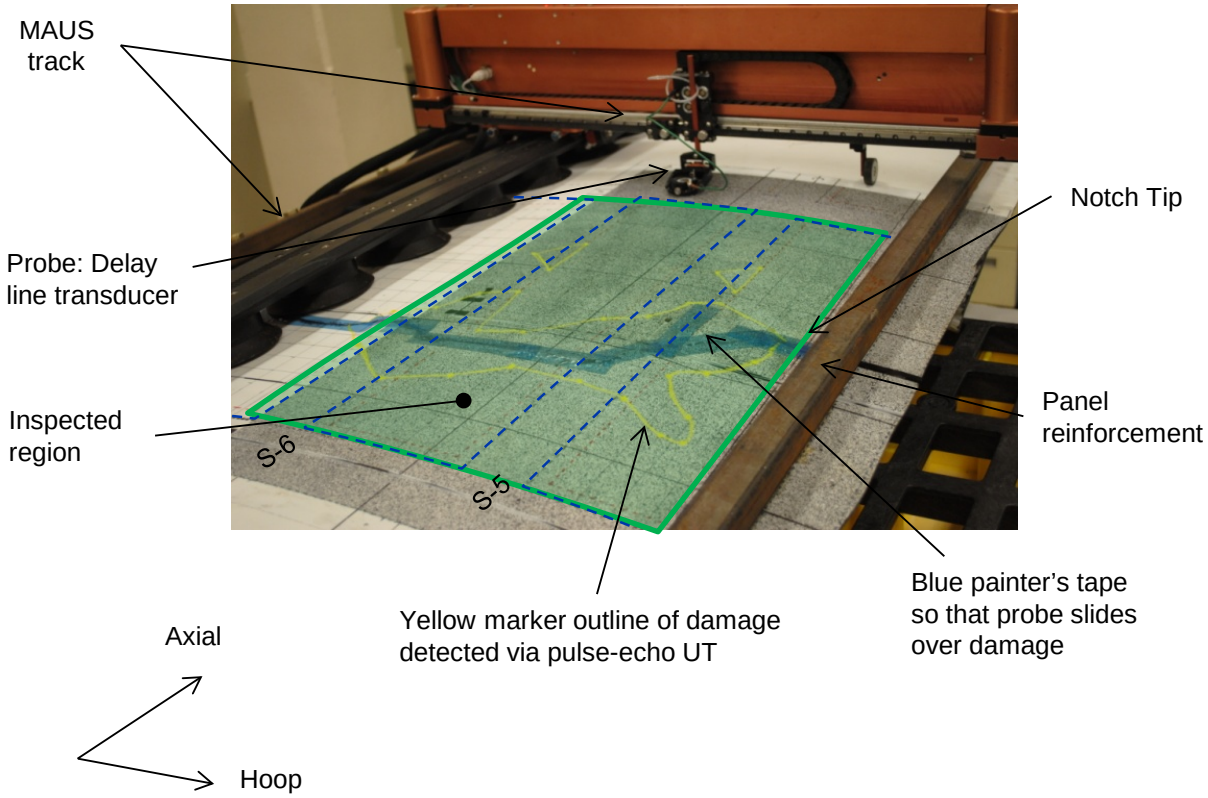

Figure 17. The MAUS V Ultrasound System

- Through-Transmission Ultrasound, using an Ultrawin E2.89 system at 1 MHz with the specimen submerged in water and a 0.5 inch probe, as shown in figure 18. The amplitude was calibrated to 90% in a good region. The probe was incremented in the axial direction by 0.06 inch after each pass of the probe.

(a) (b)

Figure 18. Through-Transmission Ultrasound System: (a) Tank and Gantry and (b) Specimen Fixture in Tank Prior to Scan

- Flash Thermography, using a Raytheon Radiance HSX camera with Mosaiq software, as shown in figure 19. The camera sensitivity was 0.025°C. Six images were taken of the damaged region from the notch tip to the edge of the panel.

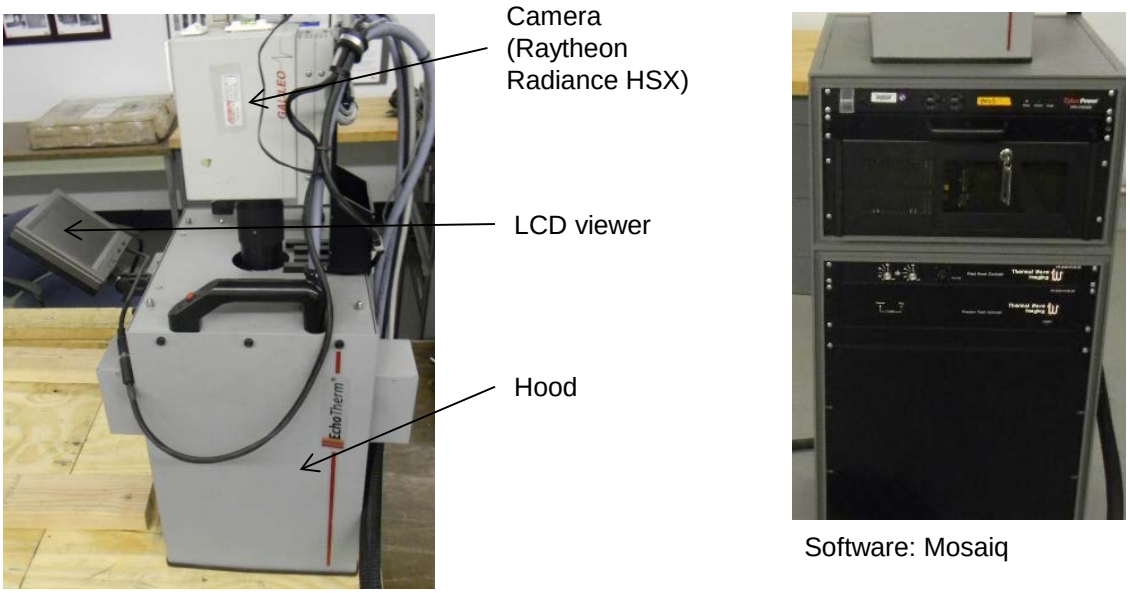

(a) (b)

Figure 19. Sandia National Labs Flash Thermography System: (a) Camera and Hood Unit and (b) Data Acquisition

- X-Radiography CT, using a Kimtron 450 set to 200kV and 3.5mA, which created a poly energetic isotropic x-ray beam and a Perkin Elmer XRD1620 detector, as shown in figure 20. The distance from the x-ray tube to the detector was 68.5 inches and the distance from the x-ray tube to the specimen was 59.1 inches. Two thousand images were captured through one complete revolution of the specimen on the rotation stage. The resolution was 0.006 inch per voxel. Because of the size limitation of the system, a smaller (8 by 18 inch) section of the panel was inspected.

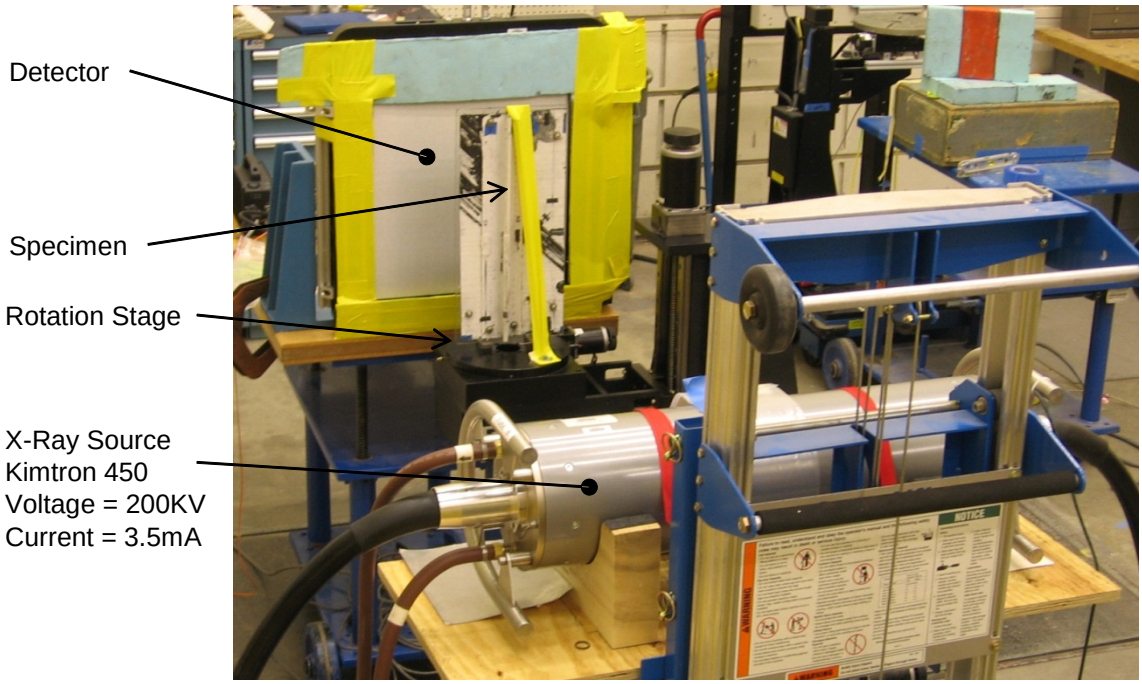

Figure 20. X-Radiographic Computed Tomography System

5.2.7 Fracture Surface Morphology.

The region of the panel directly ahead of notch tip B, which was machined from the panel for CT inspection, was examined visually in a teardown evaluation to determine the extent and location of damage. Failure in each ply was assessed qualitatively using visual inspection aided by low-magnification light microscopy for future comparisons with progressive failure analyses. Additionally, selected segments cut from this region, as highlighted in figure 21, were examined using a scanning electron microscope (SEM) to determine the active failure mechanisms.

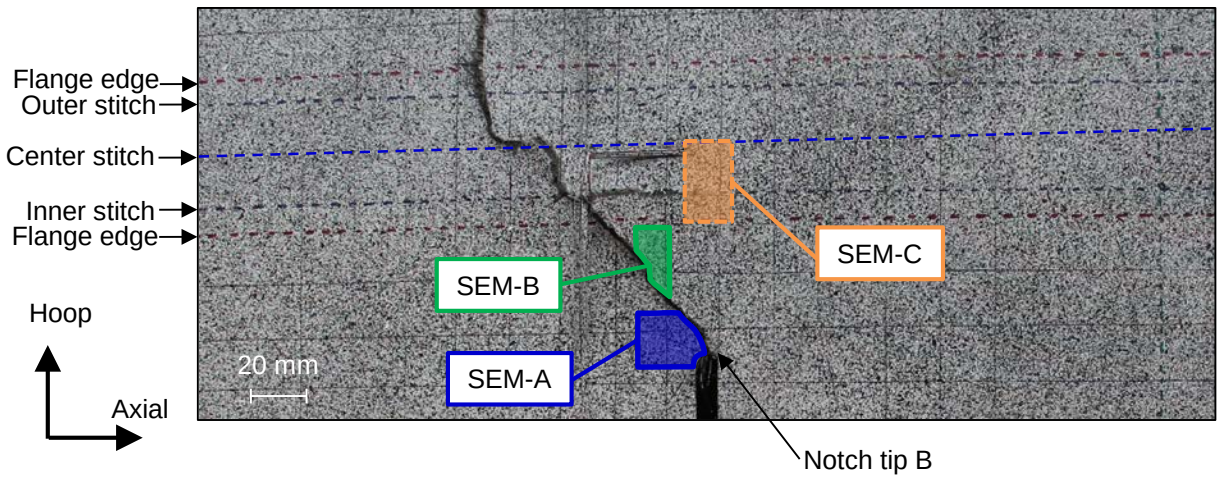

Figure 21. Locations of Post-Test Inspections

Three key areas were examined in the fractography study:

1. The damage formation region at the notch tip (SEM-A)

2. The delaminated surface ahead of the notch tip (SEM-B)

3. The disbonded surface on the stringer flange of the skin/stringer interface, including the stitch failure of the first stringer ahead of the notch (SEM-C)

All SEM specimens were fewer than 40 mm in length and width to fit within the SEM chamber.

The three specimens inspected were excised from regions of stable damage growth (observed prior to catastrophic failure) where the effects of the dynamic catastrophic failure are assumed to be minimal because strain measurements indicated that this region was almost completely unloaded before fracture. The fractography examinations were performed at Drexel University using an FEI XL30 environmental SEM to determine the mode of failure in the vicinity of the notch tip, the disbonding of the skin from the substructure, stitch failure, and of delaminated surfaces. The secondary electron detector operated in high-vacuum mode using a 0.0012-inch aperture; 2kV-3kV accelerating voltage was used. To fit in the microscope's chamber, specimens were cut to approximately 1-inch by 1-inch from selected areas of interest using a 1.5-inch diameter diamond abrasive cutting wheel. The specimens were sputter coated with an 80/20 ratio of platinum and palladium with a thickness of approximately 4 x 10^{-5} inch.

5.2.8 Ply-by-Ply Teardown.

The type and extent of damage were examined in the skin ahead of the notch in a post-test destructive inspection. Using a light microscope, segments were excised, potted in epoxy, and polished for a sectionwise inspection. The results of the sectioning inspection were used to verify the extent of damage identified through ultrasound inspections and to assess the extent and characteristics of damage not readily detected by ultrasound, including matrix cracks and the ply interface at which the delaminations occurred. The sectioning inspection was complemented

with visual observation while destructively removing delaminated plies to characterize the main path of fiber damage. A schematic representation of the damage was synthesized from a combination of the destructive and NDI observations.

It should be emphasized that these destructive inspections were merely intended to provide an approximate representation of the damage ahead of the notch tip. Far-superior methods, such as the deply method (in which the matrix is pyrolyzed [4]) or micro-computed tomography [5], could have provided a more exact description of the damage; however, these methods were not available for this inspection.

6. ANALYTICAL PROCEDURE.

A pretest linear elastic finite element model (FEM) was developed using MSC/NASTRAN [22] by Boeing. The purpose of the model was to define the load application sequence, load levels to attain the target strain levels in the test section, and required boundary conditions, and to predict failure mode and strains. A summary of the modeling procedure is provided in the remaining portion of this section; complete details of the model development and results are available in reference 17.

The model contained the details and dimensions of the panel, including the skin, frames, stringers, and load introduction buildups, as shown by the mesh rendered with section thickness in figure 22. All composite structure was modeled using shell elements, excluding the stringer rods, which were modeled as beam elements. Stiff bar elements were used to model the FASTER fixture loaders for an accurate representation of the boundary conditions. The model contained approximately 159,000 nodes and 162,000 elements. No damage was modeled; hence, results are available only for phase I. The model was calibrated based on the 50% load tests and was used to predict strains and displacement in the subsequent tests. More detail on the model can be found in reference 10. Results from the model are compared to experimental results in section 7.

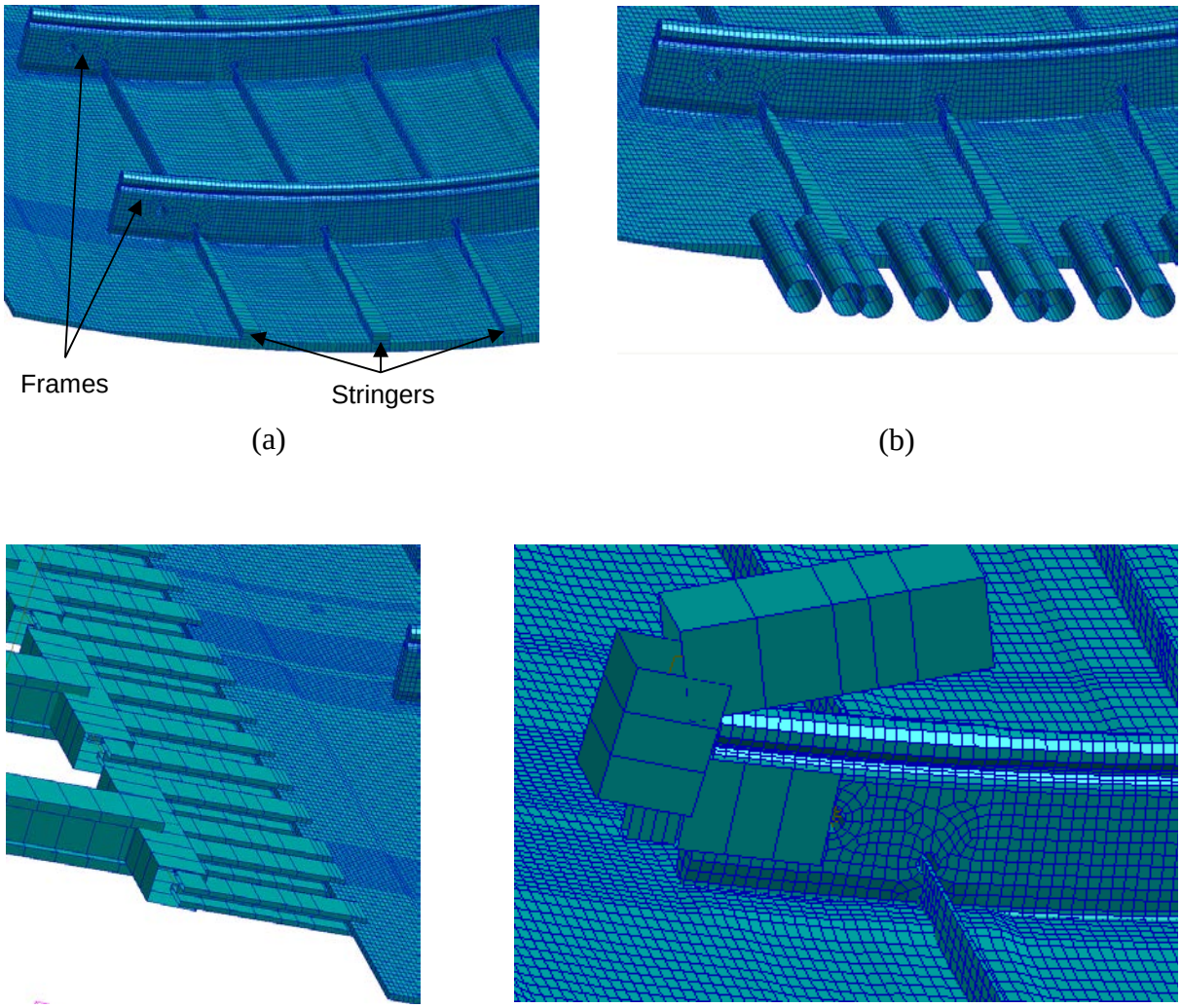

Figure 22. Typical FEM Mesh Rendered With Profiles and Thickness Showing the Panel Modeled as Shell Elements and FASTER Fixture Loaders Modeled as Stiff Bar Elements: (a) Interior, (b) Axial Load Application, (c) Hoop Load Application, and (d) Frame Load Application

7. RESULTS AND DISCUSSION.

An overview of the results for the three test phases is presented in the following sections. Complete tabulated load, strain, and displacement data are available in appendix E.

7.1 PRE-TEST ANALYTICAL PREDICTIONS.

The pretest FEM was used to predict displacements and strains and to calculate margins of safety. As shown in table 4, fringe plots were generated to illustrate the deformed shapes and maximum principal strain distribution for six loading cases. All deformation fringe plots are consistent with the applied symmetric loading. The plots predict that the load introduction

edge-effects are minimized in the test section. The FEM results also indicated the critical load case was the ultimate axial load only case, with the highest localized strains occurring in the skin. These results were used to define the load sequence in order of increasing severity.

Table 4. Deformation and Maximum Principal Strain Fringe Plots for Six Loading Cases

Case	1	2	3	4	5	6
Axial	-	-	DLL	DLL	DUL	DUL
Pressure	Operating	Ultimate	Operating	-	Operating	-

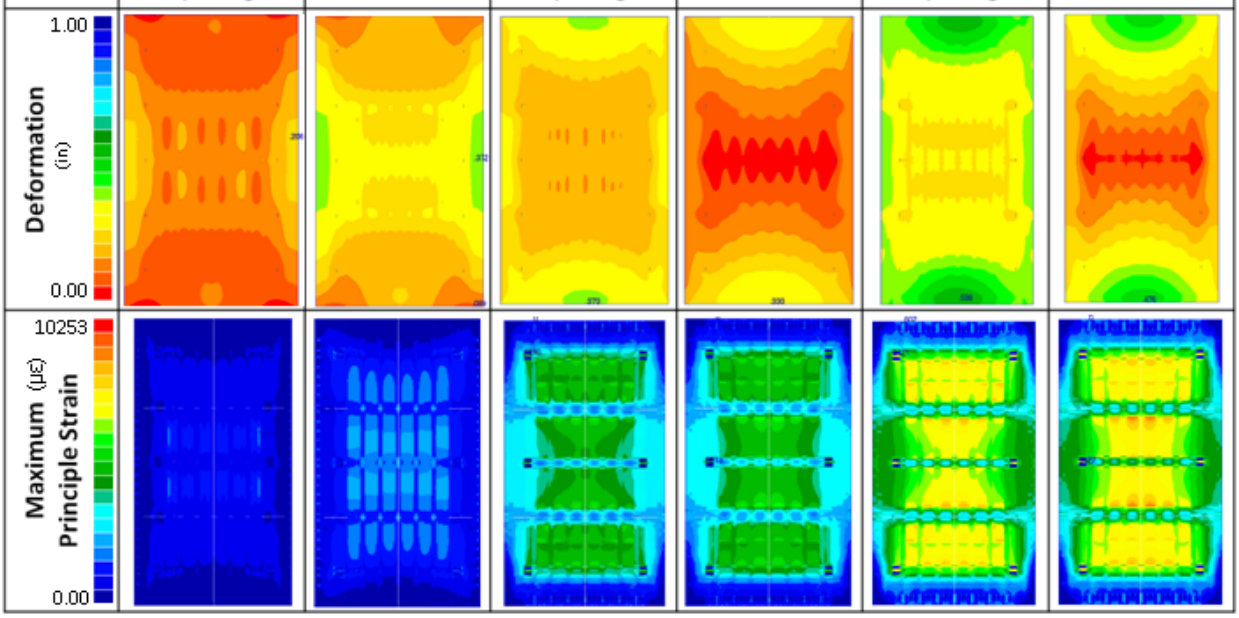

Predicted maximum principal strains, $\varepsilon_{p,max}$, in the skin, stringer wrap, stringer tear strap, and frame tear strap were compared to allowable strain, $\varepsilon_{allowable}$, from the ACT program tests and previous PRSEUS tests [17]. The stringer rod was also included in the comparison; however, maximum principal stresses, $\sigma_{p,max}$, were compared to allowable stress, $\sigma_{allowable}$, because allowable strain was not available. Table 5 shows a summary of the margin of safety comparison, where margin of safety is defined as $\varepsilon_{allowable}/\varepsilon_{p,max}$-1 and, in the case of the stringer rod, $\sigma_{allowable}/\sigma_{p,max}$-1. As expected, the margin of safety for the skin approaches zero under ultimate axial load.

Table 5. Margin of Safety Summary

Load Case		Skin 9,172 μ in/in*	Stringer Wrap 10,254 μ in/in*	Stringer Tear Strap 10,254 μ in/in*	Stringer Rod 390 ksi**	Frame Tear Strap 9,172 μ in/in*
Axial	Internal Pressure					
-	Operating	2.82	12.78	5.63	25.66	7.23
-	Ultimate	1.08	5.89	1.50	12.57	2.99
DLL	Operating	0.57	0.73	1.01	2.74	0.91
DLL	-	0.50	0.66	0.94	2.64	0.88
DUL	Operating	0.06	0.17	0.36	1.54	0.26
DUL	-	0.01	0.13	0.31	1.45	0.266

*Allowable principal strain, $\varepsilon_{allowable}$, for each structural component.

**Allowable principal stress, $\sigma_{allowable}$.

7.2 PHASE I TESTING.

In the first stage of phase I, the pristine panel was loaded in each of the three load conditions (axial, pressure, and combined pressure/axial) to 50% of the assigned limit load. This was done to confirm proper load introduction and repeatability in the strain fields, as recorded by the strain gages, LVDTs, and DIC, and to confirm the validity of the FEM. At least two loadings were applied for each of the three loading conditions. Representative strain measurements, recorded during the three loading functions, are shown in figure 23(a through c). The strain data are from two representative mid-bay strain gages, mounted on the interior of the skin, midway between stringers S-4 and S-5 and frames F-2 and F-3. Similar results were recorded with the other strain gages. All results indicated linear load-deformation relations, as expected, having excellent reproducibility and being in good agreement with the FEM. The axial displacement, recorded along the central stringer for the combined loading case, figure 23(d), also verified repeatability and agreement with the FEM. The change in slope in the data, most evident in the LVDT displacement results, was due to the two-stage load application adopted in the test program applying first internal pressure, of 0.5 P, followed by monotonically increasing axial load. Therefore, the knee seen in the figure (and in several of the subsequent figures) was caused by the reactive axial load to the initial pressure.

Subsequently, in the second stage of this phase, the panel was subjected, sequentially, to the three limit loads of pressure of 1.33 P, axial load of 100% DLL, and combined 1.0 P pressure and axial 100% DLL. Representative strain gage results for the combined loading case, recorded by the exterior and interior strain gages under combined loading, are shown in figures 24 through 26. The axial strain measurements during the limit combined load test, measured by four strain gages mounted on the exterior skin, are shown in figure 24(a and b). Strain gages SG 7 and SG 15 were atop stringer S-3; SG 9 and SG 17 were atop stringer S-5, where SG 7 and SG 9 were centered between frames F-2 and F-3 and, therefore, called mid-bay; and SG 15 and SG 17 were near frame F-4. Finite element results for the mid-bay and near frame F-4 locations bound the strain gage results, as shown in figure 24(c). Similar results are shown for four representative interior strain gages, located on the interior skin within the test section: SG 38 and SG 39 near

frame F-2 and SG 64 and SG 65 near frame F-4. Strain gage SG 66 varied from the other three strain gages, apparently because these strain gages were mounted in a high strain-gradient region (i.e., near the flange of the frame, figure 24(d)). The FEM shows good agreement with the experiments.

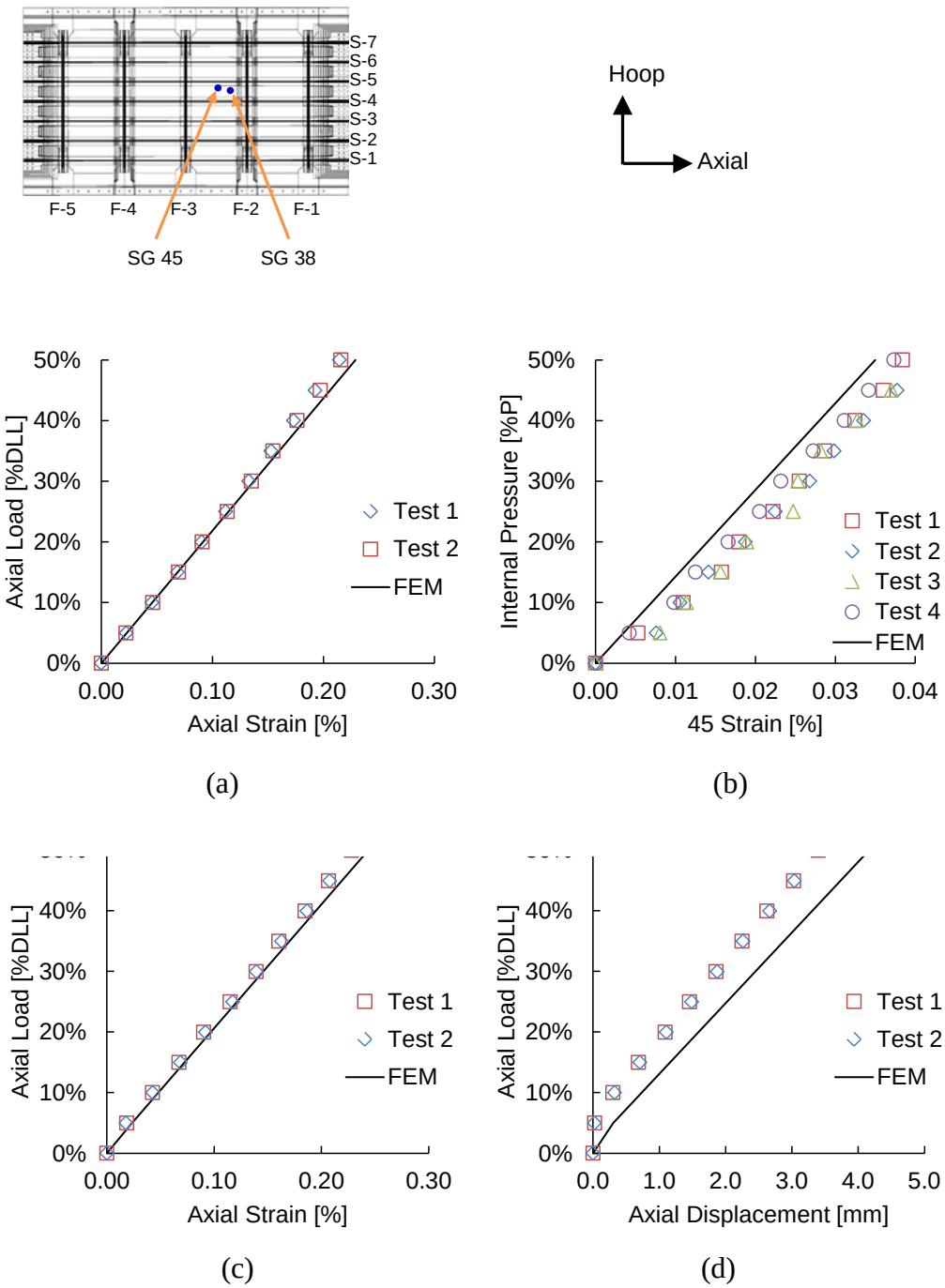

Figure 23. Typical 50% Limit Load Strain Results for Each of the Three Loading Functions Applied, Showing Good Repeatability and Agreement With the FEM: (a) Axial Load: Strain Gage 38, (b) Pressure Load: Strain Gage 45, (c) Combined Load: Strain Gage 38, and (d) Combined Load: LVDT 1

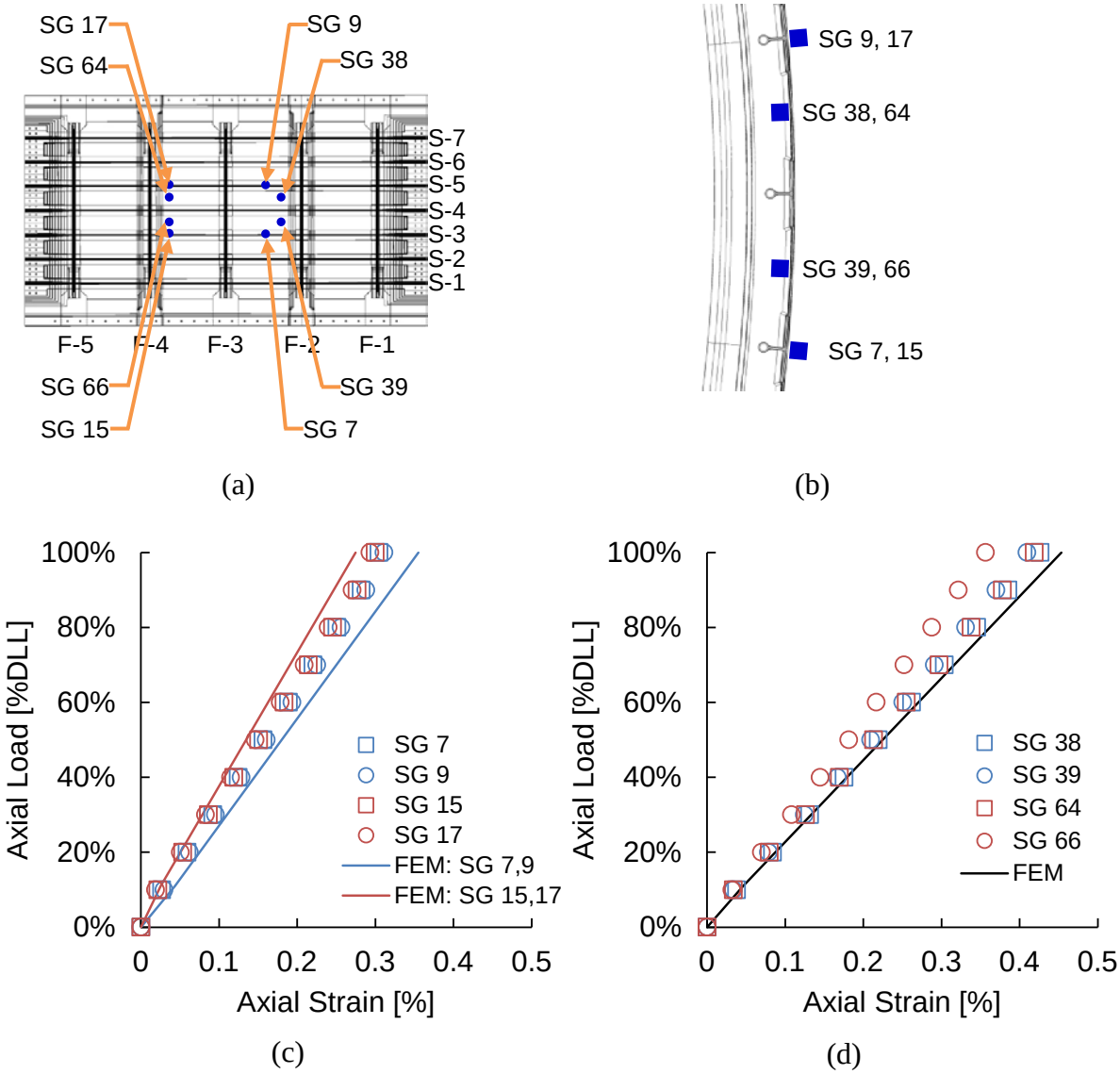

Figure 24. Typical Combined Limit Load Strain Results for Selected Strain Gage Locations: (a) Top View of Gage Locations, (b) Side View of Gage Locations, (c) Exterior, and (d) Interior

The degree of panel bending during loading in the axial direction was measured by back-to-back strain gage pairs. The exterior strain gages were mounted on the skin and the interior strain gages were mounted on the stringer rods (i.e., any measured axial bending strain would primarily be that of the stringer). The bending strains

$$\varepsilon_{bend} = \frac{|\varepsilon_{ext} - \varepsilon_{int}|}{2} \tag{1}$$

were measured in six different locations along stringers S-3, S-4, and S-5 within the test section and are shown in figure 25(a and b) for three pairs of strain gages mounted mid-bay between

frames F-2 and F-3, figure 25(c), and three pairs mounted near frame F-4, figure 25(d). The results indicate that the axial bending strain is smaller — by more than an order of magnitude — than the actual axial strain (figure 24) and the FEM is in good agreement with the measured data. The results indicate a minor bulging of the panel. The knee in the load-strain curves resulted from the two-step loading sequence, as described above, which the FEM predicted as well. Bending in the hoop direction was not measured because all hoop strain gages were mounted on the stringer/flange intersection.

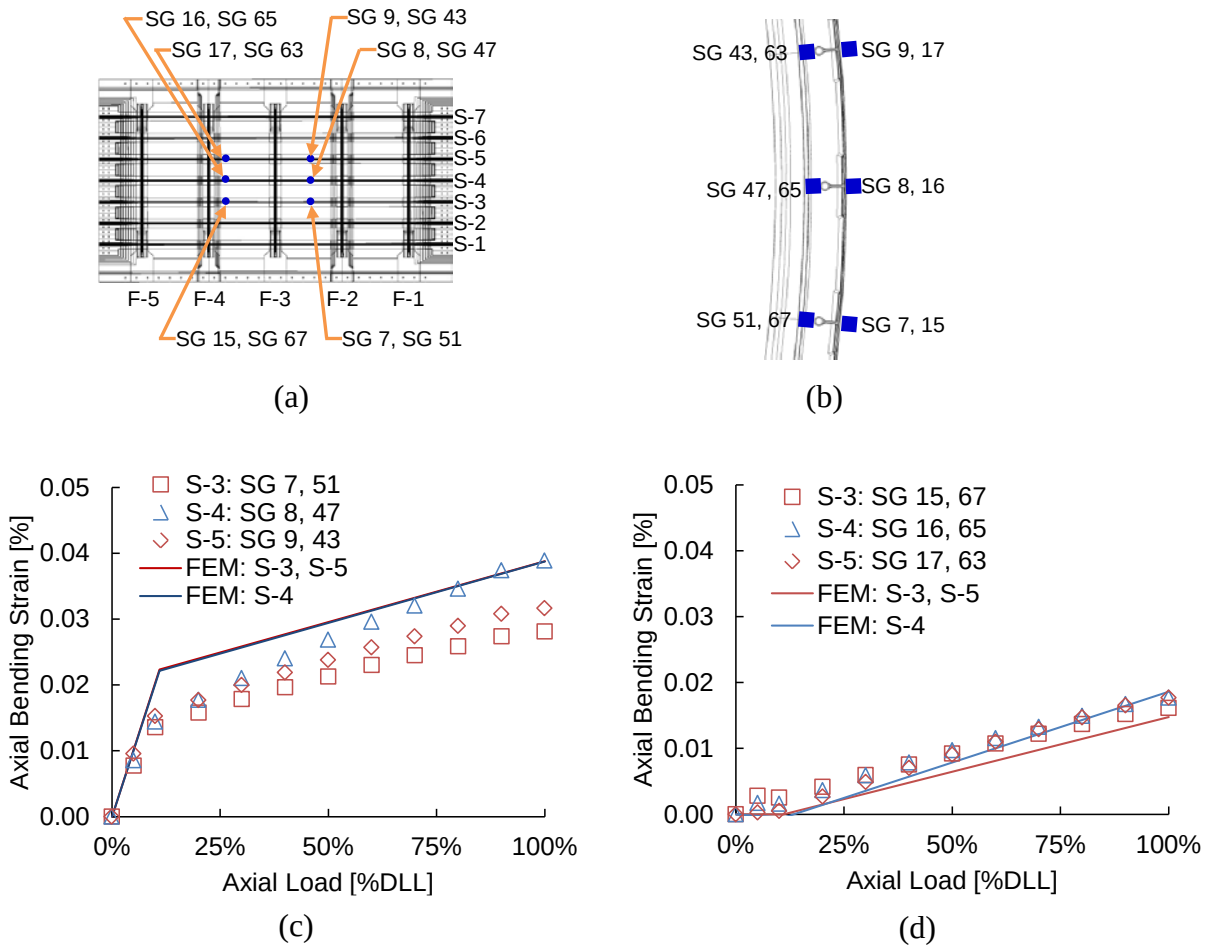

Figure 25. Combined Limit Load Axial Bending Strain: (a) Top View of Gage Locations, (b) Side View of Gage Locations, (c) Mid-Bay, Between F-2 and F-3, and (d) Near F-4

The results of axial displacement, recorded by the four LVDTs that were mounted at the ends of stringers S-1, S-2, S-3, and S-4, showed a consistent trend with analysis (see figure 26). The axial edge displacement of the stringers was not the same: the central stringer, S-4, exhibited the largest displacement and stringer S-1, along the panel's edge, the smallest.

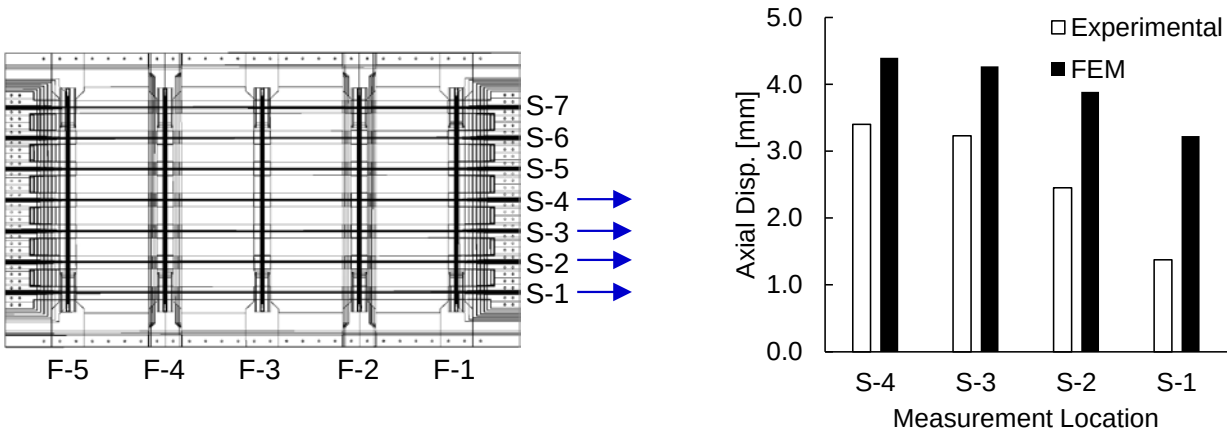

Figure 26. Combined Limit-Load Axial-Displacement Measurements

The global hoop strain field of the skin in the central test section (between stringers S-3 and S-5 and frames F-2 and F-3), recorded via the DIC, is shown as a fringe pattern in figure 27 for pressure and combined load conditions. Under pressure-only loads, higher tensile hoop strain is noted in the mid-bay areas than over the stiffeners and there is a noticeable strain gradient at the edge of the stiffener flanges as expected. It is also observed that the combined load condition leads to lower hoop strains because of Poisson's effect.

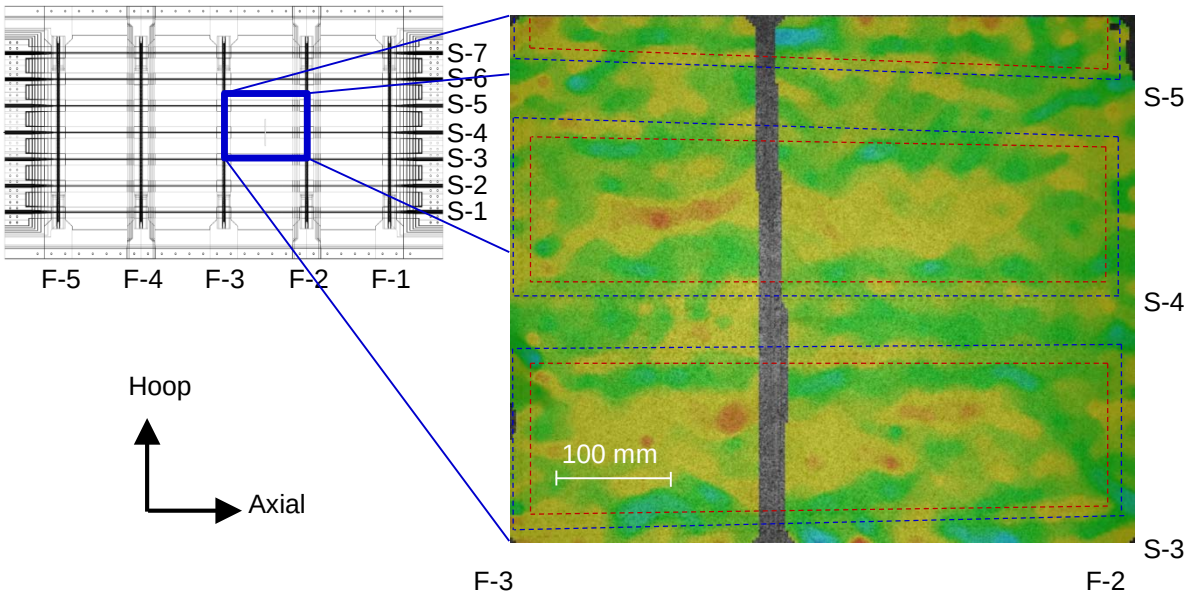

(a)

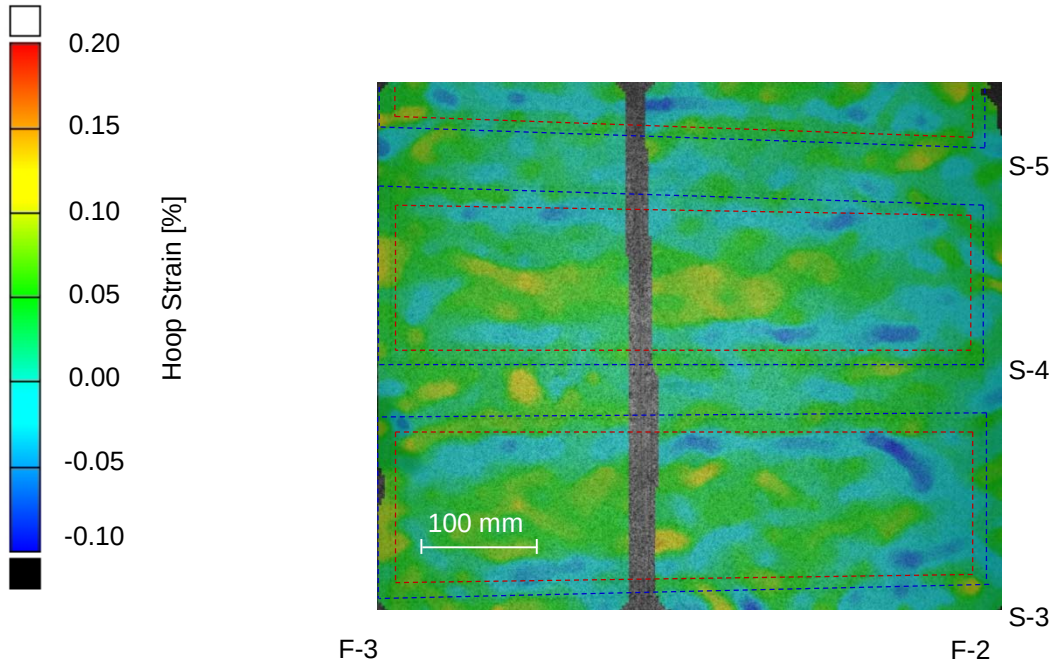

(b)

Figure 27. Hoop Strain Field in the Test Section: (a) Pressure: 1.0 P and (b) Combined: 1.0 P + 100% DLL

7.3 PHASE II TESTING, EFFECT OF BVID.

7.3.1 Introduction of BVID.

The purpose of phase II tests was to demonstrate that the panel containing a BVID met the ultimate strength and deformation requirement of 14 CFR 25.305 [13] and guidance of AC 20-107B [14]. After impact, visual inspection revealed no clear indication of fiber breakage, which is the criterion indicating a BVID for the purpose of this test [23]. Therefore, the panel was impacted a second time in the same location with the same impact energy. The BVID was inspected visually (in the exterior and interior) and via ultrasonic pulse-echo and flash thermography, as described below.

Photographs of the impact site before and after the two impacts are shown in figure 28, showing the exterior and interior state-of-BVID. The first impact caused a slight indentation on the exterior while the second impact caused a visible matrix crack along the 45° direction and short perpendicular crack, indicating fiber breakage. The exterior damage extended over a 0.16 inch x 0.38 inch area, with a dent depth of 0.015 inch, as shown in figure 28(c). The impact damage on the interior of the panel was clearly visible after both the first and the second impact. The damage included multiple matrix cracks along the 45° surface ply, approximately 2.2 inches and 2.6 inches long after the two impacts, respectively. These cracks emanated from the edge of the stringer flange into the skin. A close-up view, showing a broken fiber bundle, is shown in figure 28(d). Accordingly, this severe BVID was deemed appropriate for this test, satisfying category 1 damage, per AC 20-107B [14].

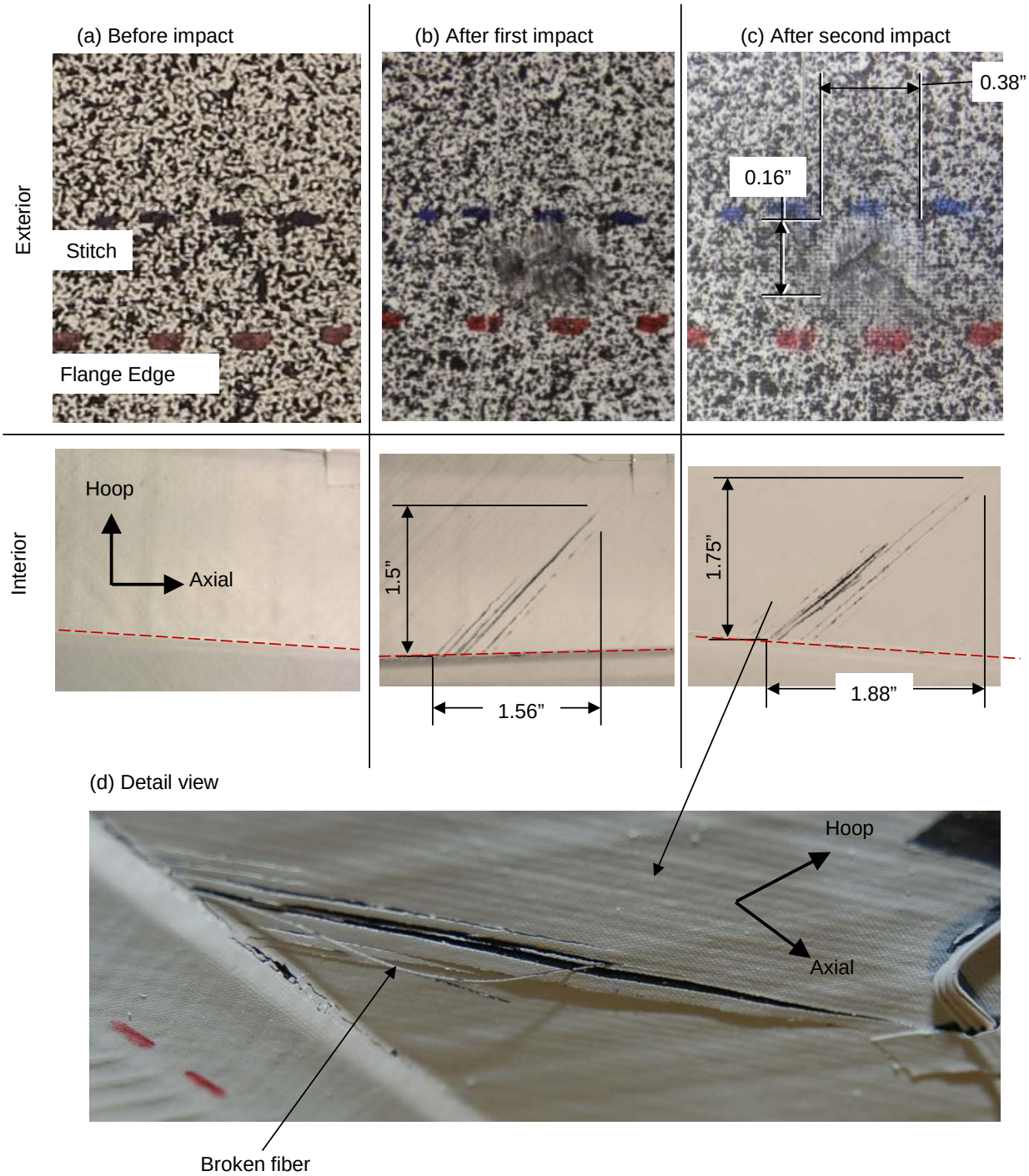

Figure 28. Photographs of the BVID Region, as Seen From the Exterior and Interior, Before and After Impact: (a) Before Impact, (b) After First Impact, (c) After Second Impact, and (d) Detail View

Pulse-echo ultrasonic and flash thermography inspections were performed in the vicinity of the impact location, as shown in figure 29. The location, size, and shape of the flange/skin disbonding are clearly seen in both the ultrasonic C-scan and flash thermography images, as shown in figures 30 and 31. These inspections show that the disbonding extended up to the inner

stitch row, close to the stringer web, as shown outlined in blue in the figures30 and 31-. In other words, the disbonding was completely arrested by the inner stitch row. Subsequent pulse-echo ultrasound and flash thermography inspections, conducted after each of the three limit-loading, and three ultimate loading, conditions showed no growth of the damage associated with the BVID. That is, the inner-stitch row effectively arrested any further extension of the impact-induced disbonded area throughout the loading sequences of phase II.

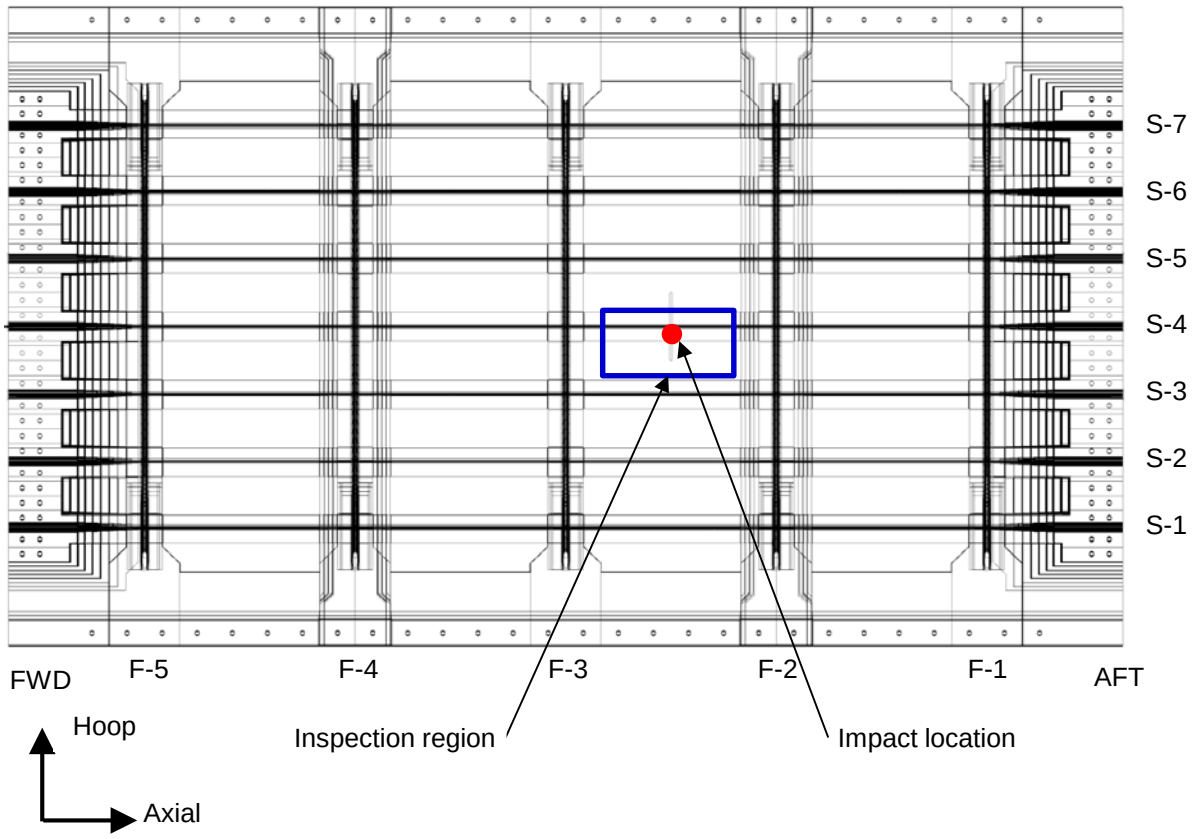

Figure 29. Location and Size of Post-Impact NDI Region

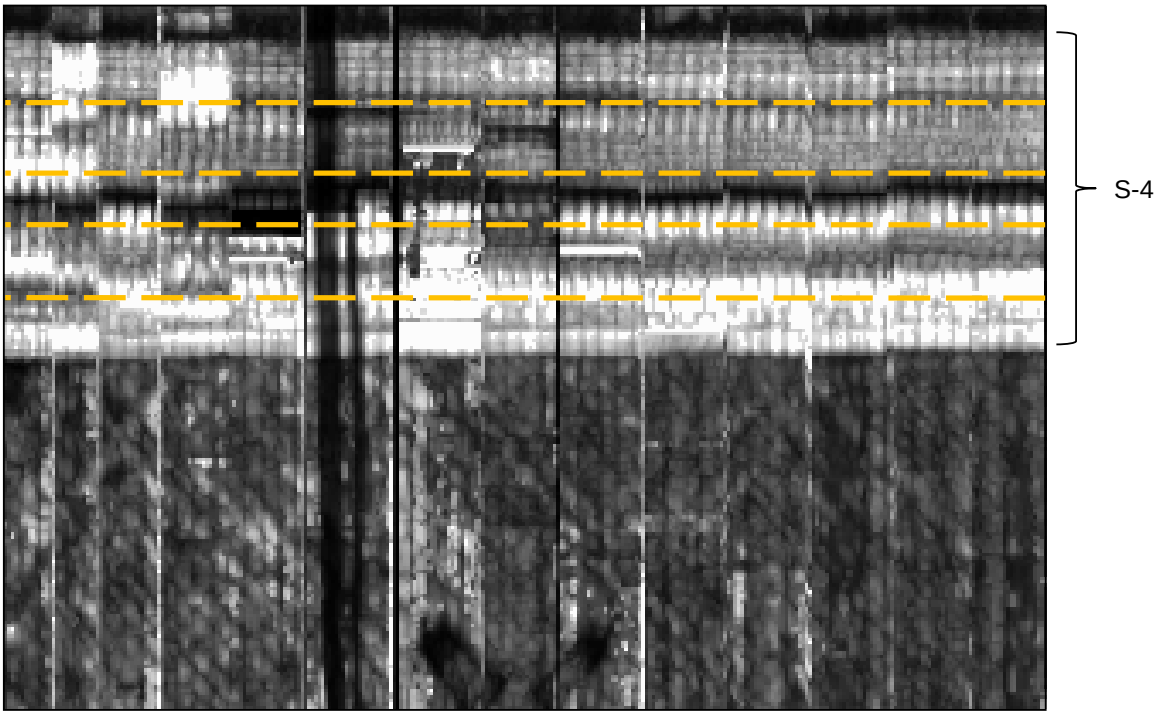

(a)

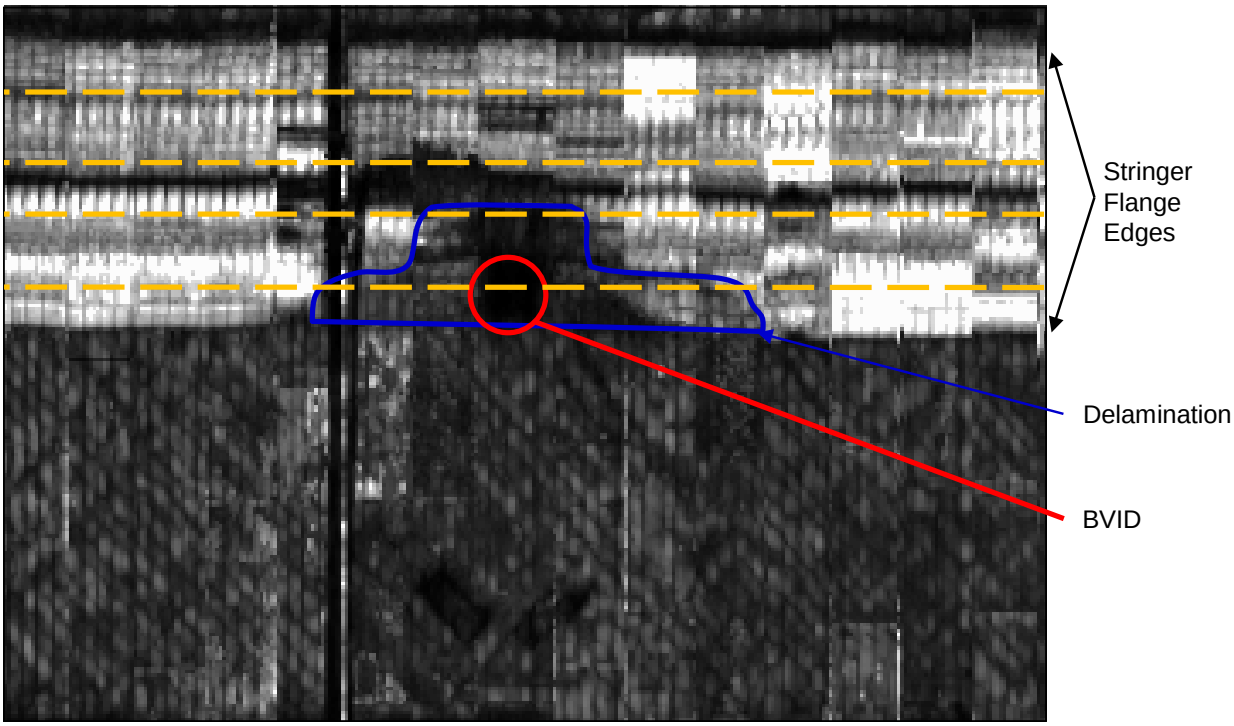

(b)

Figure 30. Pulse-Echo Ultrasound (a) Before Impact and (b) After Impact

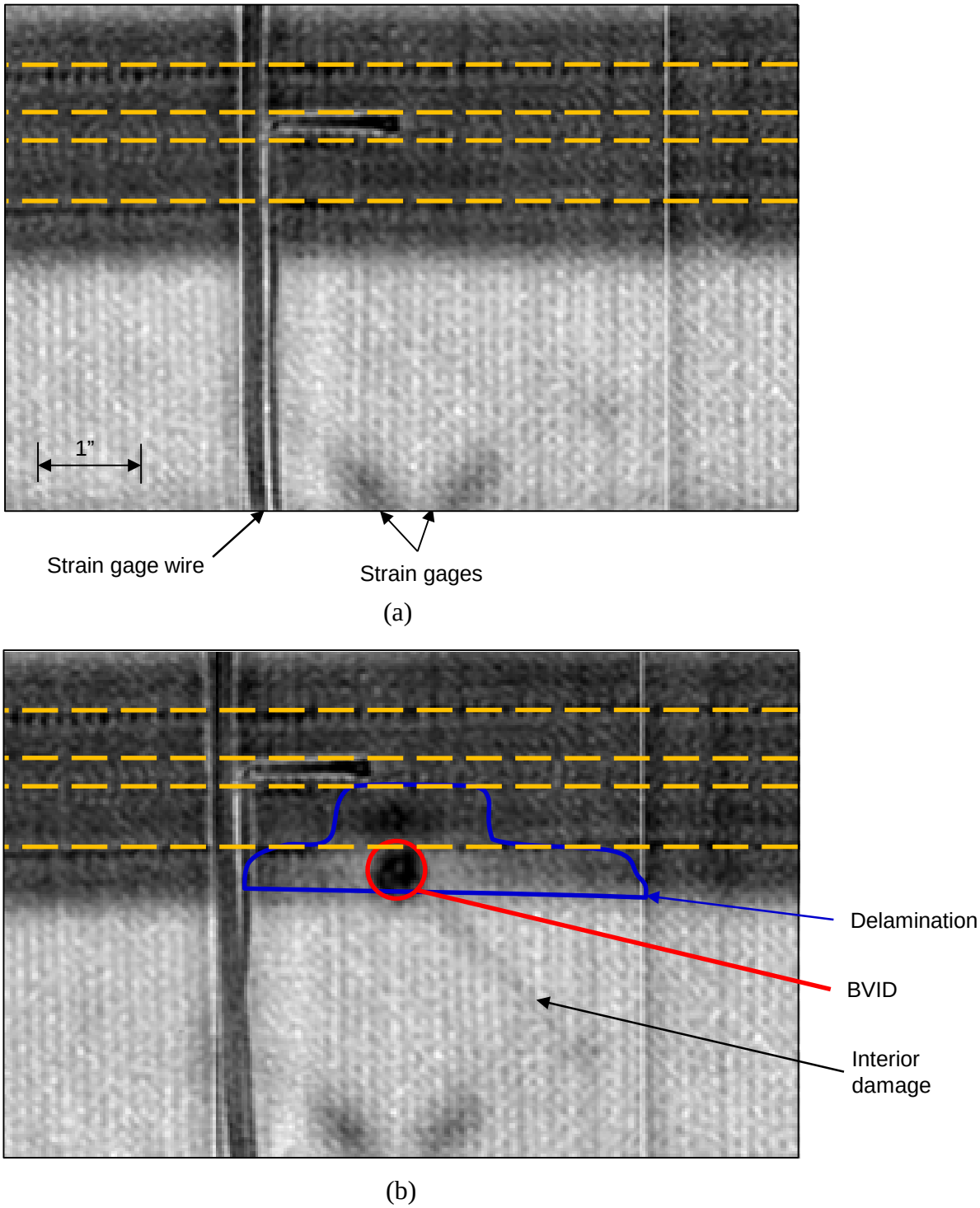

Figure 31. Flash Thermography (a) Before Impact and (b) After Impact

Following impact, a sequence of three limit-load conditions were applied (see table 2): (1) axial load of % DLL only; (2) pressure load of 1.33 P only; and (3) combined axial load of % DLL and pressure of 1.0 P. This load sequence was followed by three ultimate load conditions

(see table 2): (1) pressure overload of 2.0 P only, (2) ultimate axial load (150% DLL) only; and (3) ultimate combined load conditions (1.5 P + 150% DLL).

7.3.2 Strain and Displacement.

Global strains and displacements at limit load were observed to be nearly identical before and after the impact. Figure 32 shows representative results comparing test section skin strains and axial end displacements between phases I and II for combined limit load (1.0 P + 100% DLL). These consistent strains indicated no load redistribution due to damage growth. Similar strain distribution in the test section and global bending response as observed in phase I was seen also in phase II.

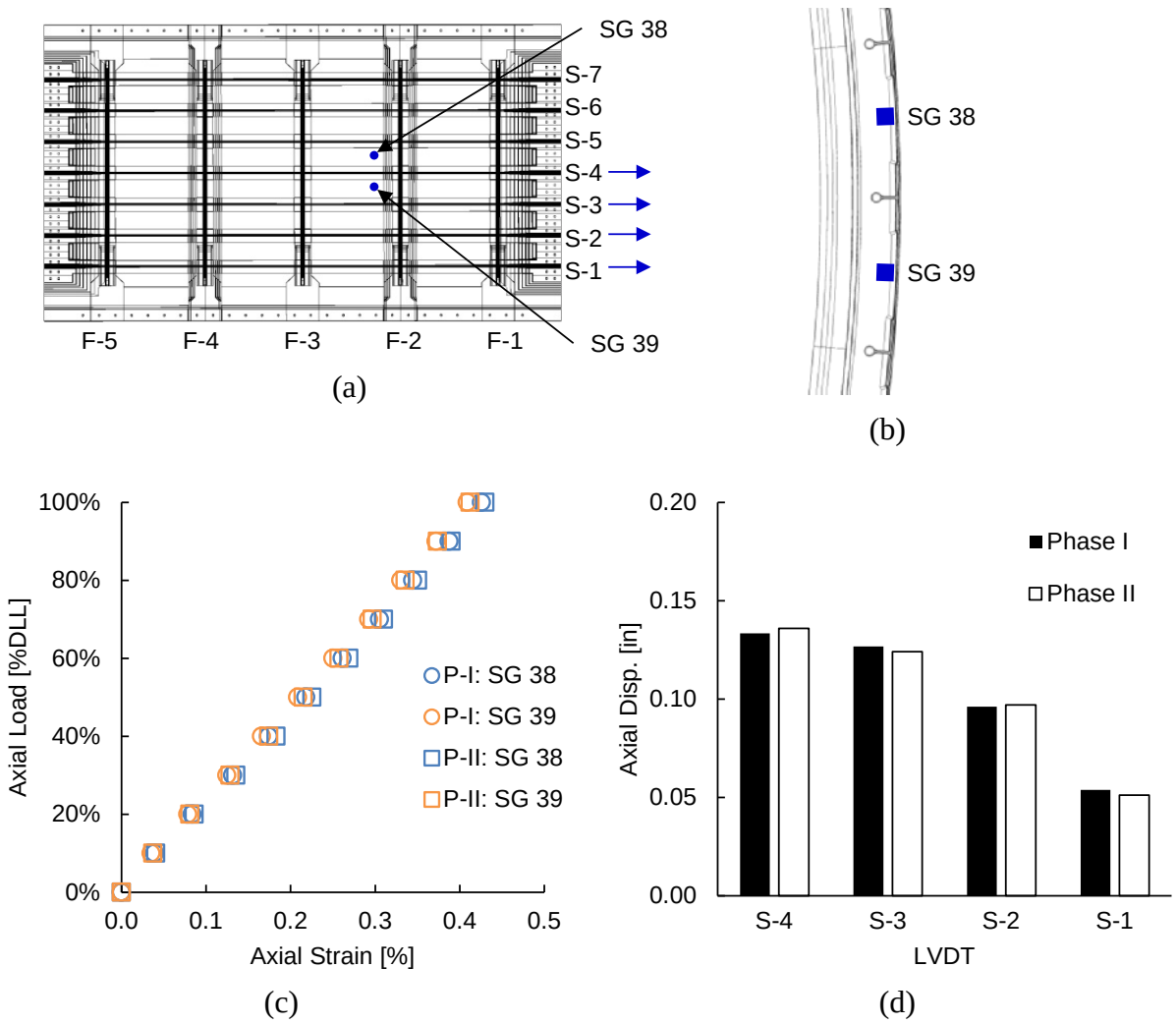

Figure 32. The BVID Had No Effect on Global Strain and Displacement Distributions: (a) Strain Gage Locations, (b) Side View of Gage Locations, (c) Mid-Bay Strain, and (d) Axial Displacement

As expected, a significant local strain concentration existed in the vicinity of the impact damage zone, as seen in the DIC-recorded strains shown in figure 33. The axial strain in the vicinity of the BVID and along cross section A-A, midway between frames F-2 and F-3, is shown in figure 34 for an axial ultimate load level of 150% DLL. The maximum magnitude of axial strain in the vicinity of the BVID remained well below the anticipated material failure strain of 0.9% for the skin [8], which is consistent with the visual observations of no damage growth.

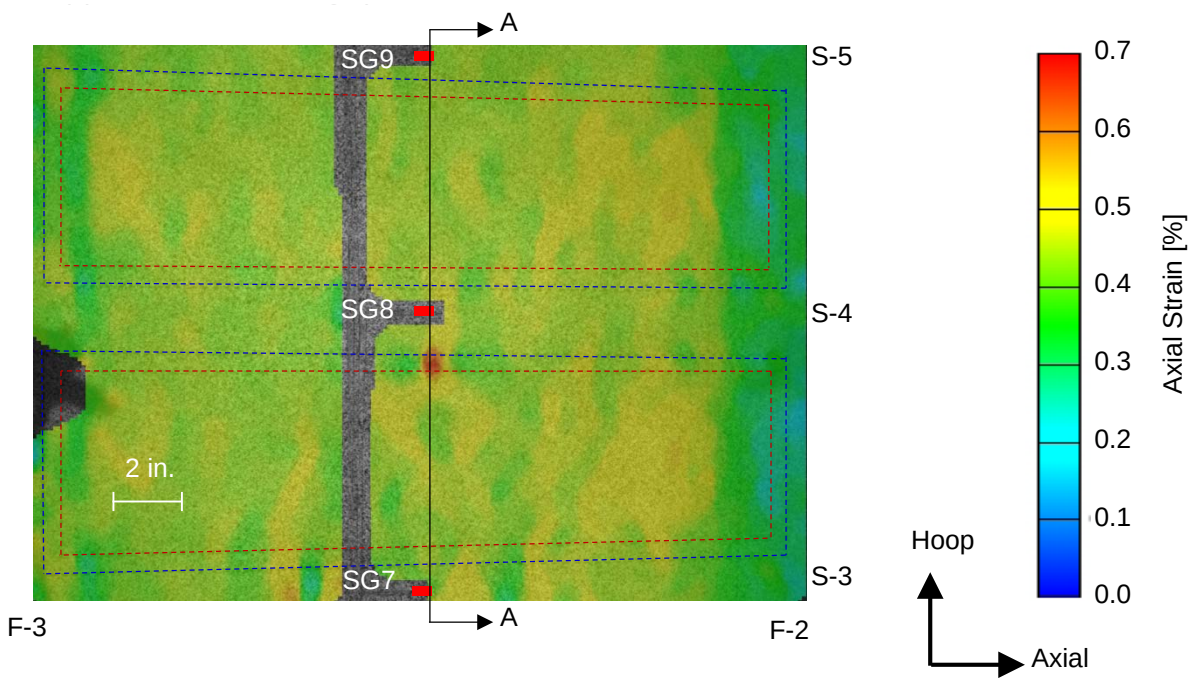

(a)

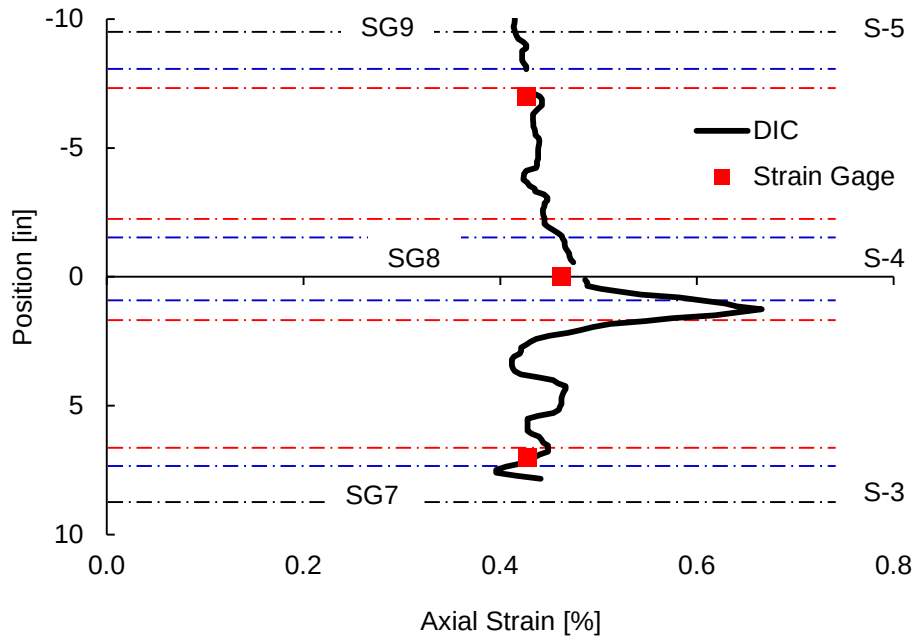

(b)

Figure 33. Axial Strain Field in the Test Section, Under Axial Ultimate Axial Load (150% DLL): (a) DIC Axial Strain Fringe Plot and (b) Axial Strain Along Section A-A

7.4 PHASE III TESTING, EFFECT OF THROUGH-THE-THICKNESS NOTCH.

In phase III, the panel was loaded to catastrophic fracture following a predetermined loading sequence with a through-thickness notch introduced, which severed the central stringer and adjacent skin as shown in figure 10.

The five-step loading sequence applied in this phase is shown in figure 34. Loading was applied monotonically, with the LS applied in increasing severity, from pressure only to axial only, as predicted by the pretest analytical model [17]. The five LS are as follows:

- LS-1: Increasing the pressure to 1.15P, as specified in 14 CFR 25.571, with minimal axial load to maintain the panel in place
- LS-2: Combined pressure of 1.0 P and increasing the axial load to 100% DLL
- LS-3: Unloading the pressure while maintaining the axial load at nearly 100% DLL
- LS-4: Increasing the pressure to 1.0 P while maintaining the axial load at 100% DLL
- LS-5: Maintaining the pressure constant at 1.0 P while increasing the axial load to catastrophic fracture

During the final LS, the hydraulic pump of the loading fixture briefly shut down, resulting in a short duration of constant axial load, which upon resumption was followed by a brief higher axial loading rate, as shown in figure 34(b). Also shown in figure 34 are key damage progression observations, denoted with capital letters A-H.

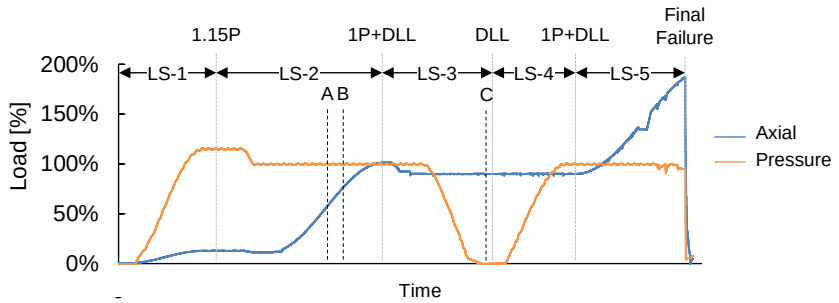

(a)

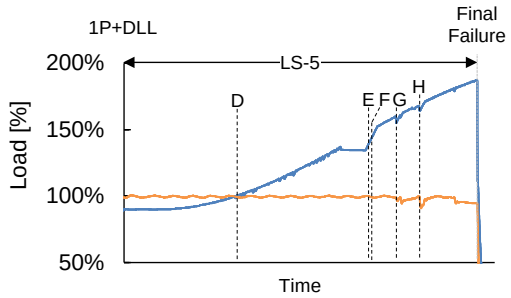

(b)

Figure 34. Phase III Load History With Key Damage Progression Observations, Letters A–H: (a) Phase III Load History and (b) Zoomed View of LS5

7.4.1 Observations During Each Load Step.

Damage progression was observed visually on the exterior and interior, starting with LS-2 and intermittently thereafter until catastrophic failure occurred. The damage was also evident through strain redistribution at several instances throughout the loading sequence. A complete record of photographs showing damage progression during phase III is available in appendix G.

7.4.1.1 Load Step 1.

No damage was detected during this loading, consistent with the analytical predictions. Limited DIC data could be collected near the notch tips because water leakage occurred mid-loading through the sealed notch region.

7.4.1.2 Load Step 2.

Prior to external surface damage formation, the axial strain fringe patterns (computed from the DIC data) showed the characteristic kidney-shaped strain concentration at the notch tip, as shown in figure 35(a). The corresponding strain gradient ahead of the notch tip, just prior to the damage formation at notch tip A, is shown in figure 35(b). These DIC data agree very well with the strain recorded by SG 7, mounted 89 mm (3.5 in.) ahead of the notch tip. The axial strain history at that location, recorded by the strain gage and the DIC, is shown in figure 35(c). Excellent

correlation is observed between the strain gage and the DIC results throughout the load history. The strain behavior corresponds well to the applied load.

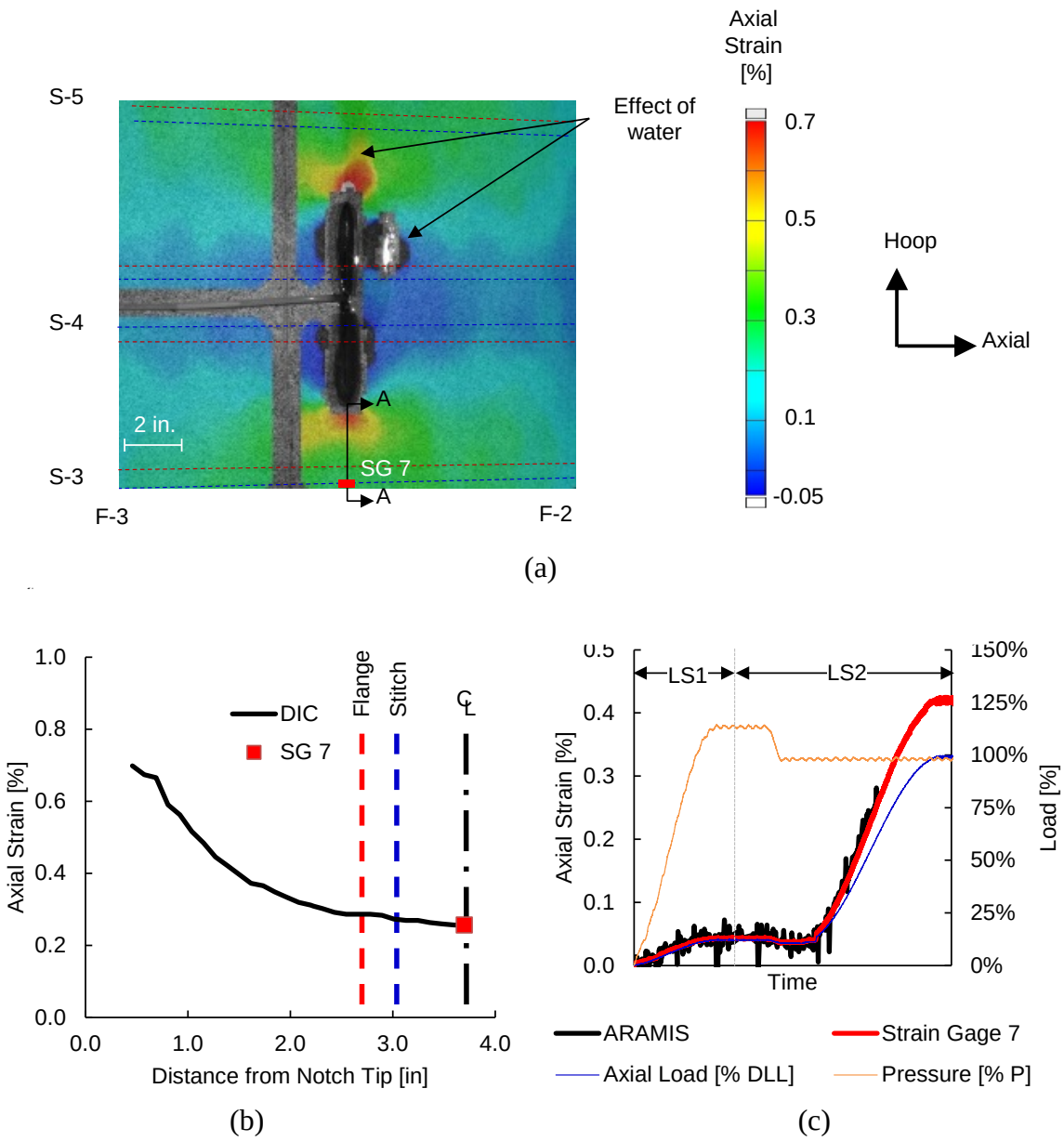

Figure 35. Axial Strain in the Vicinity of the Notch Tip Recorded via DIC and Strain Gage (parts (a) and (b) are shown at 1.0 P + 70% DLL): (a) DIC Axial Strain Fringe Plot, (b) Axial Strain Along Section A-A, and (c) Axial Strain History at SG7 Location

Normal strains along 0°, 45°, and 90° sections from notch tip A at eight load levels (see figure 36) indicate that the dominant notch tip strains approached the material failure strain at 70% DLL, which is in agreement with the observed visual damage initiation at this load level. Detailed DIC data are available in appendix F. As axial load increased beyond 70% DLL and damage propagated, significant water leakage occurred, which disrupted further DIC data acquisition.

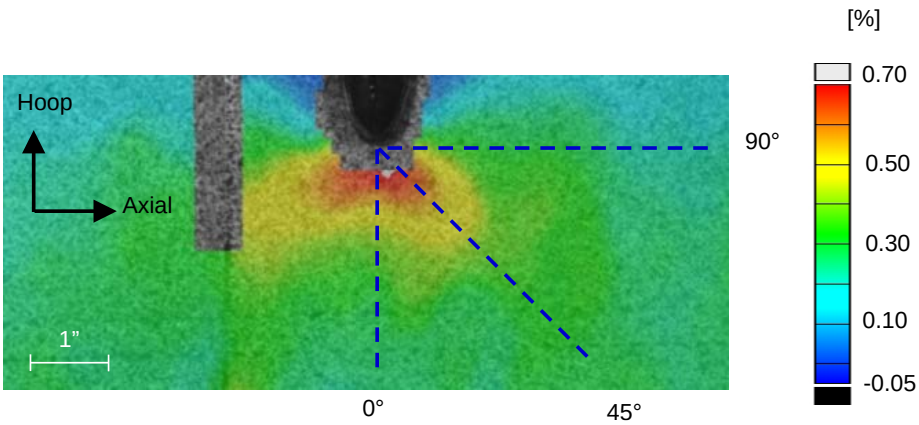

(a)

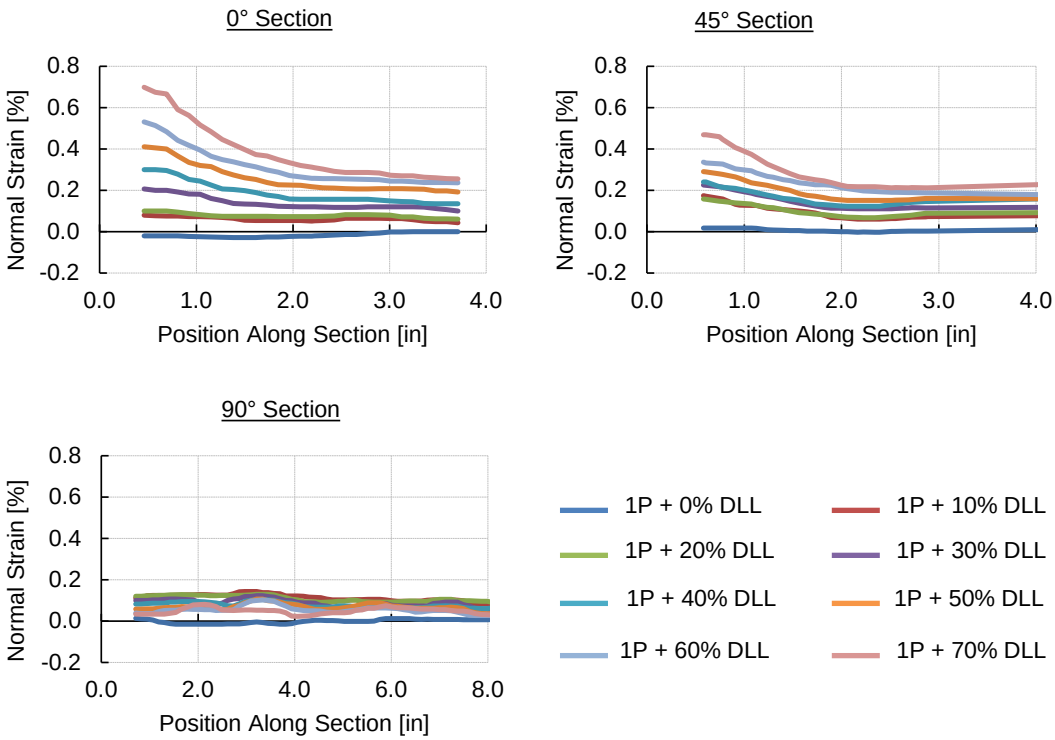

(b)

Figure 36. The Axial Strain Distribution at Notch Tip A for 1.0 P + 70% DLL and Section Plots Showing Normal Strain Along 0°, 45°, and 90° Sections: (a) DIC Axial Strain Fringe Plot and (b) Normal Strain Along Sections

Damage Growth: Visible damage was first observed at a combined load of 1.0 P + 58% DLL (point A in figure 34) in the form of a matrix crack on the interior surface, propagating antisymmetrically from the two notch tips. Further increasing the axial load, at a combined load of 1.0 P + 70% DLL (point B in figure 34), damage was observed visually on the exterior surface of the panel in the form of a crack along the 45° direction, as shown in figure 37(a). The visible damage on the exterior was in the fiberglass layer.

Throughout the remainder of LS-2 (beyond point B in figure 34), damage progressed along the 45° direction, parallel to the outer ply fibers, in the form of a single matrix crack, as shown in figure 38. Figure 37(b) shows an intermediate load level where the crack is clearly visible and measures 0.5 inch. Figure 37(c) shows the extent of the matrix crack at the end of LS-2, where the visible crack had extended 1.3 inches from the notch tip. A nearly identical crack initiation and progression pattern was observed along the other notch-tip.

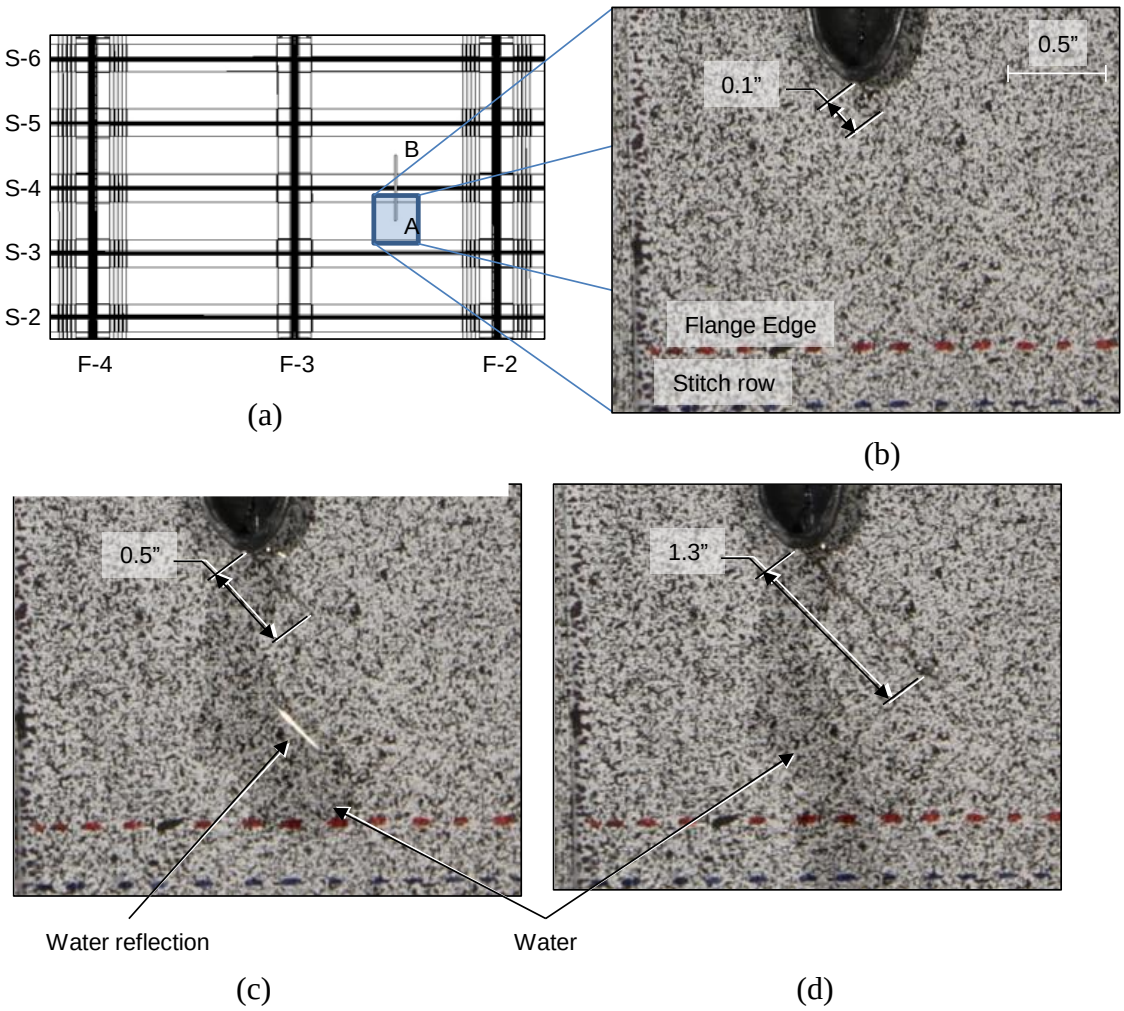

Figure 37. Photographs of Notch Tip A Exterior Surface Damage Showing Crack Progression During LS-2: (a) Panel Test Section Schematic, (b) 1P + 70% DLL, (c) 1P + 88% DLL, and (d) 1P + 100% DLL

Unlike the damage in the exterior, multiple matrix cracks occurred in the vicinity of the notch tips in the interior of the panel, also oriented along a 45° direction, as shown in figure 38. Also, paint spalling occurred as the damage progressed. The first visible damage was approximately 2 mm in length. At the end of LS-2, the maximum length of damage was 1.8 inches. Damage progression was intermittent accumulation from formation to the maximum load in LS-2.

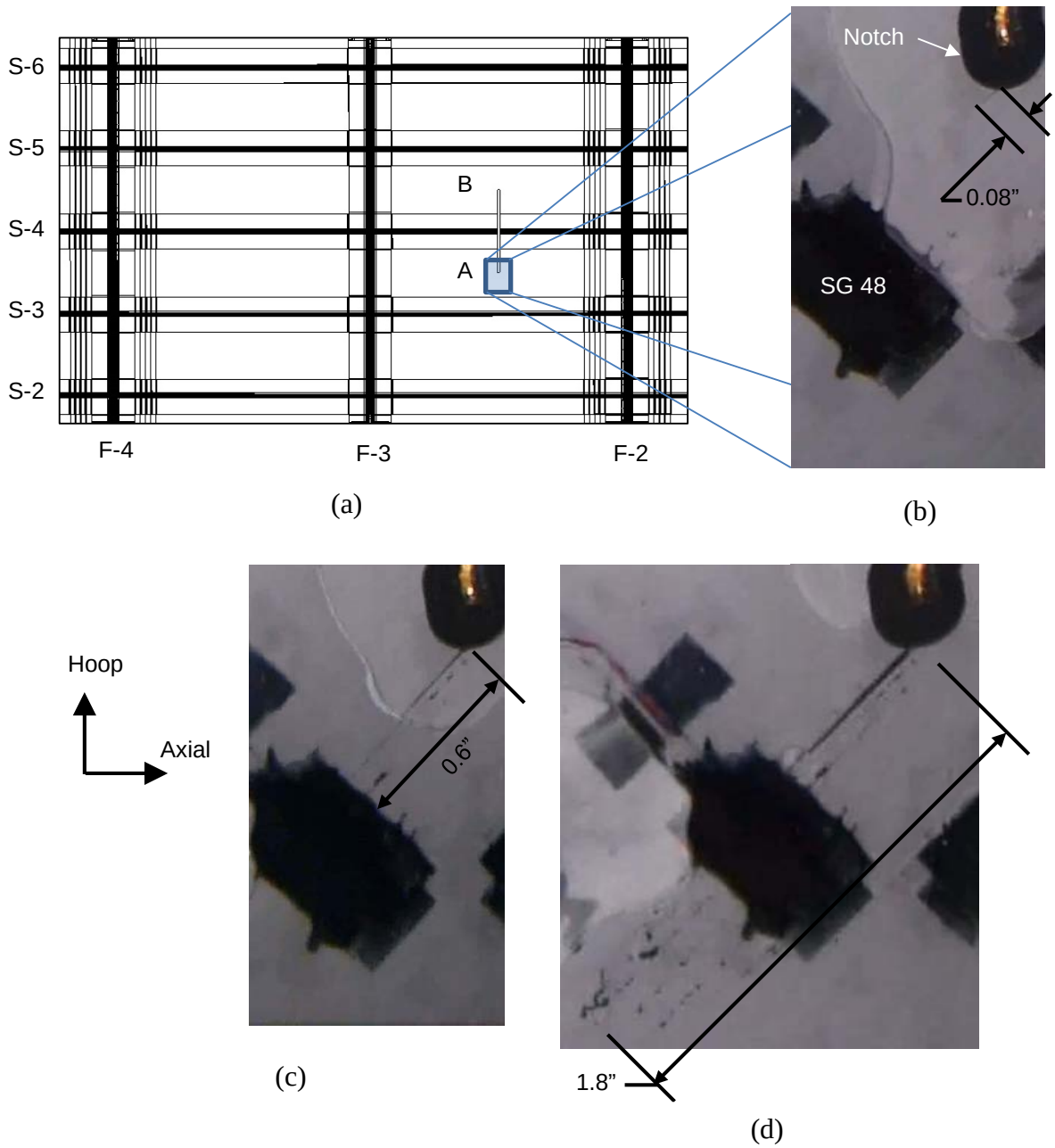

Figure 38. Photographs of Notch Tip A Interior Surface Damage Showing Crack Progression During LS-2: (a) Panel Test Section Schematic, (b) 1P + 54% DLL, (c) 1P + 67% DLL, and (d) 1P + 100% DLL

Strain Redistribution: Strain gages mounted in the two-bay region showed discontinuities and nonlinearity, while those mounted outside the two-bay region showed stable behavior, as shown in figure 39. Shortly after damage formation, several small-strain discontinuities were observed in the four 45° notch tip strain gages at 1P + 55% DLL, 1P + 60% DLL, and 1P + 62% DLL,

indicating the intermittent damage accumulation leading to local strain redistributions ahead of the notch tip, as shown in figure 39(c).

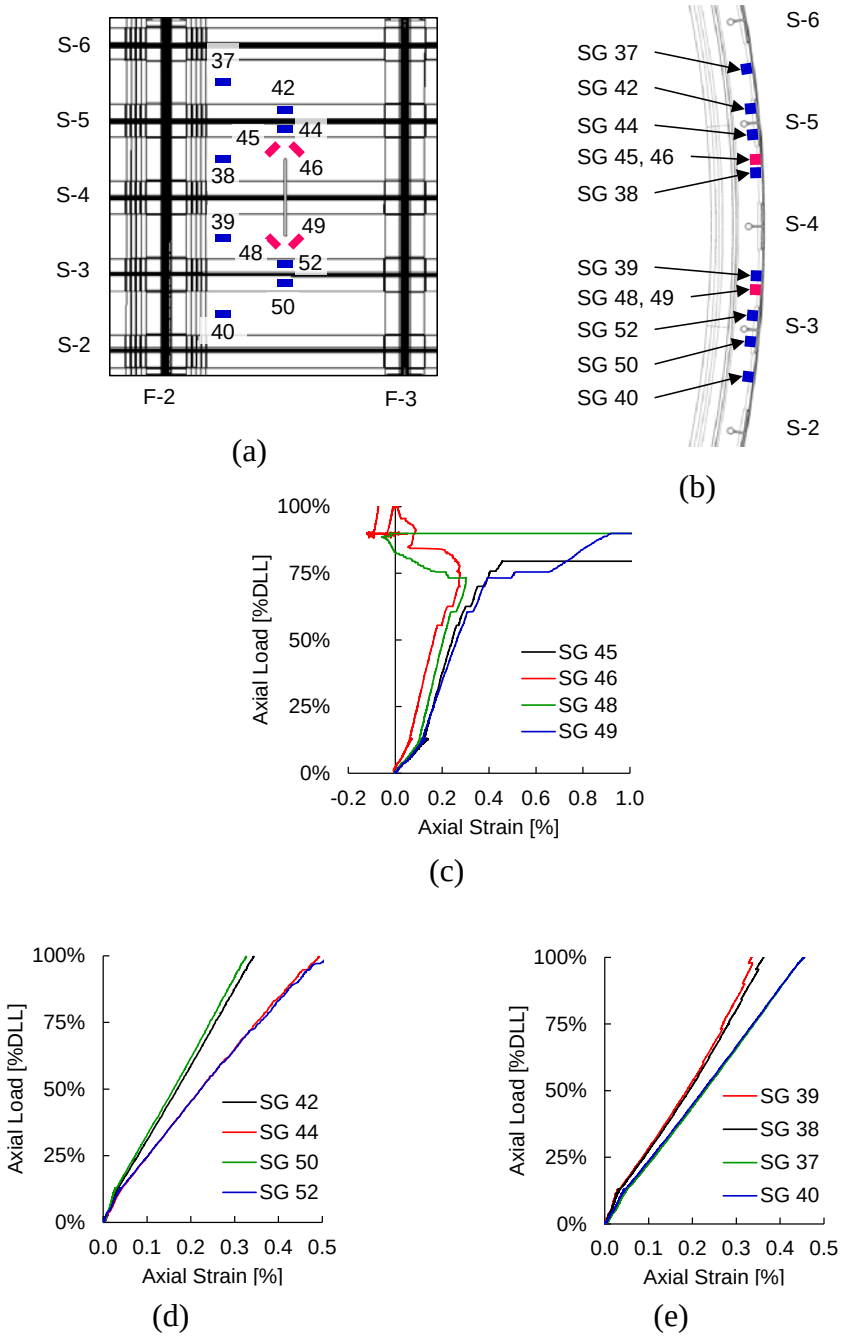

Figure 39. Photographs of Notch Tip Damage Showing Crack Progression During LS-2: (a) Interior Schematic, (b) Cross-Section Schematic, (c) Notch Tip 45° Strain, (d) Stringer Flange Axial Strain, and (e) Mid-Bay Interior Skin Axial Strain

As the damage progressed, the strain gages mounted parallel to the damage (fiber) orientation (SG 45 and SG 49) showed high tension and those mounted perpendicular to the fiber direction (SG 46 and SG 48) showed near zero strain; SG 45, SG 48, and SG 49 failed shortly afterward. Strain gages (SG 42, 44, 50, and 52) placed on the adjacent stringer flanges ahead of the notch tip showed nearly undisturbed linear response, as shown in figure 39(d). This occurred because, while damage propagated through the two-bay skin, damage remained contained within the two-bay region.

7.4.1.3 Load Step 3.

Damage progression was observed on the interior surface as a single instantaneous event in LS-3(point C in figure 34). The notch tip state-of-damage, before and after damage extension, is shown in figure 40. As seen, the crack extended to the adjacent stringer flange and arrested.

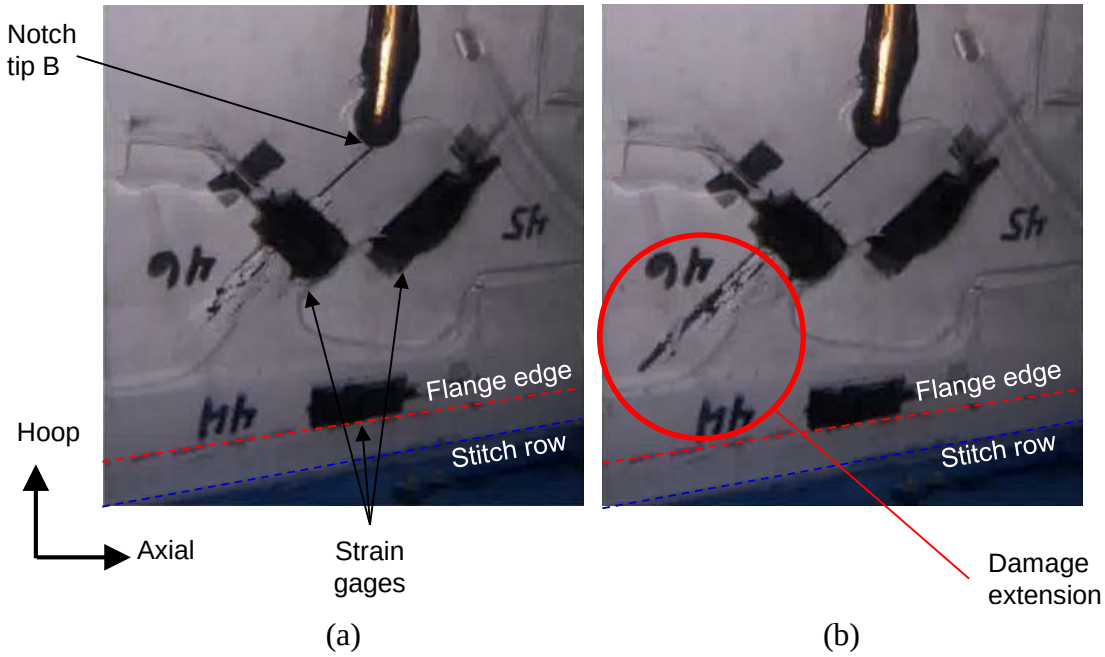

Figure 40. Photographs of the Interior Surface Showing Damage Progression From Notch Tip B During Load LS-3: (a) Before Damage Event and (b) After Damage Event

Axial strain in the mid-bay interior skin near the damage area (SG 38 and SG 39) increased slightly as the internal pressure was reduced to zero in LS-3, as shown in figure 41. Strain gages SG 64 and SG 66, which were placed symmetrically to SG 38 and SG 66, showed a similar response, and therefore verify that this strain behavior is due to the test panel configuration and not the existing damage. This confirmed that applying axial-only load (i.e., without pressure) was the most severe case, as predicted by the FEM.

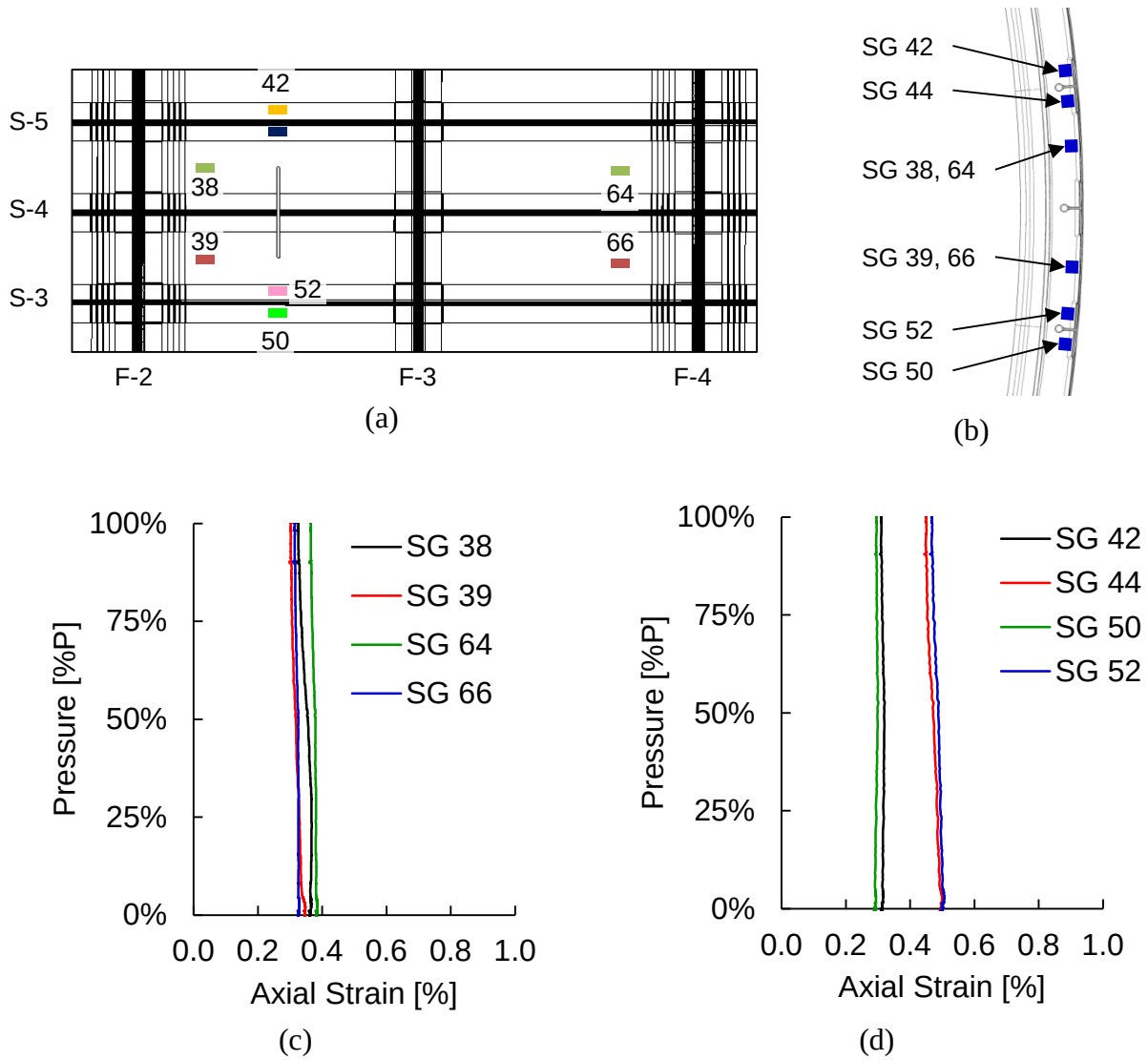

Figure 41. Strain in and Around the Two-Bay Region During LS-3 (note that (c) and (d) indicate a slight increase in axial strain as pressure is reduced from 1.0 P to 0 P): (a) Interior Schematic, (b) Cross-Section Schematic, (c) Mid-Bay Axial Strains, and (d) Stringer Flange Axial Strain

7.4.1.4 Load Step 4.

As expected, no new damage was observed during this LS because the panel had been loaded to this load level previously, during LS-2.

7.4.1.5 Load Step 5.

As the axial load was increased above 100% DLL (point D in figure 34), observed damage progression on the interior and exterior continued, as discussed below. Recall that the pressure

was maintained constant at 1P while the axial load increased monotonically; therefore, only the axial load level is discussed.

Exterior Crack Progression: Photographs of the crack progression on the exterior surface from points D through G in figure 34 (i.e., axial load increased from 100% DLL to 160% DLL) at notch tip A are shown in figure 42 (with the same orientation and scale as in figure 37). Notch tip crack progression during loading up to 147% DLL was slow, stable, intermittent, and along the 45° direction and was ultimately arrested by the inner row of stitches, figure 42(a through e). When the load was further increased to 148% DLL, the crack at notch tip progressed instantaneously from the edge of the stringer flange to the inner stitch row (point F in figure 34), before being arrested the second time, as shown in figure 42(e and f). Additional axial load was required to progress the crack beyond the stringer. When the load reached 160% DLL, figure 42(g), the damage progressed instantaneously beyond the two-bay region (point G in figure 34) and out of the exterior field of view of the camera, figure 42(h). The energy stored in the panel was released by the sudden formation of extensive damage, including the extension of the crack beyond stringer S-2, which caused a 5% axial load drop. A nearly identical crack progression pattern was observed along the other notch-tip in terms of the extent, rate, and the intermittent nature of crack progression.

High-speed video camera was used to capture damage progression at the high load levels (e.g., example point G in figure 34), with particular attention to capturing the crack at the point when it progressed beyond the two-bay region. Figure 43 shows the instant of crack progression ahead of notch tip B, which is similar to the crack progression shown in figure 42(g) and figure 42(h) for notch tip A. As seen, the crack was arrested by the inner stitch row up to a load of 160% DLL and then progressed, nearly instantaneously, past the outer two stitch rows on the other side of the stringer flange. The four high-speed frames that captured this event (figure 43) are 0.2 milliseconds apart. The red dots in the images in figure 43(a) through (c) indicate the tip of the observed crack. In figure 43(d), the red dot indicates that damage extended at least to the edge of the field of view. The damage was briefly arrested (for approximately 0.4 ms) at the outer stitch row, as shown in figure 43(b and c).

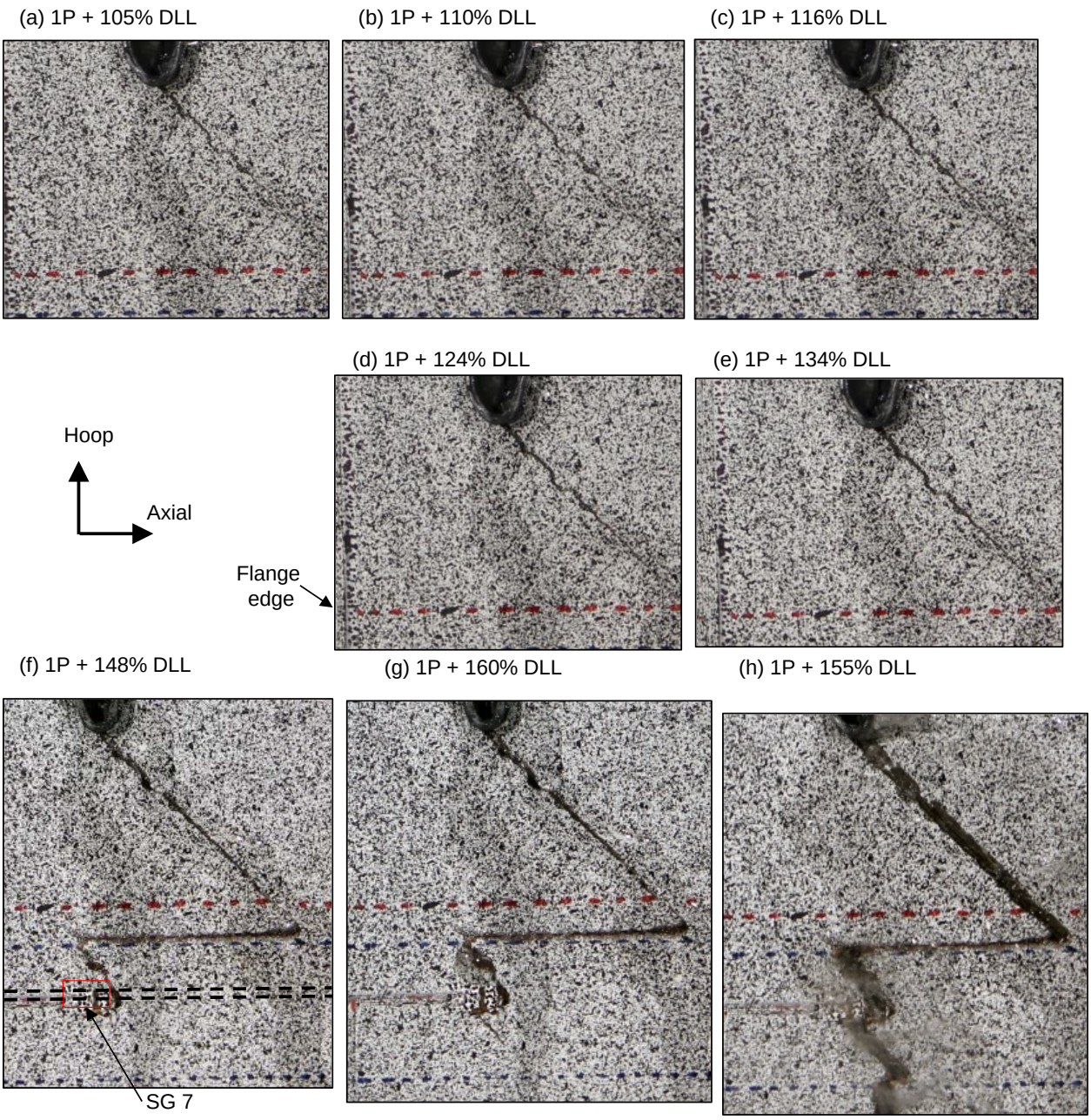

Figure 42. Exterior Surface Crack Progression During LS-5 (points D through G in figure 34), Showing the Crack Arrest Behavior of the Stitched Rows

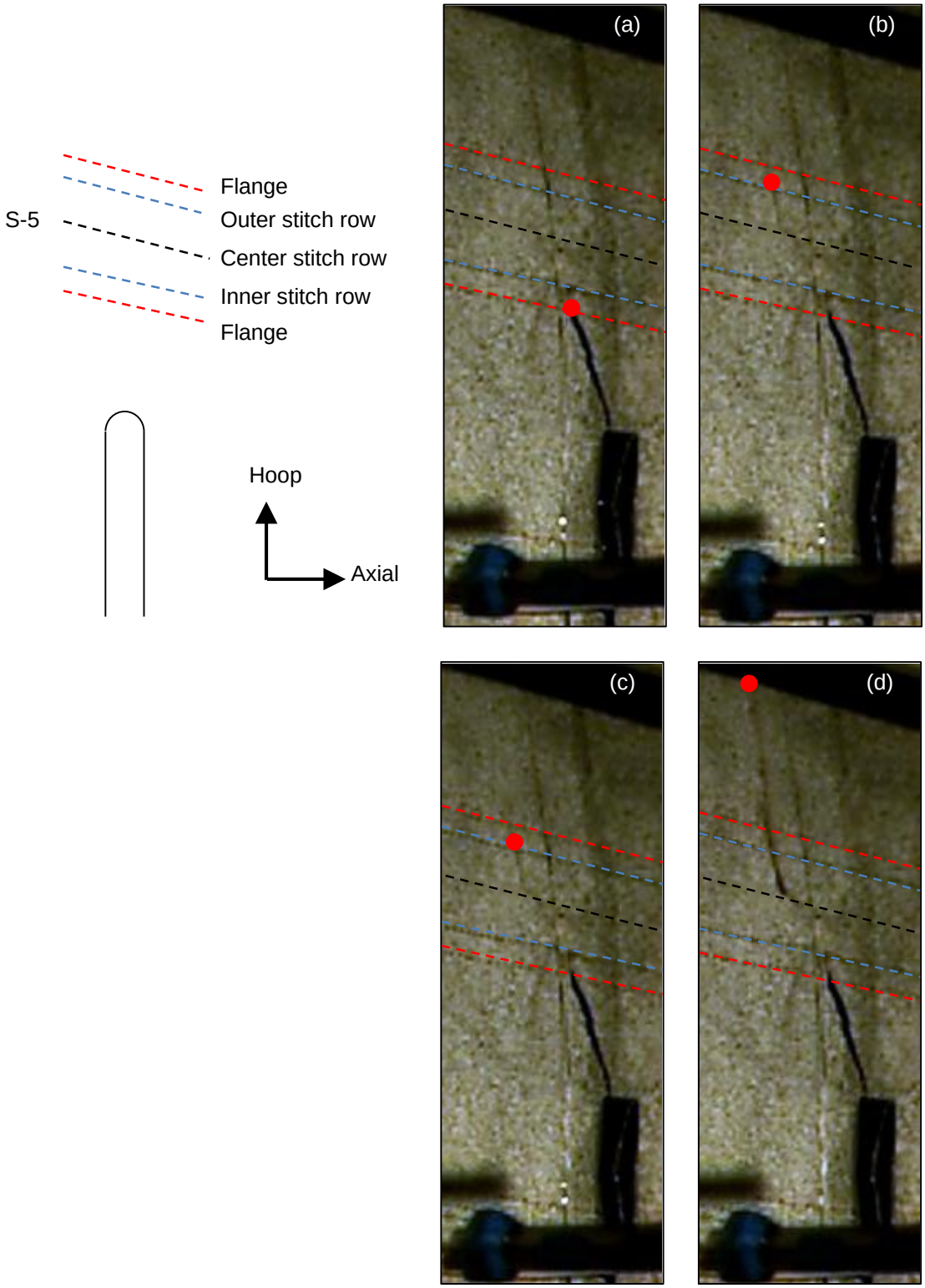

Figure 43. Sequential Frames, (a) Through (d), Captured Using High-Speed Camera Showing Crack Progression Beyond the Two-Bay Region (the red dots indicate the tips of the crack)

Interior Damage Propagation: Visible damage on the interior surface was massive and widespread as compared with the single-crack progression seen on the exterior surface. As the load was increased from point D in figure 34, visual observations on the interior surface showed slow, stable damage accumulation ahead of both notch tips, which propagated to the adjacent stringer flange edges, as shown schematically in figure 44(a) and figure 44(b). At the load level of 140% DLL (point E in figure 34) extensive skin/stringer disbonding progressed through the entire width of the bay, figure 44(c), evidenced by visible cracks along the skin/stringer interface. The skin/stringer disbonds were arrested by the stitching in the frame flanges as load was increased and remained completely contained within frames F-2 and F-3 by the stitching up to fracture. A large number of matrix cracks were observed along the 45° direction, emanating from the notch tips and stringer flanges.

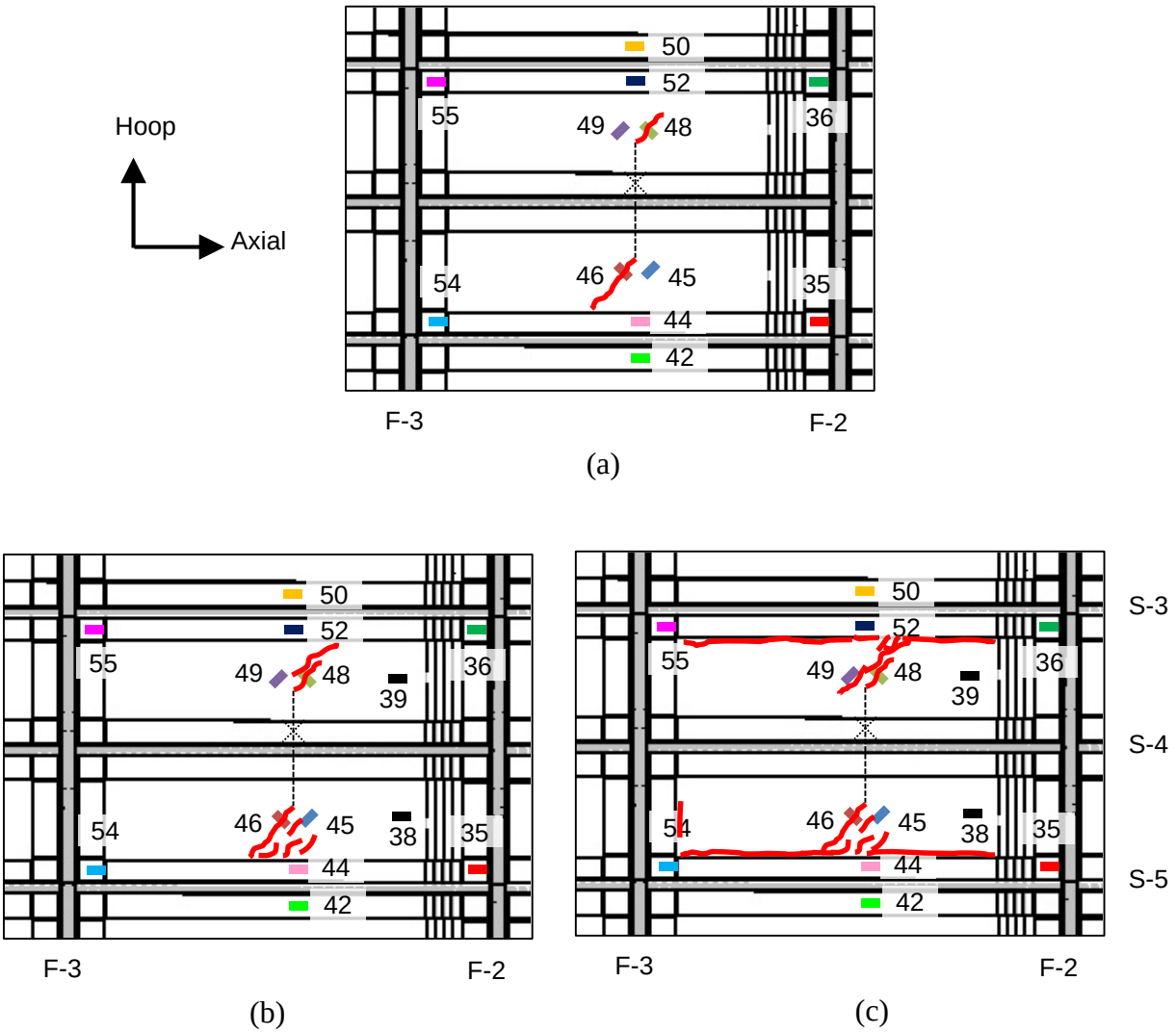

Figure 44. The Visually Observed (via the underwater camera) Damage Accumulation in the Interior Surface: (a) 1P + 100% DLL, (b) 1P + 138% DLL, and (c) 1P + 140% DLL

Several bursts of AE were heard during loading from 140% DLL (point E in figure 34) and fracture at 184% DLL. The underwater camera indicated panel shaking at these instances, indicating intermittent and rapid damage accumulation prior to fracture, apparently as a result of stringer/skin disbonding.

Measurements of crack length were taken, along the damage path, from both figures, up to the photo shown in figure 42(h) (point G in figure 34), where damage propagated beyond the two-bay region. On the interior surface of the skin, crack length measurements were taken up to the point where damage reached the adjacent stringers, S-3 and S-5 (point E in figure 34).

The exterior and interior crack length measurements are shown in figure 45. The interior crack length was consistently slightly greater than the exterior crack length. The results clearly indicate a nearly constant crack growth rate. The intermittent nature of damage progression is due to both the particular loading applied and the intermittent nature of crack extension in carbon fiber-reinforced polymer under quasistatic loading.

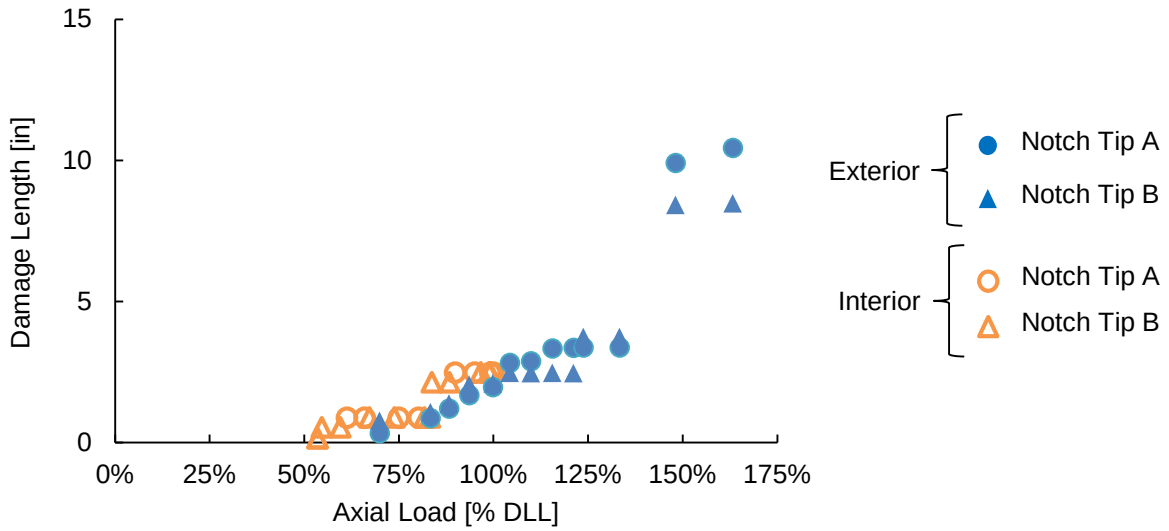

Figure 45. Crack Progression up to Point G, Figure 34,
Showing Constant Crack Growth Rate

Strain Redistribution: Damage progression was evident through displacement and strain records showing several strain redistributions that occurred before fracture load was reached. The locations of the strain gages are shown in figure 46. Figure 46(a) also shows the state-of-damage ahead of the notch tip at the load of 140% DLL (point E in figure 34). The correlation between strain redistributions and key visual observations of damage progression (i.e., points E, F, G, and H shown in figure 34), is shown by overlaying points E, F, G, and H on the displacement and strain plots in figures 47 to 52.

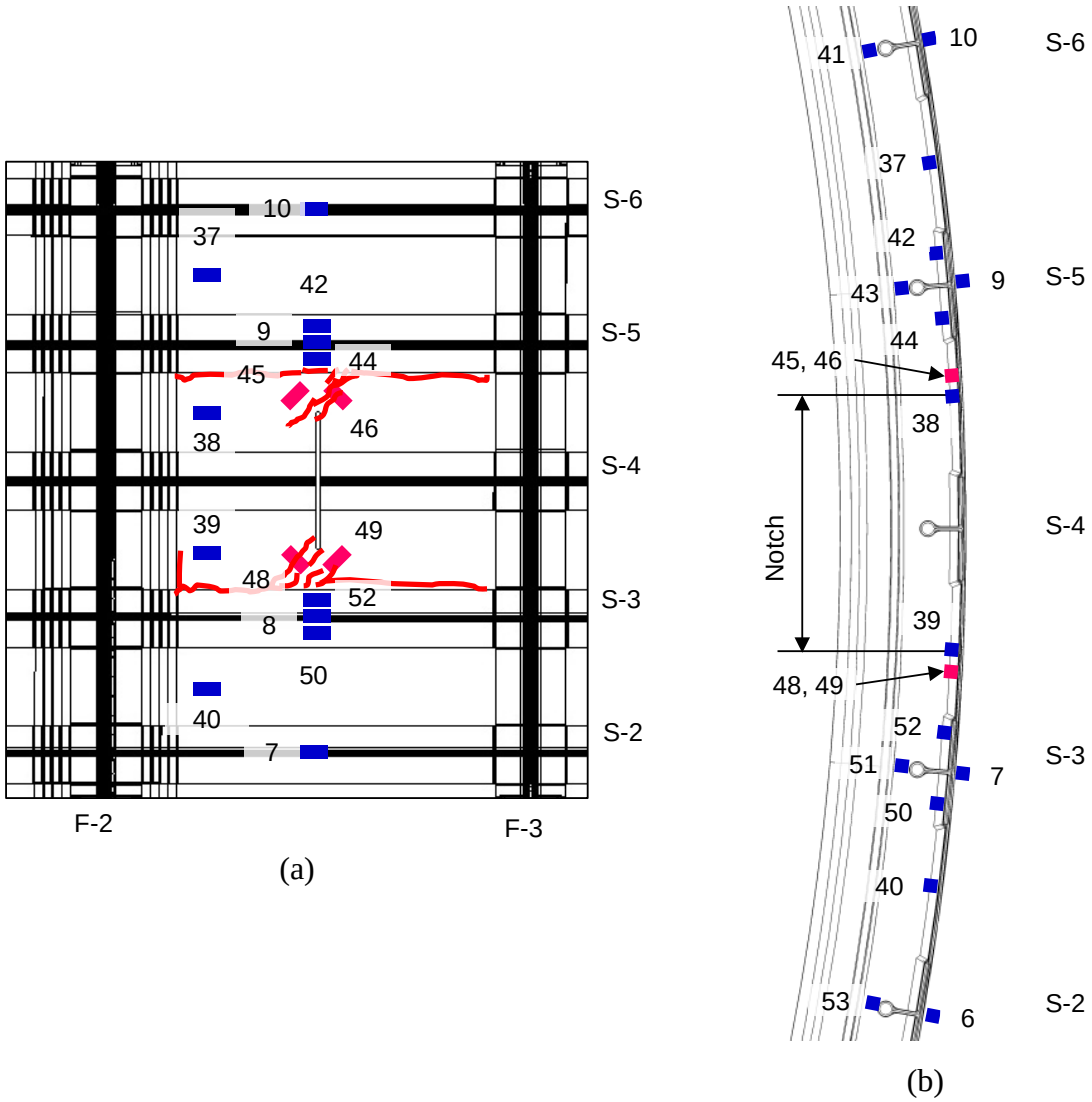

Figure 46. Selected Strain Gage and LVDT Locations: (a) Interior Schematic and (b) Cross-Section A-A Schematic

The overall axial displacement of the central stringer S-4, recorded by the LVDT, indicates a total displacement of 0.75 inch just prior to fracture (see figure 47). The discontinuities in the load displacement curve, starting at 160% DLL, point G in figure 34, resulted from the damage propagation beyond the two-bay region, as discussed previously.

The four exterior strain gages (see figure 48) clearly show the instant when the crack reached stringers S-3 and S-5, which were nearest to the notch tips. Initially, SG 7 and SG 9 (mounted on the skin, on top of stringers S-3 and S-5, respectively, mid-distance between frames F-2 and F-3), responded identically as the applied axial load increased beyond 100% DLL. The small discontinuities, seen in the plots between 100% DLL and 140% DLL, apparently resulted from the intermittent characteristics of crack extension discussed earlier. At the instant when the axial load reached 140% DLL, the two strain gages exhibited a sudden increase in strain, which

resulted from the crack progressing instantaneously to the adjacent stringer's center stitch row, observed visually in figure 42(e and f). The large increase in the strain recorded by SG 7 resulted from the damage progressing in close proximity to the strain gage. Upon further increase of the load, to 160% DLL (point G in figure 34), the strain reduced significantly as a result of further crack extension. Strain gages SG 6 and SG 10 (mounted on the skin, on top of stringers S-2 and S-6, respectively, mid-distance between frames F-2 and F-3) showed that the skin was subjected to smaller initial strains because they were farther away from the notch tip. Consequently, additional axial load was required, up to 160% DLL, before these strain gages reacted to the expanding damage: first increasing strain prior to dropping below initial values.

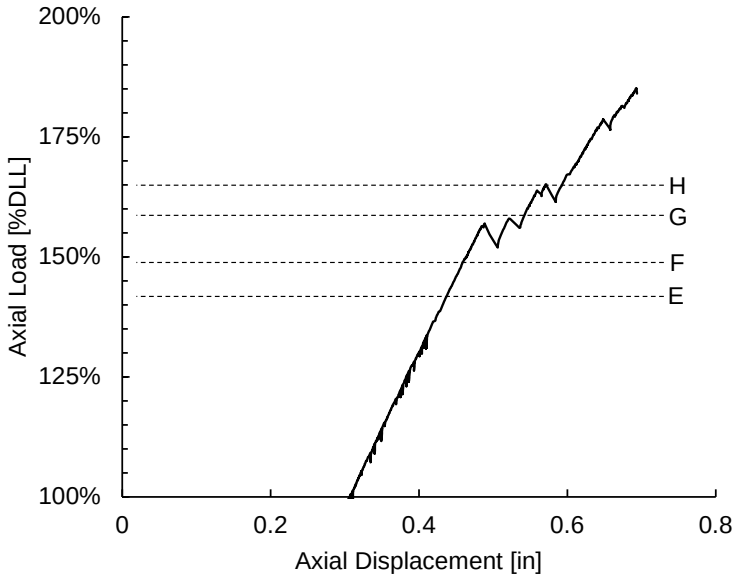

Figure 47. Overall Axial Extension

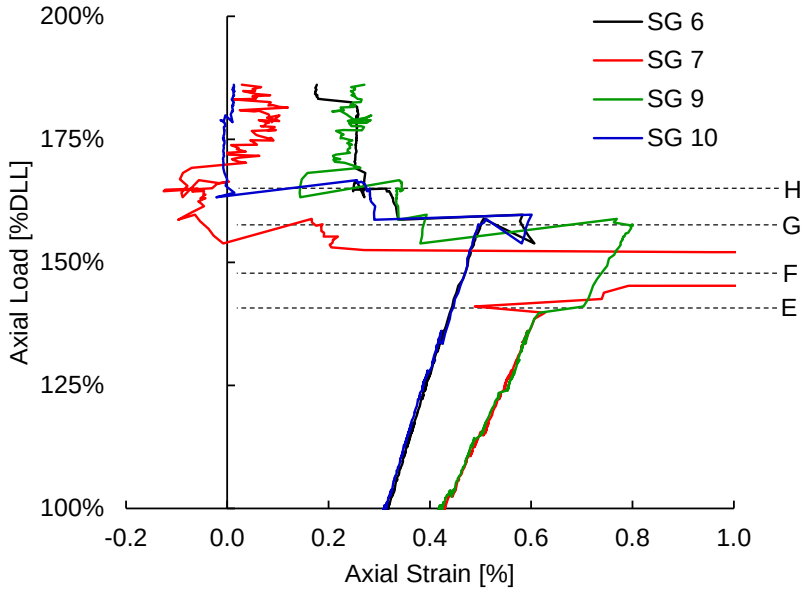

Figure 48. Exterior Skin Axial Strain

Similar behavior was recorded with the interior strain gages. For example, three of the four strain gages shown in figure 49 indicated a sudden damage progression at the load level of 160% DLL (with SG 37 exhibiting strain reduction at 167% DLL). The sudden damage extension was accompanied by a sudden reduction in the local strain, as expected. Note that the pair SG 37 and SG 40 and the pair SG 38 and SG 39 were mounted symmetrically about the notch. Each pair behaved nearly identically, validating the uniform load introduction even at the elevated load of 160% DLL. Strain gages SG 38 and SG 39, which were closer to the two notch tips, exhibited several discontinuities throughout loading from 100% to 160% DLL, corresponding again to the intermittent nature of damage accumulation. The massive damage accumulation at 160%-165% DLL nearly unloaded the skin completely in these four locations.

The four strain gages—SG 35, SG 36, SG 54, and SG 55—were mounted at the four frame/skin flange intersections—S-5/F-2, S-3/F-2, S-5/F-3, and S-3/F-3—symmetrically about the notch, as shown in figure 46. All four strain gages recorded nearly identical strain throughout the loading from 100% to 160% DLL (see figure 50) confirming proper load introduction during LS-5. The plots show that at 160% DLL (point G in figure 34), the strain in all four strain gages increased abruptly, well beyond the strain limit of these strain gages. As discussed earlier, at 140% DLL (point E in figure 34), visual observations showed skin/stringer disbond formation and progression to the stringer/frame intersections (S-3/F-2 and S-3/F-3, S-3/F-2 and S-3/F-3) before being arrested by the stitched row in the frame flanges, F-2 and F-3. As a result of this damage growth, the frame-stringer intersection strain gages (SG 35 and SG 55) showed this effect with strain discontinuities.

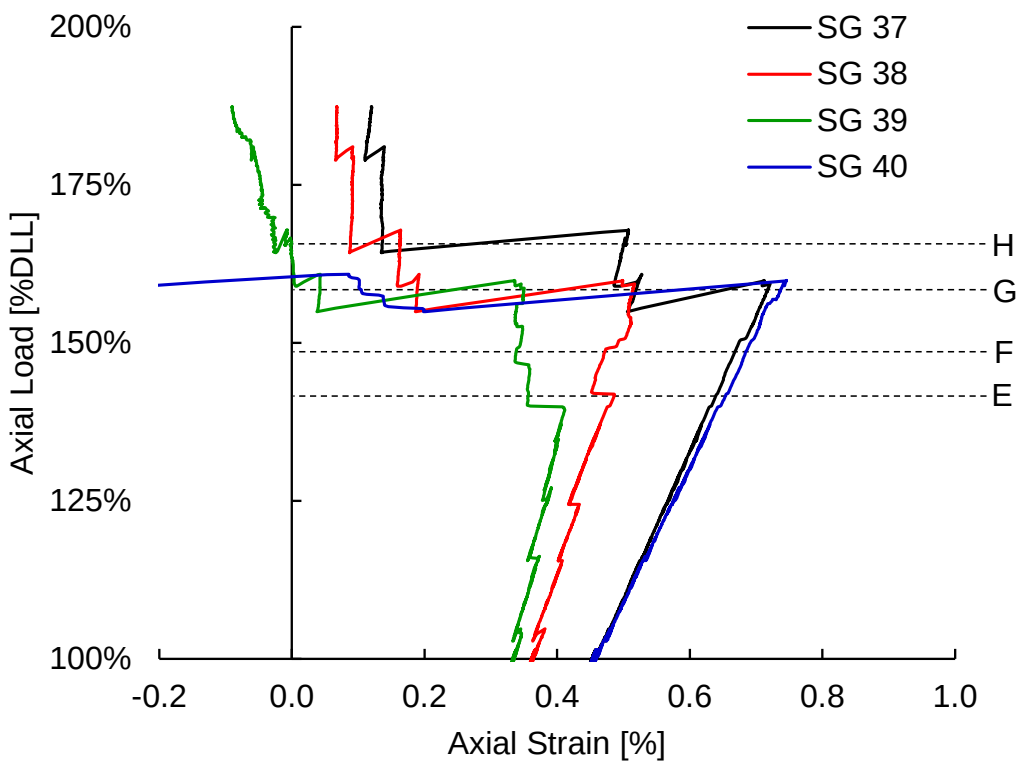

Figure 49. Interior Skin Axial Strain

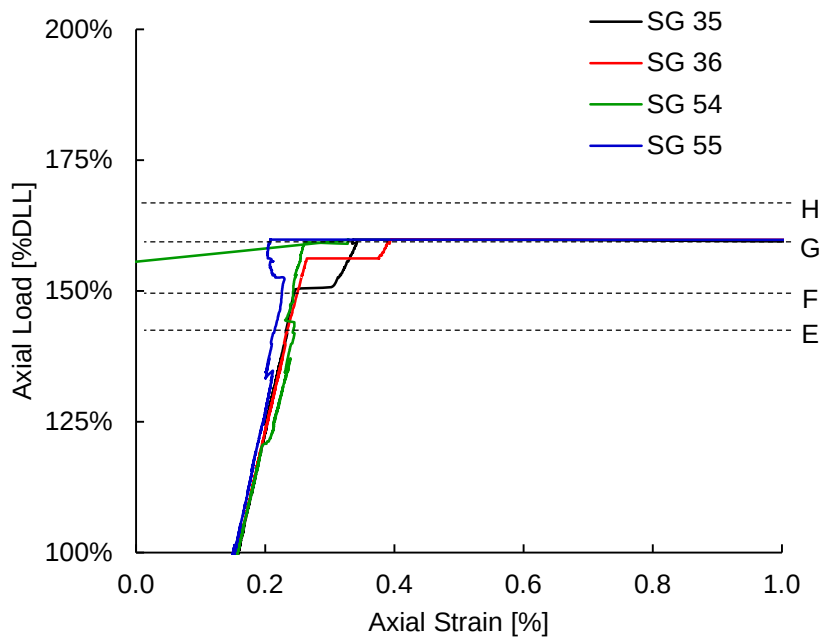

Figure 50. Frame-Stringer Intersection Strain

The load at which damage reached stringers S-3 and S-5 could be determined through the four strain gages mounted on the flanges of these stringers (see figure 51). The four strain gages were mounted along the notch centerline: SG 44 and SG 52 on the inner (notch tip side) flanges and SG 42 and SG 50 on the outer flanges. The two inner strain gages (SG 44 and SG 52) show the strain redistribution soon after increasing the load beyond 100% DLL, as manifested by the discontinuous behavior of both strain gages. The two outer strain gages (SG 42 and SG 54) initially exhibited the typical linear behavior, indicating that the damage did not affect the outer flange of the stringers. That is, the damage was arrested by the center stitch rows until the load reached 140% DLL (point E in figure 34), at which point the outer strain gages showed limited strain redistribution. It is only at 160% DLL (point G in figure 34) that both stringers S-3 and S-5 were severely affected by the damage progression: The inner strain gages show a significant and sudden drop in the strain while the outer strain gages show an increase in the strain, indicating that the outer stitch rows kept the outer stringer flange intact with the skin and maintained its capacity to carry the redistributed load. Upon further increase of the load, the four strain gages behaved linearly, albeit with some discontinuities, as damage continued to accumulate and progress, which indicated that the stringers maintained their capacity to carry the load up to catastrophic fracture at 184% DLL. It should be noted that each pair of strain gages performed nearly identically, indicating proper load introduction throughout loading to fracture.

Limited exterior and no interior visual observations where made of the damage progression and accumulation beyond 160% DLL: The loading fixture obstructed the exterior field of view and the underwater camera was unable to cover the entire test section in order to follow the rapidly expanding damage. It is likely, however, that the damage was contained within the four-bay region between stringers S-2 and S-6 until 167% DLL (point H in figure 34), at which point damage progressed to the outermost stringers. Beyond this load level, the strains recorded by

SG 41, SG 43, SG 51, and SG 53 (mounted on top of the rods of stringer S-6, S-5, S-3, and S-2, respectively) were nearly identical (see figure 52). At this load level, the skin lost most of its capacity to carry the load, as seen by the significant reduction in the strains in figure 52(d and e). That is, the stitched stringers bridged the failed skin (despite the local skin/stringer disbonding) and carried most of the load up to fracture.

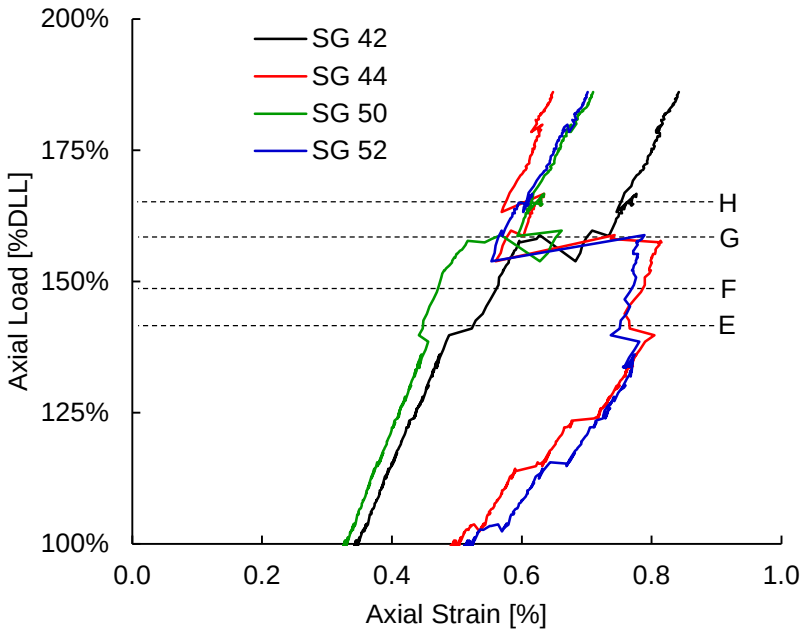

Figure 51. Stringer Flange Axial Strain

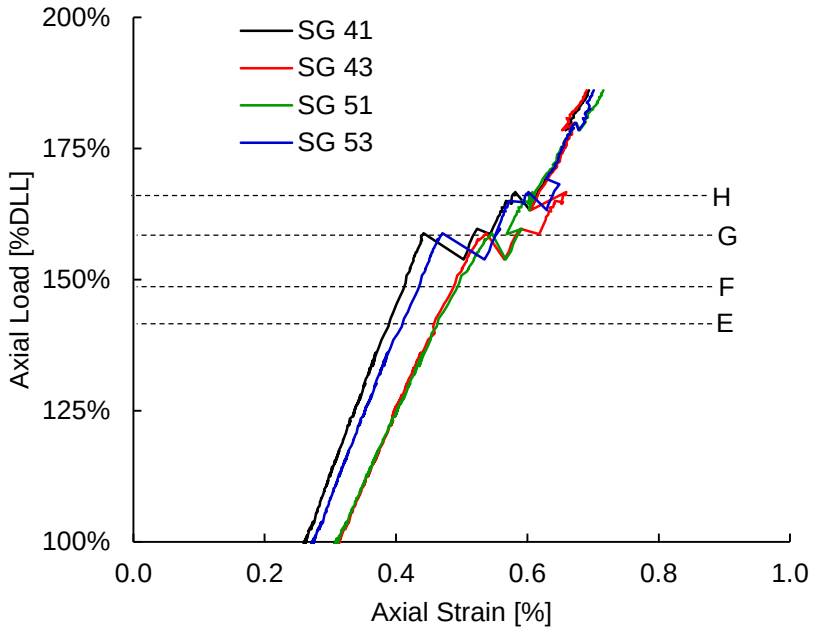

Figure 52. Stringer Axial Strain

The results also show the symmetry of the strain distribution as manifested by the strain records of stringers S-2 and S-6 (SG 53 and SG 41, respectively) and stringers S-3 and S-5 (SG 51 and SG 43, respectively) throughout the failure process.

Before catastrophic failure (184% DLL), the skin had nearly failed between frames F-2 and F-3, as shown by the low strains in the skin strain gages in figure 49.

7.4.2 The AE Results.

Figure 53 shows the accumulation of AE three-hit events recorded by the R15I sensors during phase III. No emission was recorded during LS-1. The first emission was recorded during LS-2; however, the low amplitude and saturated waveforms observed for these hits indicated that these were extraneous emission. The first legitimate emission was observed as axial load reached 15.5% DLL during LS-2. Emission was also generated during LS-3, likely due to high stress concentrations near the frame stringer intersections. The majority of the emission was generated during LS-5 as the panel reached failure load.

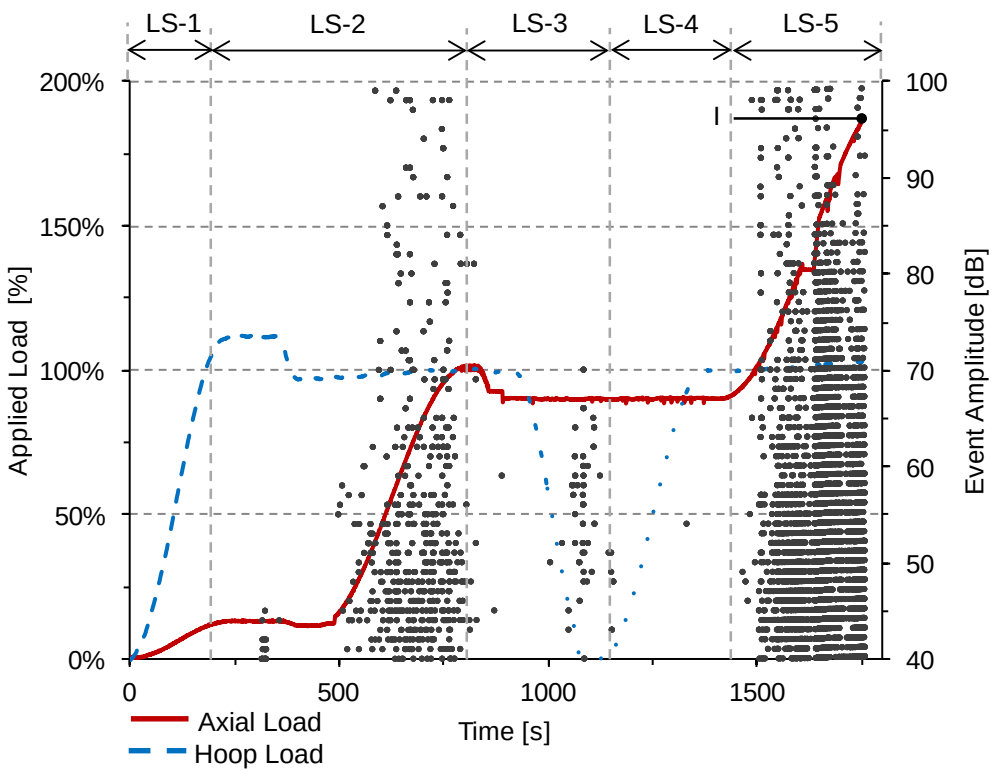

Figure 53. Load History Showing Accumulation of Three-Hit Events Recorded by the R15I Sensors and Corresponding First-Hit Amplitudes

Planar source location results obtained from the R15I sensors are shown in figure 54 for events with amplitude >90 dB. In figure 54, the black dash circle indicates the AE gage section. The sensors are shown along the circle as grey circles with black outlines and the vertical line near the center of the circle represents the location, orientation, and size of the notch. The blue dashed lines indicate the locations of the seven stringers and the red dashed lines indicate the

locations of four of the frames. The events are shown as grey circles within the AE gage section. These high-amplitude events clearly show that the most intense emission occurred directly ahead of the notch tips.

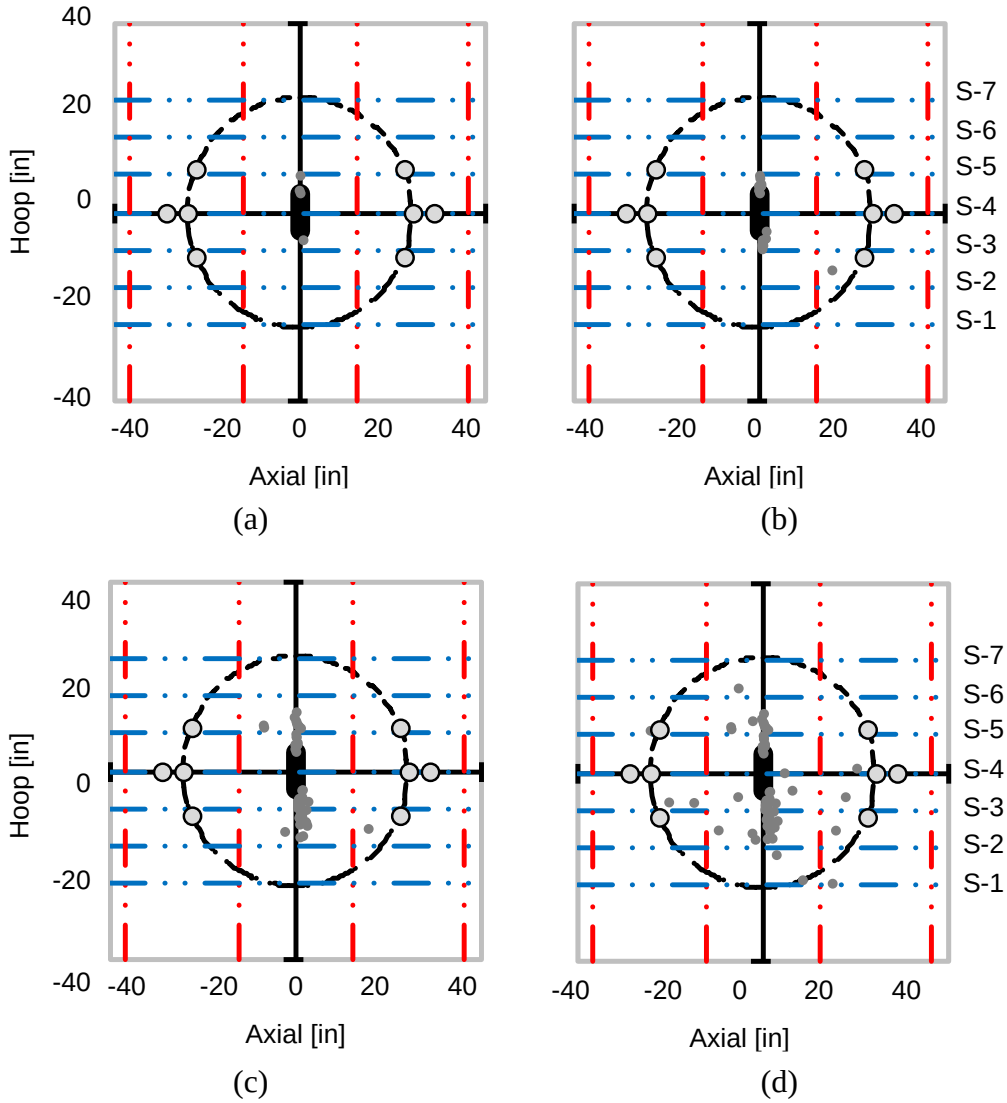

Figure 54. Planar Location Scatter Plots for Three-Hit Events With Amplitude >90 dB for R15I Sensors at Four Load Levels (similar results were recorded for the WDI Sensors): (a) 70% DLL, (b) 100% DLL, (c) 148% DLL, and (d) 184% DLL

7.5 POST-TEST NDI OBSERVATIONS.

The following sections summarize the results from the various NDI techniques used post-failure.

7.5.1 Visual Inspection.

Visual damage was found to be significantly more massive and widespread on the interior than the exterior faces. The through-thickness crack followed a meandering, partially anti-symmetrical, path. Figure 55 shows a side-by-side comparison of exterior and interior surface photographs.

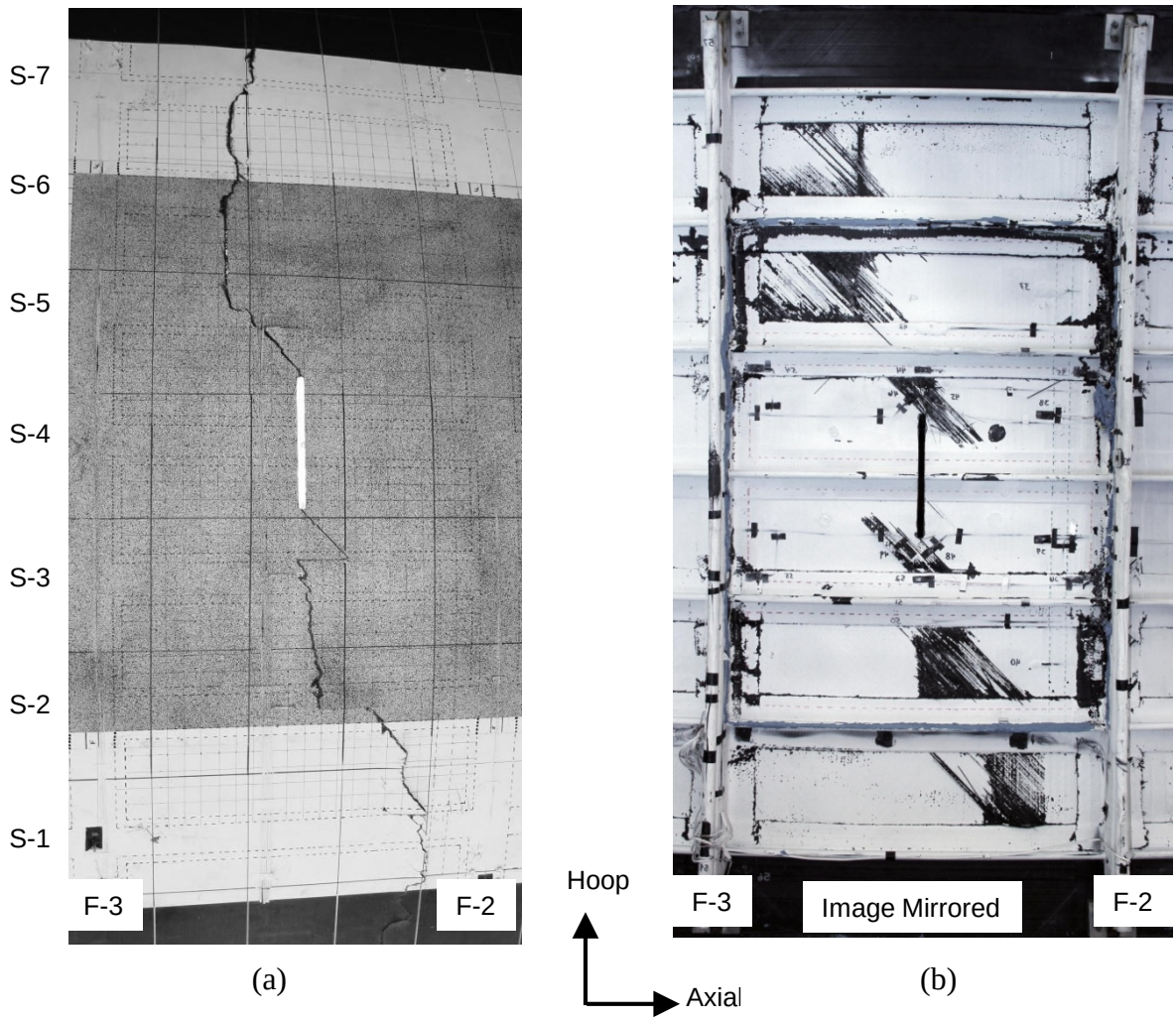

Figure 55. Post-Failure Photographs of the Panel Showing a Single Meandering Crack on the Exterior and Massive Damage on the Interior, Including Numerous Matrix Cracks and Skin/Stringer and Skin/Frame Disbonding: (a) Exterior and (b) Interior

The exterior crack was contained between frames F-2 and F-3 whereas the massive interior damage extended throughout the interior of the panel. The outer surface crack path was altered at several locations where it passed through the stitching rows, exhibiting their ability to arrest crack progression. The interior surface damage includes numerous matrix cracks, all oriented

along the 45° direction. It seems as though these matrix cracks emanated from the progressing through-the-thickness crack and stringer flanges in an antisymmetric manner. It is likely that the widespread matrix cracks on the interior surface are due to the pressure loading, which tended to separate the skin from the very stiff frames and stringers, thus leading to matrix cracks emanating from the skin/stringer flange interface. Additionally, visible damage on the exterior surface was likely affected by the fiberglass layer in limiting the number of visible matrix cracks.

Visual observations suggest that the stringer wrap plies, webs, and flanges disbonded from the surrounding load introduction buildup and skin plies in the load introduction region, resulting in catastrophic failure. Stringer rod, web, and flange pullout occurred in three of the stringers, specifically, S-3, S-5, and S-6, as shown in figure 56. Failure at the stringer and frame intersections (keyhole), circled in red in figure 56, indicates that, in the failed state, the stringers were displaced axially relative to the frame. Measurements of the stringer rod pullout distance were taken and are summarized in table 6.

Table 6. Measured Stringer Rod Pull-Out Distance

Stringer	Rod Pull-Out Distance
S-3	0.74”
S-5	0.84”
S-6	0.78

During the dynamic events of the catastrophic fracture, a large number of stitches failed, yielding complete disbonding between the stringers and the skin, such as that shown in figure 57. Disbonding was seen in all stringers, covering most of the region between frames F-1 and F-4. The disbonding was accompanied by additional matrix cracking along the 45° direction as portions of the interior skin were delaminated, as shown in figure 57(a). Such disbonding occurred also between the frame and the skin, as seen in the intersection between stringer S-7 and frame F-2 in figure 57(b). As discussed earlier: (1) the underwater camera showed that the frames/skin interface was intact up to catastrophic failure (i.e., frames were not disbonded) and (2) the stringer/skin interface was intact outside frames F-2 and F-3. Thus, the majority of stiffener/skin disbonding occurred during the sudden release of energy at fracture. Overall, stitch failures were widespread, resulting in disbonding of the frame and stringer flanges from the skin throughout most of the panel.

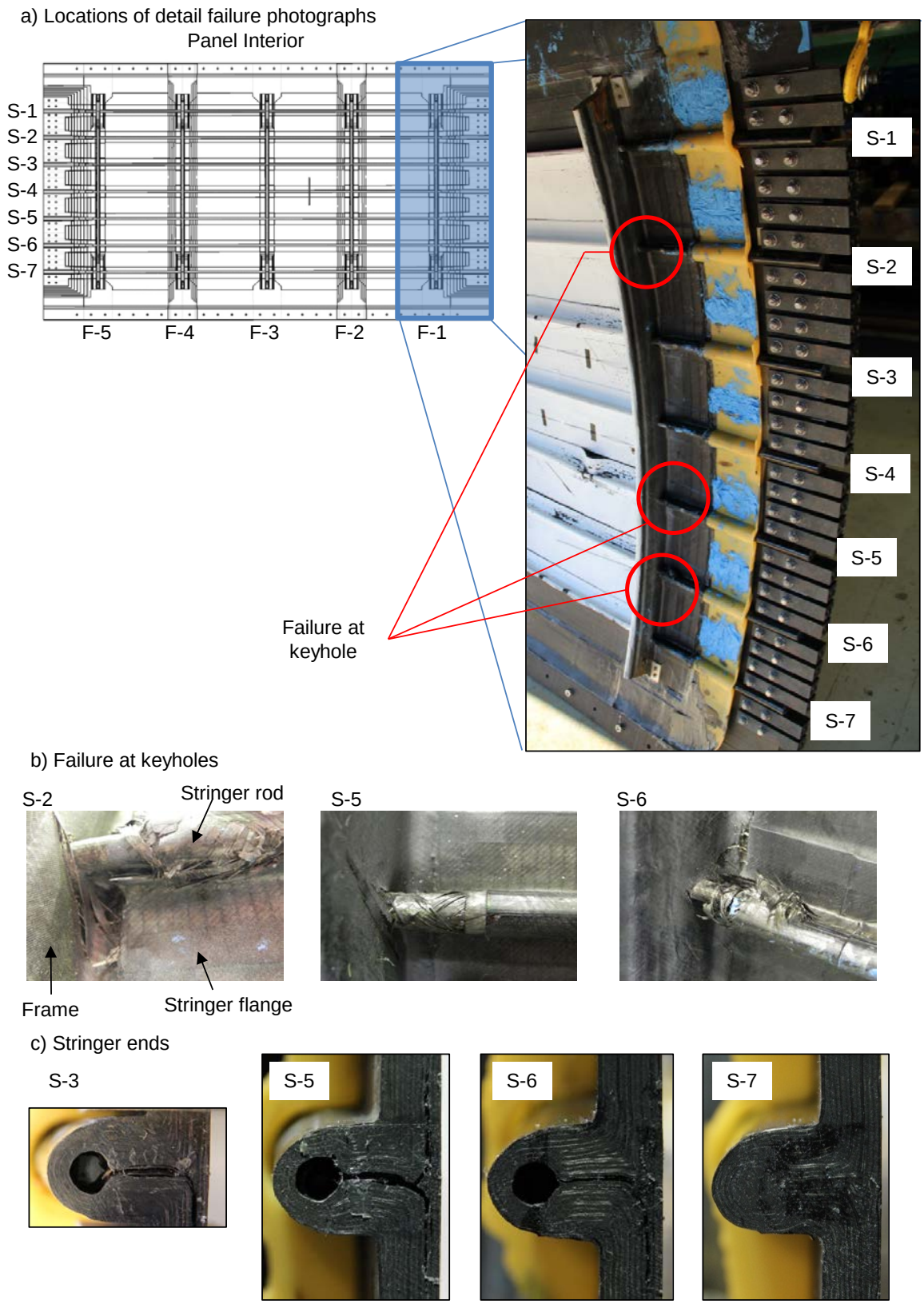

Figure 56. Detailed Photographs of Select Areas Critical to Catastrophic Failure: (a) Locations of Detail Failure Photographs, (b) Failure at Keyholes, and (c) Stringer Ends

(a) (b)

Figure 57. Photographs of Select Disbonded Stringers: (a) 5-5 Disbond and (b) S-7 Disbond

7.5.2 Pulse-Echo Ultrasound.

Pulse-echo MAUS inspection covered an area that measured 610 mm x 406 mm (24 in. x 16 in.), which included frames F-2 to F-3 in the axial direction and notch tip B to stringer S-6 in the hoop direction. Amplitude and time-of-flight results clearly show a large delaminated region in the skin ahead of the notch tip, as shown in figure 58. It is also observed that the reduction in amplitude and increase in time-of-flight in the frame areas indicated the frames were still partially attached to the skin, figure 58(a) and figure 58(b), whereas the stringers are completely disbonded. The time-of-flight C-scan shows that the delamination surrounding the crack path occurred at approximately the same location through the thickness throughout the inspected region. Some of the 45° matrix cracking around the crack path is visible in both the amplitude and time-of-flight results. The significance of the two triangular damaged regions along the two stringers was not clear from the NDI results.

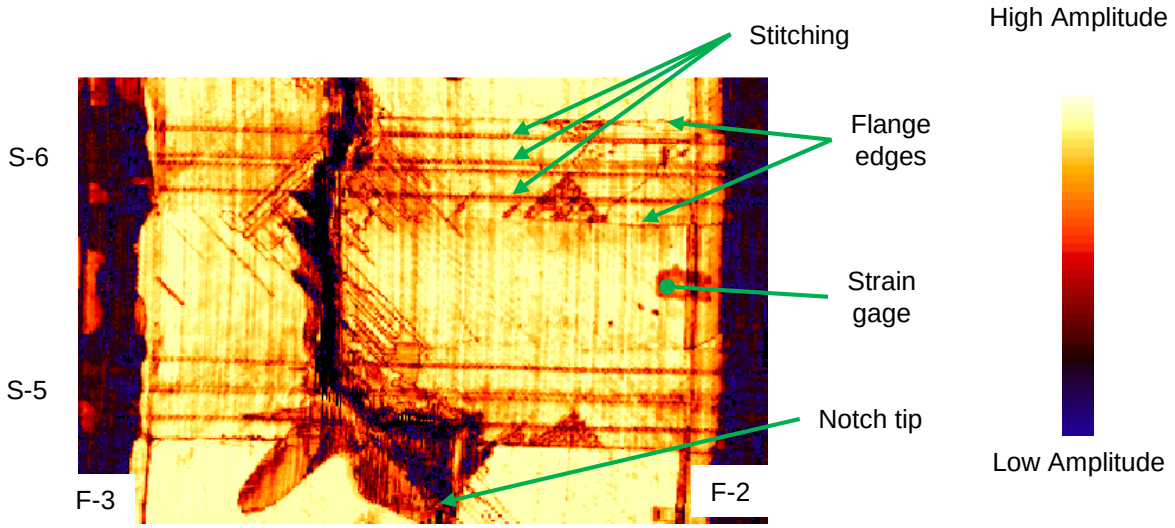

(a)

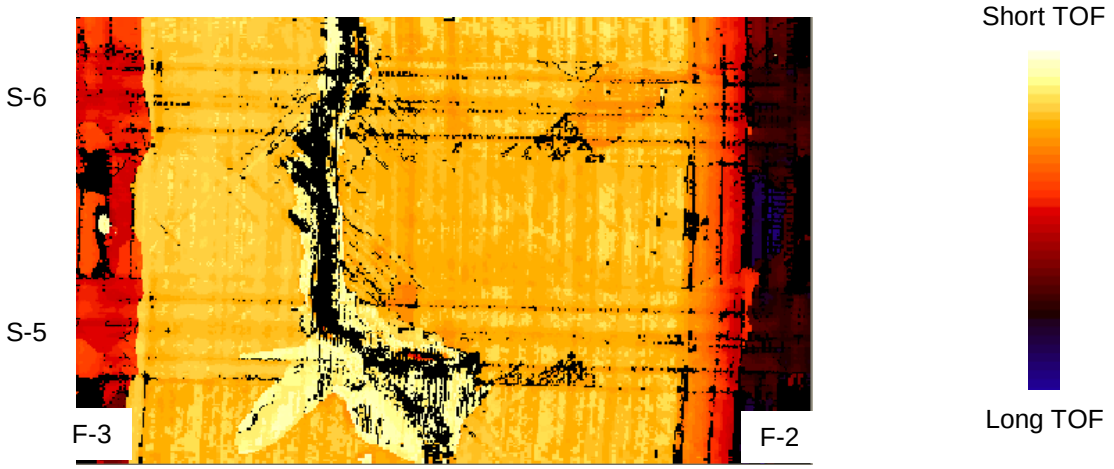

(b)

Figure 58. Pulse-Echo C-Scans of the Notch Tip B Region Showing Significant Delamination at the Notch Tip and Partial Frame/Stringer Disbonding: (a) Amplitude C-Scan and (b) Time-of-Flight C-Scan

7.5.3 Through-Transmission Ultrasound.

The TTU results showed less resolution than the MAUS inspection. The result for the inspected region, which includes the area from the notch tip to midway between S-5 and S-6 and from F-2 to F-3, is shown in figure 59. Damage and delamination were evident in similar areas when compared with the MAUS inspections, as shown by the red and white areas labeled as damage areas in figure 59. The TTU inspection clearly shows the thickness change between the skin and stringer flange where the undamaged skin is green and the undamaged stringer flange is blue;

however, there is no indication from the results that there is a delamination between the stringer flange and skin.

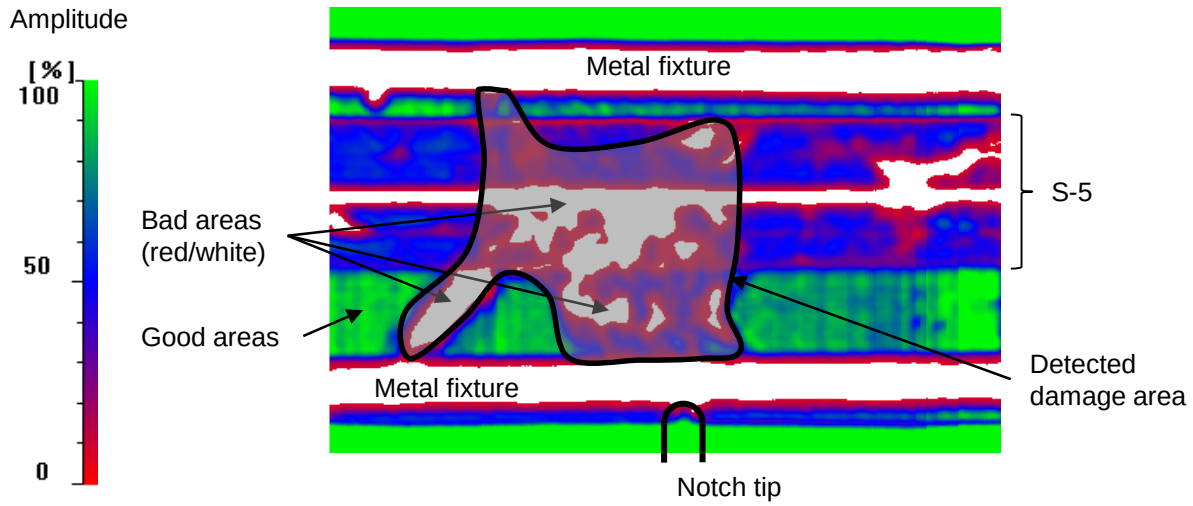

Figure 59. The TTU Results

7.5.4 Flash Thermography.

The flash thermography system was able to identify the major structural components similar to the ultrasonic scans, as shown in figure 60. The delamination surrounding the translaminar crack was shown to be slightly smaller in the flash thermography results when compared with the ultrasonic results. The delaminations surrounding the translaminar crack extended to the edge of the panel. The stitching appeared slightly darker than the skin results and was partially highlighted with red by the software. This was an artifact of the post-processing. The flash thermography results showed no indication of damage in the stitching.

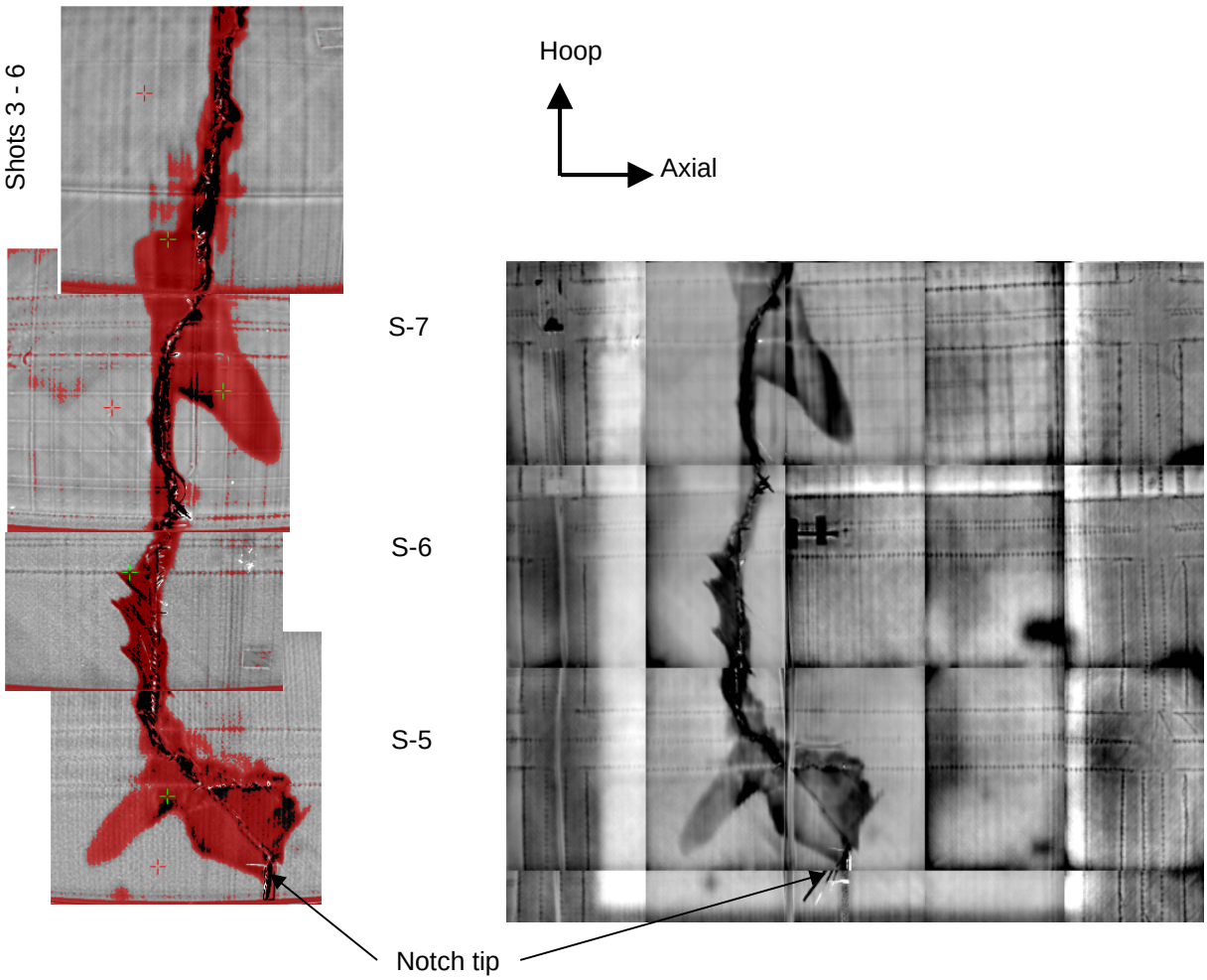

Figure 60. Flash Thermography Results (left shows results from inspection at Sandia; right shows results from inspection at FAA William J. Hughes Technical Center)

7.5.5 X-Radiographic Computed Tomography.

X-Ray CT provided insight into the skin delamination and skin/stringer disbonding. The three-dimensional data are shown via cross-sectional view, as depicted in figure 61. Similar damage was identified, as seen in the ultrasonic results. No stitching was visible along the skin/stringer disbonded area, which confirmed that the stitches completely failed at this interface. In the surrounding portions of the stringer, the stitching was intact on the exterior surface of the skin and interior surface of the stringer flange. Section view through the skin/stringer interface showed some areas with holes (i.e., voids) in the skin where the stitches apparently pulled out, indicating that the stitch failure occurred somewhere in the skin rather than at the skin/stringer interface.

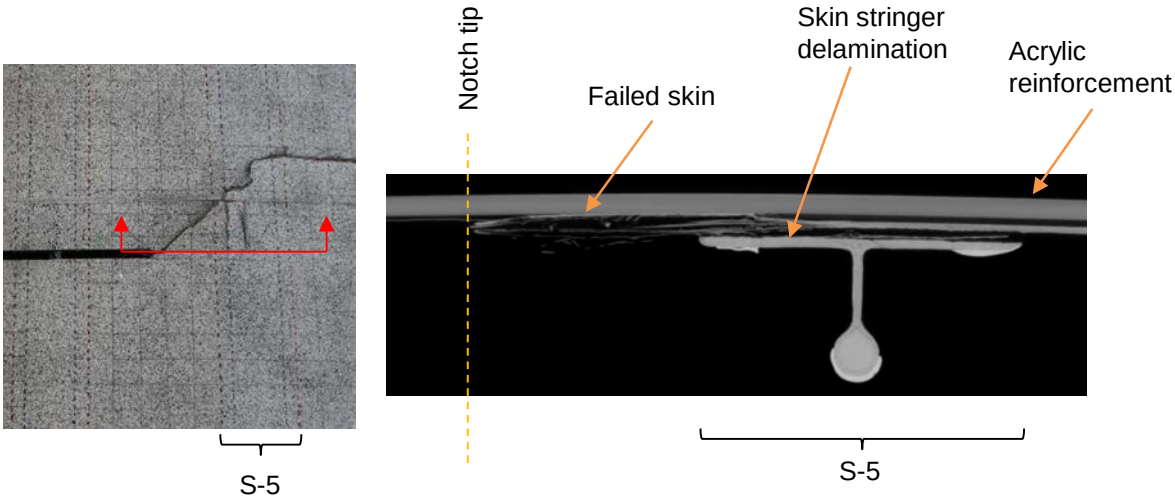

Figure 61. The CT Image of Skin/Stringer Cross Section View Near the Notch Tip

7.6 TEARDOWN OBSERVATIONS.

Teardown examinations of key panel segments were performed to quantify the extent and location of damage and determine areas for subsequent fractography to identify the failure mechanisms involved.

7.6.1 Global Observations.

Visual inspections of teardown of stringer S-5 confirmed that it was not attached to the skin. Figure 62(a and b) show the skin and stringer segments and disbond surfaces. Figure 62(b) shows the stringer lifted off the skin and rotated 180° about the hoop axis. The disbond surface reveals the mostly intact warp knitting and broken stitches, shown in figure 62(c and d).

The failed stitches appeared similar on both the skin and stringer disbond surfaces with small segments of the stitch protruding approximately 0.5 mm from each surface, indicating that the stitches typically stretched and failed at the skin/stringer interface. In some instances, particularly along the translaminar damage path, a much longer segment of the stitch (up to several millimeters) was observed protruding from the laminate, indicating the stitch failure occurred somewhere other than the skin/stringer interface. In two regions, skin and stringer flange delamination occurred, such that the failure between the skin and stringer did not occur uniformly at the skin/stringer interface. In these areas, the warp knitting failed in addition to the stitches.

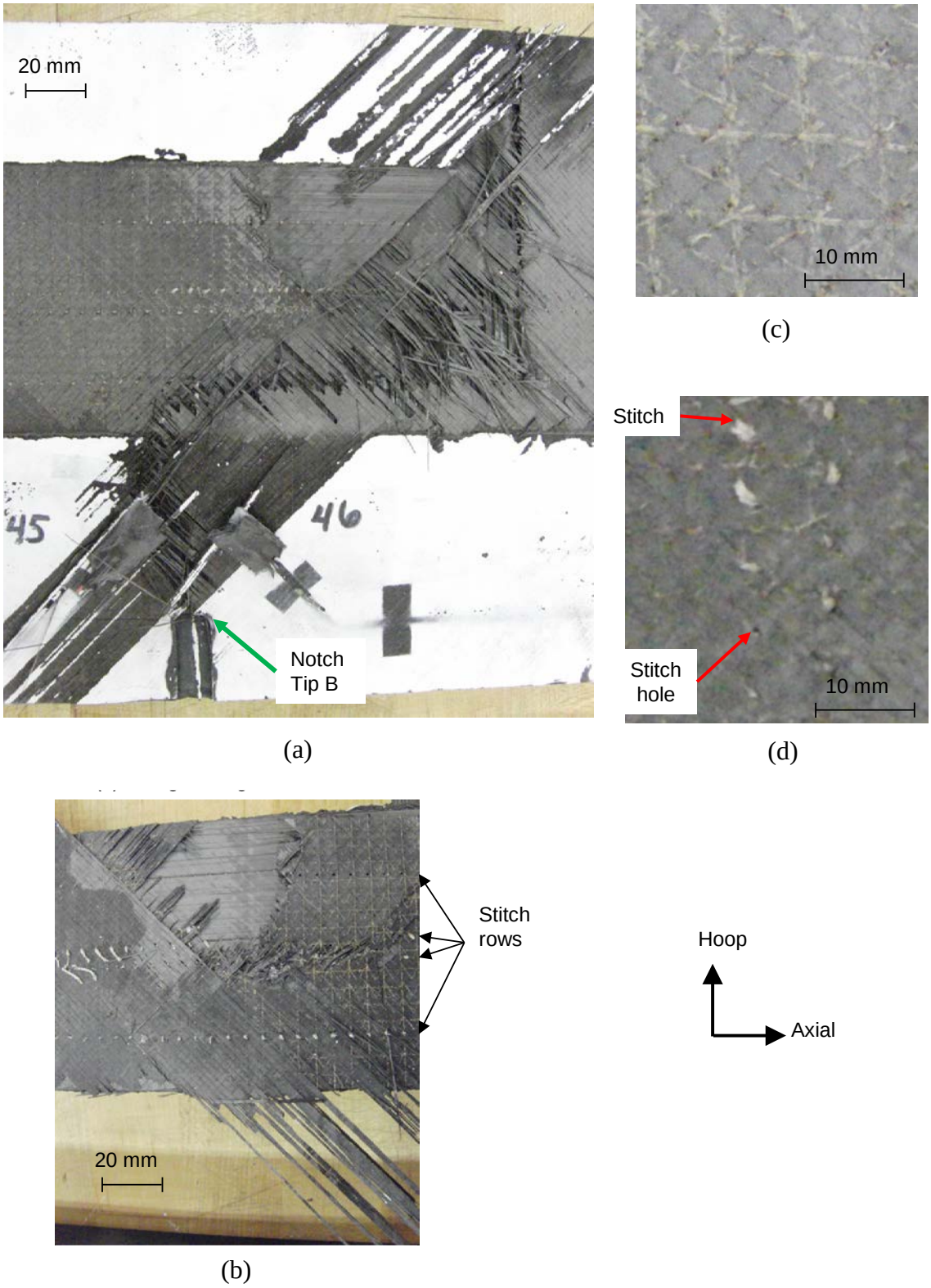

Figure 62. Visual Inspection of Tear-Down Segments of the S-5 Skin Stringer Disbond: (a) Skin, (b) Stringer Flange, (c) Warp-Knitting, and (d) Stitch Failures

7.6.2 Ply-by-Ply Teardown.

Teardown of the skin showed delaminations, extensive matrix cracking in nearly all plies, and a well-defined crack path in all but the 90° plies. A schematic representation of the major crack path and delaminations is shown in figure 63 for each ply through the thickness. The schematic starts with the exterior ply, shown in figure 63(a), and shows sequentially each ply up to the interior ply, shown in figure 63(g). The exterior ply (-45°) shows the damage that was visible on the exterior surface, shown in figure 63(a). A crack extends in the -45° direction, parallel to the ply fiber direction, from the notch tip to the inner stitch row. The crack branched at this point, and the secondary crack progressed along the stitch row approximately 80 mm before ending. The main crack briefly progressed along the stitch row in the opposite direction and then continued in the hoop direction. The next ply (+45°) has a slightly different crack path, as shown in figure 63(b). The crack progressed in the hoop direction to the inner stitch row and then continued along the same path as observed on the exterior ply.

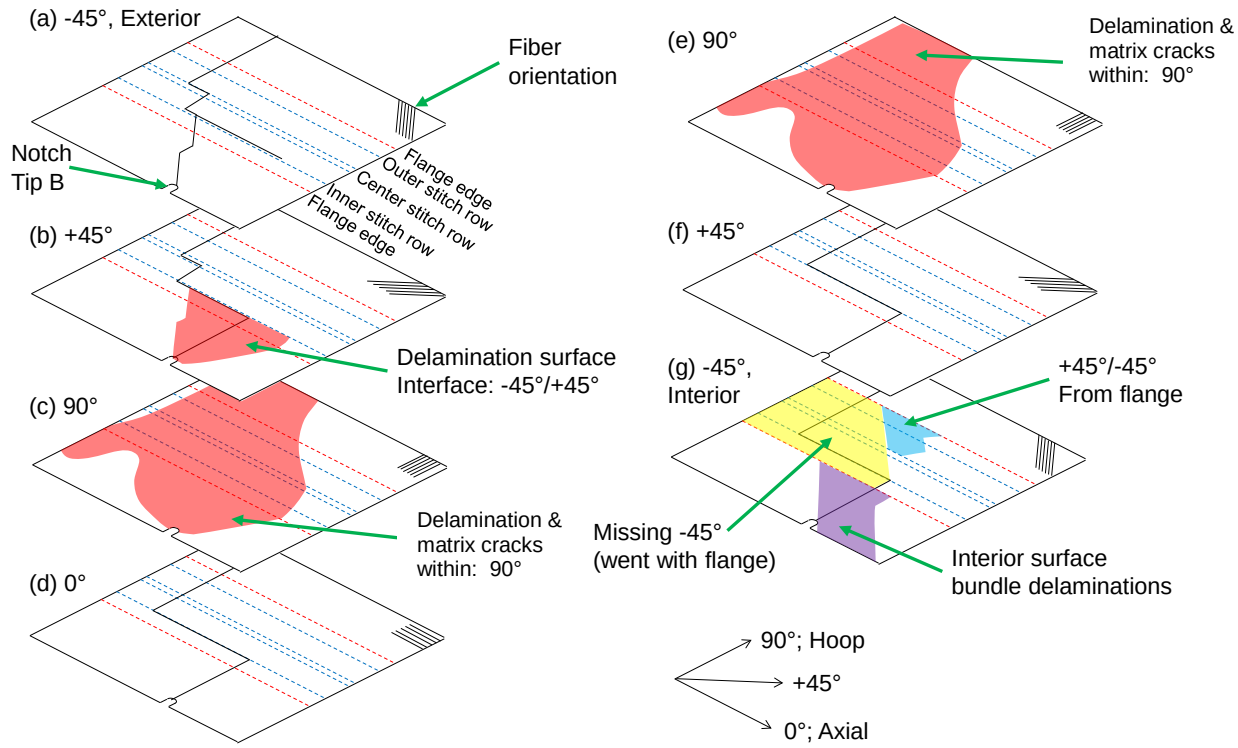

Figure 63. Significant Failure Extent, Ply-By-Ply

A delamination was observed between the +45° and -45° ply, bounded by the inner-stitch row and the 45° crack in the outer ply (highlighted in red in figure 63(b)). The third ply (90°, double thickness) showed extensive delamination within the ply (the large region highlighted in red in figure 63(c)). In the select areas that were destructively examined, this delamination matched the delamination size and shape detected by the ultrasonic inspection. The fourth ply (0°, center ply in layup) showed a crack in a similar location as the second ply, with a slightly different path between the inner stitch row and the outer stitch row, as shown in figure 63(d). The fifth ply (90°) showed damage very similar to the third ply, which had the same orientation. The

sixth ply (+45°) showed the same crack path observed in the central ply (0°) and no delaminations. The last ply, (-45°, interior surface) showed the same crack path as the central and sixth plies. In the region highlighted in blue in figure 63(g), delamination in the stringer flange occurred and the flange's +45° and -45° plies nearest the skin remained on the skin. The yellow-highlighted region shows where the -45° ply from the skin delaminated and stayed with the stringer flange. Extensive delaminated bundles occurred between the notch and the flange (highlighted in blue). This ply-by-ply damage map will be used for comparisons with damage predicted by future progressive failure analysis.

7.6.3 Fractography.

The fracture surface across the skin thickness (segment SEM-A in figure 21), along the crack emanating from the notch tip, shows typical failure modes in graphite/epoxy laminates, including matrix cracking, delamination, and fiber breakage, as shown in figure 64(a). Most of the adjacent plies at the notch tip delaminated. A representative close-up view indicates that most fibers fractured perpendicular to their axes with no fiber pullout, as shown in figure 64(b). Fiber surfaces in the 0° and 45° plies were clean of matrix residue with scattered matrix debris remaining on the fiber surface, as shown in figure 64(b), indicating a complete fiber/matrix interface disbonding.

The ultrasonic inspections revealed a relatively wide delaminated area ahead of the notch tip (see figure 58). Examination of this delamination surface (segment SEM-B in figure 21) revealed resin-rich areas around the warp knitting, as shown in figure 65(a). The warp knitting process disturbs the path of the fibers, causing them to bend around the knitting, resulting in resin-rich pockets and nonuniform fiber distribution and orientation. The width of the resin-rich area is the width of the warp knit thread, which is approximately 400 μm. The length was observed to be 6–8 mm. Figure 65(b) shows a detailed view of a representative warp knit failure region showing interface failure between the matrix and knitting fibers as well as knitting fiber pullout and cleavage type fracture surfaces, characteristic of brittle fracture, in the resin-rich pocket surrounding the knitting. Previous studies [24] indicated warp knitting may reduce the in-plane properties. Results from this investigation show that warp knitting did affect the failure mechanism and, therefore, may be important to the failure process. Close examination of the delaminated fracture surface also revealed that the fiber surface is clean of matrix, indicating failure at the fiber/matrix interface and matrix serrations characteristic of shear failure, as shown in figure 66.

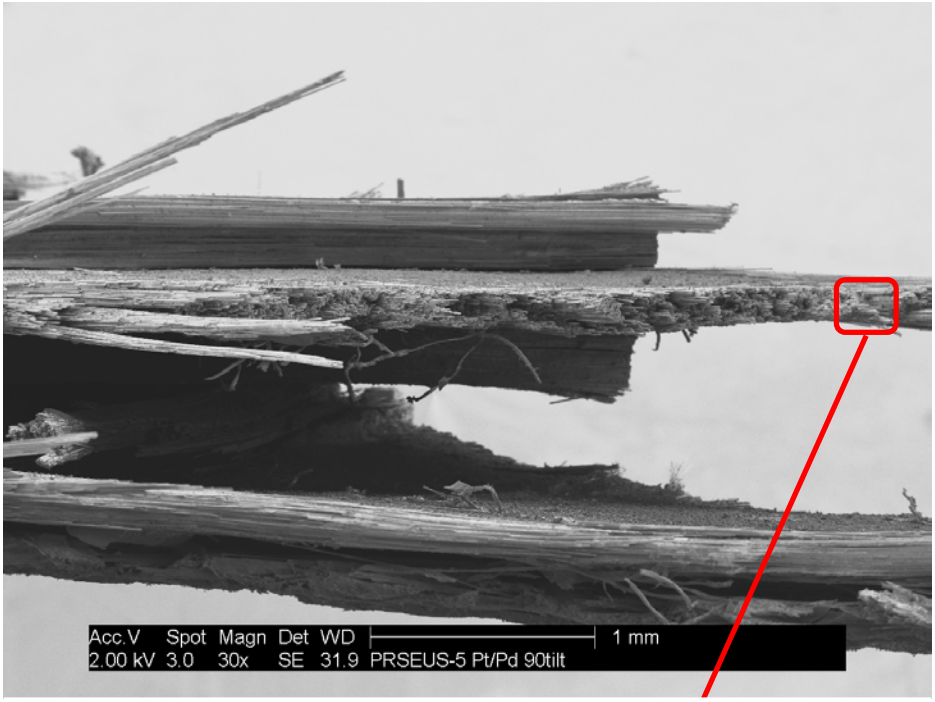

(a)

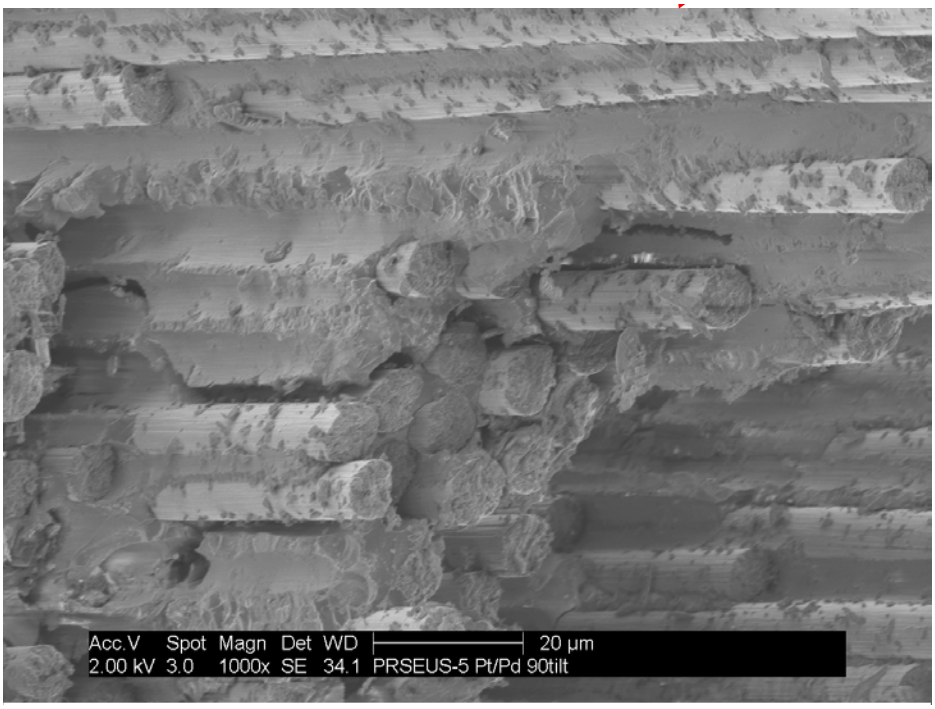

(b)

Figure 64. Fracture Surface Morphology Across the Skin Thickness and Along a Crack Emanating From the Notch Tip (segment SEM-A in figure 21): (a) Plies at Notch Tip and (b) Fiber/Matrix Interfacial Failure

(a)

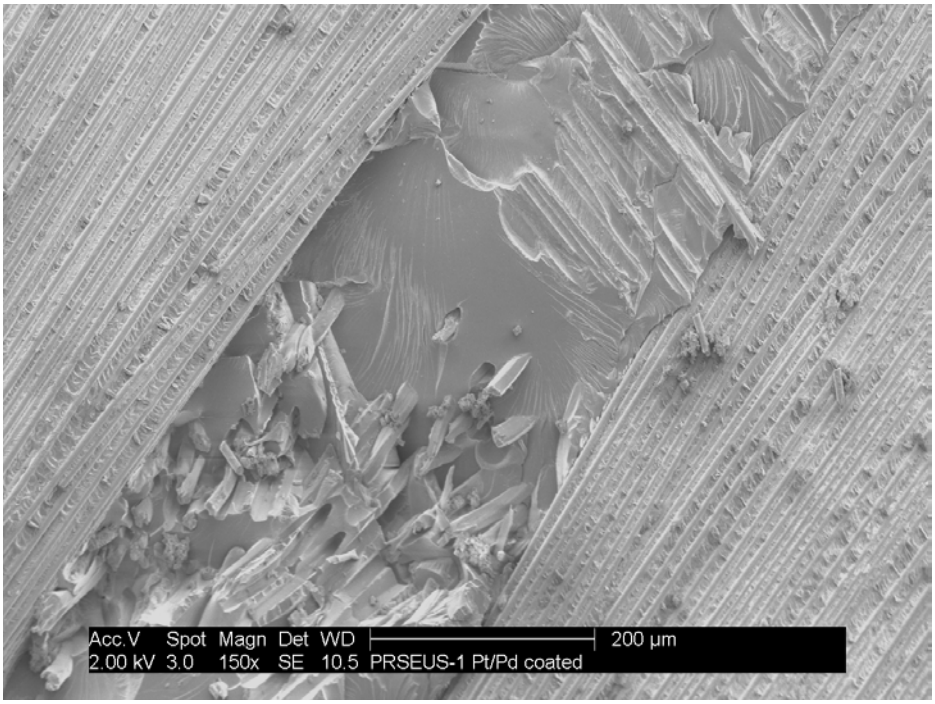

(b)

Figure 65. Fracture Surface of a Delaminated Region Ahead of the Notch Tip Showing Failed Warp-Knit Fibers (segment SEM-B in figure 21): (a) Warp-Knit Resin-Rich Areas and (b) Warp-Knit Detail

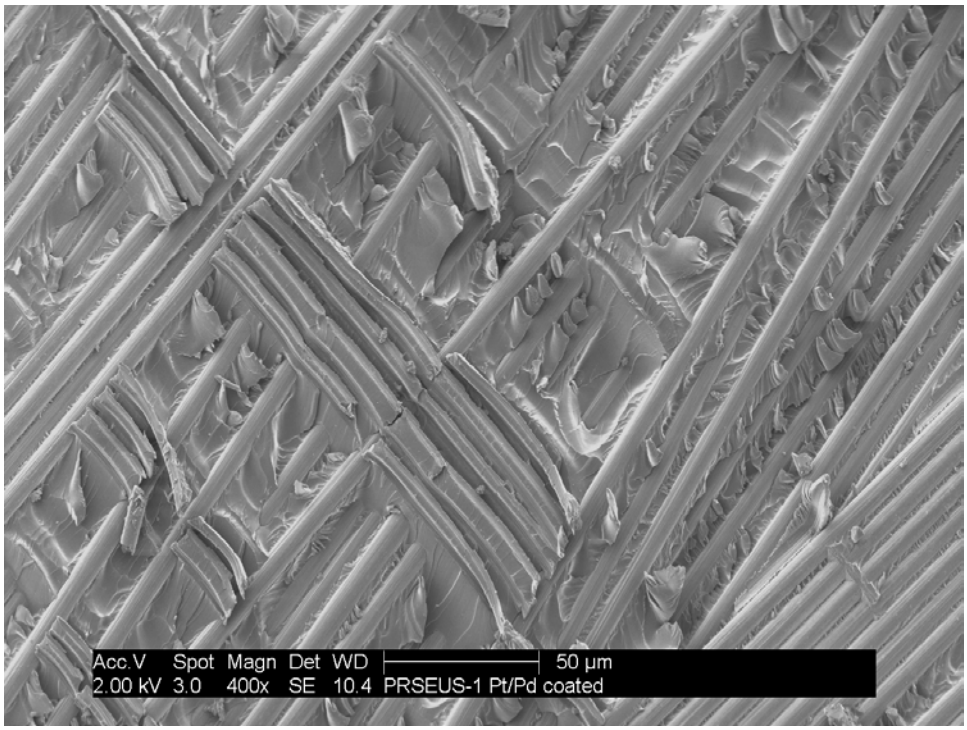

Figure 66. Fracture Surface of a Delaminated Region Ahead of the Notch Tip Showing Fibers Clean of Matrix (segment SEM-B in figure 21)

The skin stringer disbond area (segment SEM-C in figure 21) exhibited regularly spaced matrix serrations, apparently the result of shear failure, as shown in figure 67(a and b). Fiber imprints on the disbond surface indicate failure at the fiber/matrix interface.

A typical broken stitch from the inner stitch row of stringer S-5, closest to the notch tip on specimen SEM-C, is shown in figure 68(a). As shown, the stitch failed in tension, as a result of the skin/stringer disbonding, with its end spreading out in a broom-like failure. The stringer flange and the skin apparently came in contact during the dynamic fracture process, pressing and crushing the end of the stitch. No indication of stitch/matrix interfacial disbonding was observed. However, because stitch stretching was noted, it is likely there was some degree of stitch/matrix interfacial disbonding; further investigation is required to examine this interface. As mentioned previously, in some areas, the stitches failed inside the laminate, resulting in a hole on the flange surface. One example is shown in figure 68(b). Imprints and portions of the stitch thread remained on the resin-rich surface.

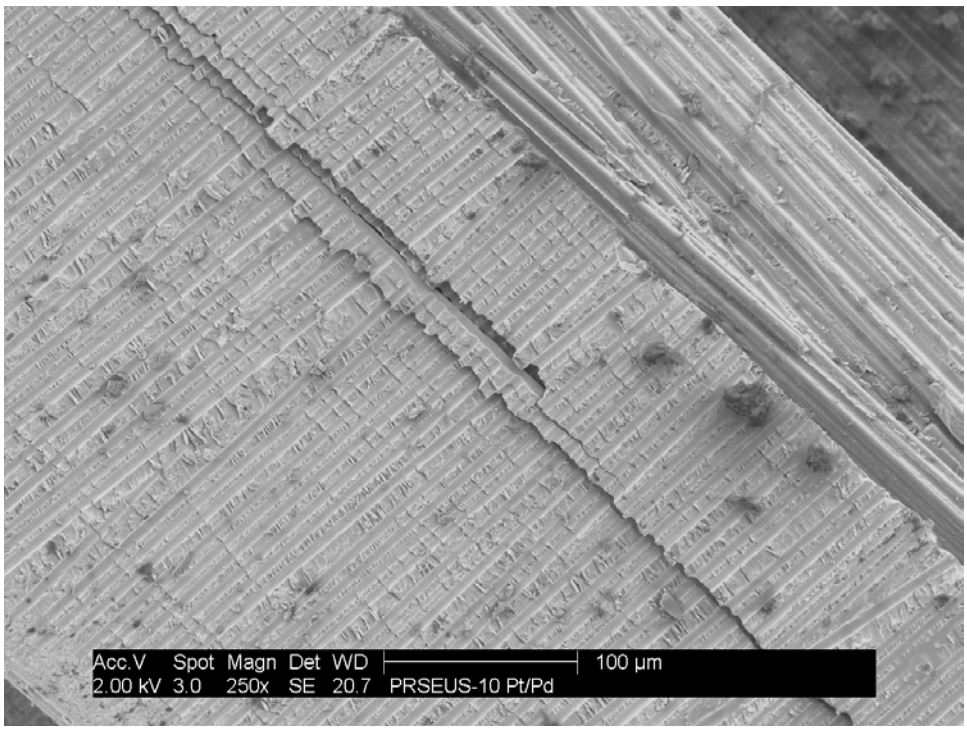

(a)

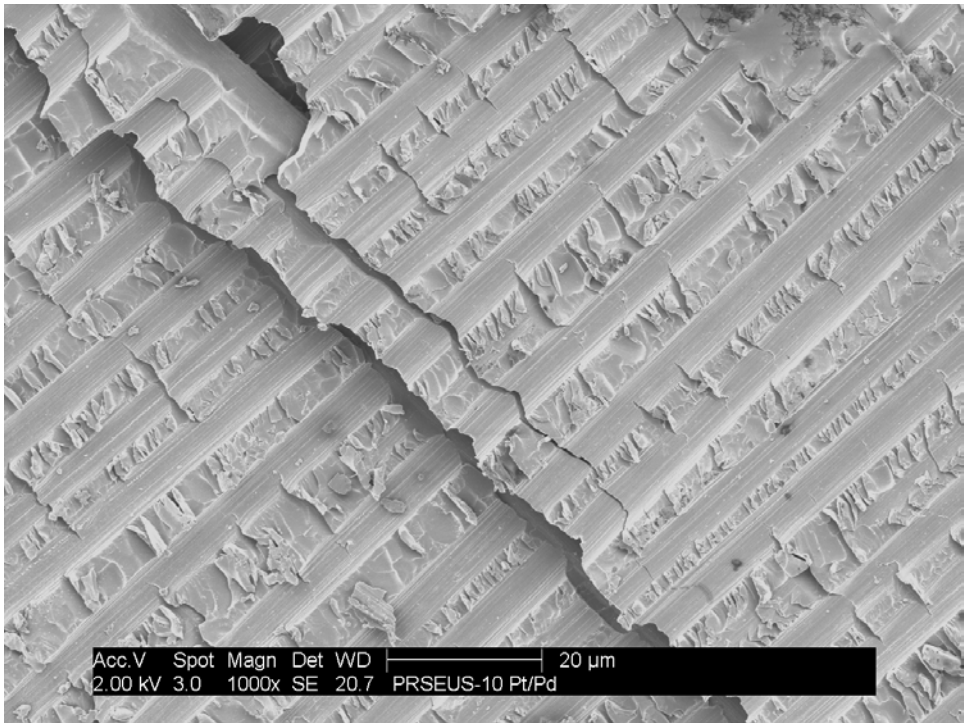

(b)

Figure 67. Fracture Surface Morphology of the Resin-Rich Disbond Region Ahead of the Notch Tip (segment SEM-C in figure 21): (a) Disbond Surface and (b) Matrix Serrations

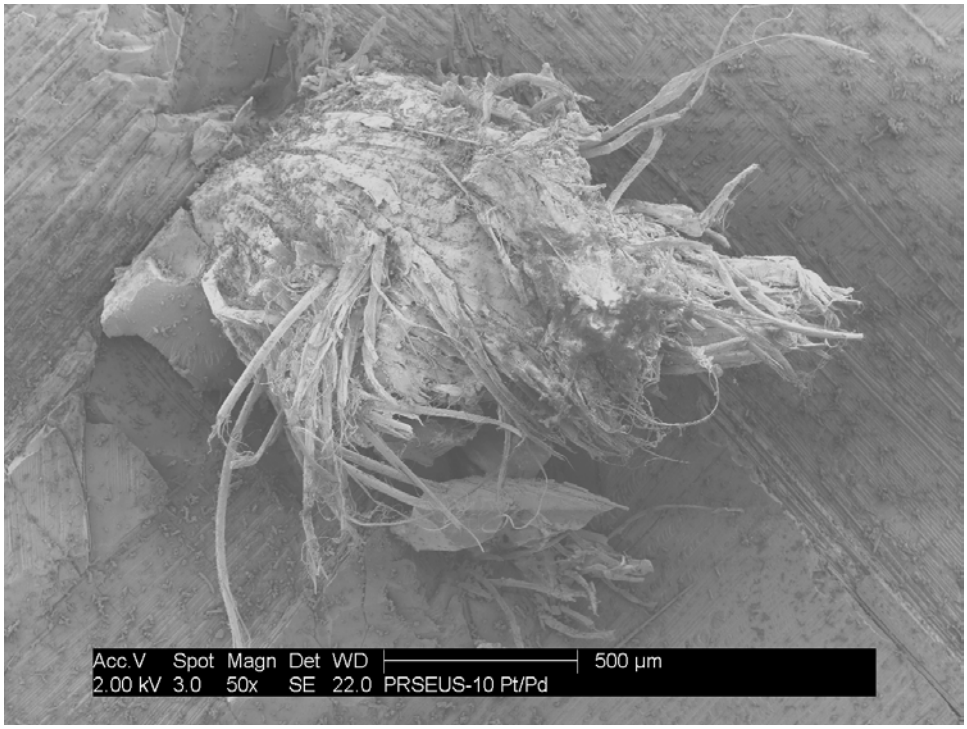

(a)

(b)

Figure 68. Characteristic Failures of Stitches Located in the First Stitched Row of S-5, Immediately Ahead of the Notch Tip (segment SEM-C in figure 21): (a) Protruding Stitch and (b) Stitch Hole

The SEM results revealed fiber/matrix interface failure in the regions examined, which provides a plausible explanation for the multiple widespread delaminations ahead of the notch tip. Additionally, matrix serrations indicate a mode II dominant failure [25] in the delaminated and disbonded regions. These results show the active failure mechanisms that should be considered and provide a basis for development and verification of future progressive failure analysis of PRSEUS under tensile loads.

8. SUMMARY.

A curved PRSEUS panel was subjected to different combinations of internal pressure and axial tensile loading. The pristine panel was subjected to limit load to show compliance with the strength and deformation requirements of 14 CFR Part 25. Subsequently, two different damage scenarios were introduced: (1) a BVID, to demonstrate that the panel with BVID met the ultimate strength and deformation requirements of 14 CFR 25.305, using guidance from AC 20-107B; and (2) a two-bay through-the-thickness notch to demonstrate compliance with 14 CFR 25.571, by showing that the panel could sustain limit loads with a two-bay notch severing the central stringer. The test results demonstrated that the panel met all stated requirements. All structural tests were conducted at the FAA FASTER facility.

The baseline results obtained with the pristine panel showed linear strain and displacement results under all limit load conditions. Good agreement between the FEM and test results, as recorded via interior and exterior strain gages, radial and axial LVDTs, and DIC strain measurements, was also observed.

The BVID, which was introduced through drop weight impacts, resulted in nonpenetrating visual damage, including matrix cracks, fiber breaks, and delamination between the skin and stringer flange. However, it was demonstrated that the stitches limited the extent of the impact damage. Visual, ultrasonic, and flash thermography inspections revealed that no damage occurred during panel loading to ultimate loads, which exceeded the design goal of no damage growth at limit load.

The panel, having a two-bay through-the-thickness notch severing the central stringer, was loaded to catastrophic fracture following a specific loading sequence of internal pressure and axial loading. Strain, deformation, and the interior and exterior damage progression were monitored throughout loading to fracture. Loading of the last LS consisted of constant internal pressure of 1.0 P (i.e., cabin pressure) while monotonically increasing the axial load from 100% DLL to fracture. Visual observations showed that damage was contained within the two-bay region by the surrounding stitch rows until 160% DLL. Axial load was increased to 184% DLL, well above the design goal, at which point several stringers pulled out from the load introduction area, resulting in catastrophic failure. Between 140% and 184% DLL, several audible emissions resulting from stringer disbond and skin failure provided an early warning of imminent fracture. Interior monitoring showed that the frame/skin interface remained intact (i.e., no indication of disbond) up to catastrophic failure. Interior and exterior strain gages mounted strategically throughout the test section on the skin, stringers, and frames provided indication of the various stages of damage progression via strain redistributions.

Post-test visual inspections revealed that the damage on the interior was much more extensive compared with the single, meandering crack observed on the exterior. The interior damage included extensive delamination near the notch tips, skin/stiffener disbanding, stitch failure, and extensive matrix cracking along the surface ply fiber direction. The dynamic event of the fracture caused disbonding of the frames and generally widespread stitch failure. One stringer, which pulled-out at fracture, was buckled during the elastic recovery of the panel. The specific size and shape of the damage was identified via an array of NDI methods, showing delaminations in the skin between the notch tips and the adjacent stringers. Fractographic examinations of the delaminated fracture surfaces revealed the characteristic failure mechanisms of polymer matrix composite laminates. The examinations also revealed that the fiber surfaces were clean of matrix material, fiber distribution and alignment were altered by the warp-knitting, and broken fibers were found along the delaminated surface. The disbond surface characteristics showed the resin-rich co-cured interface, tensile stitch failure at the interface, and scattered stitch failure in the laminate and associated stitch pullout.

9. FUTURE WORK.

The test program continues in two major directions: (1) testing of coupon and element scale test specimens constructed of the same materials used in this test and including stringer and frame details, and (2) developing a damage model to predict initiation and progression of damage at the notch tips. Coupon tests, including notch and un-notched tension, shear, double cantilever beam, end notched flexure, mixed mode bending, and compact tension, are planned to characterize the elastic, strength, and fracture toughness properties for inputs to future progressive failure analysis of the current test panel. A global-local approach is planned to implement a damage model for progressive failure analysis to capture the global response of the structure with damage progression up to the adjacent stringer from the notch tip. This damage model will be semi-predictive and, therefore, useful in future design and optimization of the PRSEUS concept for application to traditional fuselage structures.

10. REFERENCES.

1. Dransfield, K.A., Baillie, C., and Mai, Y.W., “Improving the Delamination Resistance of CFRP by Stitching - A Review,” *Composites Science and Technology*, Vol. 50, No. 3, 1994, pp. 305–317.

2. Jegley, D.C. and Velicki, A., “Status of Advanced Stitched Unitized Composite Aircraft Structures,” Presented at *The 51st AIAA Aerospace Sciences Meeting*, Grapevine, Texas, 2013.

3. Jegley, D.C., “Improving Strength of Postbuckled Panels Through Stitching,” *Composite Structures*, Vol. 80, No. 2, 2007, pp. 298–306.

4. Tan, Y., Guocai, W., Suh, S.S., Yang, J.M., and Hahn, H.T., “Damage Tolerance and Durability of Selectively Stitched Stiffened Composite Structures,” *International Journal of Fatigue*, Vol. 30, No. 3, March 2008, pp. 483–92.

5. Dow, M.B. and Dexter, H.B., "Development of Stitched, Braided and Woven Composite Structures in the ACT Program and at Langley Research Center (1985-1997)," 1997.

6. Mouritz, A.P. and Cox, B.N., "A Mechanistic Approach to the Properties of Stitched Laminates," *Composites Part A (Applied Science and Manufacturing)*, Vol. 31, 2000, pp. 1–27.

7. Karal, M., "AST Composite Wing Program - Executive Summary," 2001.

8. Velicki, A., "Damage Arresting Composites for Shaped Vehicles," NASA/CR-2009-215932, 2009.

9. Velicki, A., "Advanced Structural Concept Development Using Stitched Composites," Presented at the *49th AIAA/ASME/ASCE/AHS/ASC Structures, Structural Dynamics and Materials Conference*, Schaumburg, Illinois, 2008.

10. Hoffman, K., "Air Vehicle Technology Integration Program (AVTIP), Delivery Order 0059: Multi-role Bomber Structural Analysis," AFRL-VA-WP-TR-2006-3067, May 2006.

11. Lovejoy, A.J., Rouse, M., Linton, K.A., and Li, V.P., "Pressure Testing of a Minimum Gauge PRSEUS Panel," 2011.

12. Yovanof, N.P. and Jegley, D.C., "Compressive Behavior of Frame-Stiffened Composite Panels," Presented at the *52nd AIAA/ASME/ASCE/AHS/ASC Structures, Structural Dynamics, and Materials Conference*, Denver, CO, 2011.

13. "'Airworthiness Standards: Transport Category Airplanes,' Title 14 Code of Federal Regulations," 2011.

14. Federal Aviation Administration, Advisory Circular (AC 20-107B), "Composite Aircraft Structure," August 8, 2009.

15. Federal Aviation Administration, Advisory Circular (AC 25.571-1D), "Damage Tolerance and Fatigue Evaluation of Structure," January 13, 2011.

16. Bakuckas, J.G.J., "Full-Scale Testing of Fuselage Structure Containing Multiple Cracks," DOT/FAA/AR-01/46, July 2002.

17. Linton, K., Neal, A., Mills, G., Velicki, A., and Thrash, P., "Design, Analysis, and Fabrication of a Curved PRSEUS Panel," December 2010.

18. Woods, J.A., Modin, A.E., Hawkins, R.D., and Hanks, D.J., "Controlled Atmospheric Pressure Infusion Process."

19. Bergan, A., Korkosz, G., and Bakuckas, J.G., “FASTER Fixture Modification: PRSEUS Test.”

20. “ARAMIS User Manual-Software v6.1.” GOM GmbH, August 2009.

21. Leone, F.A., Ozevin, D., Awerbuch, J., and Tan, T.M., “Detecting and Locating Damage Initiation and Progression in Full-Scale Sandwich Composite Fuselage Panels Using Acoustic Emission,” *Journal of Composite Materials*, June 2012.

22. “MSC NASTRAN 2005 Quick Reference Guide.” MSC Software Corporation, 2004.

23. Bergan, A., Bakuckas, J.G., Lovejoy, A.E., et al., “Full-Scale Test and Analysis of a PRSEUS Fuselage Panel to Assess Damage-Containment Features,” 2011.

24. Mouritz, A.P., Bannister, M.K., Falzon, F.J., and Leong, K.H., “Review of Applications for Advanced Three-Dimensional Fibre Textile Composites,” *Composites Part A*, Vol. 30, No. 12, 1999, pp. 1445–1461.

25. Hayes, B.S. and Gammon, L.M., “Fractography,” in *ASM Handbook*, Vol. 21: Composites, D.B. Miracle and S.L. Donald, eds. ASM International, 2001, pp. 977–987.

APPENDIX A—PANEL ENGINEERING DRAWINGS

A.1 PANEL ENGINEERING DRAWINGS.

Detailed engineering drawings for the panel tested are presented in this appendix. The panel is cross referenced in the accompanied engineering drawings, as listed in table A-1, and are shown in the following figures. Some drawings were made for large format printing and, therefore, have been divided into a series of figures for readability; these are the drawings in table A-1 with several figure numbers. The selected panel configuration represents a generic fuselage structure for a transport aircraft. All linear and angular dimensions are given in inches and degrees, respectively. Tolerances are summarized in table A-2, except where noted differently in the drawings.

Table A-1. Panel Engineering Drawings

Drawing Name	Description	Figures	Parts List	Notes
Panel Assembly	Shows final dimensions of machined cured panel, with clevises and radius blocks	Figure A-1 and Figures A-3 to A-6	Table A-3	Figure A-2
Panel Interface Control Document	Shows dimensions of all portions that interface with the test fixture	Figure A-7 to Figure A-12	N/A	N/A
Panel Details	Shows details of panel layup and construction	Figure A-13; Figure A-15 through Figure A-48	Table A-4	Figure A-14
Foam Core	Shows details of frame foam cores	Figures A-49 to A-56	Table A-5	Figure A-5
Frame Insert	Shows the block used to reinforce the frame loader attachment point	Figure A-57	N/A	N/A
Radius Block	Shows the block used to reinforce the frame ends	Figure A-58	N/A	N/A
Peelable Shim	Shows the peelable shim	Figure A-59	N/A	N/A
Clevis Installation Template	Shows the template used to align the clevises during installation	Figure A-60	N/A	N/A

Table A-2. Dimensional Tolerances

Dimension	Tolerance
2 decimal places	±0.030
3 decimal places	±0.010
angles	0°30’

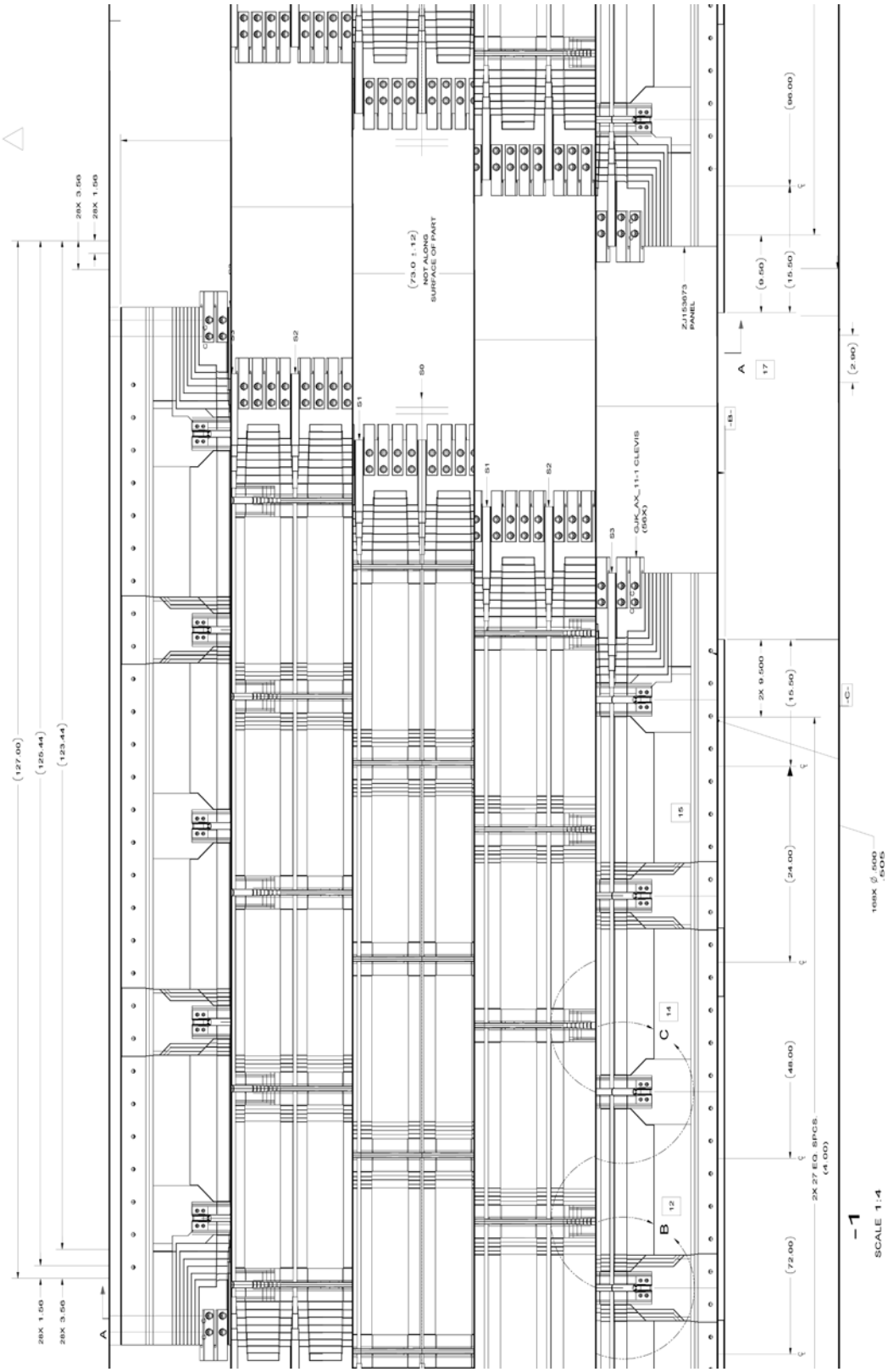

Figure A-1. Panel Assembly, Interior

Table A-3. Panel Assembly Parts List

20	ZB153697-1	Radius Block			12
56	ZB153421-1	Laminated Shim			19
40	MS21042L3	Nut	CRES		12
40	NAS1149C0332	Washer	CRES		12
24	NAS6703U6	Bolt	CRES		14
16	NAS6703U7	Bolt	CRES		12
112	MS21245L8	Nut	CRES		20
112	NAS1149C0863	Washer	CRES		20
112	NAS6308U27	Bolt	CRES		20
56	GJK_AX_11-1	Clevis			4
1	ZJ153673-1	FAA Panel			11
*	-1				7
QTY	Part Number	Description	Material	Size	Zone
-1					

GENERAL NOTES:
UNLESS OTHERWISE NOTED

1. DIMENSIONAL TOLERANCES AND SYMBOLS PER ANSI Y14.5M-1982.
2. FILE NAME/PATH:
   \\SW\HBCDATA\PWDATA\PWDATA1\UHS1112002\A1XX\MGR_COMP\RELEASE\ZJ153695
3. CENTERLINES ARE DETERMINED BY LOCATING THE CENTER OF THE FRAME OR STRINGER AT THE BASE (AT THE INNER MOLD LINE SURFACE) AT EACH END OF THE PART.
4. INSTALL HI-LOK FASTENERS PER S7933655 CLEARANCE FIT (-12)
5. SHIM GAP USING ZB153421-1 LAMINATED SHIM. MAX GAP .003
6. APPLY TORQUE STRIP TO ALL FASTENER HEADS AND NUTS.
7. ASSY SHOP PRACTICE PER DPS 2.70-2
8. PREPARE HOLED IN CFRP PER DPS 3.67-22.1
9. IDENTIFY PER DPS 3.02 & DPS 3.27-1
10. FABRICATION STANDARDS PER DPS 4.710
11.

A ARE NAS6703U6 BOLT HOLE Ø = .190
NAS1149C0332 WASHER .194
MS21042L3 NUT

B ARE NAS6703U7 BOLT HOLE Ø = .190
NAS1149C0332 WASHER .194
MS21042L3 NUT

C ARE NAS6308U27 BOLT HOLE Ø = .500
NAS1149C0863 WASHER .505
MS21245L8 NUT TORQUE: 250 IN-LBS

12. TORQUE FASTENERS PER DPS 2.70-2 EXCEPT AS NOTED.
13. ENGINEERING REFERENCE: TEST PER SPECIFICATION ZA153422.
14. USE SHOP AID ZD153696 FOR GJK_AX_11-1 CLEVIS POSITIONING.

Figure A-2. Panel Assembly General Notes

Figure A-3. Assembly, Section A-A

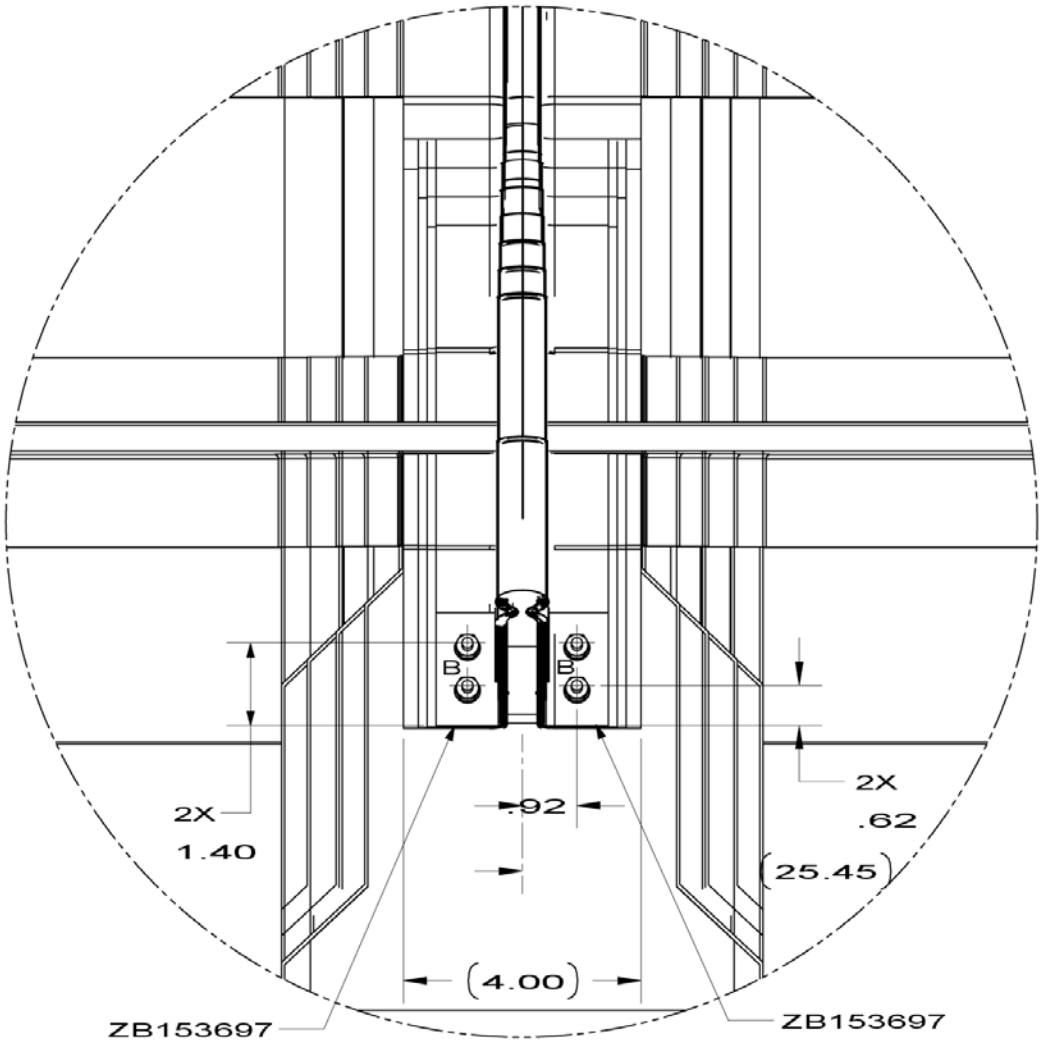

DETAIL B
SCALE 1:2

8

TYP ALL SKIN SPLICE FRAMES

Figure A-4. Assembly, Detail B

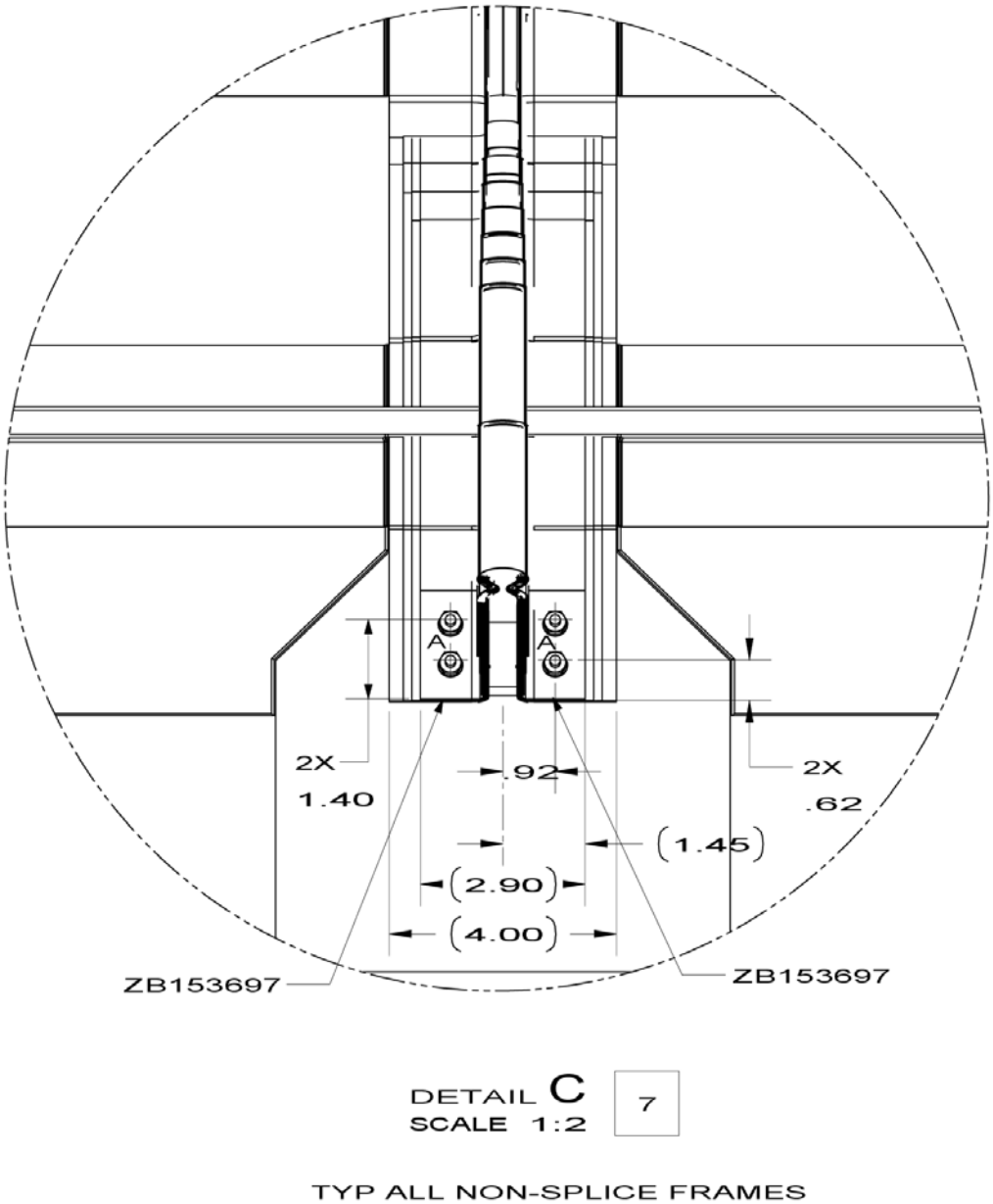

Figure A-5. Assembly, Detail C

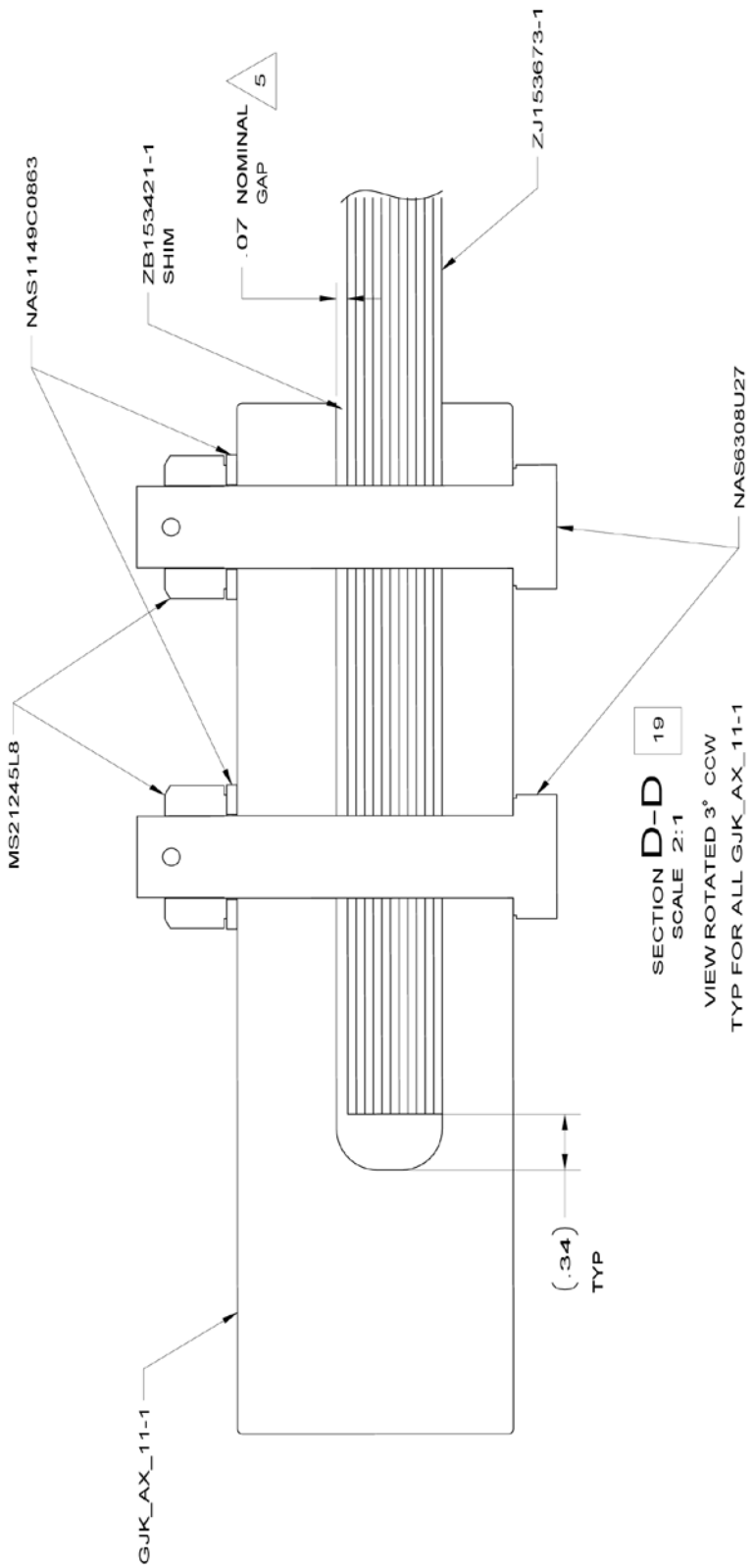

Figure A-6. Assembly, Section D-D

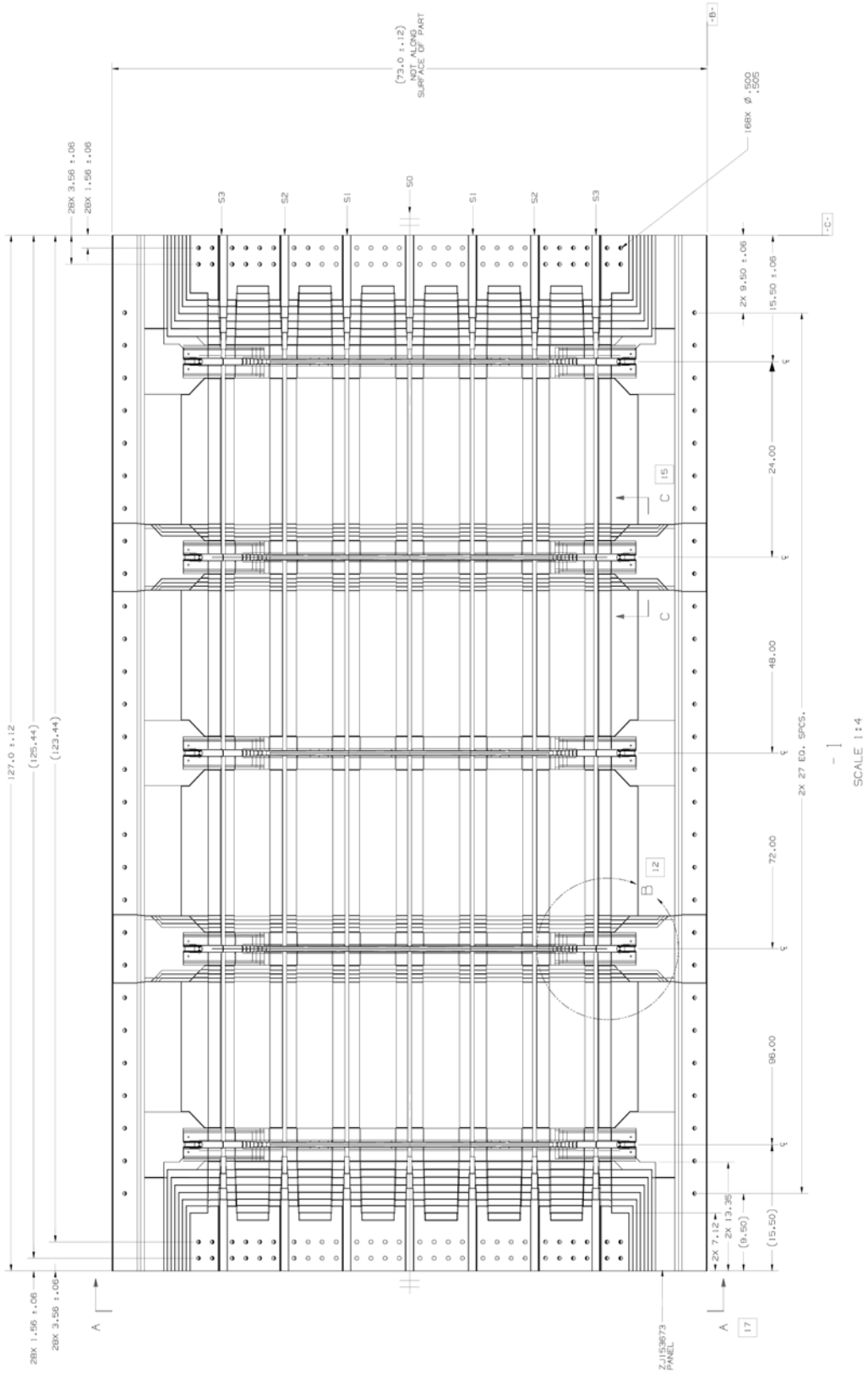

Figure A-7. ICD, Interior

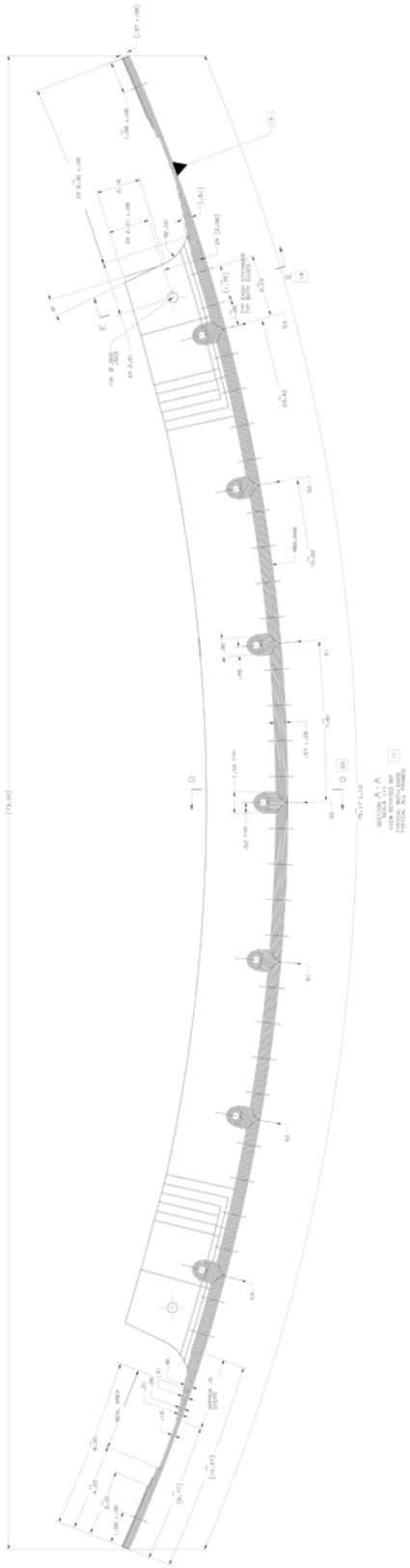

Figure A-8. ICD, Section A-A

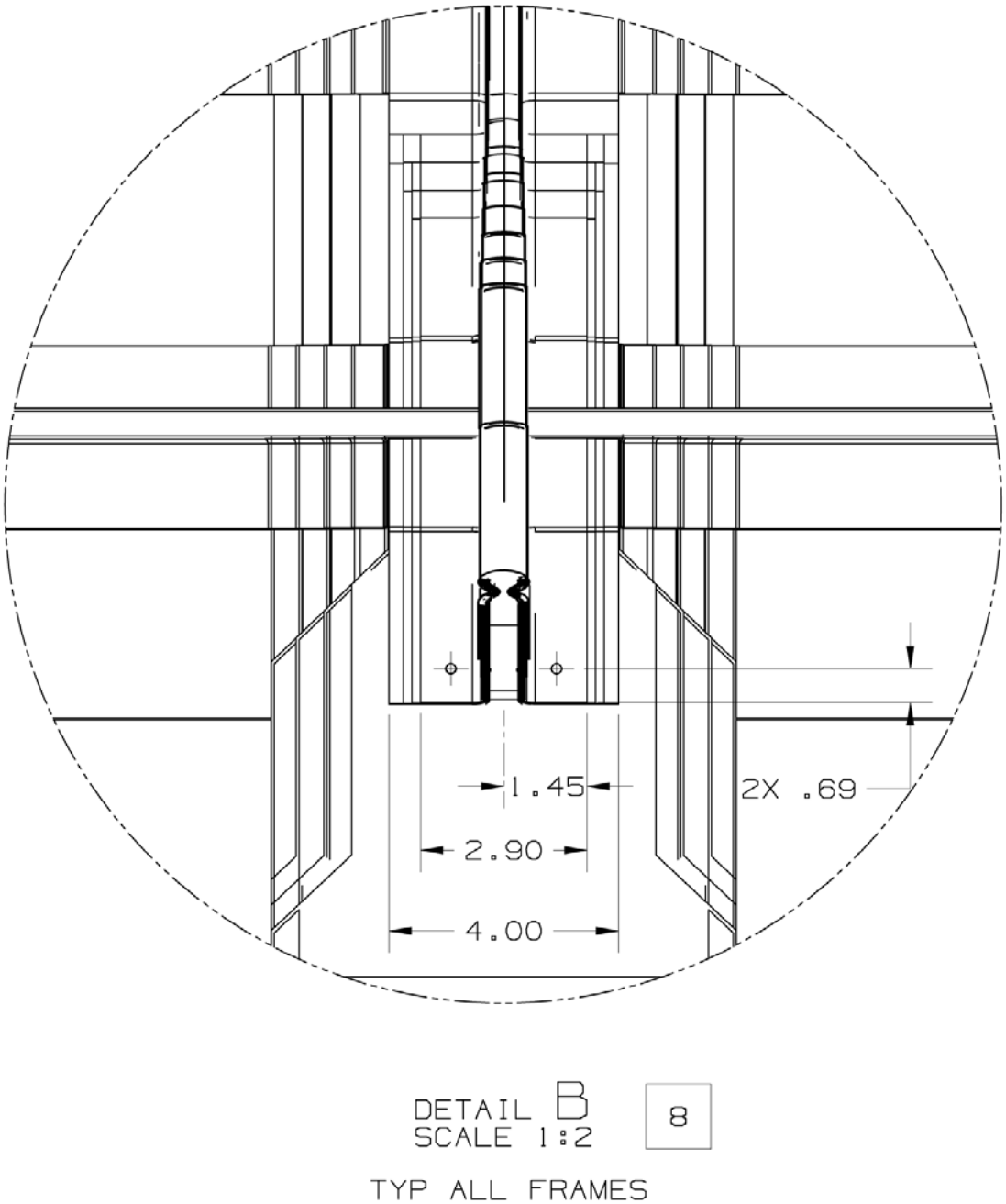

Figure A-9. ICD, Detail B

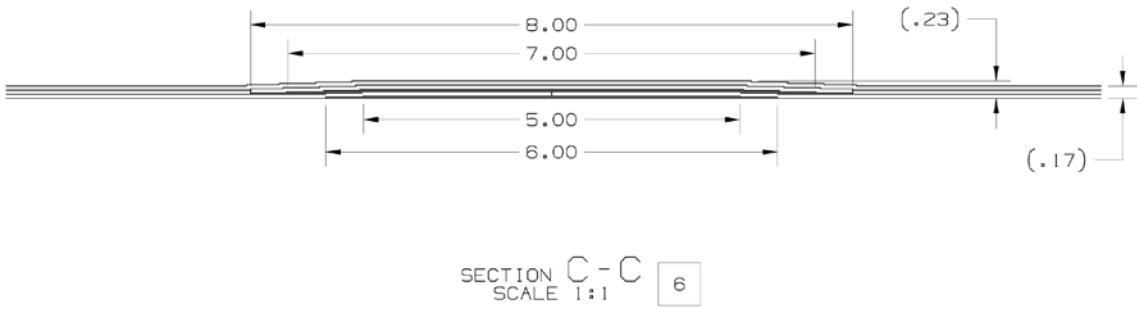

Figure A-10. ICD, Section C-C

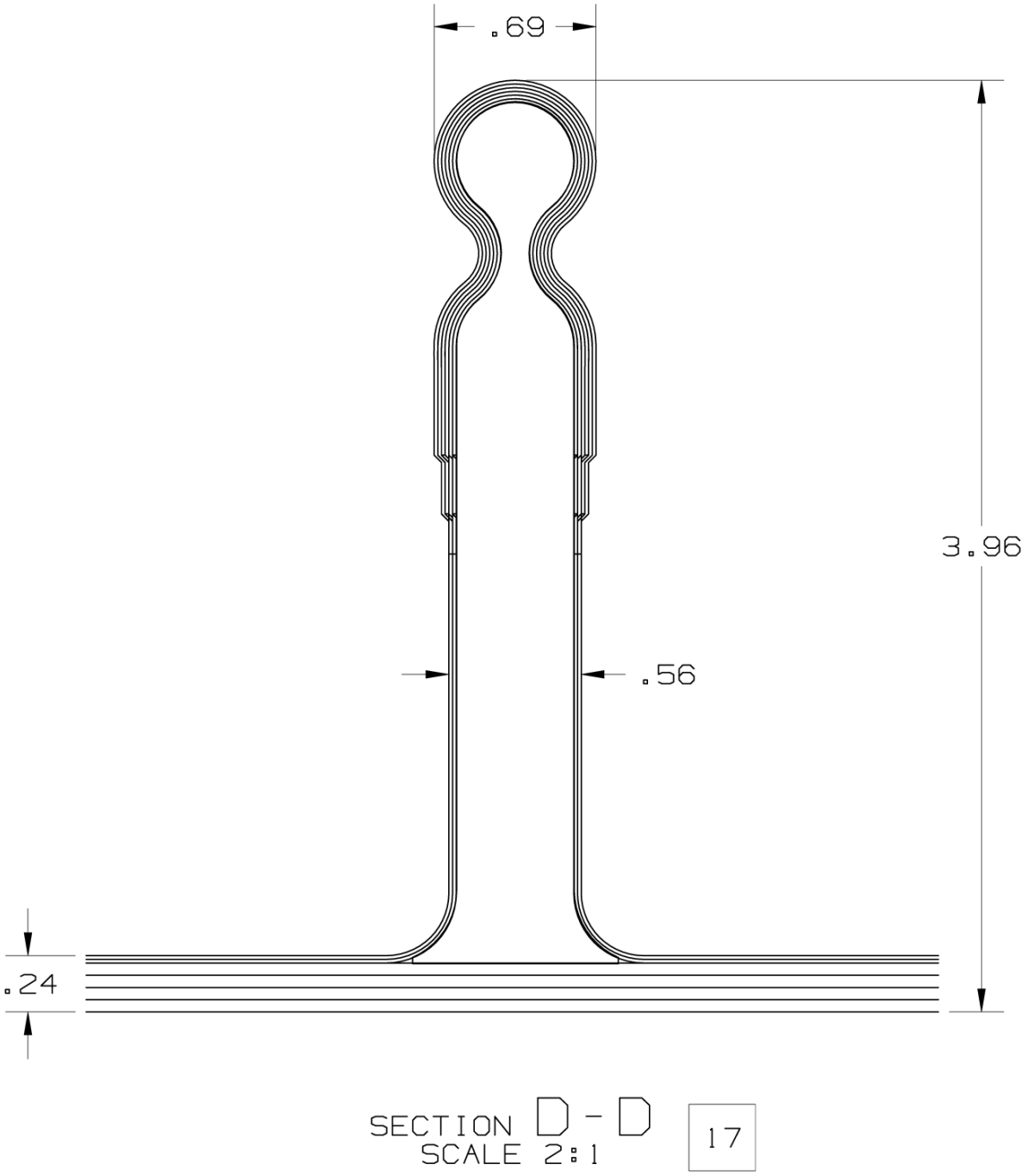

Figure A-11. ICD, Section D-D

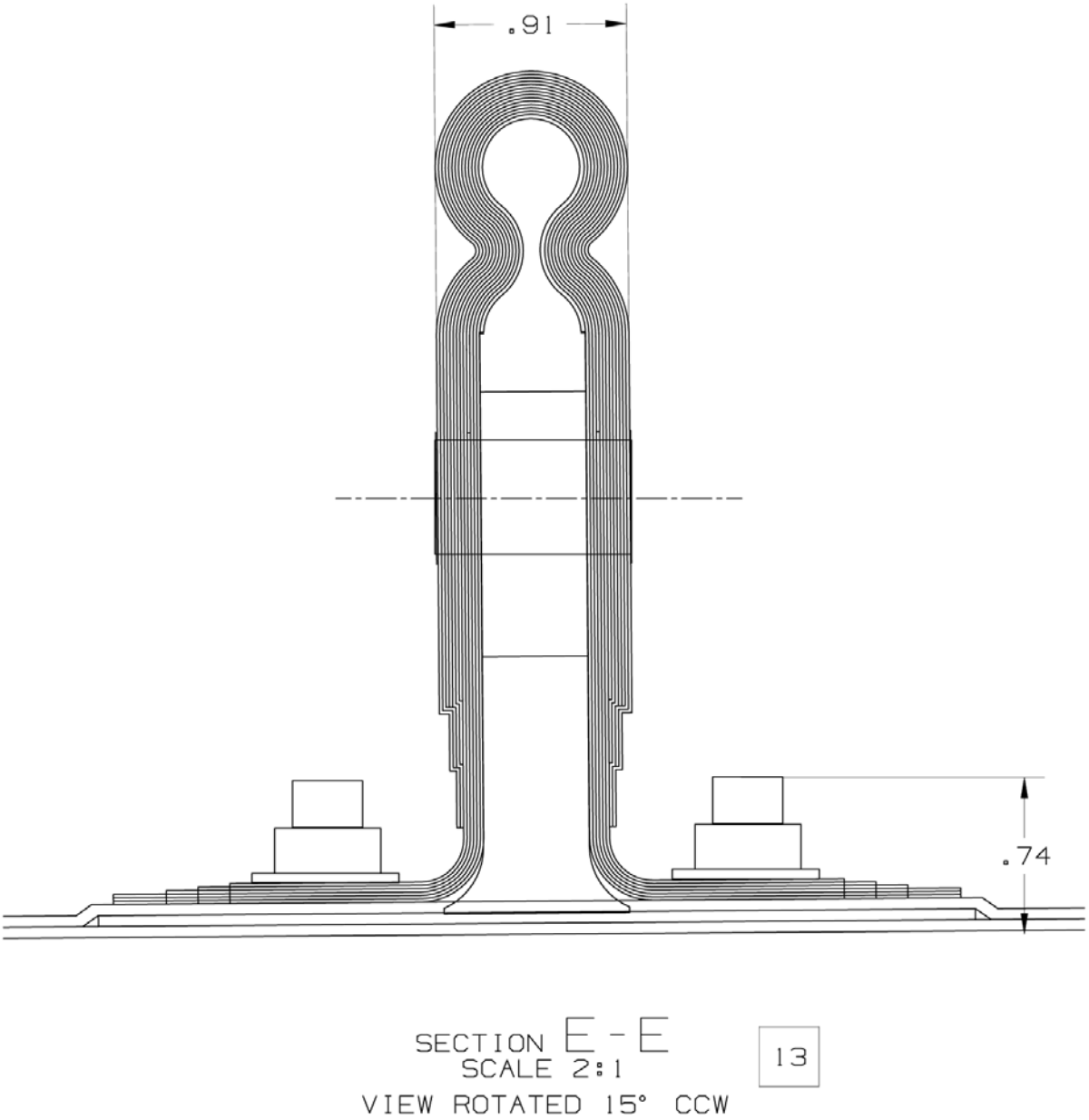

Figure A-12. ICD, Section E-E

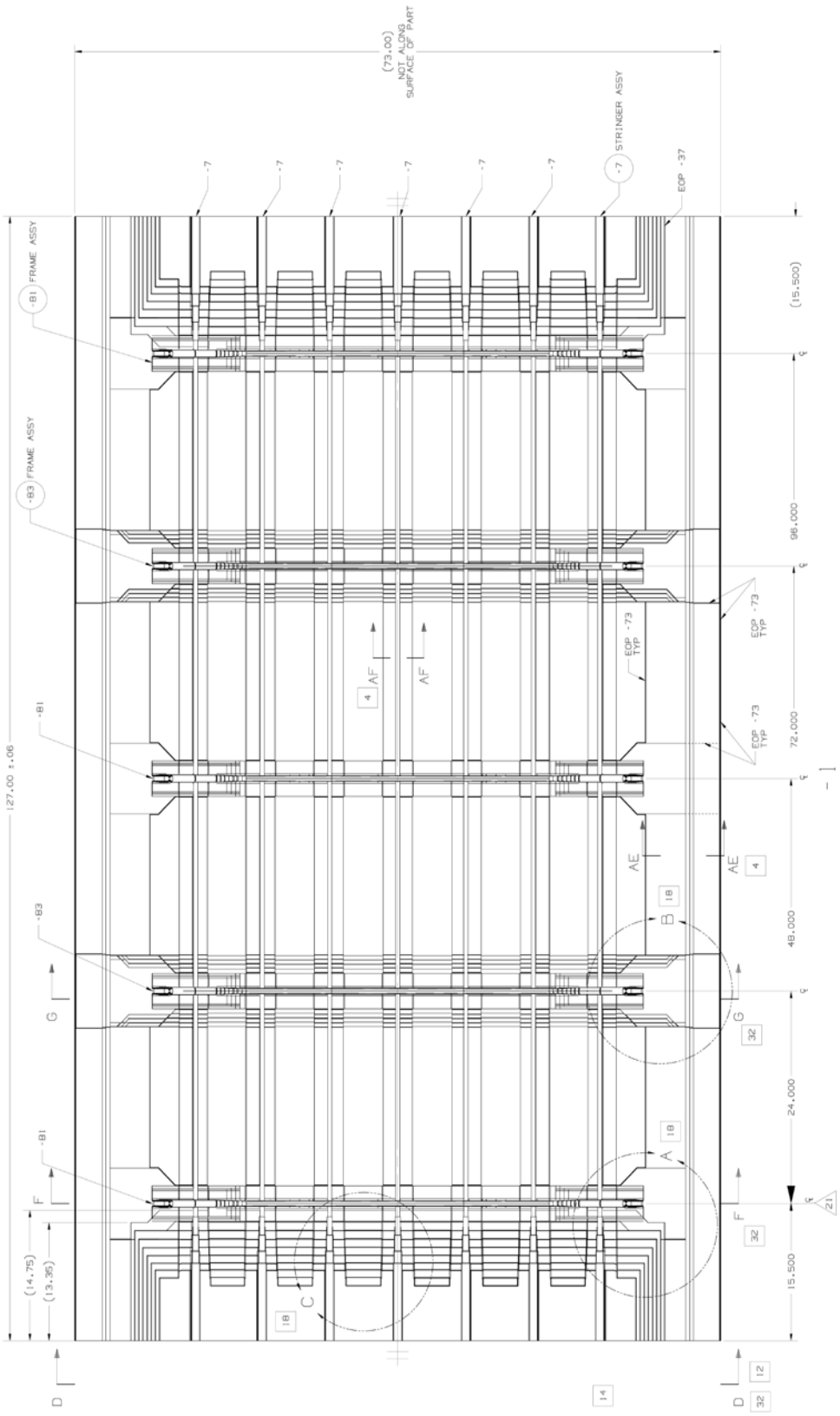

Figure A-13. Panel Details, Interior

Table A-4. Panel Details, Parts List

PARTS LIST

	AR	AR					STAPLE, .375 WIDE, .5 DEEP	CRES WIRE #8700855 (PRO-TECH SUPPLY CO.)		
AR			AR				THREAD, 400	DMS 2443, TYPE 2, CLASS 1, GRADE A		
AR			AR	AR			THREAD, 1200	DMS 2443, TYPE 2, CLASS 3, GRADE A		
					AR	VRM-34	RESIN	DMS 2479, TYPE 2, CLASS 1		
	1					ZJ153671-501	CORE ASSY, FRAME, SPLICE	(ROHACELL FOAM 110WF)		37
		1				ZJ153671-1	CORE ASSY, FRAME	(ROHACELL FOAM 110WF)		38
				7		-117	FILLET, 11'	MAKE FROM ZA151384-503-D-132	132"	11
					3	-115	BARRIER, OML GLASS PLY	AMS-C9084 TYPE III	.0045" X 78" X 127"	16
				1		-113	SKIN ASSY			13
				5		-111	TEAR STRAP, FRAME	CARBON FIBER FABRIC PER DMS 2436 TYPE 1, CLASS 72, GRADE A	.052" X 8" X 76"	57
					10	-109	DOUBLER, FRAME END	" CLASS 78	.0157" X 4.5" X 9"	42
					10	-107	DOUBLER, FRAME END	" CLASS 78	.0157" X 4.5" X 8.5"	41
					10	-105	DOUBLER, FRAME END	" CLASS 78	.0157" X 4.5" X 8"	41
					10	-103	DOUBLER, FRAME END	" CLASS 75	.0157" X 4.5" X7.5"	41
					10	-101	DOUBLER, FRAME END	" CLASS 75	.0157" X 4.5" X 7"	41
					10	-99	DOUBLER, FRAME END	" CLASS 75	.0157" X 4.5" X 6.5"	41
					10	-97	DOUBLER, FRAME END	" CLASS 75	.0157" X 6.4" X 4"	41
	1	1			5	-95	CAP, FRAME	" CLASS 78	.0157" X 10.8" X 76"	70
	1	1			5	-93	CAP, FRAME	" CLASS 78	.0157" X 10.8" X 76"	70
	1	1			5	-91	CAP, FRAME	" CLASS 75	.0157" X 10.8" X 76"	70
	1	1			5	-89	CAP, FRAME	" CLASS 75	.0157" X 10.8" X 76"	70
	1	1			5	-87	WEB, OUTER FRAME, STACK (-/+45)	" CLASS 78	.0157" X 10.8" X 76"	70
	1	1			5	-85	WEB, INNER FRAME, STACK (+/-45)	" CLASS 75	.0157" X 10.8" X 76"	70
				2		-83	FRAME ASSY, SPLICE	N/A		7
				3		-81	FRAME ASSY	N/A		6
					2	-79	DOUBLER, SKIN EDGE	CARBON FIBER FABRIC PER DMS 2436 TYPE 1, CLASS 72, GRADE A	.052" X 4.3" X 127"	4
					2	-77	DOUBLER, SKIN EDGE	"	.052" X 3.6" X 127"	4
					2	-75	DOUBLER, SKIN EDGE	"	.052" X 3.1" X 127"	4
					8	-73	DOUBLER, SKIN EDGE	"	.052" X 16" X 12"	4
2						-71	STRAP, SKIN SPLICE	CARBON FIBER FABRIC PER DMS 2436 TYPE 1, CLASS 78, GRADE A	.0157" X 8" X 76"	78
2						-69	STRAP, SKIN SPLICE	" CLASS 78	.0157" X 8" X 76"	78
2						-67	STRAP, SKIN SPLICE	" CLASS 75	.0157" X 8" X 76"	75
2						-65	STRAP, SKIN SPLICE	" CLASS 75	.0157" X 8" X 76"	75
1						-63	SKIN STACK, CENTER	CARBON FIBER FABRIC PER DMS 2436 TYPE 1, CLASS 72, GRADE A	.052" X 48" X 76"	83
2						-61	SKIN STACK, END	"	.052" X 39.5" X 76"	81
					12	-59	DOUBLER, STRINGER	"	.052" X 8" X 14.1"	13
					12	-57	DOUBLER, STRINGER	"	.052" X 6.9" X 13.2"	14
					12	-55	DOUBLER, STRINGER	"	.052" X 8" X 12.3"	14
					12	-53	DOUBLER, STRINGER	"	.052" X 8.3" X 11.42"	13
					12	-51	DOUBLER, STRINGER	"	.052" X 7.3" X 10.5"	14
					12	-49	DOUBLER, STRINGER	"	.052" X 8.7" X 9.6"	14
					12	-47	DOUBLER, STRINGER	"	.052" X 7.5" X 8.7"	14
					12	-45	DOUBLER, STRINGER	"	.052" X 9.1" X 7.8"	14
					12	-43	DOUBLER, STRINGER	"	.052" X 4.4" X 7.4"	15
					14	-41	DOUBLER, STRINGER ROD	"	.052" X 2.8" X 14"	11
					14	-39	DOUBLER, STRINGER ROD	"	.052" X 2.8" X 12"	11
					14	-37	DOUBLER, STRINGER ROD	"	.052" X 2.8" X 10.2"	11
					14	-35	DOUBLER, STRINGER ROD	"	.052" X 3" X 8.8"	11
					2	-33	DOUBLER, EDGE STRINGER	"	.052" X 7.6" X 14.1"	17
					4	-31	DOUBLER, EDGE STRINGER	"	.052" X 6.6" X 13.2"	19
					4	-29	DOUBLER, EDGE STRINGER	"	.052" X 14.3" X 12.3"	18
					2	-27	DOUBLER, EDGE STRINGER	"	.052" X 6.7" X 11.4"	17
					4	-25	DOUBLER, EDGE STRINGER	"	.052" X 5.2" X 10.5"	19
					4	-23	DOUBLER, EDGE STRINGER	"	.052" X 6.3" X 9.6"	19
					4	-21	DOUBLER, EDGE STRINGER	"	.052" X 4.8" X 8.7"	19
					4	-19	DOUBLER, EDGE STRINGER	"	.052" X 5" X 7.8"	19
					4	-17	DOUBLER, EDGE STRINGER	"	.052" X 1.7" X 7"	19
				2		-15	TEAR STRAP, EDGE STRINGER	"	.052" X 18" X 127"	4
						-13	NOT USED	N/A		
				5		-11	TEAR STRAP, STRINGER	CARBON FIBER FABRIC PER DMS 2436 TYPE 1, CLASS 72, GRADE A	.052" X 7.8" X 127"	15
			1			-9	STACK, STRINGER	"	.052" X 6.1" X 127"	10
				7		-7	STRINGER ASSY	N/A		6
				7		-5	ROD	MAKE FROM ZB153292-501-132	132"	11
				*	1	-3	PREFORM ASSY	N/A		12
					*	-1	PANEL ASSY	N/A		9
QTY	QTY	QTY	QTY	QTY	QTY	DET	NAME	MATERIAL	SIZE	ZONE
-113	-83	-81	-7	-3	-1					

GENERAL NOTES:
UNLESS OTHERWISE NOTED

1. PLY ORIENTATION TOLERANCE ±3°.
2. FABRICATE AND PROCESS COMPOSITE LAMINATES PER ENGINEERING F.A.C.T. SHEETS.
3. FABRICATE STITCHED PREFORM PER DPS 1.640.
4. STITCH ROW POSITION TOLERANCE ±.03.
5. DIMENSIONAL TOLERANCES AND SYMBOLS PER ANSI Y14.5M-1982.
6. INSPECT SKIN & STRINGER FLANGES EXCEPT WHAT IS HIDDEN BY STRINGER BULB AND LIMITED BY SCANNER HEAD NEAR FRAME WEB PER DPS 4.738 AND DPS 4.738-1 CLASS B.
7. TRIM CARBON/EPOXY PARTS PER DPS 3.67-22-1.
8. BREAK ALL SHARP EDGES TO .03 MAX EDGE RADIUS PER DPS 4.710-1.
9. ASSEMBLY SHOP PRACTICE PER DPS 2.70-2.
10. STITCHING AND THREAD GUIDELINES INDICATED THUS:

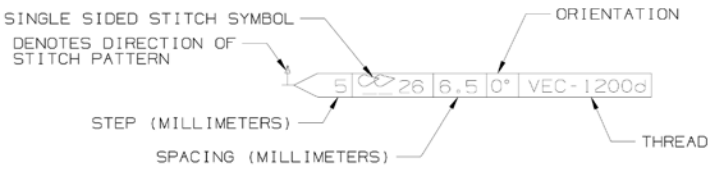

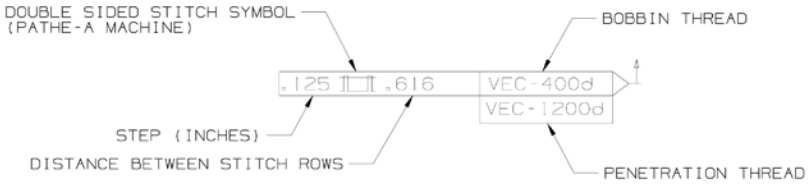

11. STACK ORIENTATION FOR ALL PARTS IS 0° UNLESS OTHERWISE STATED.
12. INFUSE DRY PRE-FORM (-3) WITH RESIN (VRM-34) PER DPS 1.631.
13. FILE NAME/PATH:
    \\SW\HBCDATA\PWDATA1\UHS112002\A1XX\MGR_COMP\RELEASE\ZJ153673
14. CURE -1 IN PLASTIC LAMINATING MOLD(PLM) EXPERIMENTAL TOOL #XN-ZJ153290-1-PLM1.
15. OML TO BE COVERED BY -115 (120 GLASS CLOTH). CLOTH IS PLACED ON OML SURFACE OF -3 STITCHED PREFORM PRIOR TO INFUSION. SPLICE AS REQUIRED ALONG THE WIDTH OF THE PANEL IN THE STRINGER DIRECTION. OVERLAY ALL SPLICE LAPS .50 INCHES.
16. SPLICE -89 THRU -95 FRAME CAPS AS REQUIRED. SPLICES MUST BE STAGGERED MID SPAN OF TWO STRINGERS ±1.0" & HAVE AN OVERLAP OF .5" to 1.0". ONLY ONE CAP SPLICE PER STRINGER PAIR. CUT PLIES TO MINIMIZE THE NUMBER OF CAP PLIES.
17. FOR ENGINEERING REFERENCE ONLY
    CURED MATERIAL THICKNESS:
    CLASS 72 = .052
    CLASS 75 = .0157
    CLASS 78 = .0157
18. DRILL PRECISION HOLES PER DPS 3.67-22-1. DIMENSIONS ARE TAKEN ALONG THE SURFACE OF THE PART.
19. ASSEMBLE PREFORM USING AJ# ZJ153290-1-ATP1.
20. CENTERLINES ARE DETERMINED BY LOCATING THE CENTER OF THE FRAME OR STRINGER AT THE BASE (AT THE INNER MOLD LINE SURFACE) AT EACH END OF THE PART.
21. SEAL FRAME ENDS AFTER TRIMMING PER DPS 1.04-3.1 TYPE 2B USING DPM 5535-5 (EA9396) ADHESIVE. SURFACE PREP COMPOSITE SURFACES PER DPS 1.07-39.
22. SPLICE SKIN SPLICE STRAP MATL A/R> AVOID OVERLAP OF SPLICE & AVOID MID-BAY.
23. PREFORM SIZE SHALL INCLUDE 1.0" OF TOA ON ALL SIDES.
24. TOLERANCE ON ALL BUTT SPLICES SHALL BE .00 TO .06 INCHES.
25. CURE -1 PANEL ASSY IN PLASTIC LAMINATING MOLD TOOL #XN-ZJ153290-PLM1
26. POSITION -65 AND -71 SKIN SPLICE STRAPS TO MATE +45° FIBERS ON -63 SKIN WITH +45° FIBERS ON -65 AND -71.

Figure A-14. Panel Details, General Notes

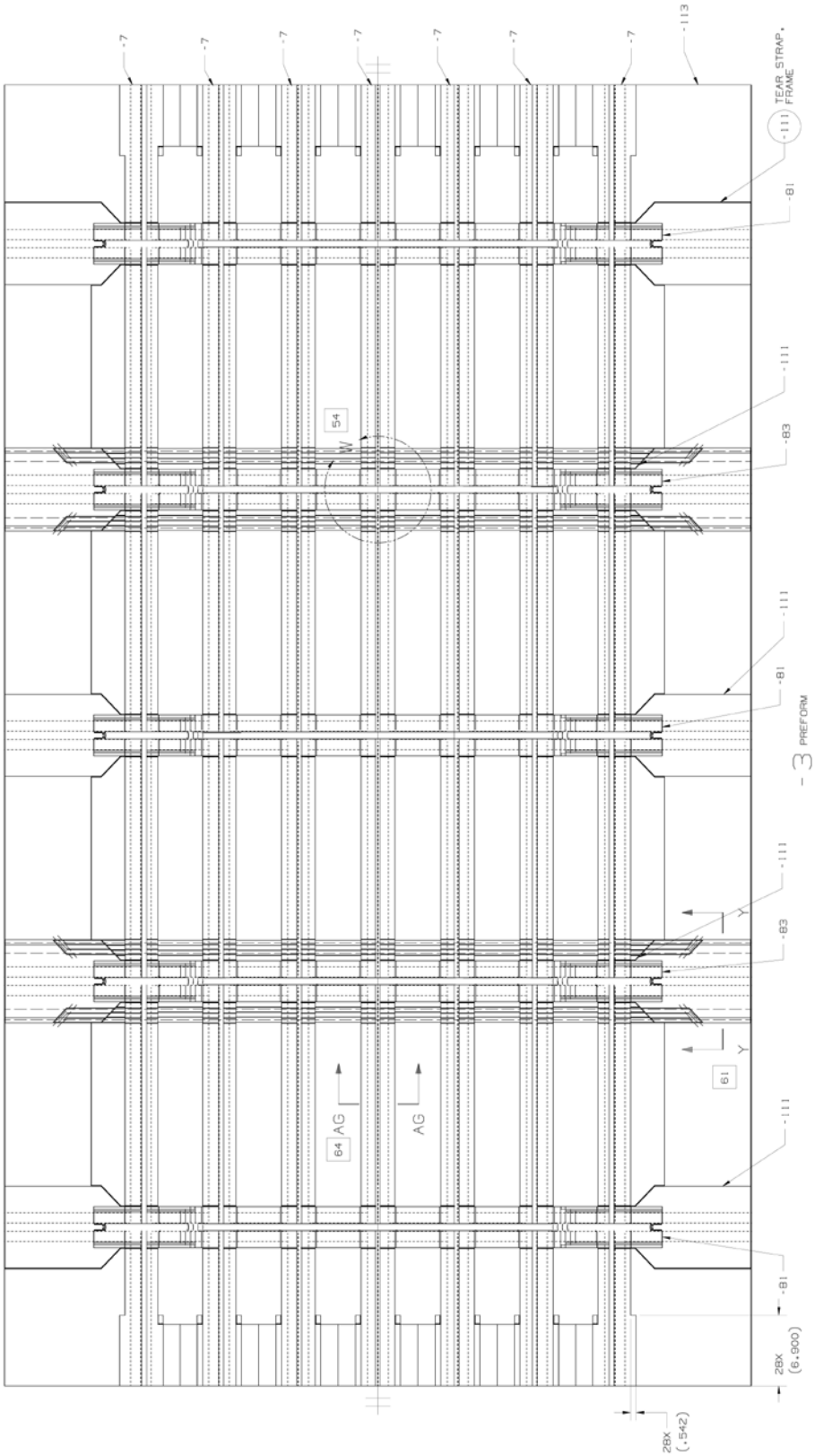

Figure A-15. Panel Details, Preform, Interior

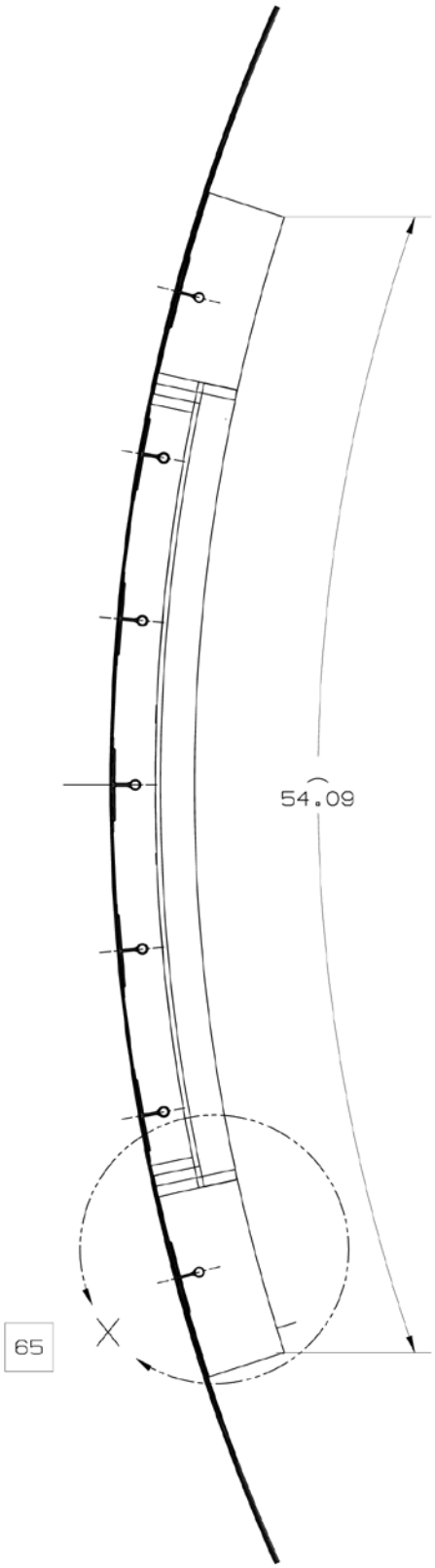

Figure A-16. Panel Details, Preform, Side

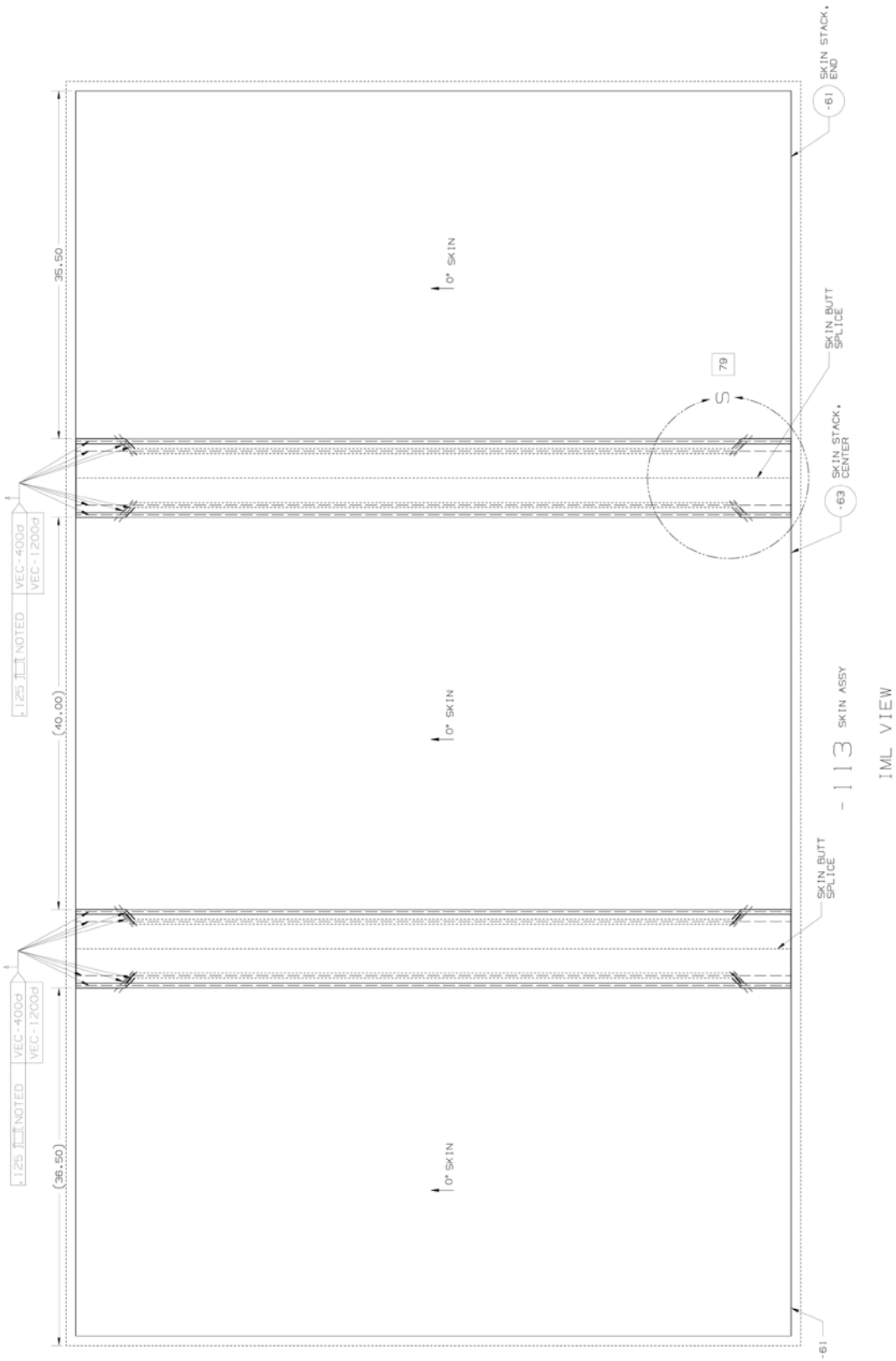

Figure A-17. Panel Details, Skin Assembly, Interior View

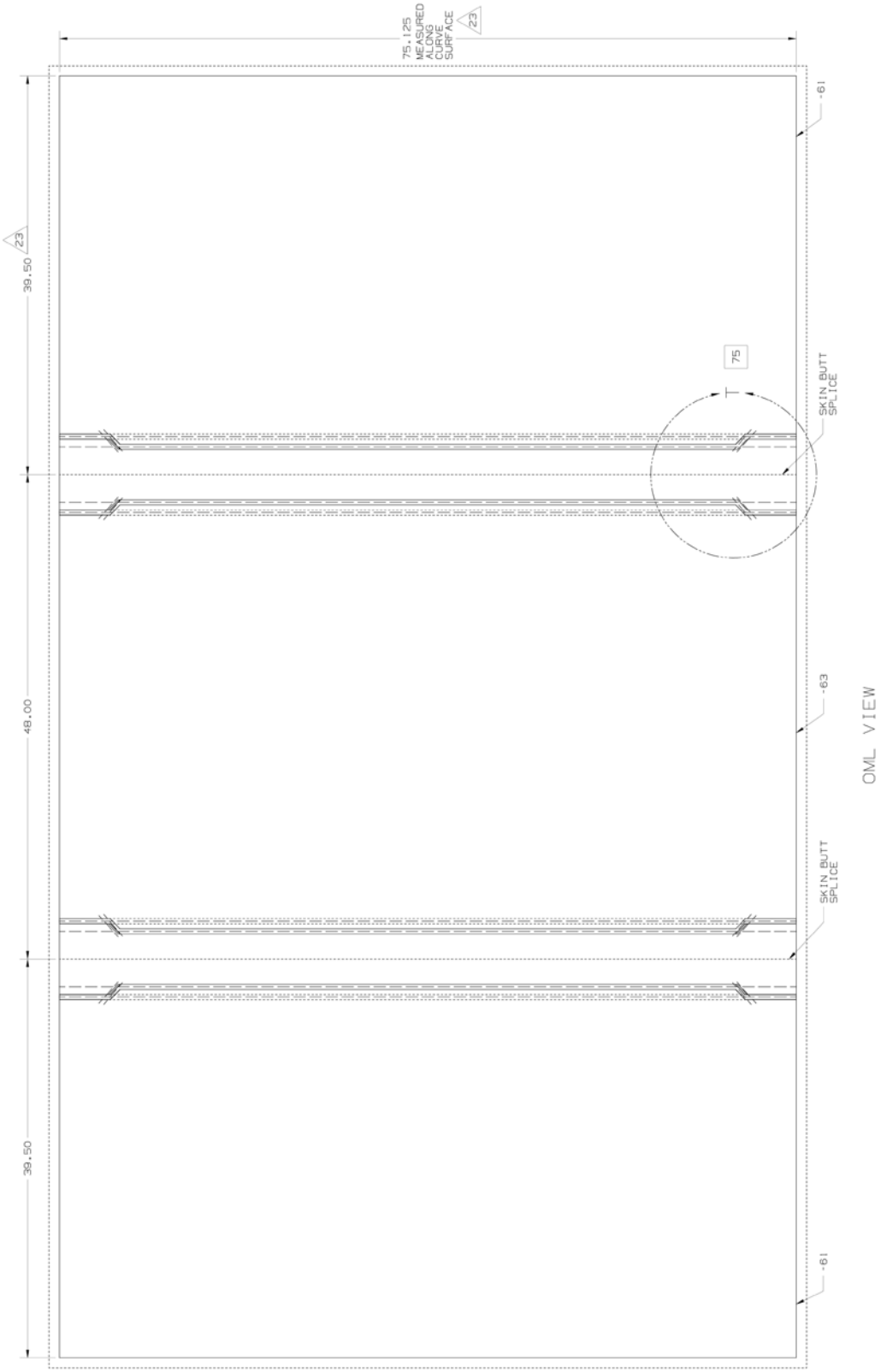

Figure A-18. Panel Details, Skin Assembly, Exterior

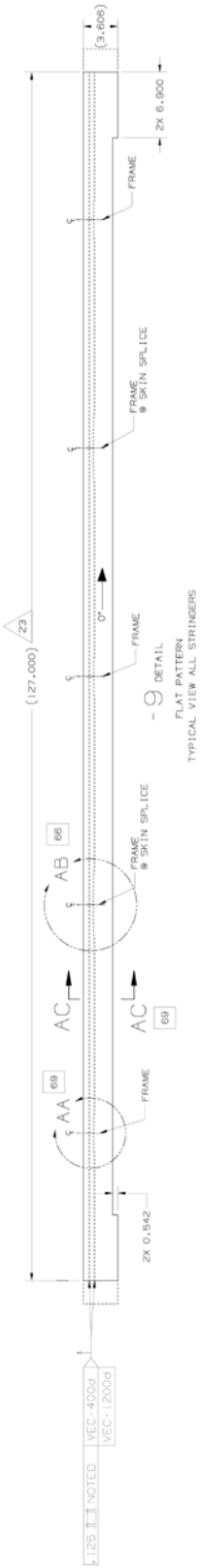

Figure A-19. Panel Details, Stringer Stack

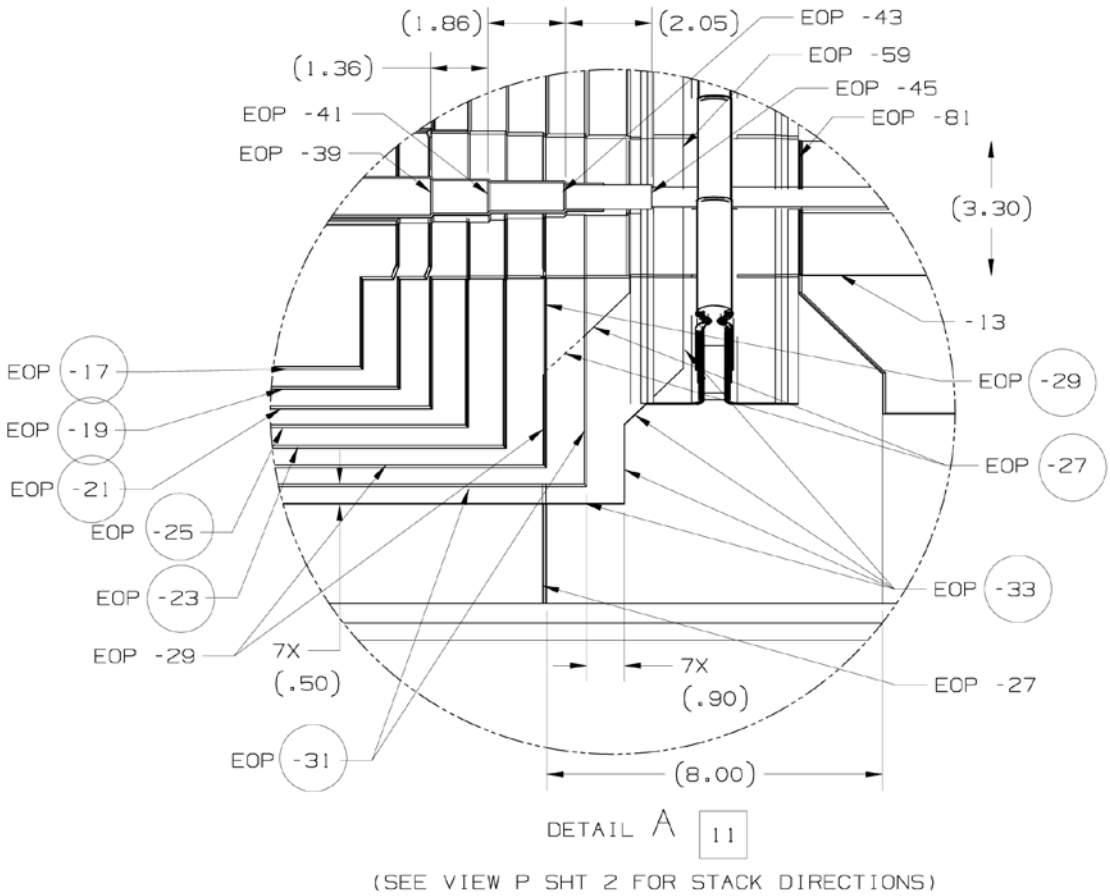

Figure A-20. Panel Details, Detail A

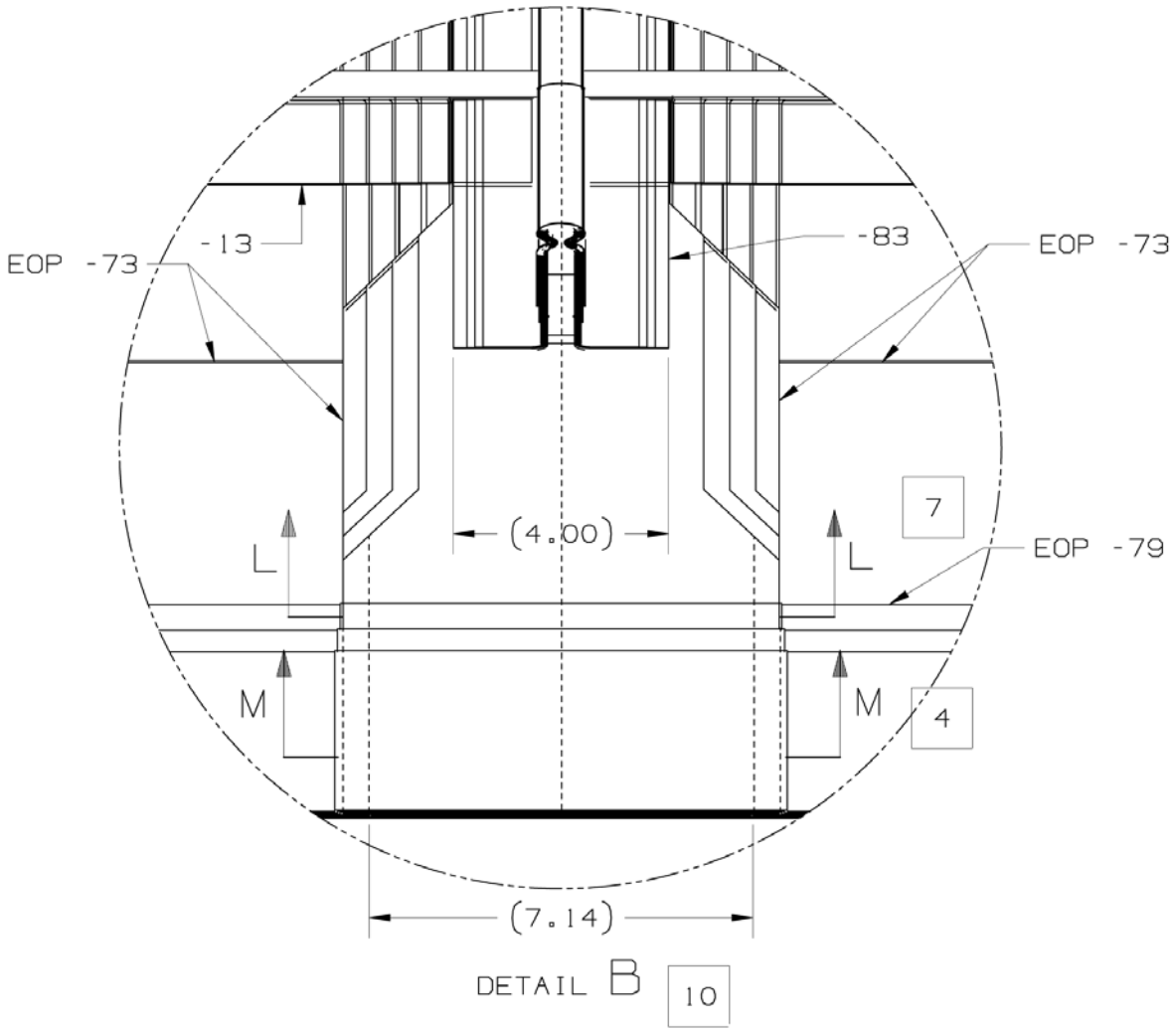

Figure A-21. Panel Details, Detail B

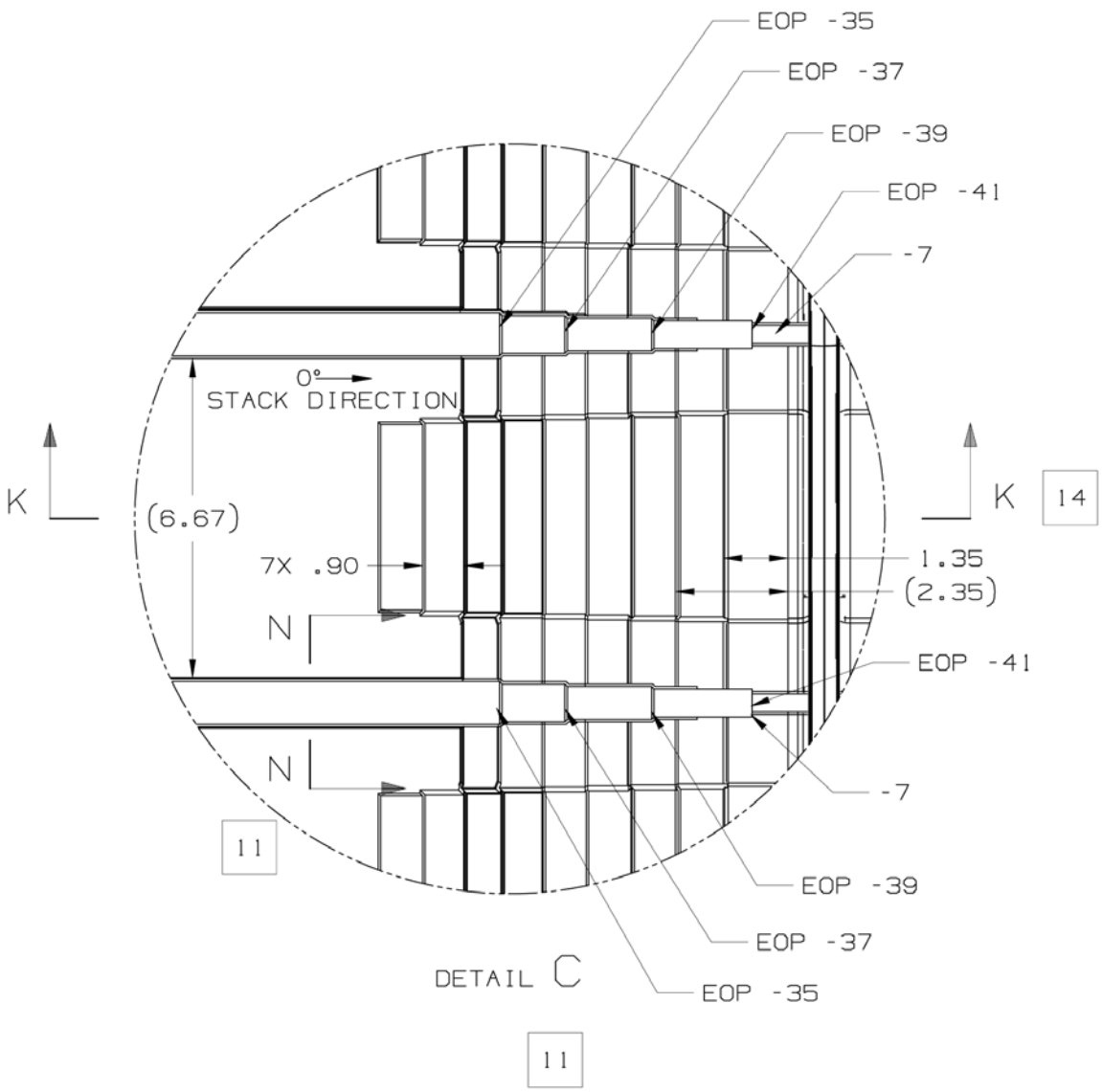

Figure A-22. Panel Details, Detail C

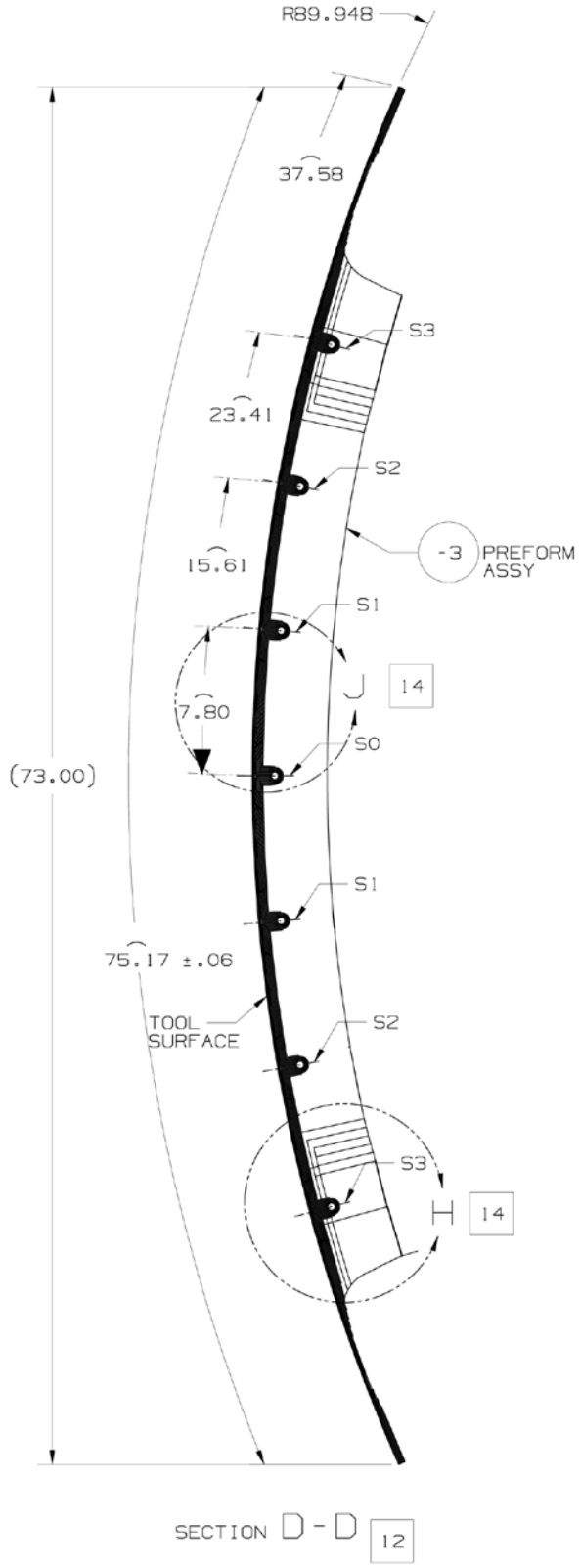

Figure A-23. Panel Details, Section D-D

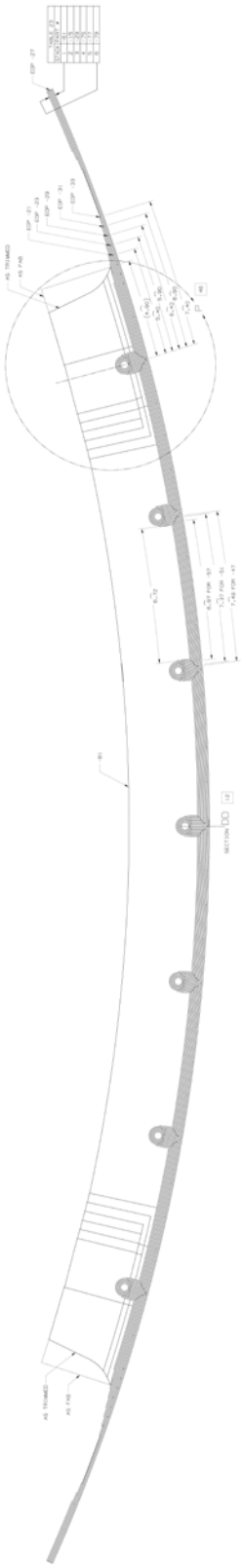

Figure A-24. Panel Details, Section D-D

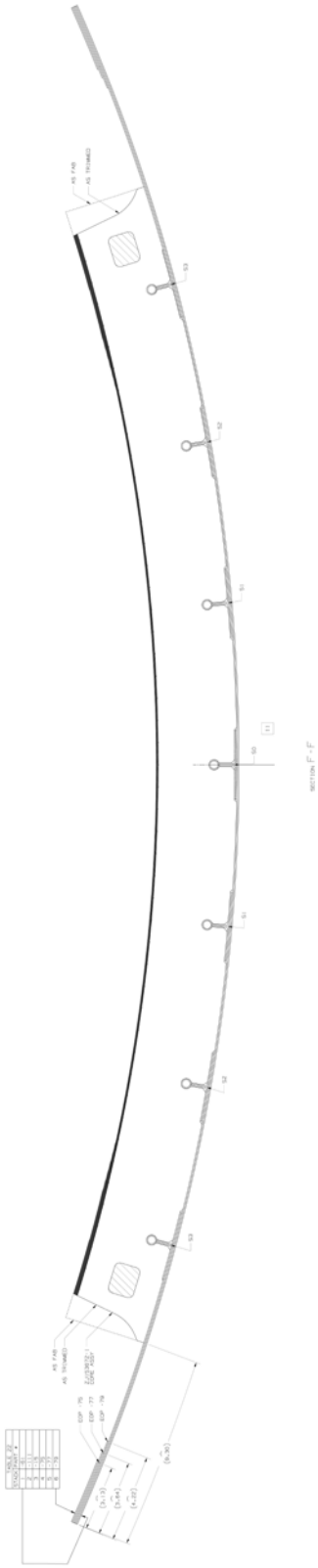

Figure A-25. Panel Details, Section F-F

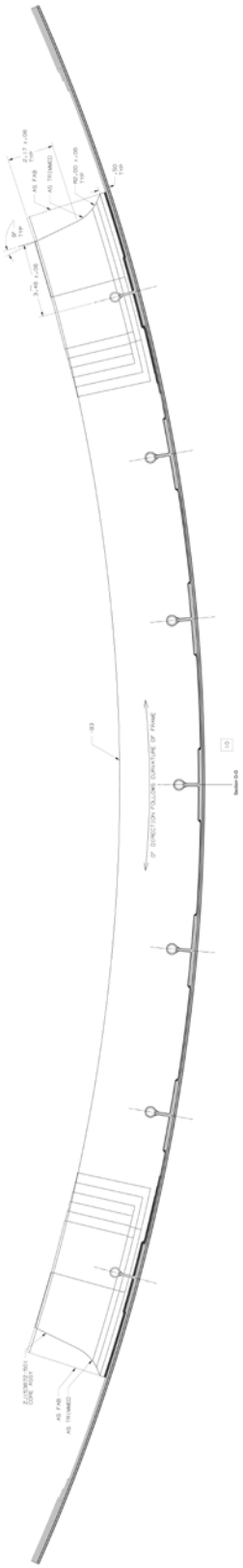

Figure A-26. Panel Details, Section G-G

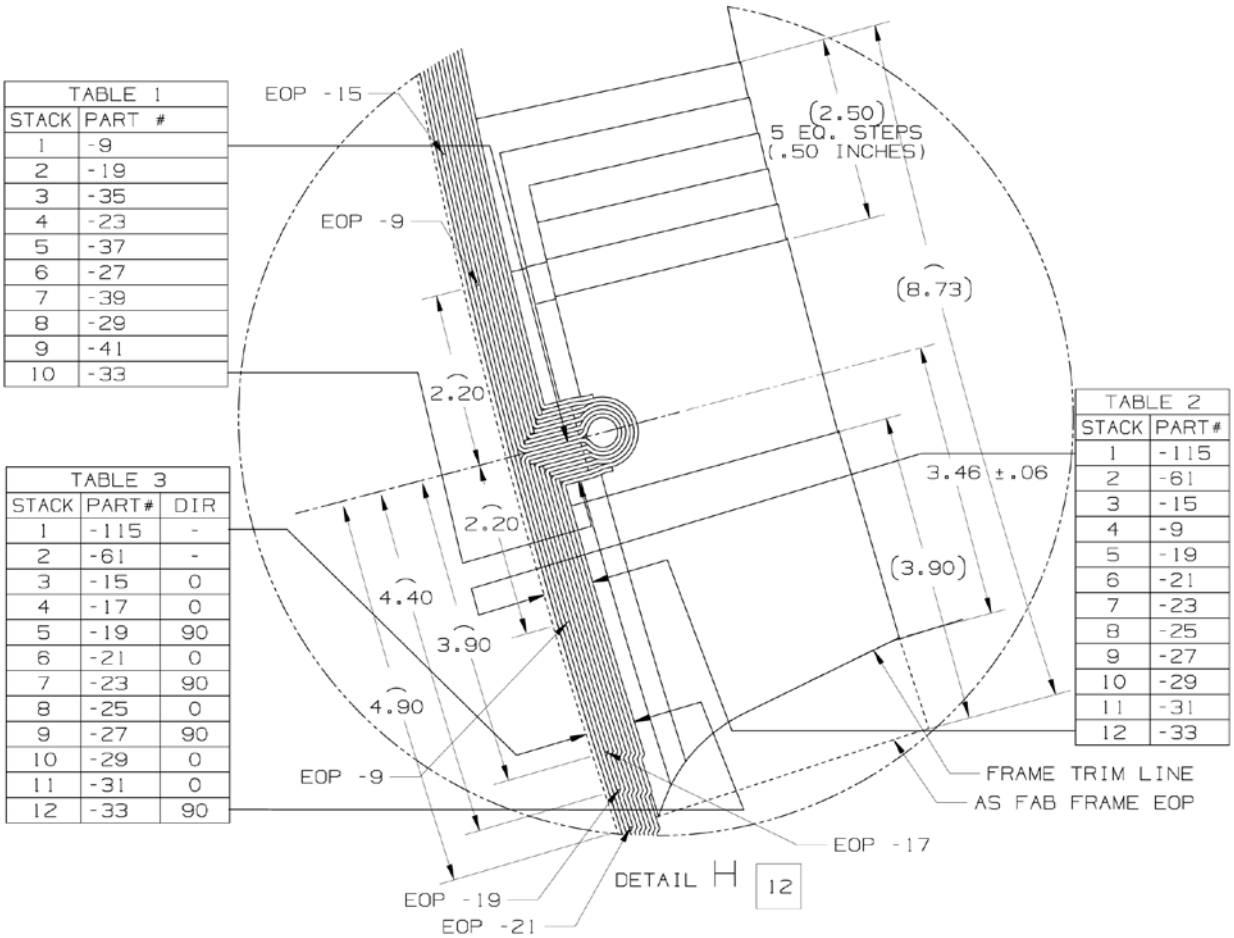

TABLE 1	
STACK	PART #
1	-9
2	-19
3	-35
4	-23
5	-37
6	-27
7	-39
8	-29
9	-41
10	-33

TABLE 2	
STACK	PART#
1	-115
2	-61
3	-15
4	-9
5	-19
6	-21
7	-23
8	-25
9	-27
10	-29
11	-31
12	-33

TABLE 3		
STACK	PART#	DIR
1	-115	-
2	-61	-
3	-15	0
4	-17	0
5	-19	90
6	-21	0
7	-23	90
8	-25	0
9	-27	90
10	-29	0
11	-31	0
12	-33	90

Figure A-27. Panel Details, Detail H

TABLE 4	
STACK	PART #
1	-9
2	-45
3	-35
4	-49
5	-37
6	-53
7	-39
8	-55
9	-41
10	-59

TABLE 5	
STACK	PART #
1	-115
2	-61
3	-11
4	-43
5	-45
6	-47
7	-49
8	-51
9	-53
10	-55
11	-57
12	-59

TABLE 6	
STACK	PART #
1	-115
2	-61
3	-11
4	-9
5	-45
6	-47
7	-49
8	-51
9	-53
10	-55
11	-57
12	-59

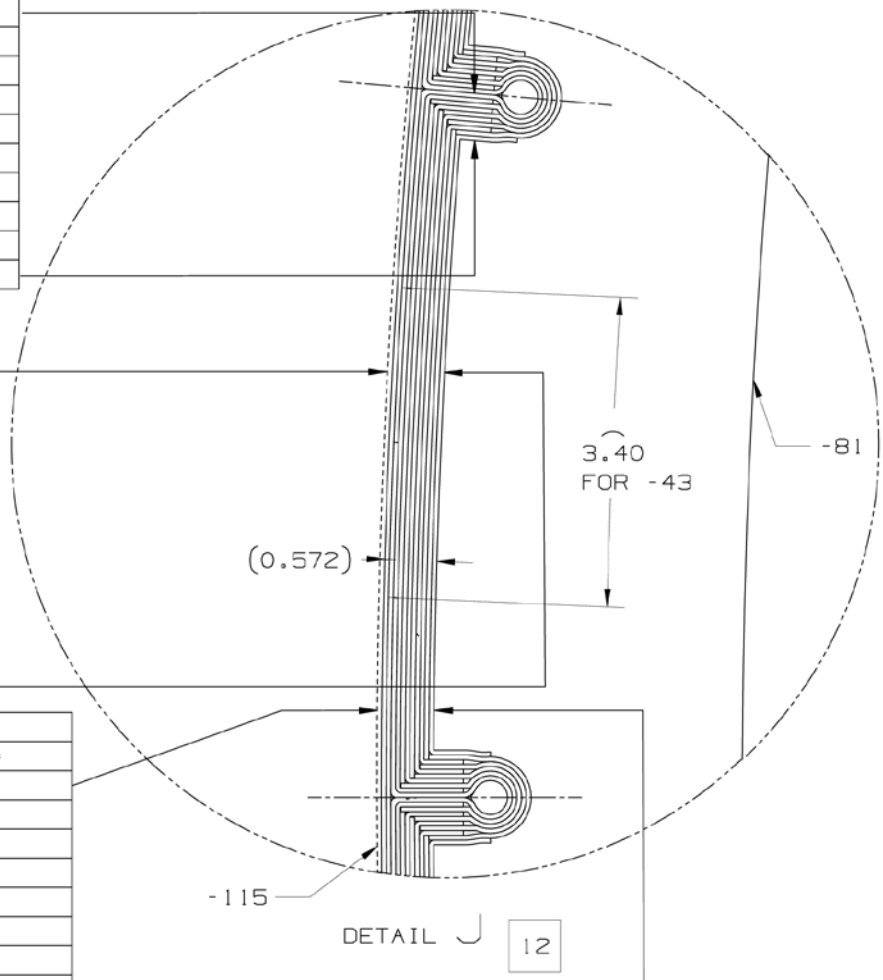

Figure A-28. Panel Details, Detail J

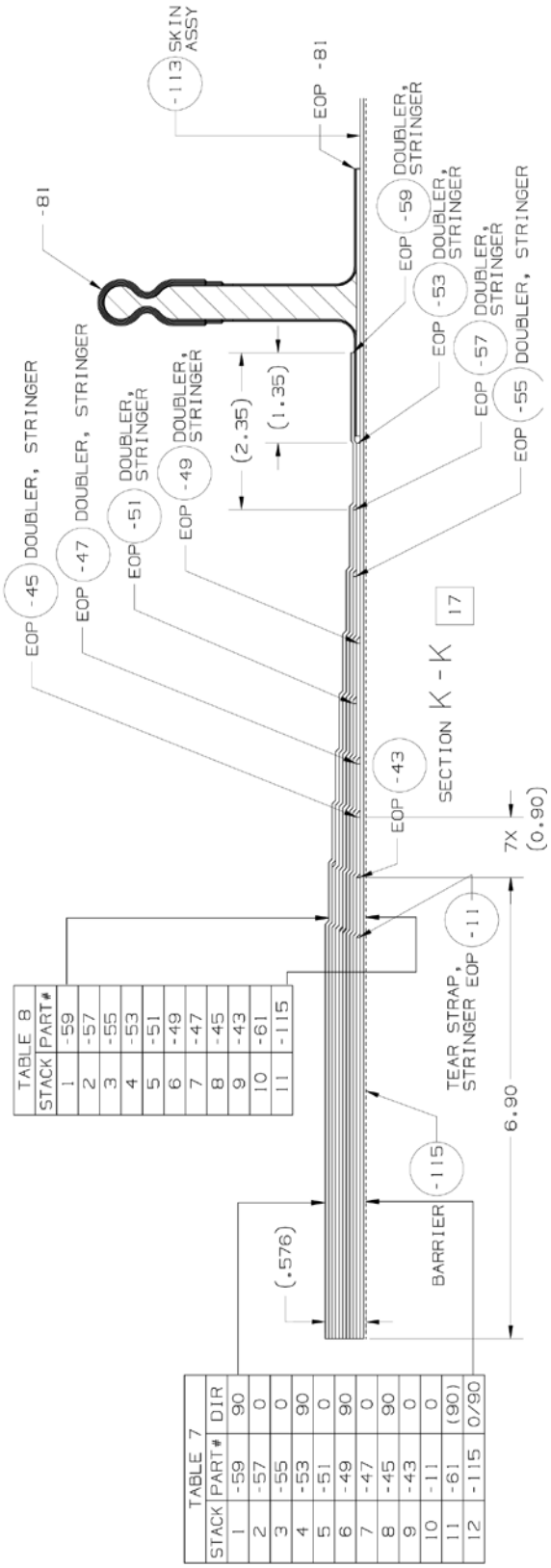

Figure A-29. Panel Details, Section K-K

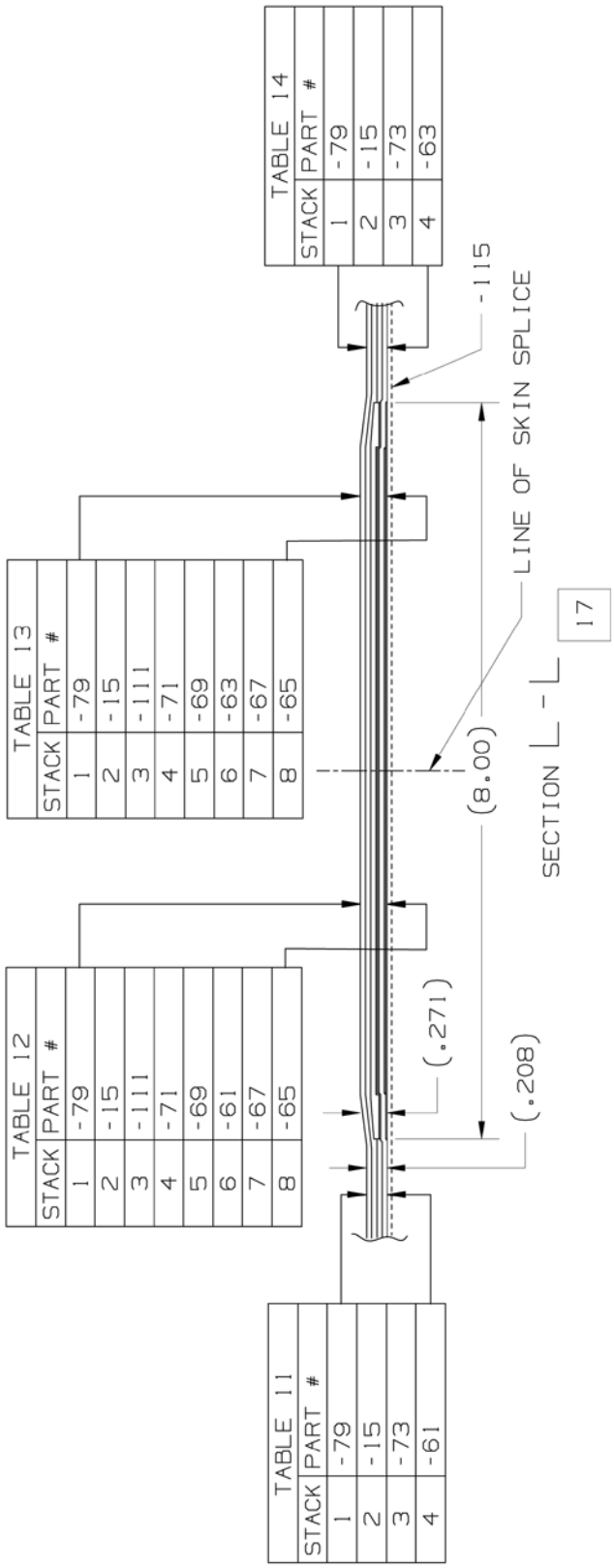

Figure A-30. Panel Details, Section L-L

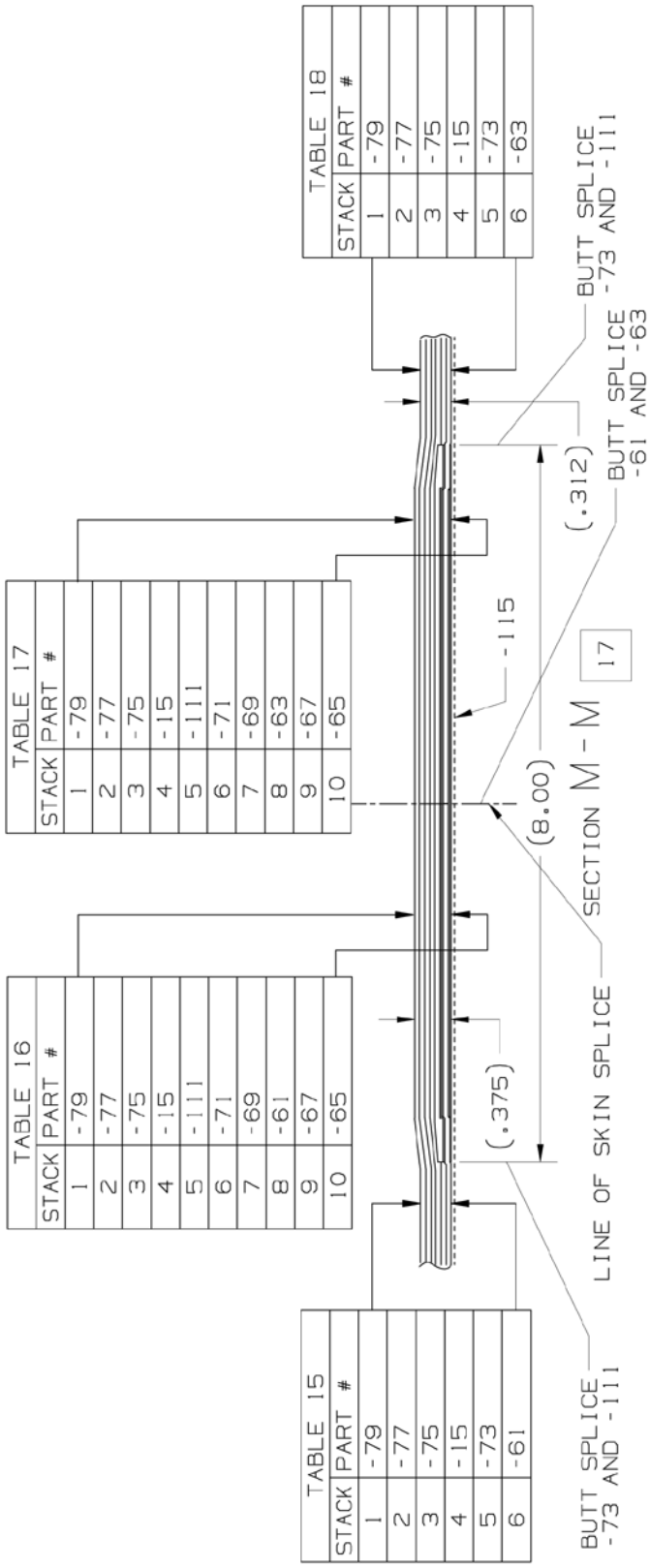

Figure A-31. Panel Details, Section M-M

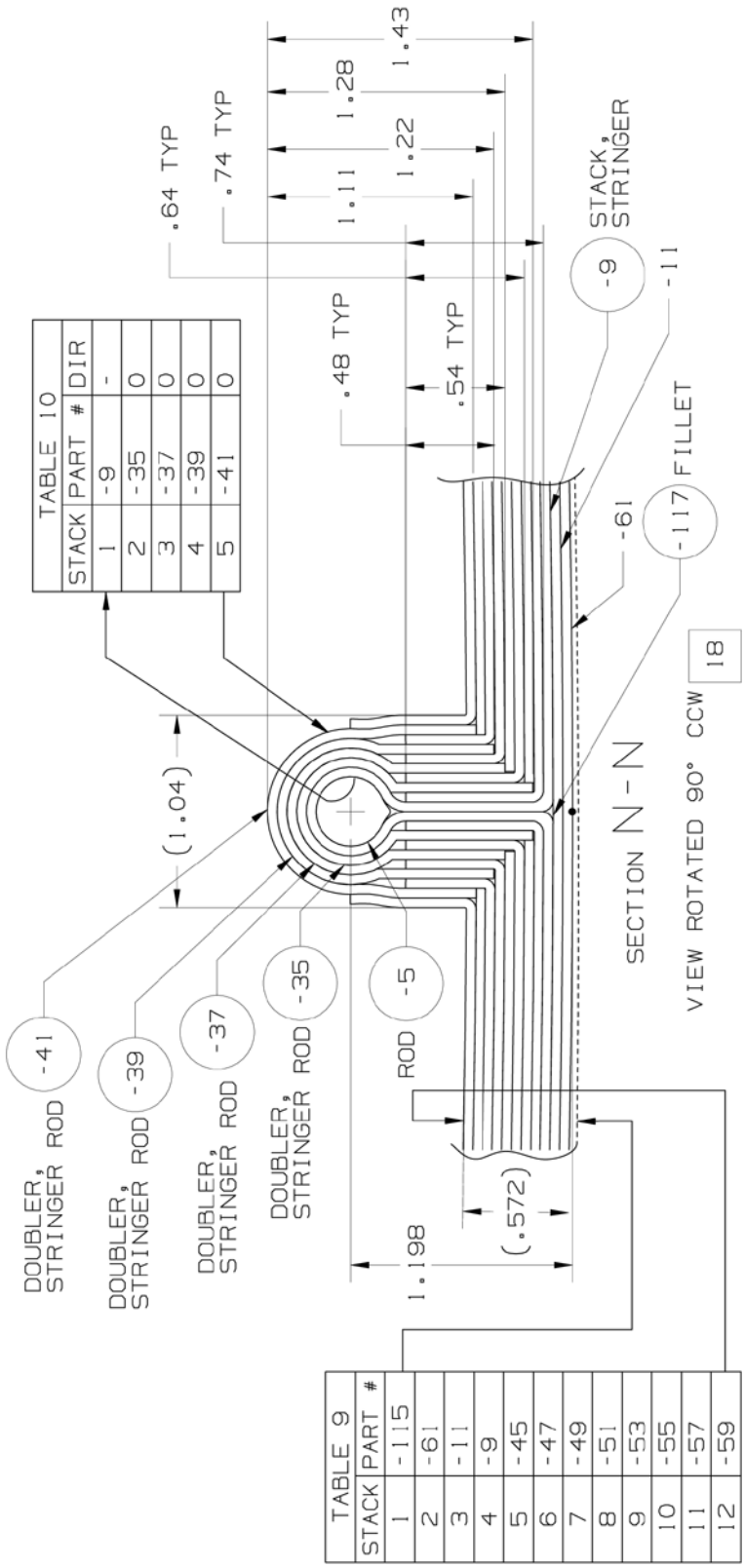

Figure A-32. Panel Details, Section N-N

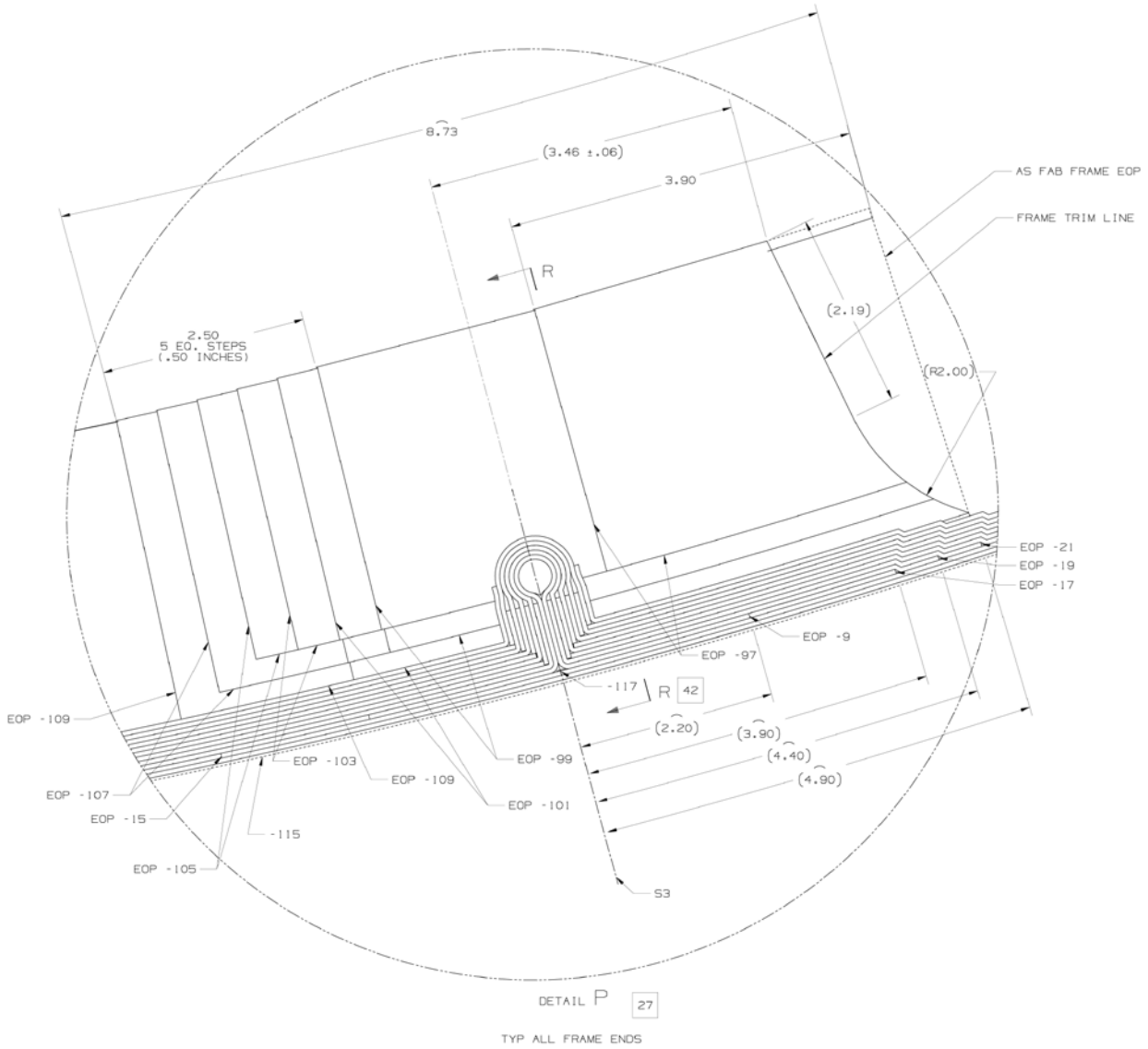

Figure A-33. Panel Details, Detail P

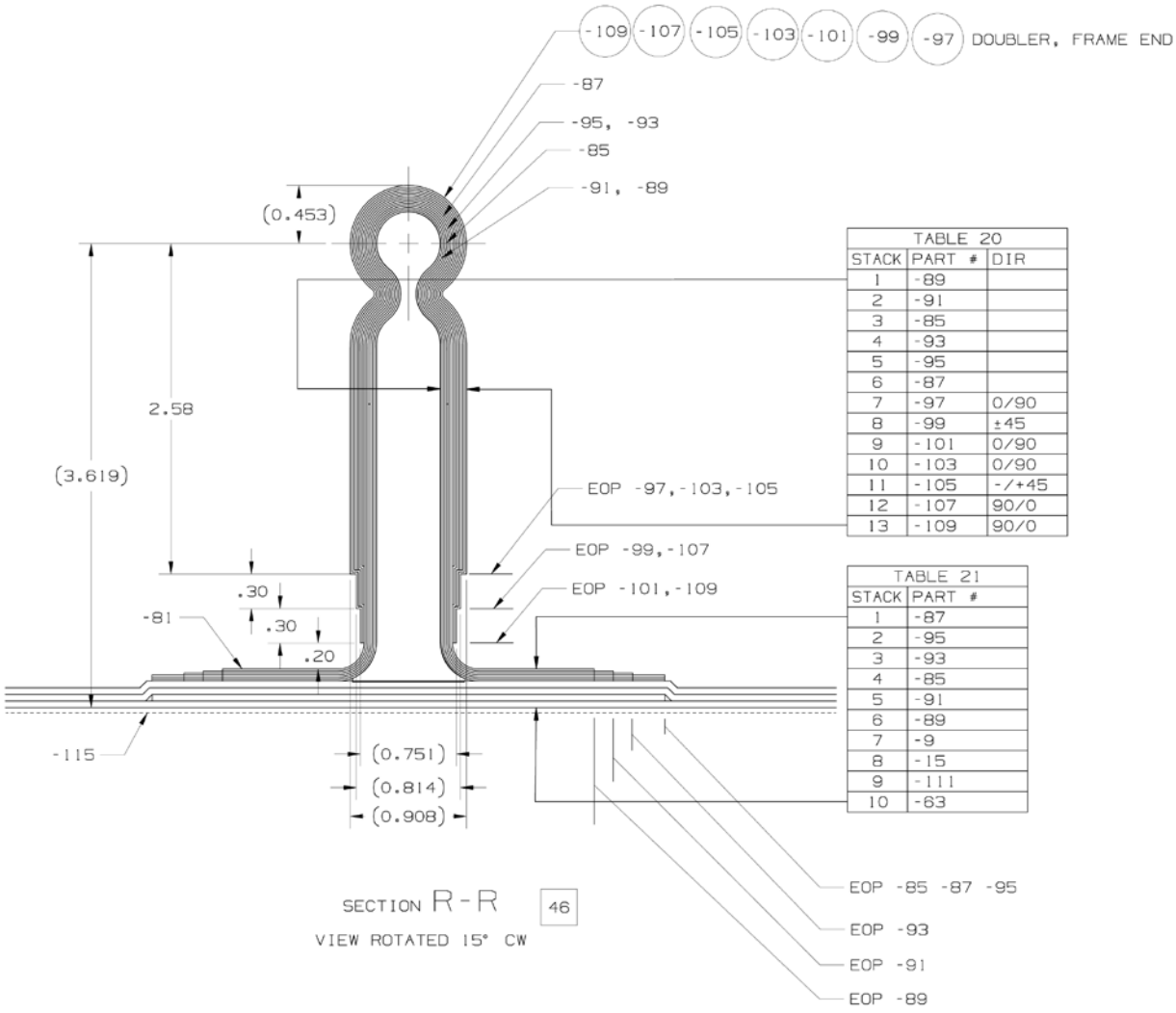

TABLE 20

STACK	PART #	DIR
1	-89	
2	-91	
3	-85	
4	-93	
5	-95	
6	-87	
7	-97	0/90
8	-99	±45
9	-101	0/90
10	-103	0/90
11	-105	-/+45
12	-107	90/0
13	-109	90/0

TABLE 21

STACK	PART #
1	-87
2	-95
3	-93
4	-85
5	-91
6	-89
7	-9
8	-15
9	-111
10	-63

Figure A-34. Panel Details, Section R-R

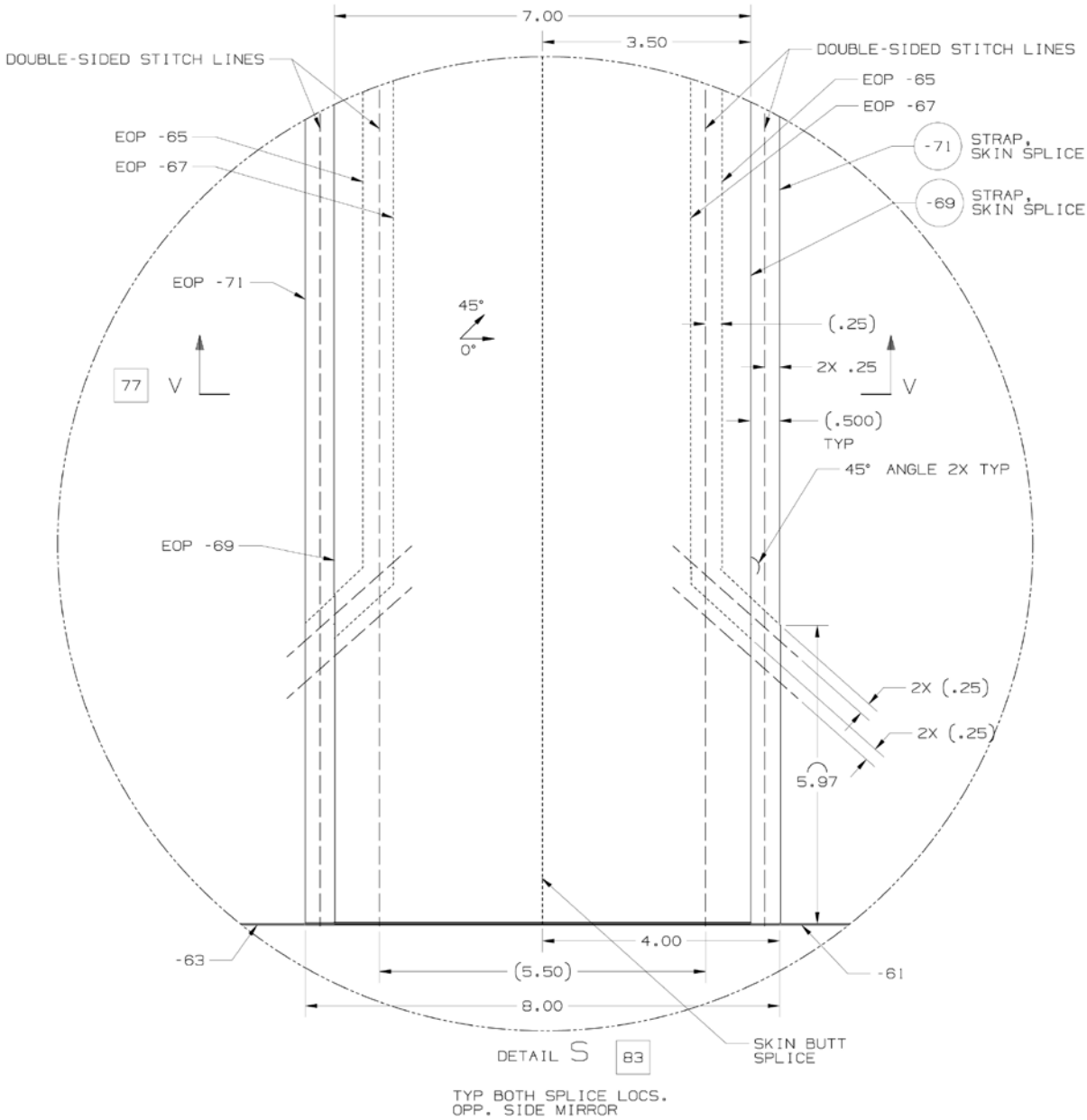

Figure A-35. Panel Details, Detail S

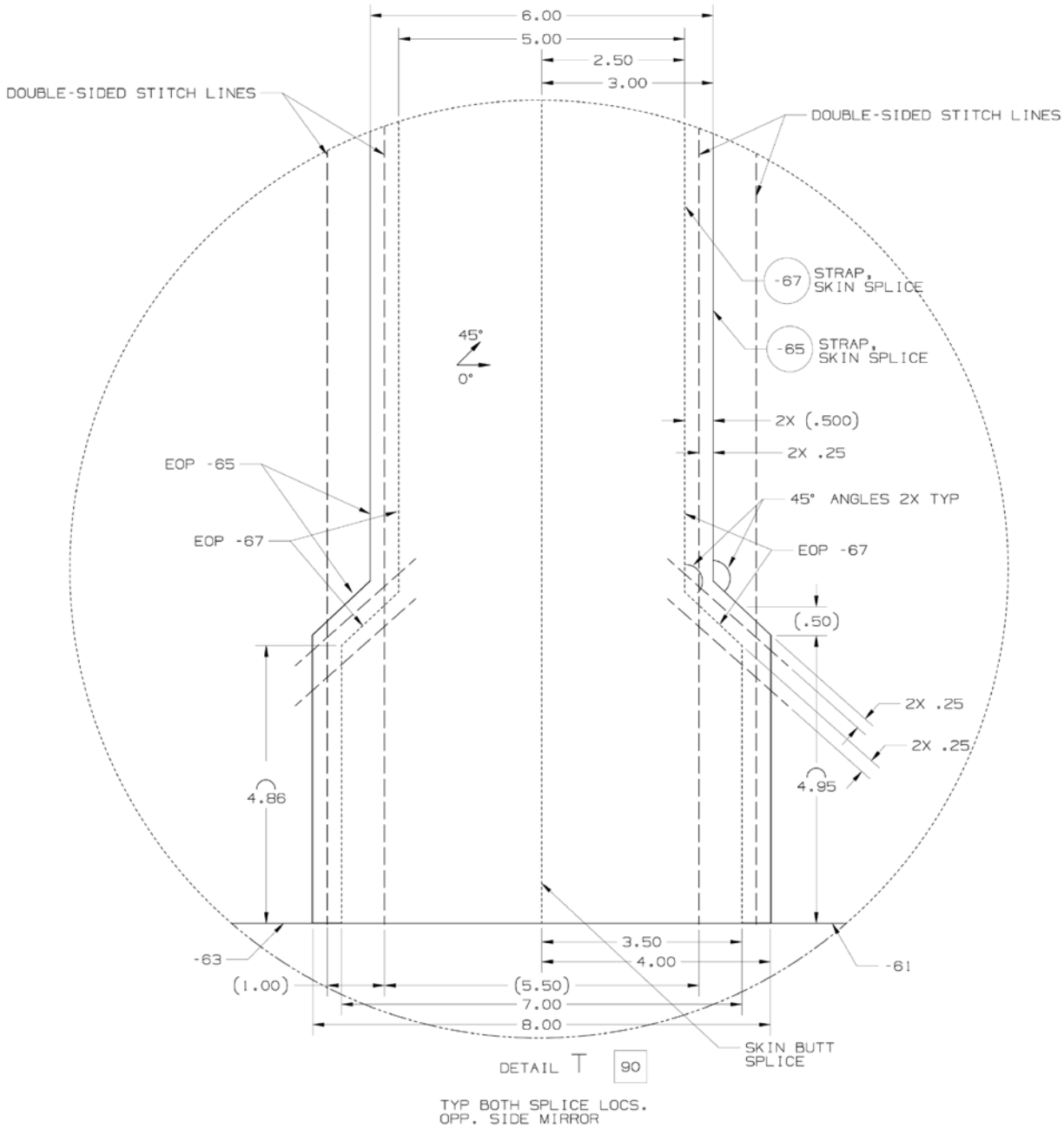

Figure A-36. Panel Details, Detail T

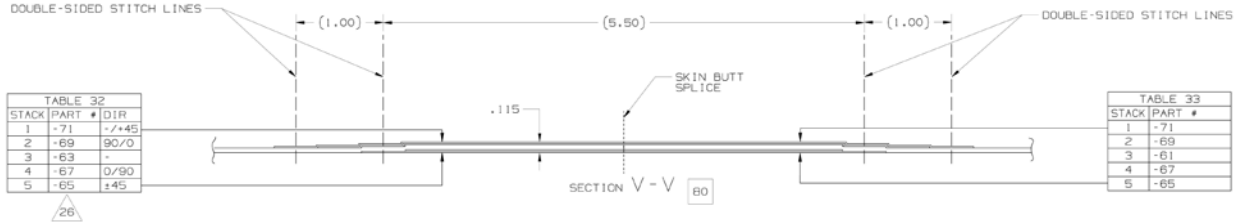

TABLE 32		
STACK	PART #	DIR
1	-71	-/+45
2	-69	90/0
3	-63	-
4	-67	0/90
5	-65	±45

TABLE 33	
STACK	PART #
1	-71
2	-69
3	-61
4	-67
5	-65

Figure A-37. Panel Details, Section V-V

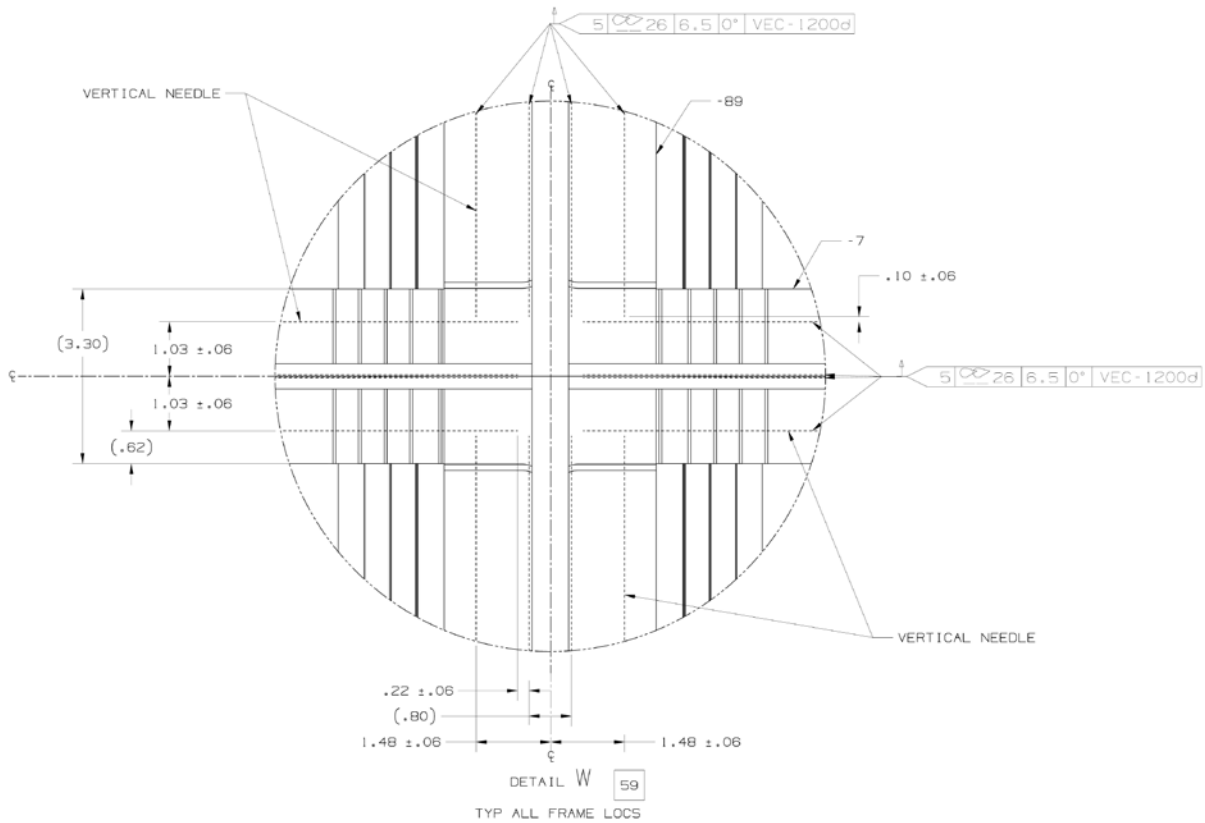

Figure A-38. Panel Details, Detail W

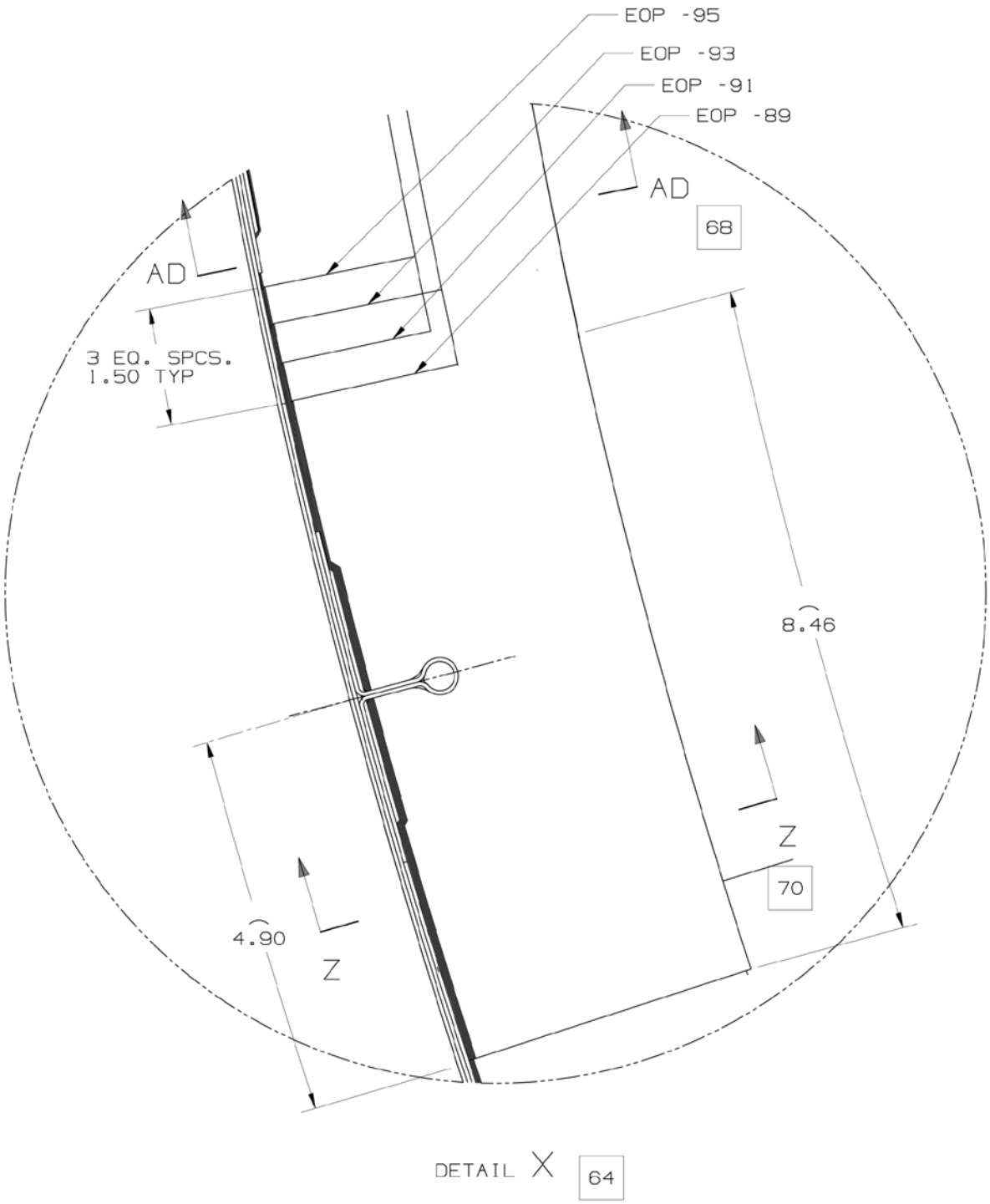

Figure A-39. Panel Details, Detail X

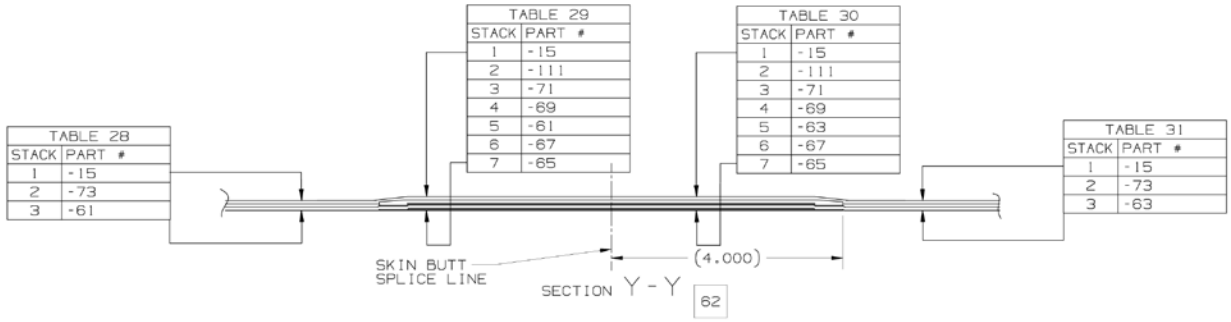

Figure A-40. Panel Details, Section Y-Y

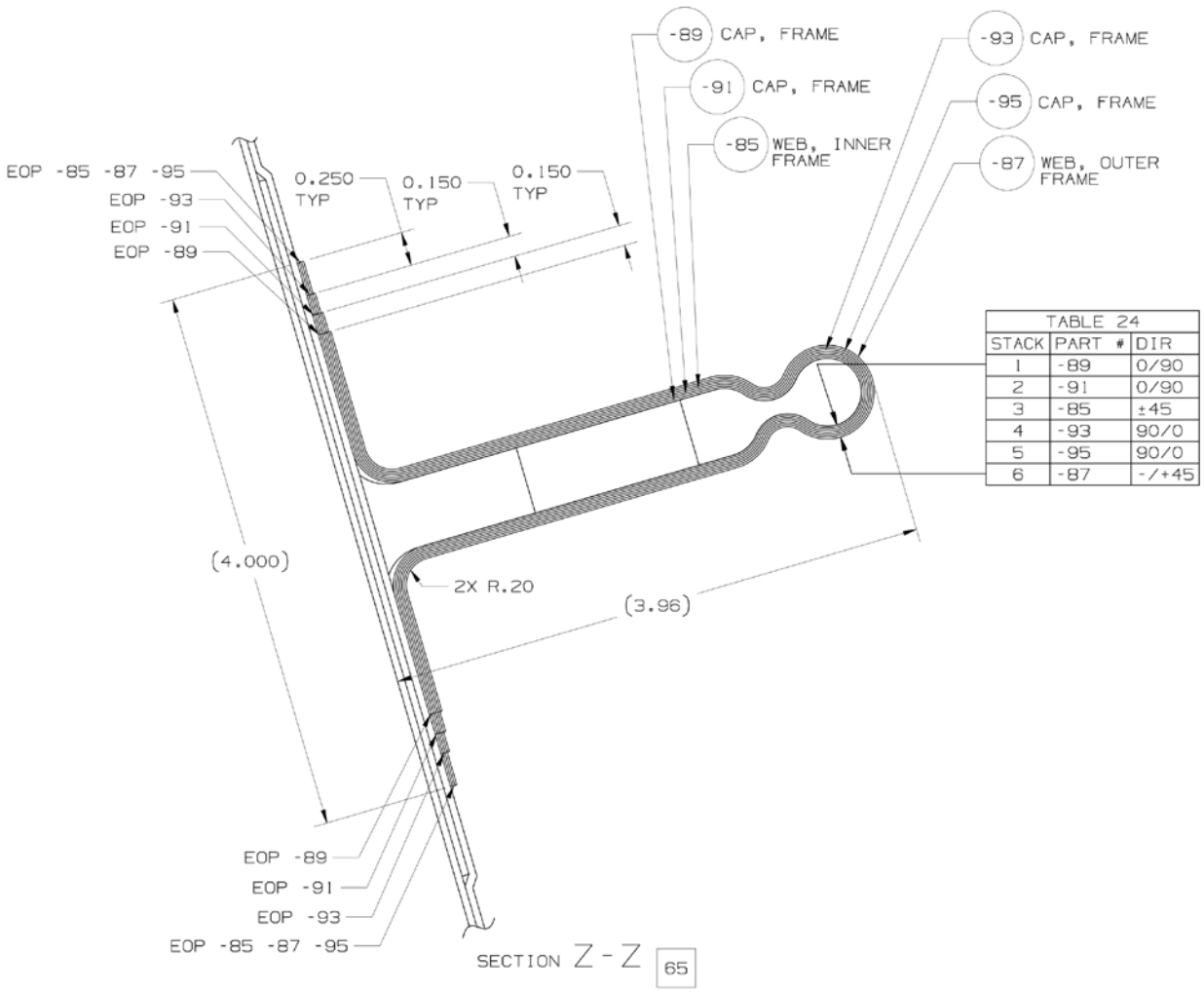

Figure A-41. Panel Details, Section Z-Z

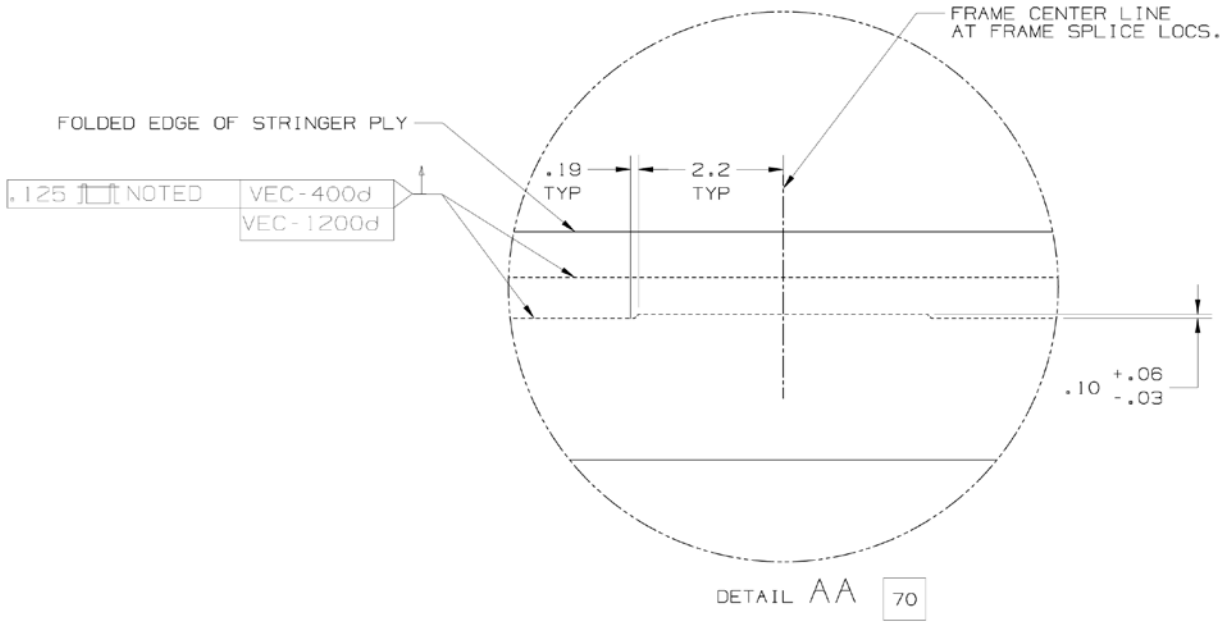

Figure A-42. Panel Details, Detail AA

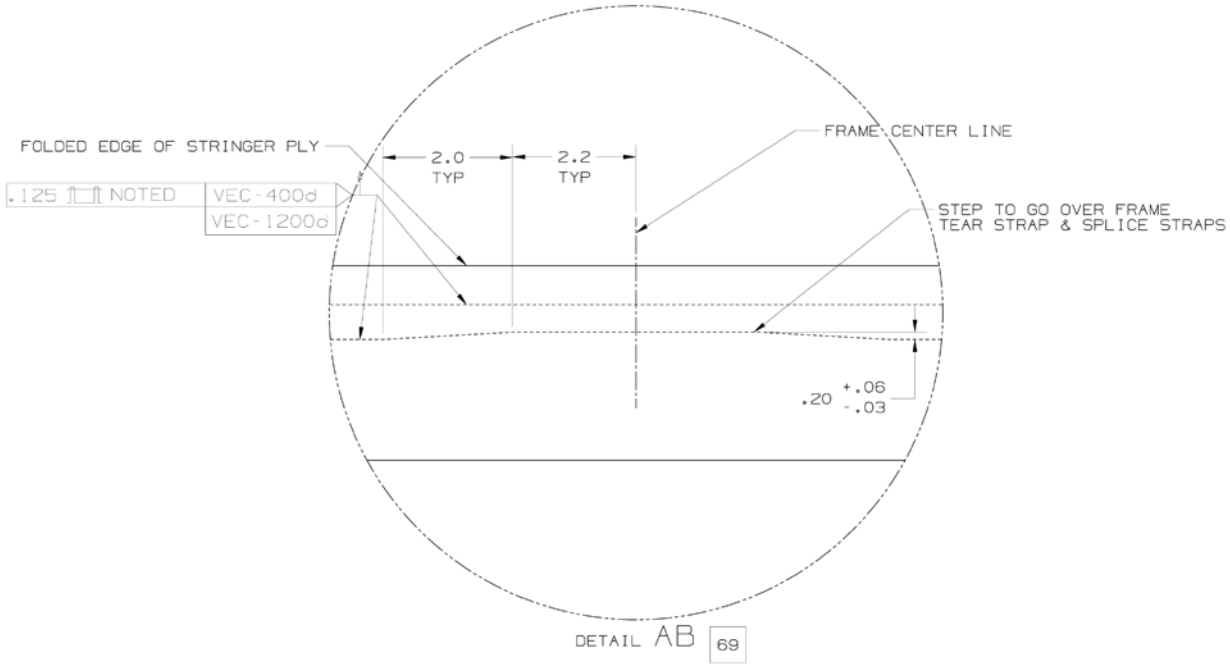

Figure A-43. Panel Details, Detail AB

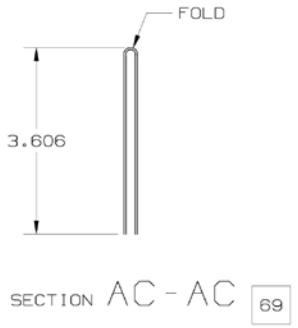

Figure A-44. Panel Details, Section AC-AC

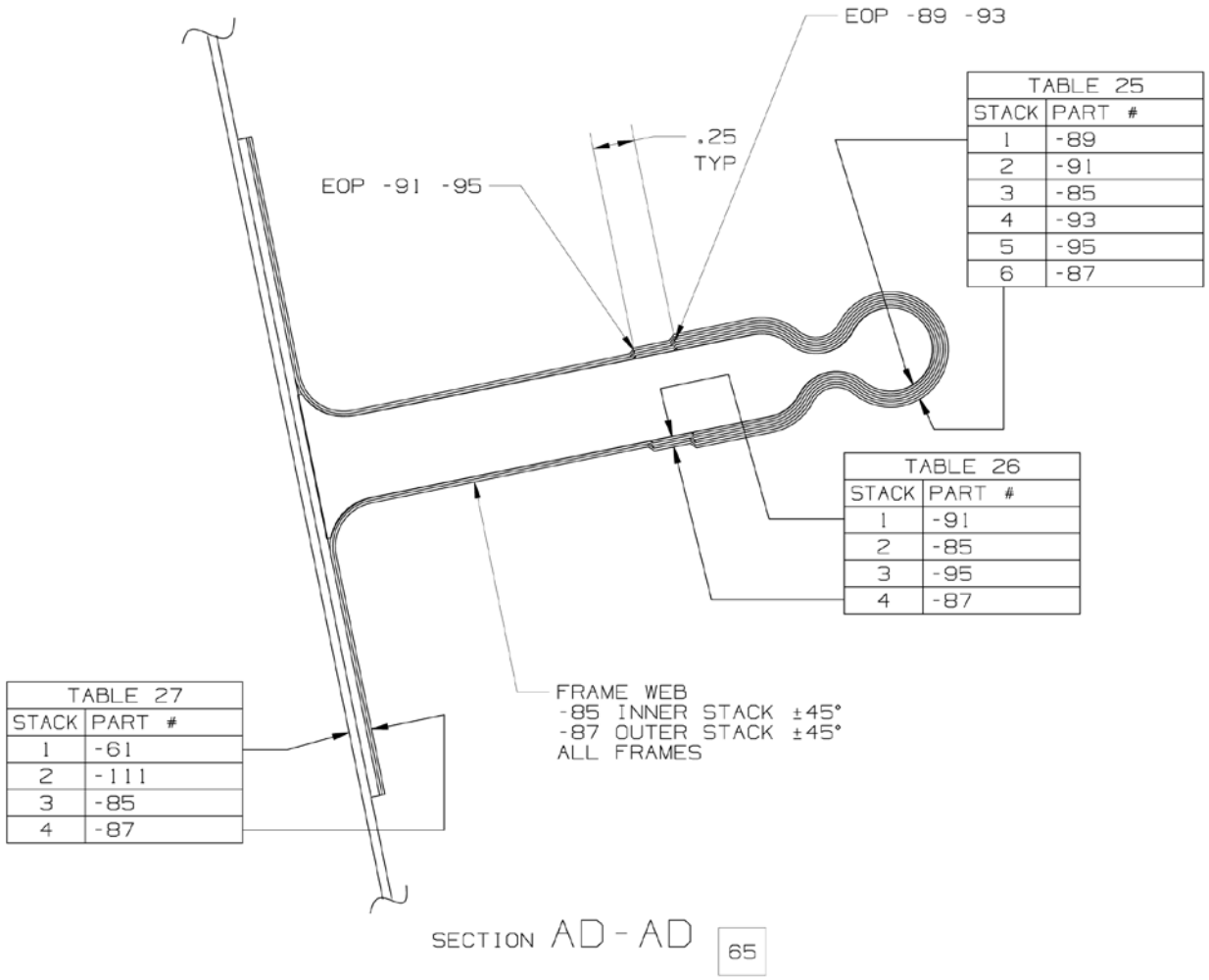

Figure A-45. Panel Details, Section AD-AD

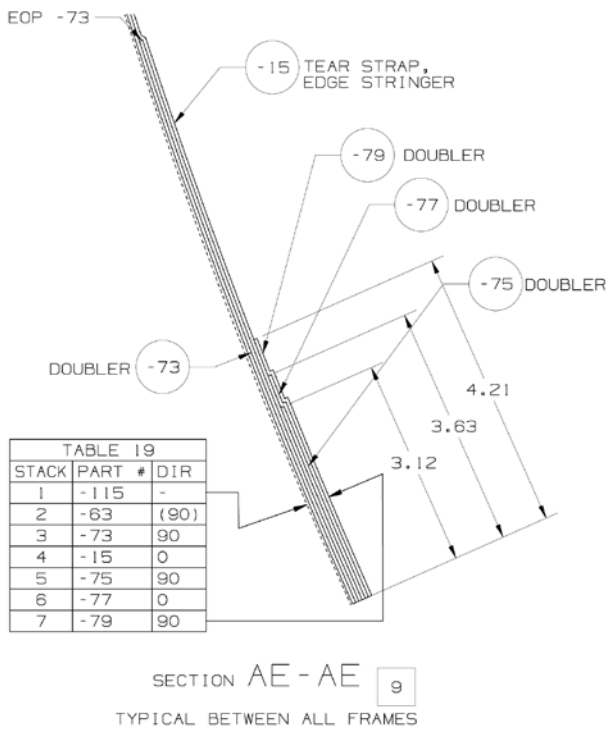

Figure A-46. Panel Details, Section AE-AE

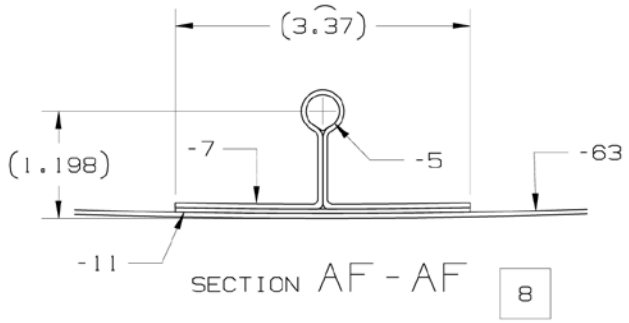

Figure A-47. Panel Details, Section AF-AF

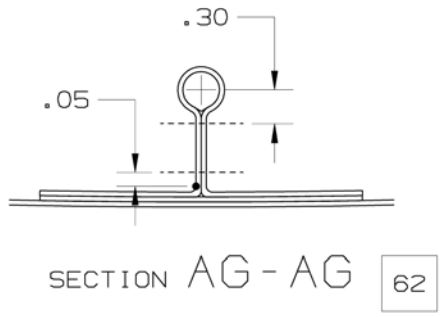

Figure A-48. Panel Details, Section AG-AG

Figure A-49. Foam Core, Front

Table A-5. Foam Core Parts List

*			-501	Core Assy—FAA Frame @Splice		1.00 x 4 x 56	G11
	*		-1	Core Assy—FAA Frame		1.00 x 4 x 56	G11
		2	ZB153672-1	Insert Frame			E13
1	1	*	-3	Core Assy		1.00 x 4 x 56	D13
		1	ZJ153293-5	PRSEUS Frame Core		1.00 x 4 x 46	D24
		1	ZJ153293-3	PRSEUS Frame Core		1.00 x 4 x 38	C9
Quantity			Part Number		Material	Size	Zone
-501	-1	-3					

GENERAL NOTES:
UNLESS OTHERWISE NOTED

1. DIMENSIONAL TOLERANCES AND SYMBOLS PER ANSI Y14.5M-1982.
2. IDENTIFY BY LABEL ON BAG PER DPS 3.02.
3. PART TO BE STRAIGHT/FLAT WITHIN .010/FT.
4. FOAM CORE IS MADE FROM WF-110 ROHACEL FOAM PER DMS 2278, CLASS 4.
5. FILE NAME\PATH:
   \\SW\HBCDATA\PWDATA\PWDATA1\UHS111202\A1XX\MGR_COMP\RELEASE\ZJ153671
6. MACHINE FOAM PER DPI-G049, EXCEPT FOAM MUST BE COMPLETELY SATURATED AT APPROXIMATELY 50% RELATIVE HUMIDITY PRIOR TO MACHINING.
7. BOND SEGMENTS TOGETHER PER DPS 1.960-1.12 EXCEPT USE DPM 5535-4 (EA9394)PER DPS 1.07-39.
8. FILL AND SAND ANY MISMATCHED SURFACES WITH DPM 5534-4.
9. CUT OUT CORE AND BOND -3 INSERTS TO FOAM PER DPS 1.960-1.12 EXCEPT USE DPM 5535-4(EA9394)PER DPS 1.07-39. USE INSERT AS AN INSTALLATION TEMPLATE. TRIM CORE AN ADDITIONAL .010 FOR THE BOND LINE.
10. SCRIBE ADDITIONAL RESIN GROOVES AT -3 LOCS USING -3 AS A TEMPLATE.
11. USE FRAME CORE BOND TOOL# ZJ153415

Figure A-50. Foam Core General Notes

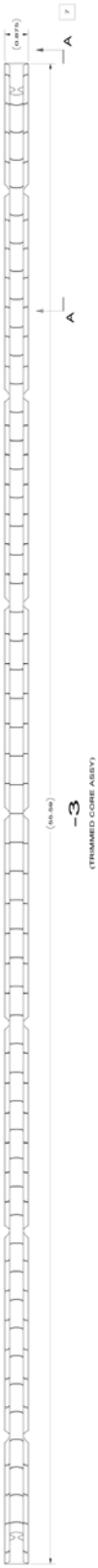

Figure A-51. Foam Core, Trimmed, Side

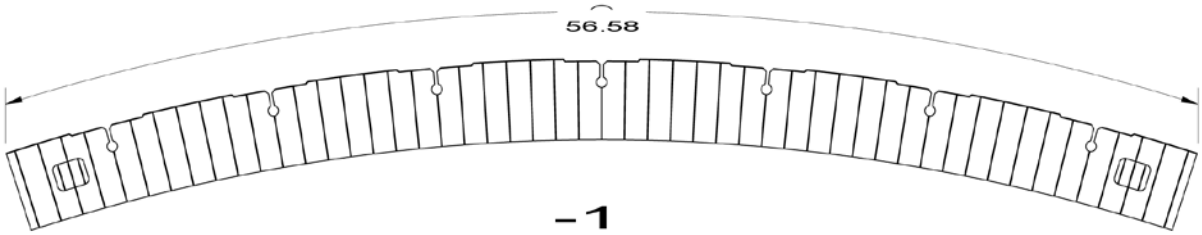

Figure A-52. Foam Core, Part -1, Front

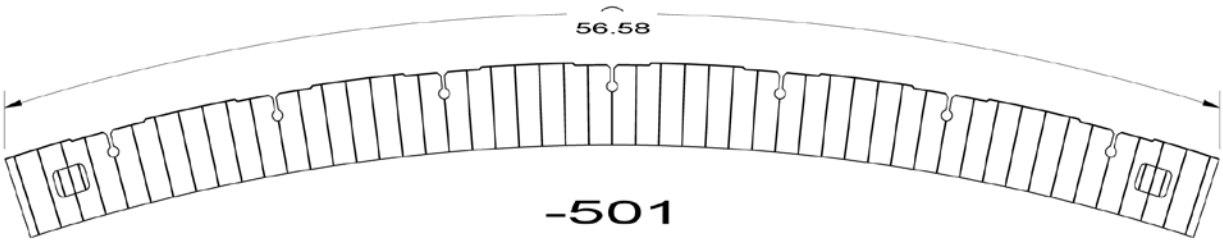

Figure A-53. Foam Core, Part -501, Front

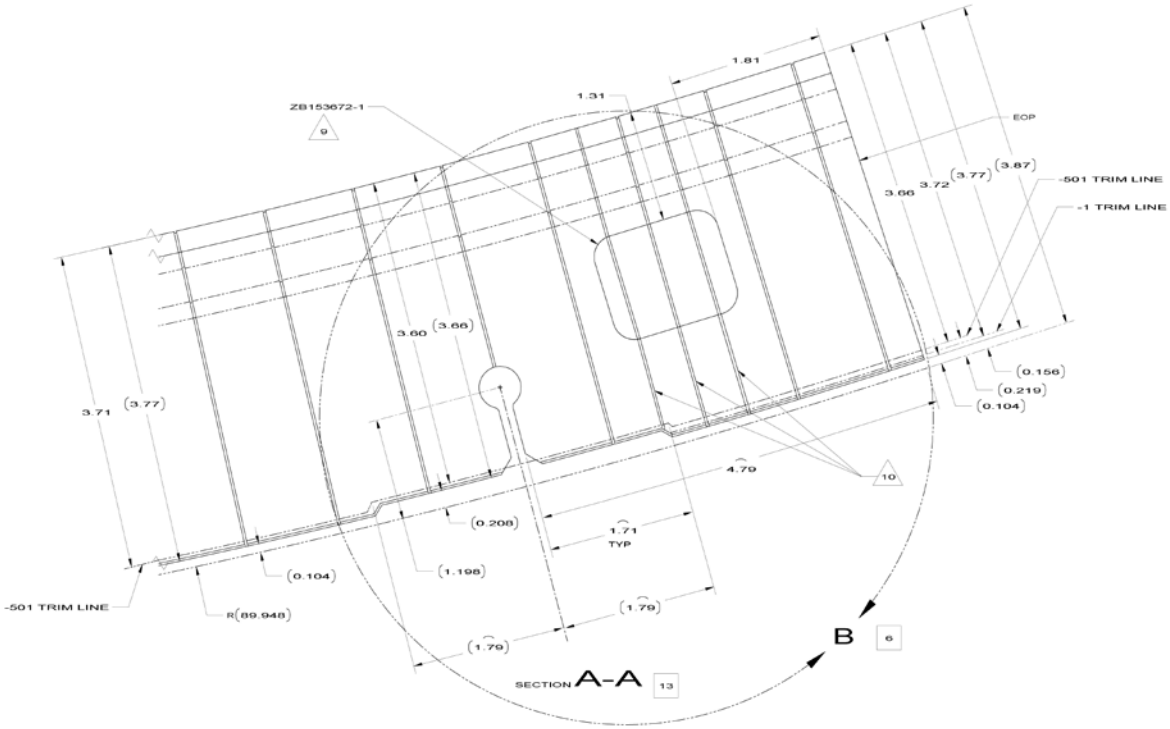

Figure A-54. Foam Core, Section A-A

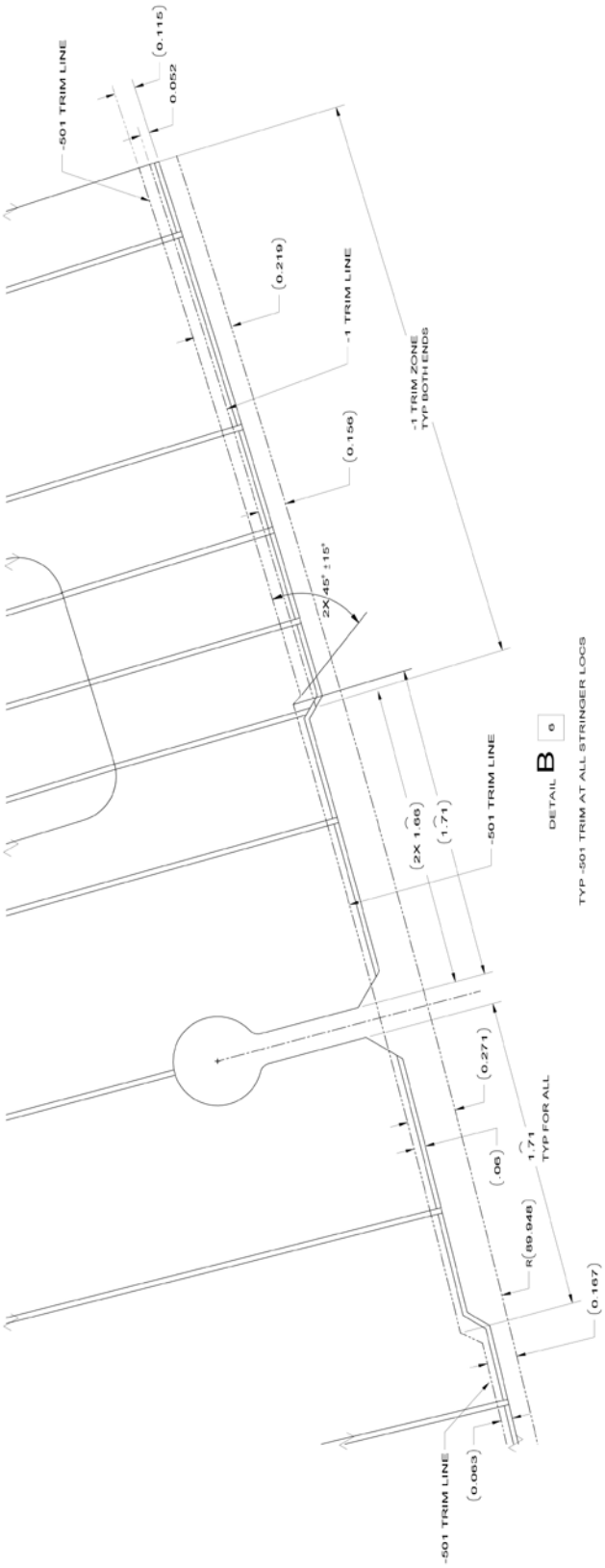

Figure A-55. Foam Core, Detail B

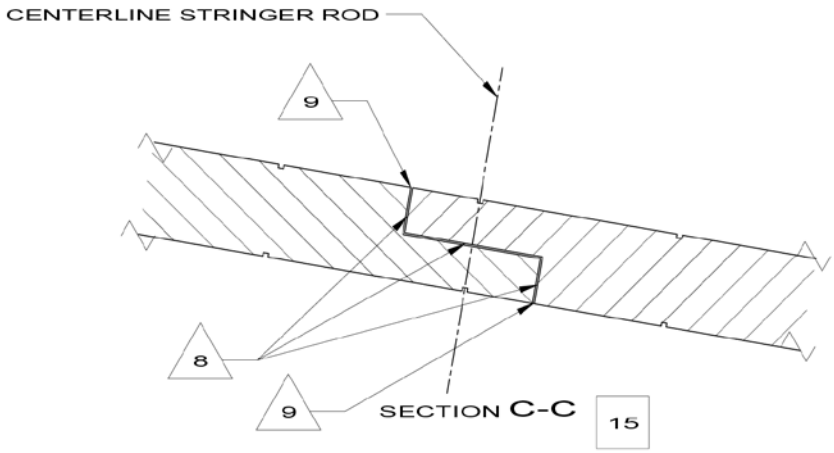

Figure A-56. Foam Core, Section C-C

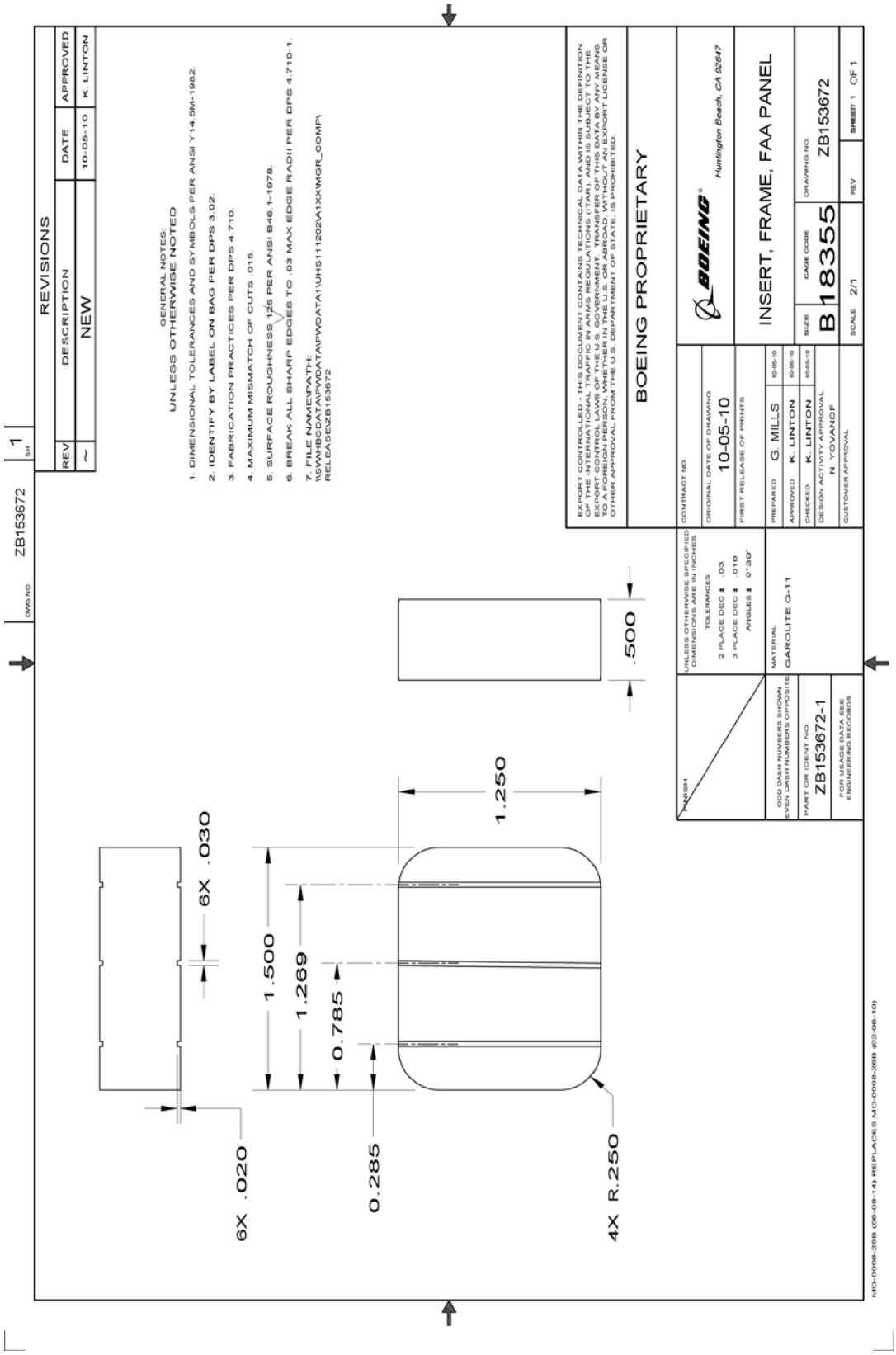

Figure A-57. Frame Insert

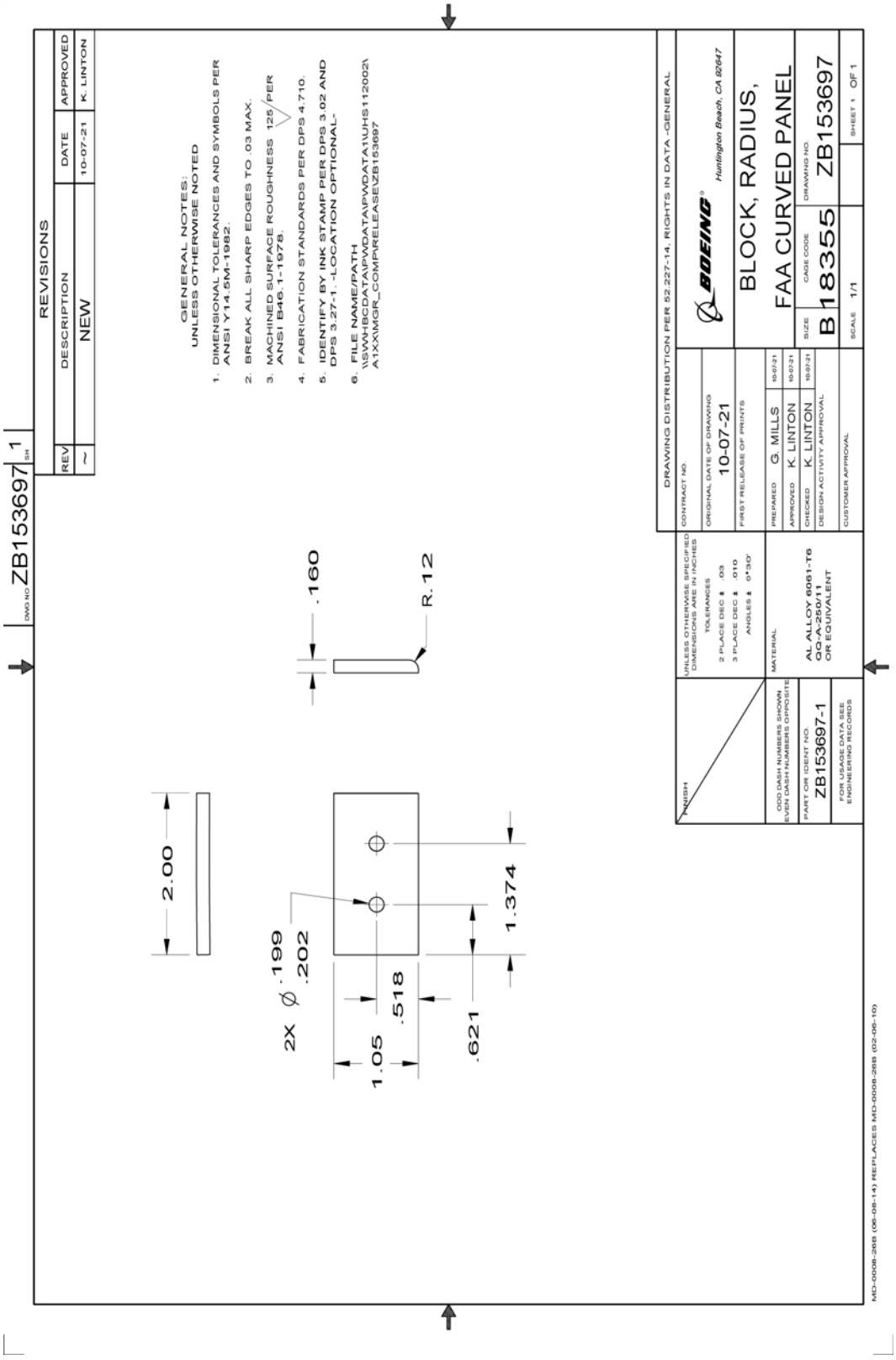

Figure A-58. Radius Block

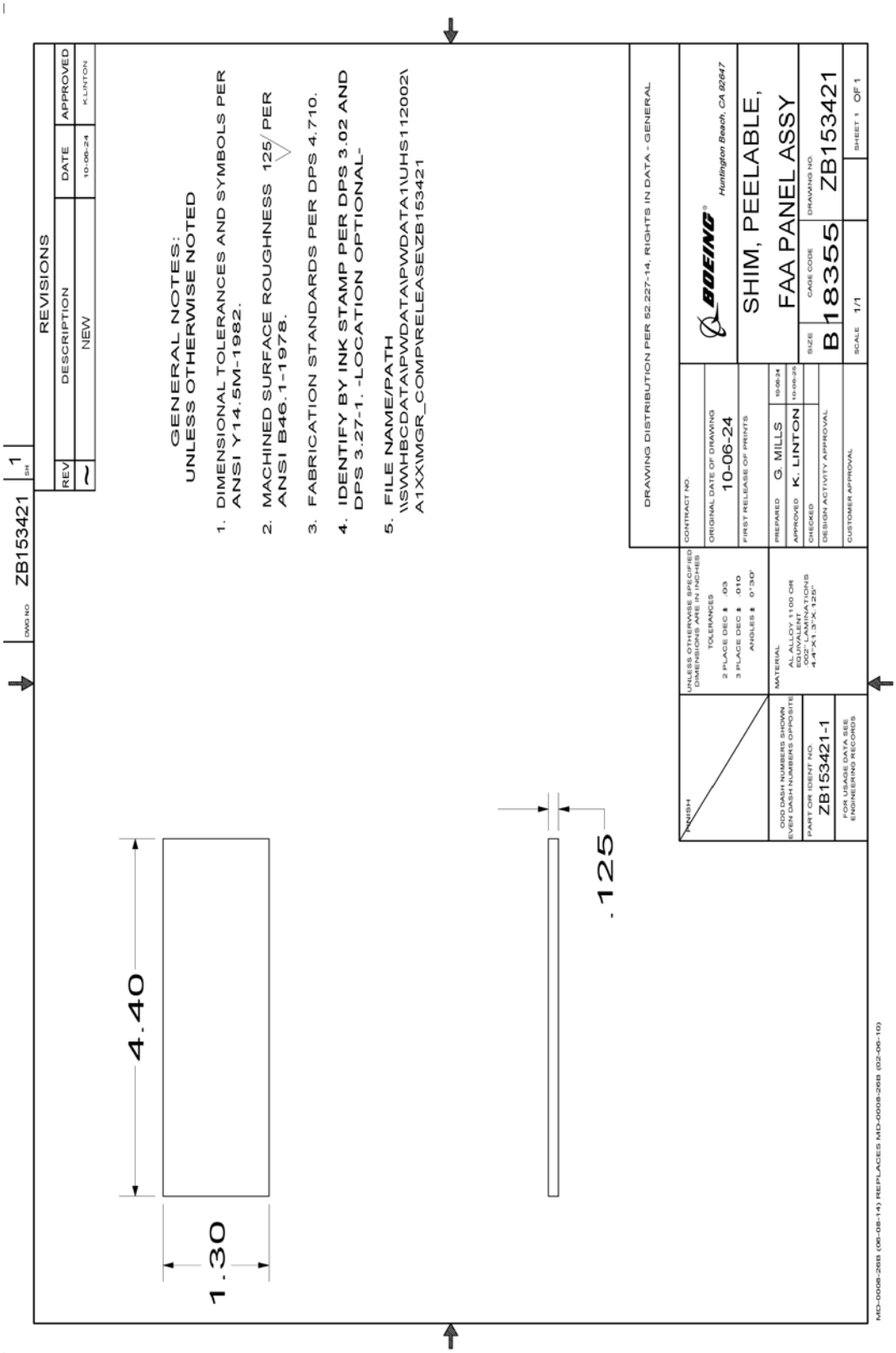

Figure A-59. Peelable Shim

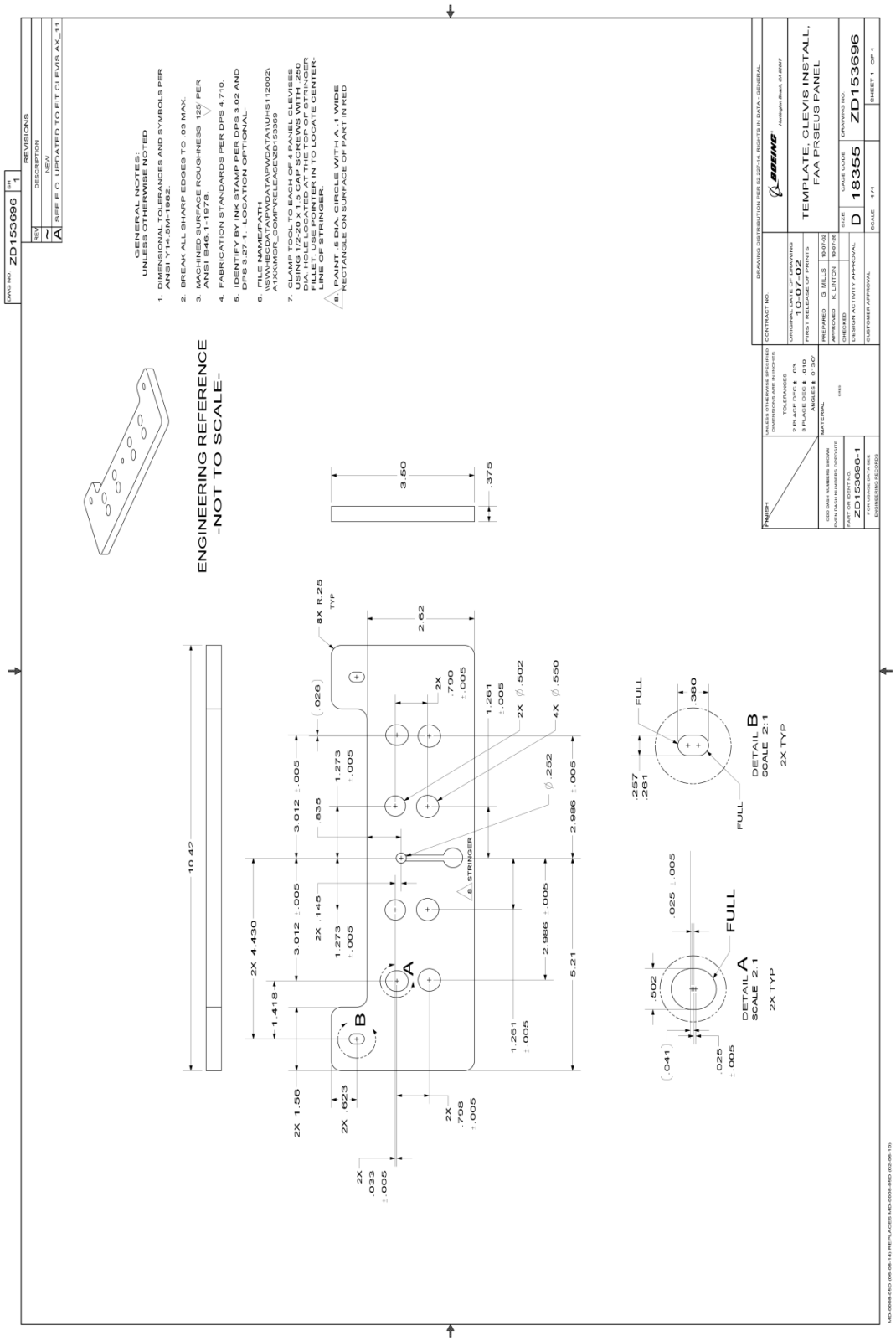

Figure A-60. Clevis Installation Template

APPENDIX B—LOCATIONS OF STRAIN GAGES AND LINEAR VARIABLE DIFFERENTIAL TRANSFORMERS

The locations of strain gages and linear variable differential transformers (LVDTs) are provided in this appendix. The strain gages and cables were installed by the National Aeronautics and Space Administration–Langley Research Center prior to shipping the panel to the Federal Aviation Administration William J. Hughes Technical Center.

Strain gages were placed on the fuselage panel skin, stiffener flanges, and stiffener caps to monitor the strain distribution and ensure proper load introduction. The type and location of the strain gages used are provided in the tables and figures of this appendix. All strain gages were 350 ohms with a Constantan® foil alloy and maximum strain limit of 3% strain. A three conductor, Teflon®-coated cable was used for connection to the strain gages.

Strain gages were numbered 1 through 80: Gages 1 through 25 were mounted on the exterior side of the panel and gages 26 through 80 were mounted on the interior side of the panel. Details of the global locations of exterior and interior strain gages are summarized in figures B-1 and B-2, and table B-1. Gage positions were given a two-letter location code, which indicated the location of the gage to nearby stiffeners, as shown in figures B-3 and B-4. Seventy seven gages were mounted in the axial direction, 19 were mounted in the hoop direction, and 4 were mounted in the 45°-direction. The interior gages were exposed to water (used as a pressurization medium in the Full-Scale Aircraft Structural Test, Evaluation, and Research [FASTER] fixture). To avoid ingression of water, these gages were covered with a piece of Teflon tape and sealed using 1422 B-1/2 sealant. The strain gage, coating, cable, and adhesive types are listed in table B-2. Two gage sizes were used: Twenty-six smaller gages were used on the rounded stiffener caps (location codes ‘SR’ and ‘FC’) while the larger gages were used in all other locations.

The LVDTs were placed on the exterior of the panel and numbered 1 through 11. The LVDTs numbered 1 through 5 measured axial displacements while the LVDTs numbered 6 through 11 measured radial displacements. Details of the LVDT locations are summarized in figure B-1 and table B-3. All LVDTs, except LVDT 1, were mounted rigidly to the test fixture, such as LVDTs in figure B-18. The LVDT 1 was mounted using a reference bracket (engineering drawings summarized in table B-4 and shown on the following six pages in figures B-5 through B-16) so that it measured the overall displacement of S-4. Therefore, it is denoted with two markers in figure B-1, indicating that displacement was measured between the two points in the figure. The LVDT 2 was positioned to measure displacement at the same point as LVDT 1, but mounted to measure rigid displacement so that rigid body motion could be calculated, as shown in figure B-17. All measurements were made with RPD Group transducers that had a full-scale range of one inch (part no: LDC500A), except LVDT 1 during phase III only, which had a full-scale range of two inches (part no: LDC1000A). The LVDTs were calibrated using gage blocks prior to each load application.

Data acquisition was performed using the built-in VXI system in the FASTER lab for 64 strain gages and 6 LVDTs. A supplementary portable data-acquisition system, HBM MCGplus, was used for the remaining 16 strain gages and 5 LVDTs because the VXI system did not have sufficient available channels for the number of strain gages and LVDTs required. The HBM

system was set to acquire data at the test plan-required data acquisition rate of 10 Hz, whereas the VXI system had a preconfigure data-acquisition rate of 143 Hz. Axial loads from transducer AD7-4, as well as pressure signals, were also logged by the HBM system for synchronization between the two systems. The data-acquisition system (VXI or HBM) used for each strain gage and LVDT is provided in tables B-1 and B-3, respectively. The rationale for the choice of which strain gages were connected to which data acquisition system was based on real-time display capabilities for monitoring during loading. The HBM system display showed all instrumentation with data-plotted verse load while the VXI system showed a subset of the instrumentation with data-plotted verse time. Therefore, strain gages in the expected damage propagation region were mostly logged with the HBM system. The LVDTs were grouped by direction of displacement measured: axial LVDT data were logged by the HBM system and radial LVDT data were logged by the VXI system.

Axial LVDTs were mounted using magnetic bases and 3/8″ diameter stainless steel rods connected with swivel joints. Direct access to the panel edge was not available because of the axial load whiffle trees, so aluminum tabs of approximately 1″ x 2″ were hot glued to the stringer panel edge, creating a reference surface accessible for LVDTs to measure, as shown in figure B-17. Radial LVDTs were mounted using a combination of 3/8″ diameter stainless steel rods, 3/4″ diameter aluminum rods, and 1-inch aluminum t-slotted framing attached to the camera mounting structure, as shown in figure B-17. This setup allowed for moving the LVDTs for panel access required for inspections, impacting, and notch machining and then consistently repositioning the LVDTs afterward. The specified LVDT positions for LVDTs 6, 7, and 8 coincided with strain gages locations, so the LVDT probes were positioned adjacent to the strain gages. Perfectly rigid LVDT mounts were difficult to construct because of the space constraints imposed by the fixture and inspection requirements. However, efforts were made to ensure that the LVDT mounting was as stiff as possible.

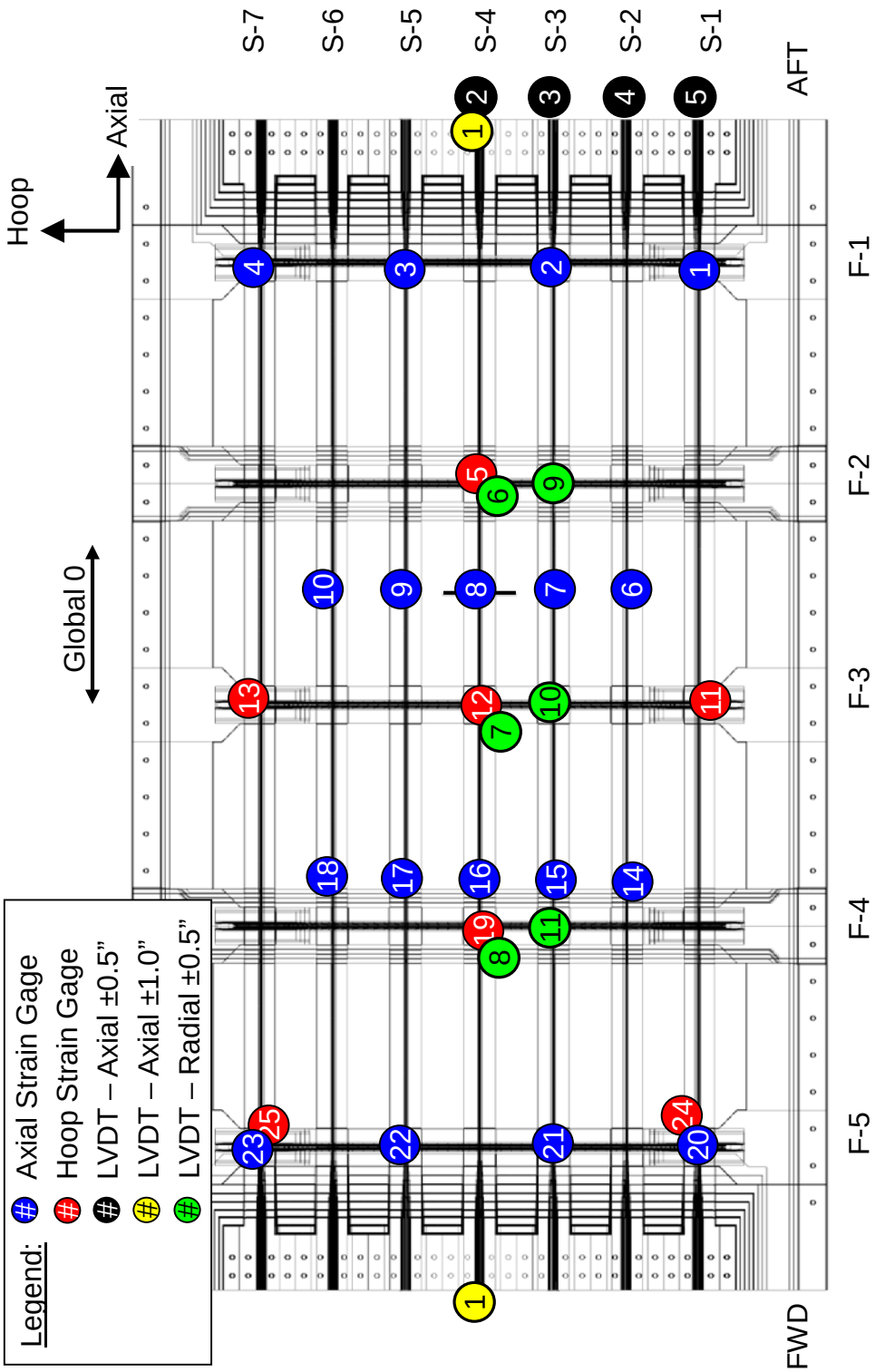

Figure B-1. Exterior Strain Gage and LVDT Map

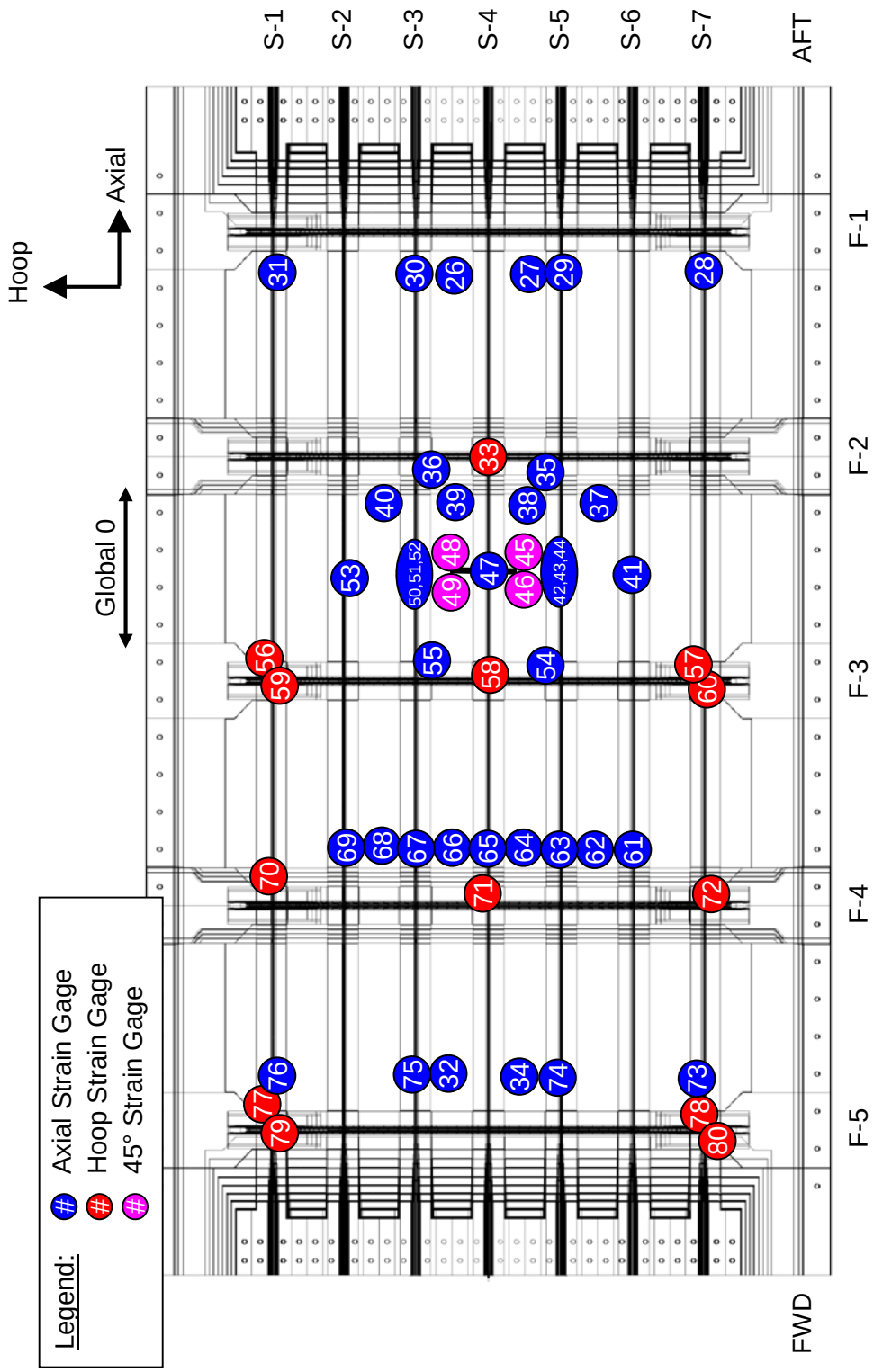

Figure B-2. Interior Strain Gage and LVDT Map

Table B-1. Strain Gage Location Information

Strain Gage No.	Location Code	Axial Position [in.]*	Hoop Position [in.]**	Location description	Orientation	Data Acquisition System
1	AS	18.00	23.41	Exterior skin, intersection of F-1 and S-1	Axial	VXI
2	AS	18.00	7.80	Exterior skin, intersection of F-1 and S-3	Axial	VXI
3	AS	18.00	7.80	Exterior skin, intersection of F-1 and S-5	Axial	VXI
4	AS	18.00	23.41	Exterior skin, intersection of F-1 and S-7	Axial	VXI
5	AS	39.50	0.00	Exterior skin, intersection of F-2 and S-4	Hoop	VXI
6	AS	51.50	15.61	Exterior skin, midway between F-2 and F-3, above S-2	Axial	VXI
7	AS	51.50	7.80	Exterior skin, midway between F-2 and F-3, above S-3	Axial	VXI
8***	AS	51.50	0.00	Exterior skin, midway between F-2 and F-3, above S-4	Axial	VXI
9	AS	51.50	7.80	Exterior skin, midway between F-2 and F-3, above S-5	Axial	VXI
10	AS	51.50	15.61	Exterior skin, midway between F-2 and F-3, above S-6	Axial	VXI
11	AS	63.50	23.41	Exterior skin, intersection of F-3 and S-1	Hoop	VXI
12	AS	63.50	0.00	Exterior skin, intersection of F-3 and S-4	Hoop	VXI
13	AS	63.50	23.41	Exterior skin, intersection of F-3 and S-1	Hoop	VXI
14	AS	83.50	15.61	Exterior skin, adjacent to F-4, above S-2	Axial	VXI
15	AS	83.50	7.80	Exterior skin, adjacent to F-4, above S-3	Axial	VXI
16	AS	83.50	0.00	Exterior skin, adjacent to F-4, above S-4	Axial	VXI
17	AS	83.50	7.80	Exterior skin, adjacent to F-4, above S-5	Axial	VXI
18	AS	83.50	15.61	Exterior skin, adjacent to F-4, above S-6	Axial	VXI
19	AS	87.50	0.00	Exterior skin, intersection of F-4 and S-4	Hoop	VXI
20	AS	109.00	23.41	Exterior skin, intersection of F-5 and S-1	Axial	VXI
21	AS	109.00	7.80	Exterior skin, intersection of F-5 and S-3	Axial	VXI
22	AS	109.00	7.80	Exterior skin, intersection of F-5 and S-5	Axial	VXI

Table B-1. Strain Gage Location Information (Continued)

Strain Gage No.	Location Code	Axial Position [in.]*	Hoop Position [in.]**	Location description	Orientation	Data Acquisition System
23	AS	109.00	23.41	Exterior skin, intersection of F-5 and S-7	Axial	VXI
24	AS	111.50	23.41	Exterior skin, intersection of F-5 and S-1	Hoop	VXI
25	AS	111.50	23.41	Exterior skin, intersection of F-5 and S-7	Hoop	VXI
26	BS	18.00	3.90	Interior skin, near F-1 and midway between S-3 and S-4	Axial	VXI
27	BS	18.00	3.90	Interior skin, near F-1 and midway between S-4 and S-5	Axial	VXI
28	SR	18.00	23.41	Stringer rod cap, near F-1 and on top of S-7	Axial	VXI
29	SR	18.00	7.80	Stringer rod cap, near F-1 and on top of S-5	Axial	VXI
30	SR	18.00	7.80	Stringer rod cap, near F-1 and on top of S-3	Axial	VXI
31	SR	18.00	23.41	Stringer rod cap, near F-1 and on top of S-1	Axial	VXI
32	BS	109.00	3.90	Interior skin, near F-5 and midway between S-3 and S-4	Axial	VXI
33	FC	39.50	0.00	Frame cap, intersection of F-2 and S-4	Hoop	VXI
34	BS	109.00	3.90	Interior skin, near F-5 and midway between S-4 and S-5	Axial	VXI
35	FF	40.00	6.44	Frame flange, intersection of F-2 and S-5, forward-inboard corner	Axial	HBM
36	FF	40.00	6.44	Frame flange, intersection of F-2 and S-3, forward-inboard corner	Axial	HBM
37	BS	44.00	11.70	Interior skin, near F-2 and midway between S-5 and S-6	Axial	HBM
38	BS	44.00	3.90	Interior skin, near F-2 and midway between S-5 and S-6	Axial	HBM
39	BS	44.00	3.90	Interior skin, near F-2 and midway between S-5 and S-6	Axial	HBM
40	BS	44.00	11.70	Interior skin, near F-2 and midway between S-5 and S-6	Axial	HBM
41	SR	51.50	15.61	Stringer rod cap, midway between F-2 and F-3 and on top of S-6	Axial	VXI
42	SF	51.50	9.20	Outboard stringer flange, midway between F-2 and F-3 and on the flange of S-5	Axial	VXI
43	SR	51.50	7.80	Stringer rod cap, midway between F-2 and F-3 and on top of S-5	Axial	VXI

Table B-1. Strain Gage Location Information (Continued)

Strain Gage No.	Location Code	Axial Position [in.]*	Hoop Position [in.]**	Location description	Orientation	Data Acquisition System
44	SF	51.50	6.44	Inboard stringer flange, midway between F-2 and F-3 and on the flange of S-5	Axial	VXI
45	BS	51.00	4.90	Interior skin, between F-2 and F-3 and midway between S-4 and S-5	-45°	HBM
46	BS	52.00	4.90	Interior skin, between F-2 and F-3 and midway between S-4 and S-5	45°	HBM
47***	SR	51.50	0.00	Stringer rod cap, midway between F-2 and F-3 and on top of S-4	Axial	VXI
48	BS	51.00	4.90	Interior skin, between F-2 and F-3 and midway between S-3 and S-4	-45°	HBM
49	BS	52.00	4.90	Interior skin, between F-2 and F-3 and midway between S-3 and S-4	45°	HBM
50	SF	51.50	9.20	Outboard stringer flange, midway between F-2 and F-3 and on the flange of S-3	Axial	VXI
51	SR	51.50	7.80	Stringer rod cap, midway between F-2 and F-3 and on top of S-3	Axial	VXI
52	SF	51.50	6.44	Inboard stringer flange, midway between F-2 and F-3 and on the flange of S-3	Axial	VXI
53	SR	51.50	15.61	Stringer rod cap, midway between F-2 and F-3 and on top of S-2	Axial	VXI
54	FF	63.00	6.44	Frame flange, intersection of F-3 and S-5, aft-inboard corner	Axial	HBM
55	FF	63.00	6.44	Frame flange, intersection of F-3 and S-3, aft-inboard corner	Axial	HBM
56	FF	63.00	24.75	Frame flange, intersection of F-3 and S-1, aft-outboard corner	Hoop	VXI
57	FC	63.50	23.41	Frame cap, intersection of F-3 and S-7	Hoop	VXI
58	FC	63.50	0.00	Frame cap, intersection of F-3 and S-4	Hoop	VXI
59	FC	63.50	23.41	Frame cap, intersection of F-3 and S-1	Hoop	VXI
60	FF	64.00	24.75	Frame flange, intersection of F-3 and S-7, forward-outboard corner	Hoop	VXI
61	SR	83.00	15.61	Stringer rod cap, near F-4 and on top of S-6	Axial	VXI
62	BS	83.00	11.70	Interior skin, near F-4 and midway between S-5 and S-6	Axial	HBM

Table B-1. Strain Gage Location Information (Continued)

Strain Gage No.	Location Code	Axial Position [in.]*	Hoop Position [in.]**	Location description	Orientation	Data Acquisition System
63	SR	83.00	7.80	Stringer rod cap, near F-4 and on top of S-5	Axial	VXI
64	BS	83.00	3.90	Interior skin, near F-4 and midway between S-4 and S-5	Axial	HBM
65	SR	83.00	0.00	Stringer rod cap, near F-4 and on top of S-4	Axial	VXI
66	SR	83.00	3.90	Interior skin, near F-4 and midway between S-3 and S-4	Axial	HBM
67	SR	83.00	7.80	Stringer rod cap, near F-4 and on top of S-3	Axial	VXI
68	BS	83.00	11.70	Interior skin, near F-4 and midway between S-2 and S-3	Axial	HBM
69	SR	83.00	15.61	Stringer rod cap, near F-4 and on top of S-2	Axial	VXI
70	FF	87.00	24.75	Frame flange, intersection of F-4 and S-1, aft-outboard corner	Hoop	VXI
71	FC	87.50	0.00	Frame cap, intersection of F-4 and S-4	Hoop	VXI
72	FF	87.00	24.75	Frame flange, intersection of F-4 and S-7, forward-outboard corner	Hoop	VXI
73	SR	109.00	23.41	Stringer rod cap, near F-5 and on top of S-7	Axial	VXI
74	SR	109.00	7.80	Stringer rod cap, near F-5 and on top of S-5	Axial	VXI
75	SR	109.00	7.80	Stringer rod cap, near F-5 and on top of S-3	Axial	VXI
76	SR	109.00	23.41	Stringer rod cap, near F-5 and on top of S-1	Axial	VXI
77	FF	111.00	24.75	Frame flange, intersection of F-5 and S-1, aft-outboard corner	Hoop	VXI
78	FC	111.50	23.41	Frame cap, intersection of F-5 and S-7	Hoop	VXI
79	FC	111.50	23.41	Frame cap, intersection of F-5 and S-1	Hoop	VXI
80	FF	112.00	24.75	Frame flange, intersection of F-5 and S-7, forward-outboard corner	Hoop	VXI

*Measured from aft end
**Measured from centerline
***Removed for Phase III tests due to interference with notch location

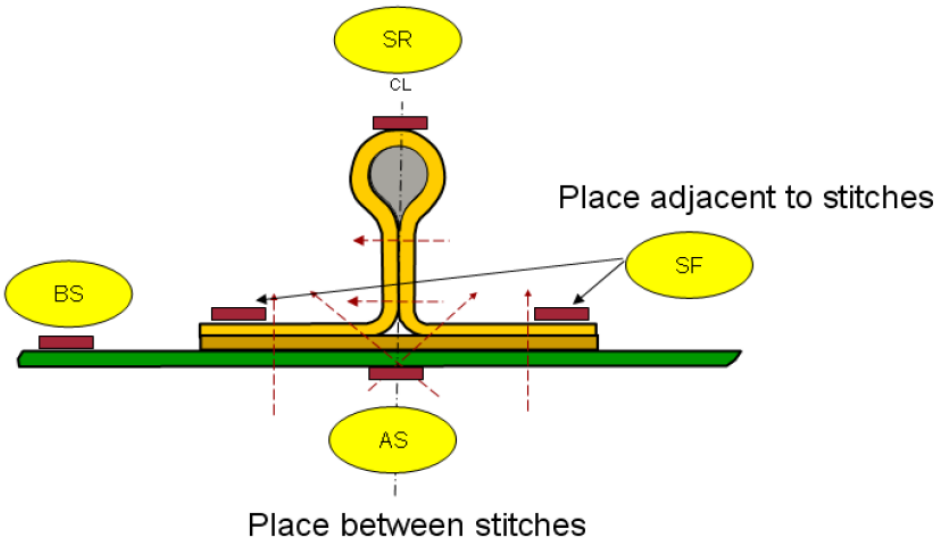

Figure B-3. Location Codes for Strain Gages Near Stringers

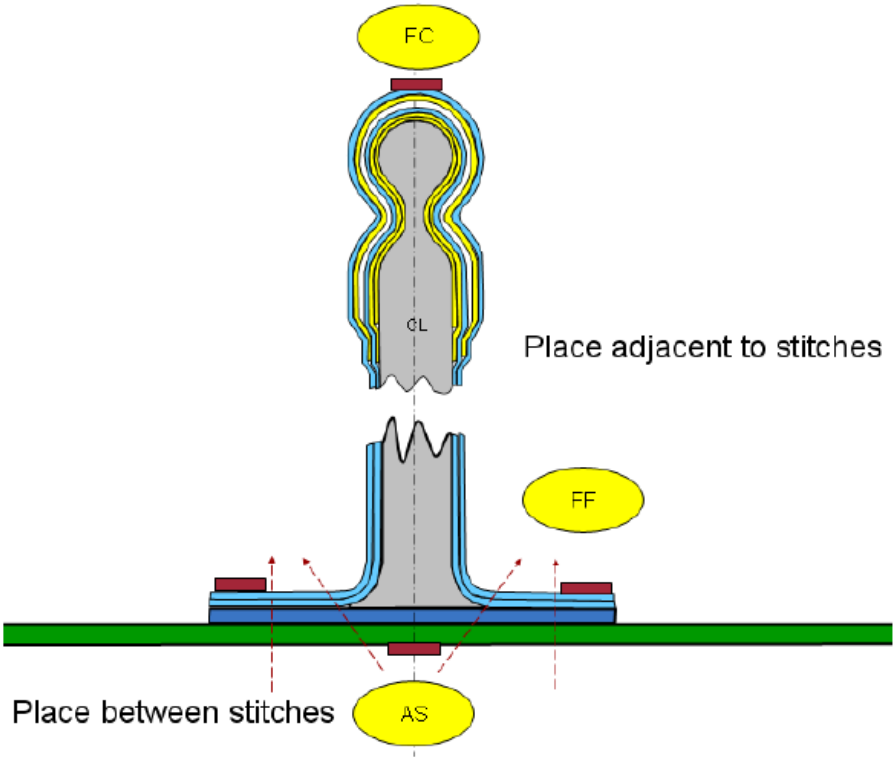

Figure B-4. Location Codes for Strain Gages Near Frames

Table B-2. General Strain Gage Information

Item	Vishay Micro Measurement Part No.
Large gages	CEA-00-250UW-350
Small gages	EA-00-125AC-350
Coating	M-Coat D
Cable	330-FFE
Adhesive	EPY-150

Table B-3. LVDT Location Information

LVDT No.	Axial Position [in.]*	Hoop Position [in.]**	Location description	Orientation	Data Acquisition System
1	0.00	0.00	Aft axial end, at termination of S-4	Axial	HBM
2	0.00	0.00	Aft axial end, at termination of S-4	Axial	HBM
3	0.00	7.81	Aft axial end, at termination of S-3	Axial	HBM
4	0.00	15.62	Aft axial end, at termination of S-2	Axial	HBM
5	0.00	23.42	Aft axial end, at termination of S-1	Axial	HBM
6	39.50	0.00	Intersection of F-2 and S-4	Radial	VXI
7	63.50	0.00	Intersection of F-3 and S-4	Radial	VXI
8	87.50	0.00	Intersection of F-4 and S-4	Radial	VXI
9	39.50	7.80	Intersection of F-2 and S-3	Radial	VXI
10	63.50	7.80	Intersection of F-3 and S-3	Radial	VXI
11	87.50	7.80	Intersection of F-4 and S-3	Radial	VXI

*Measured from aft end
**Measured from centerline

Table B-4. LVDT-1 Bracket Drawing List

Drawing Title	Quantity
LVDT Mount Assembly	1
LVDT Mount Detail (subassembly)	1
LVDT Hoop Strap	2
Lateral Guide LVDT End	1
LVDT Foot Hook	1
LVDT Mounting Angle	1

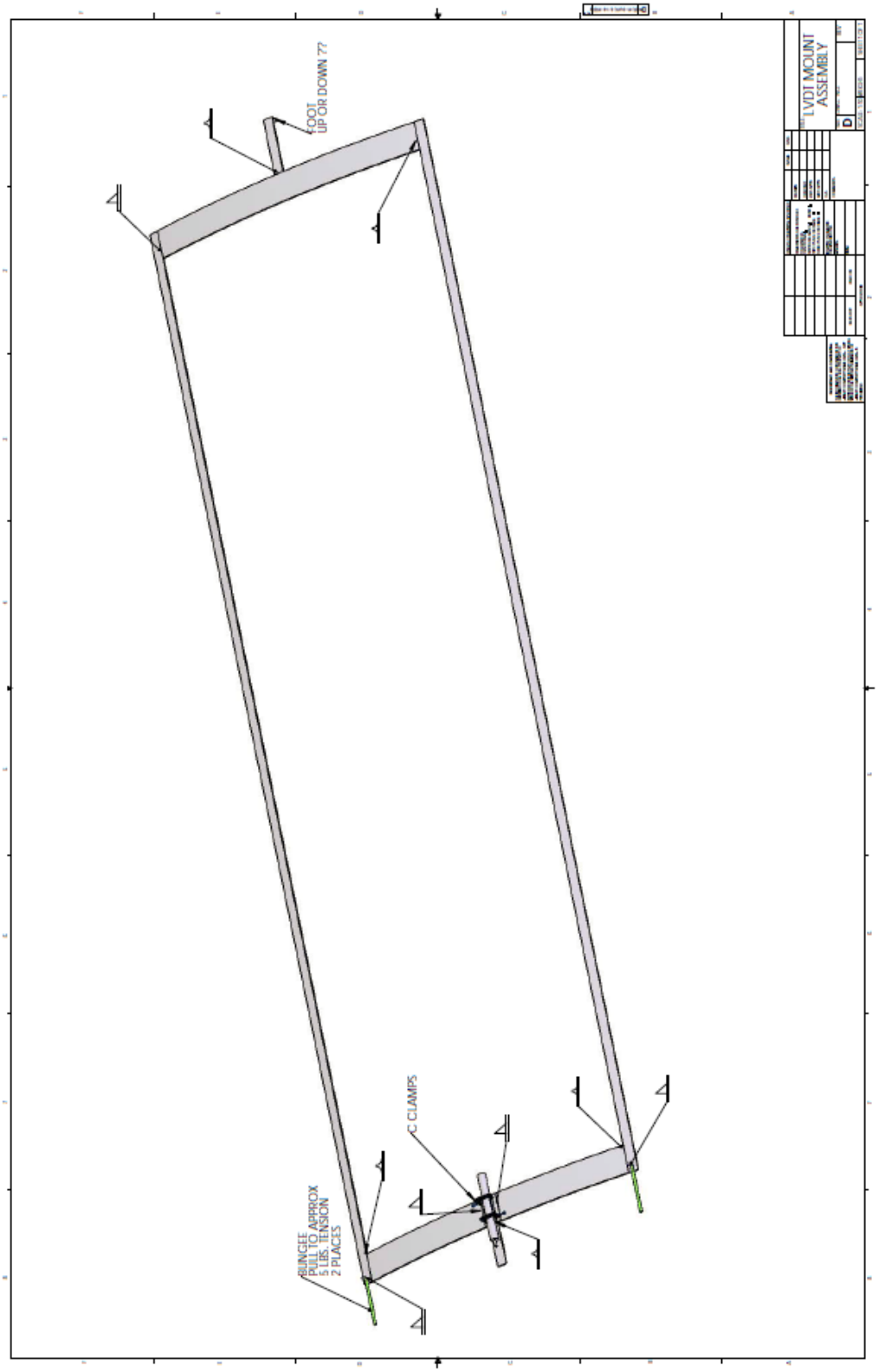

Figure B-5. The LVDT Mount Assembly

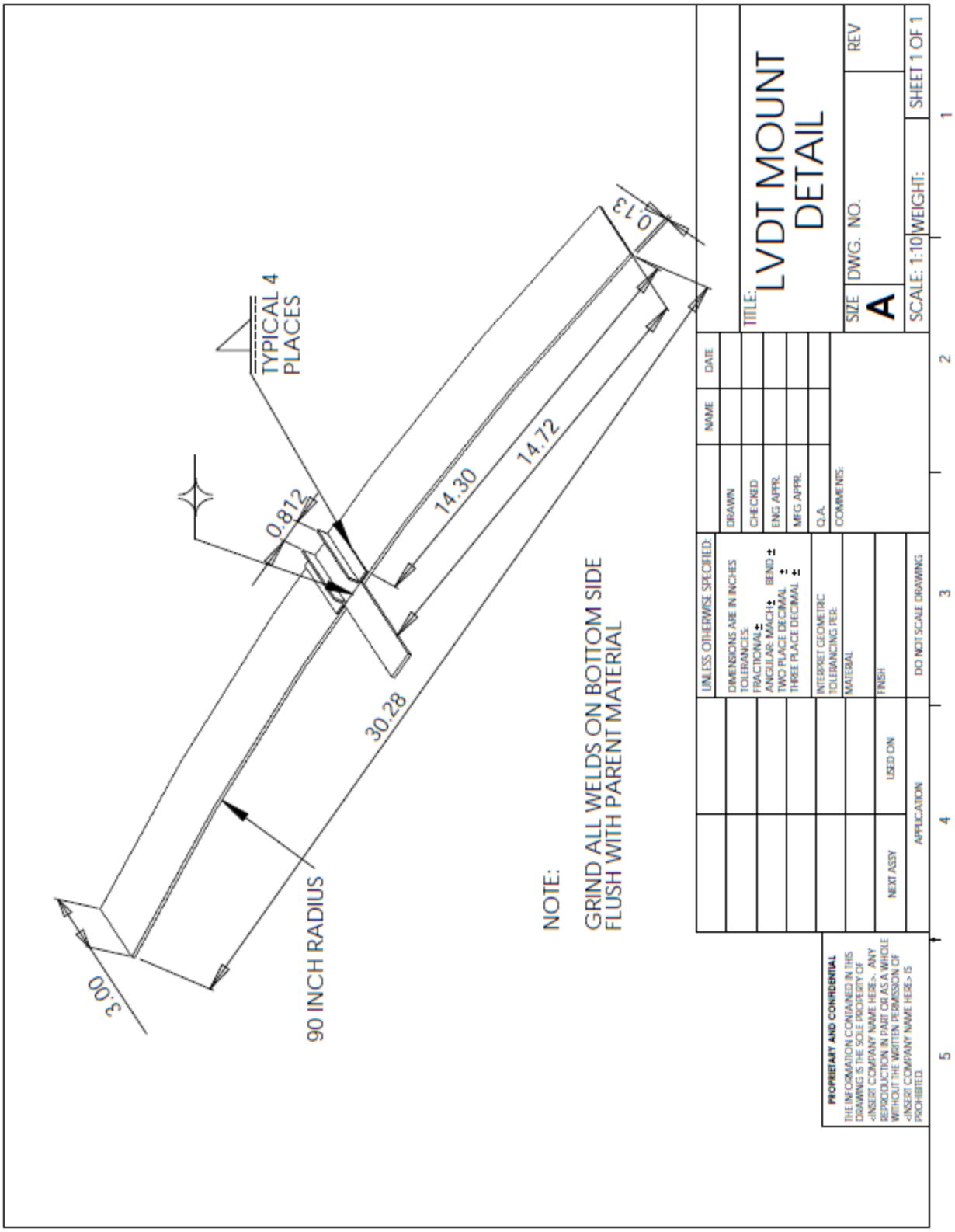

Figure B-6. The LVDT Mount Detail (subassembly)

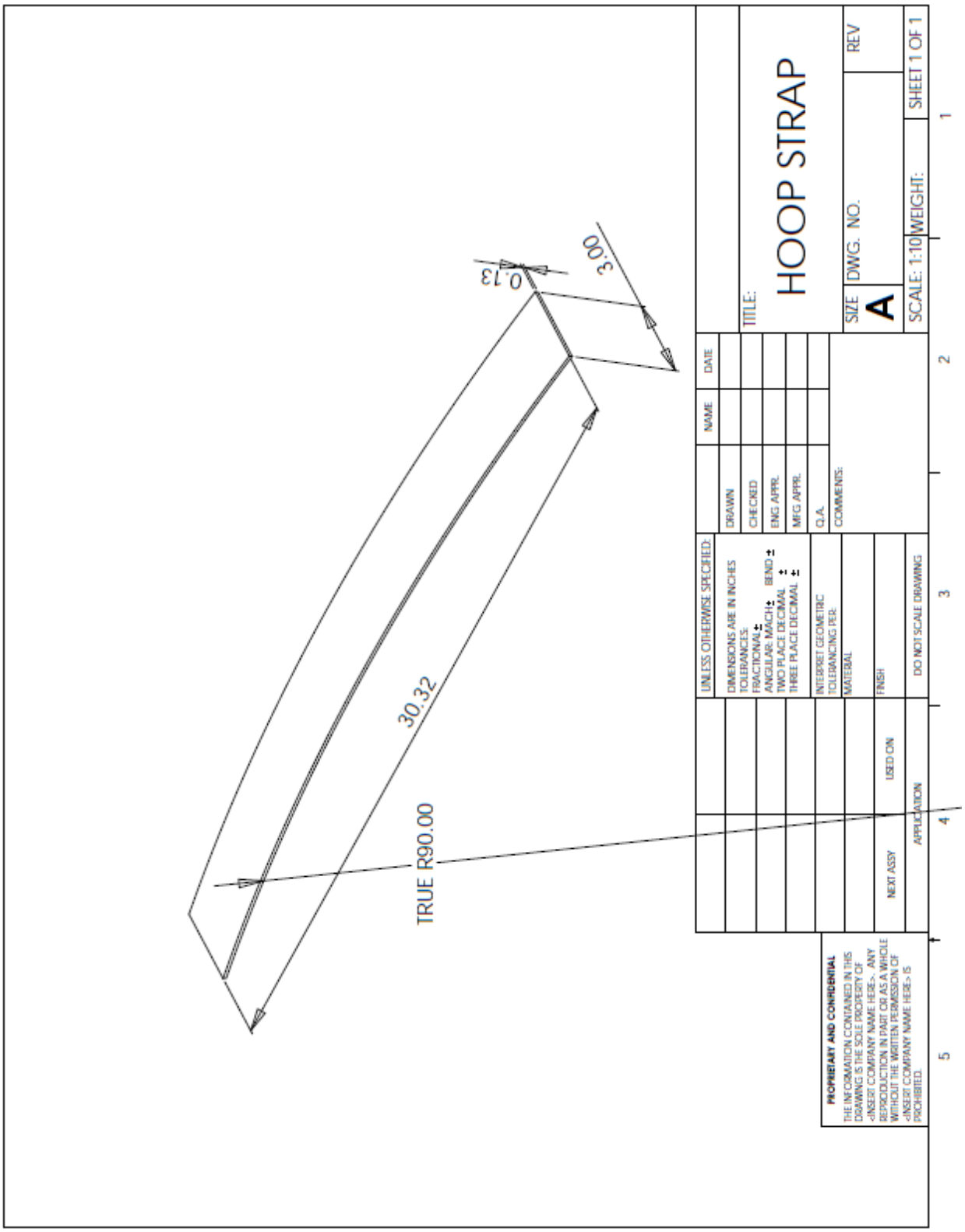

Figure B-7. The LVDT Hoop Strap

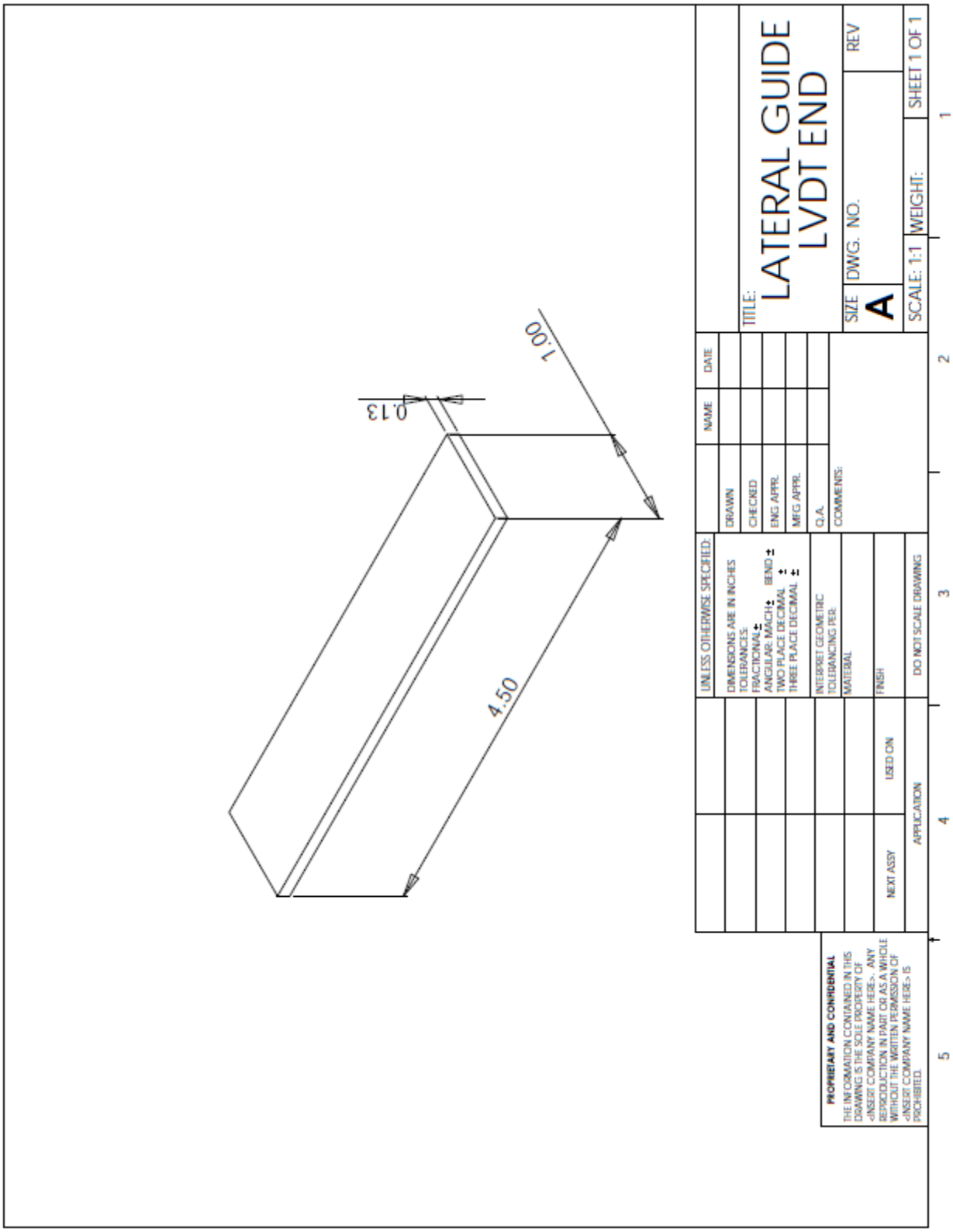

Figure B-8. Lateral Guide, LVDT End

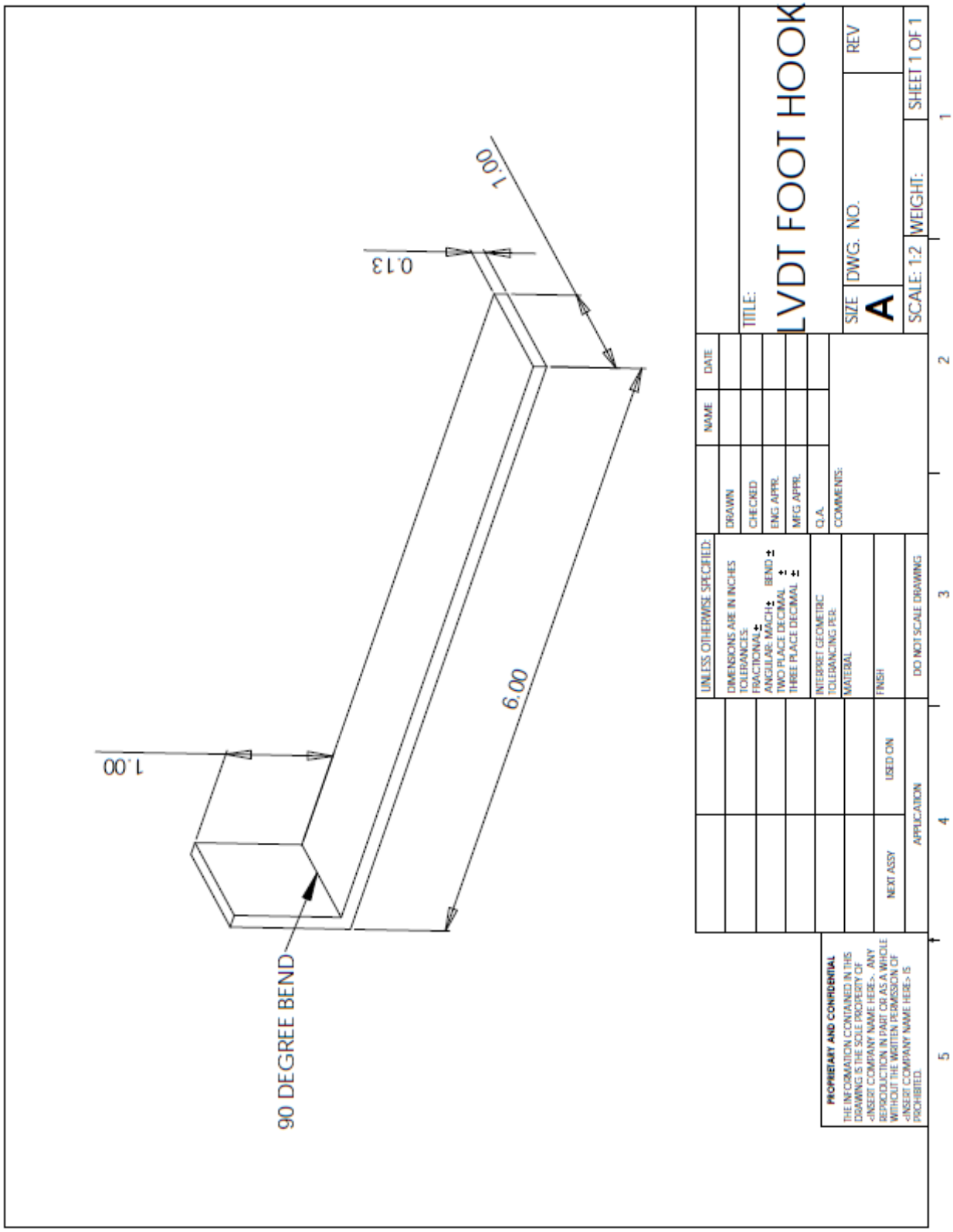

Figure B-9. The LVDT Foot Hook

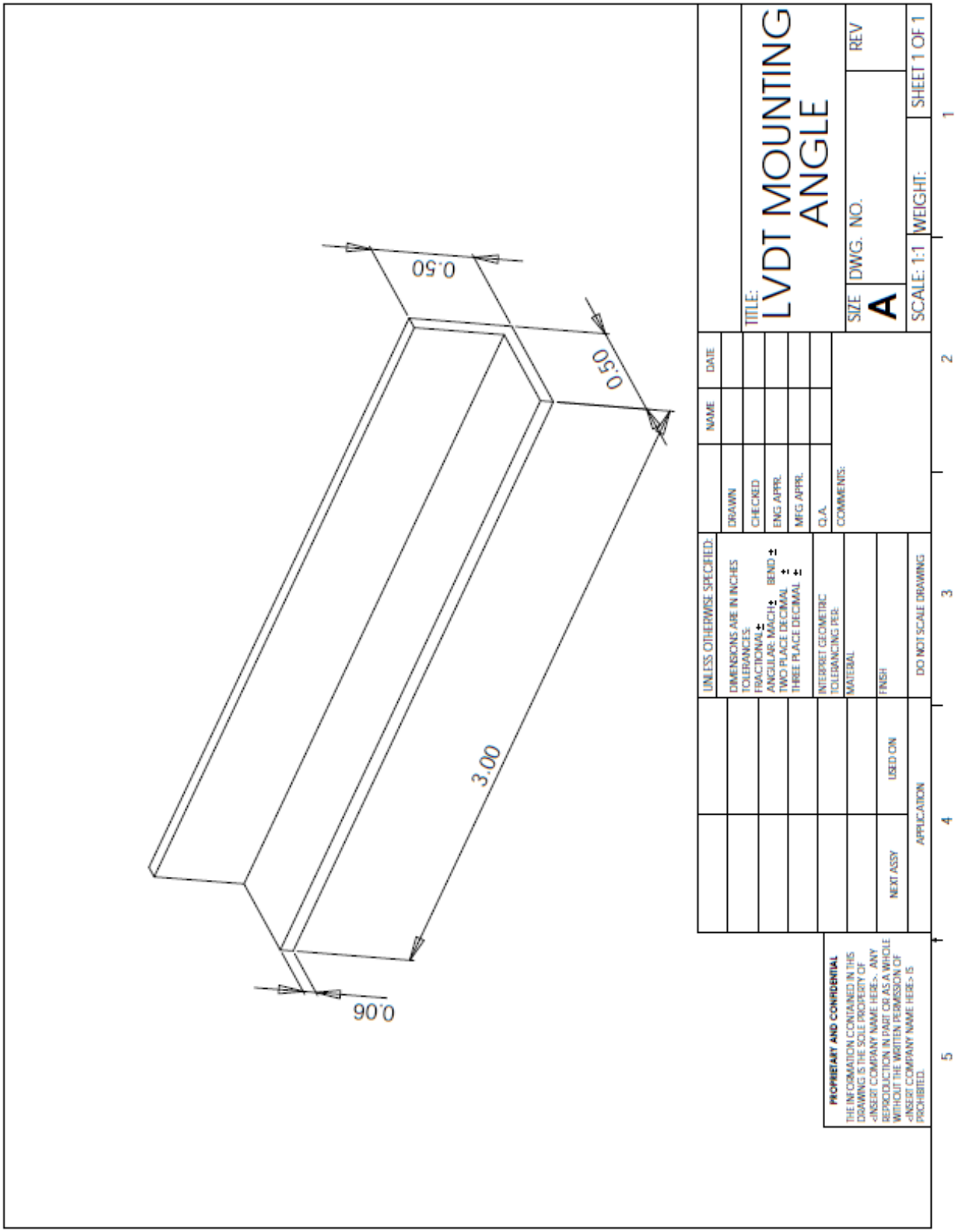

Figure B-10. The LVDT Mounting Angle

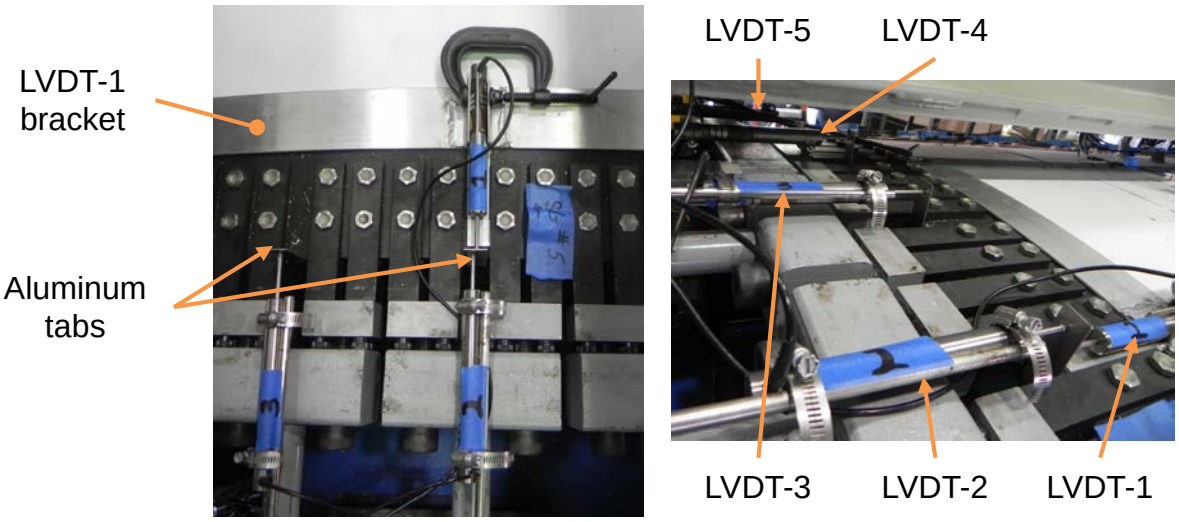

Figure B-17. Axial LVDT Mounting Configuration

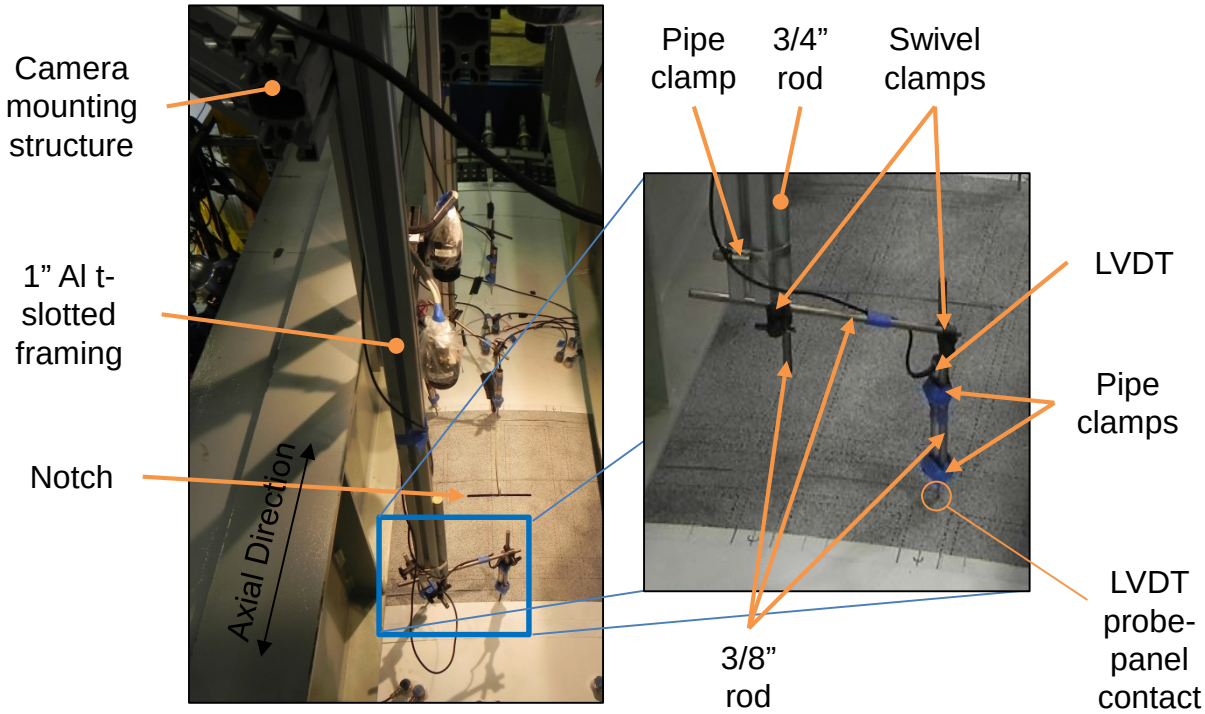

Figure B-18. Radial LVDT Mounting Configuration

APPENDIX C—DIGITAL IMAGE CORRELATION AND VISUAL MONITORING SETUP

Several cameras were used to visually monitor damage formation and progression during the test and for digital image correlation (DIC). The cameras used are listed in table C-1. With the exception of high-speed cameras, all cameras were set to record continuously during the test and live views of each camera were displayed on monitors in the control room. The high-speed cameras were manually triggered at the event of interest using a 50% buffer so that half of the total duration that could be stored was taken before the trigger and the remaining half was after the trigger. A frame rate of 5,000 frames per second was selected for the high-speed cameras because it represented the best compromise in film duration, resolution, frame rate, and light requirements. The three high-definition cameras were load stamped by recording the test computer screen into a synchronized recording deck. Manual synchronization of the interior camera with the exterior cameras was performed post-test.

Table C-1. Summary of Visual Monitoring Cameras

Description	Location	Model	Qty
High-definition exterior video camera	Exterior global fixture and test section	Sony XDCAM EX HD, model PMW-EX1	3
High-speed video camera	Exterior test section	Olympus i3	2
High-resolution still camera	Exterior test section	Canon EOS Rebel T2i	1
High-definition interior video camera	Interior variable via crawler system	N/A (custom)	1

The high-resolution still camera was triggered manually from the control room and the load level at which the camera was triggered was noted. This camera was relatively inexpensive compared to the other cameras used and, therefore, was placed much closer to the test section in a more exposed environment with greater risk for damage to the camera (though no damage actually occurred). The high resolution combined with the much closer placement of the still camera produced very clear, useful photos of the damage progression. The remote trigger functionality was achieved using the Canon EOS software, which allows for USB-based control of the camera via Microsoft Windows® software. Most functionality was available through the software except zoom, which was set before the test began.

Figure C-1 shows a map of the locations where the cameras were mounted. The high-speed and exterior high-definition video cameras were mounted on the forward and aft walls of the test cell, far enough from the fixture that it was unlikely they would be damaged during catastrophic failure of the panel. Figure C-2 shows a map of the camera fields of view: two of the high-definition exterior cameras were used for surveillance and one was used in the test section. The other cameras were set up for the test section, except as noted.

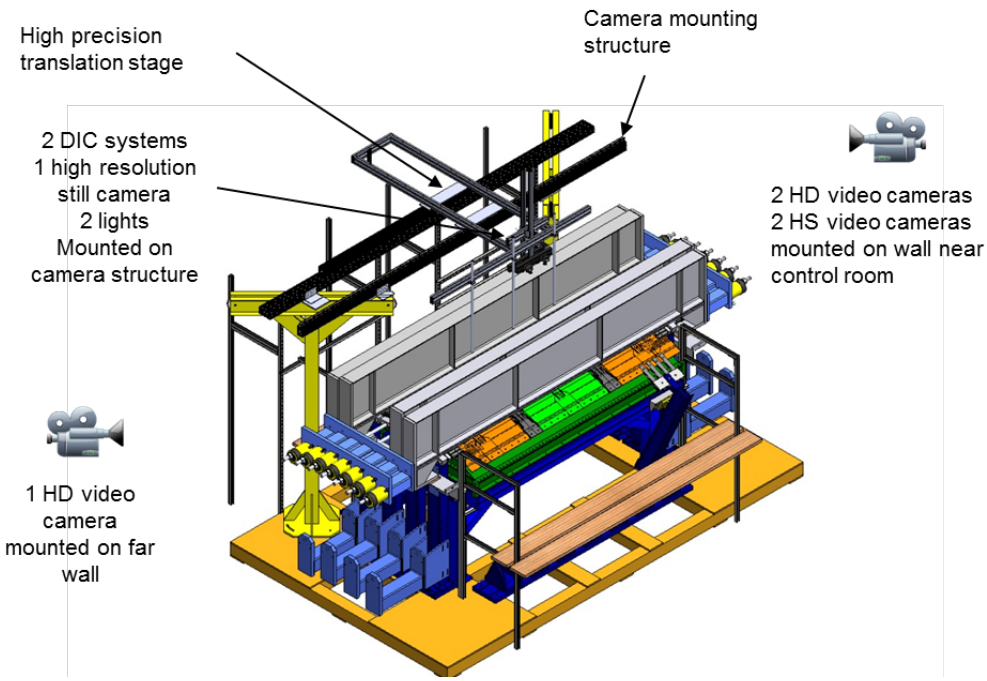

Figure C-1. Map of Camera Mounting Locations

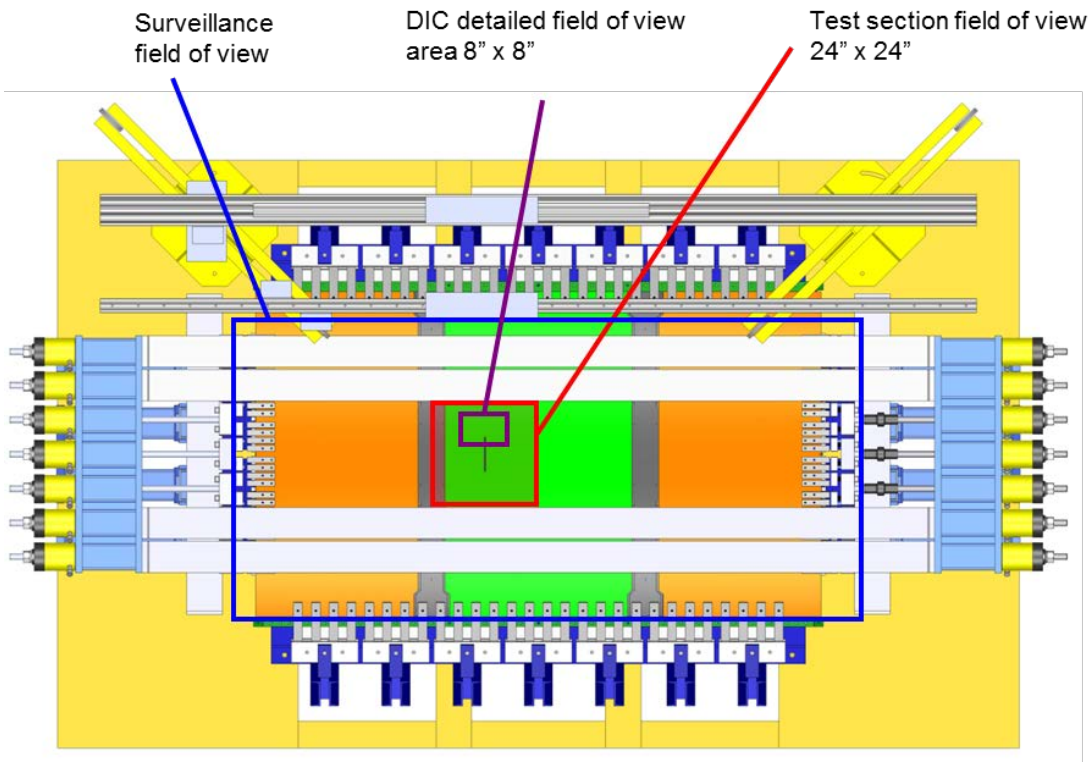

Figure C-2. Map of Camera Fields of View

A modification to the remote-controlled crack monitoring (RCCM) system was designed and built to meet the following requirements:

- Mounting of various cameras, including DIC cameras; lights; and LVDTs above the panel
- Increased working distance for DIC system to accommodate large field of view
- Translating the entire assembly fully out of the test section to accommodate the impactor
- Relocating the slave axial slide of the RCCM so that the impactor did not need to be hoisted above the RCCM; this was not possible due to height limitations of the test bay

The modified RCCM is shown in figure C-3. The motor and control systems were retained unmodified; only the structure was altered. T-slot framing from McMaster-Carr (size: 45 mm) was used to construct the modified structure. Gusseting was used to ensure rigidity of the structure, which was required for mounting the LVDTs. The DIC mount was designed to slide vertically to aid in DIC calibration, which was performed above the axial loading fixture because of the calibration panel clearance.

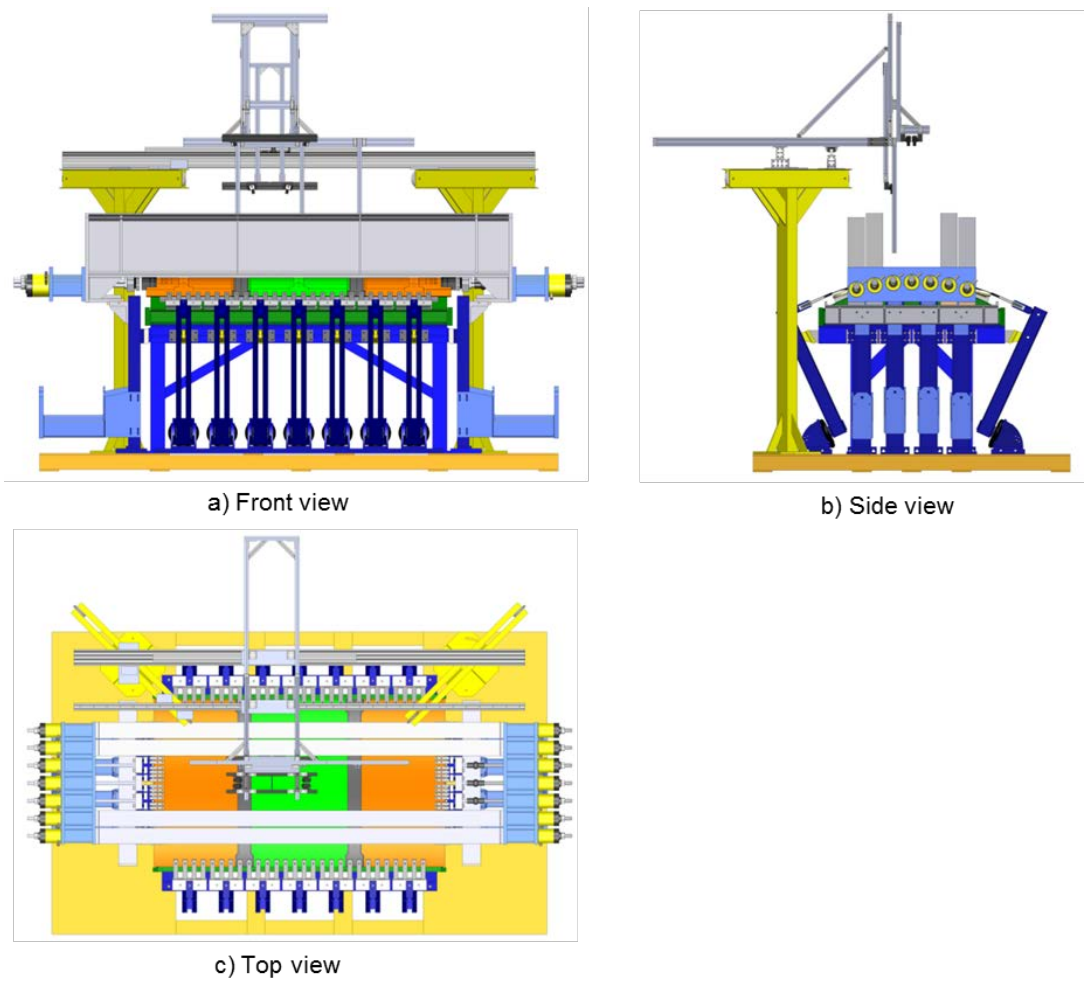

Figure C-3. Camera Mounting Structure

APPENDIX D—NOTCH MACHINING

For phase III, an 8-in. notch was machined into the panel, severing S-4 and the adjacent skin. The notch was machined with a 5/16 inch-diameter carbide router bit as shown in figure D-1. A template was used to assist in properly aligning and positioning the notch, as shown in figure D-2. During machining, the template was held in place with weights. First, a through hole was drilled as a starting point for machining the notch. The notch was then cut, as shown in figure D-3. Because the cutting tool was not long enough to sever the stringer completely in one pass, a secondary cut was performed from the interior of the panel to completely sever the stringer. Before and after photos of the region where the notch was machined are shown in figure D-4.

The machining process produced a clean edged notch with minor breakout observed in one area, shown circled in red in figure D-4(b) and in detail in figure D-5. The area was inspected using flash thermography before and after notch machining and no indication of internal damage due to the machining process was observed, as shown in figure D-6.

After machining, the notch was measured to be 7.85 inches long and 0.31 inches wide.

Figure D-1. Cutting Tool Used to Machine the Notch

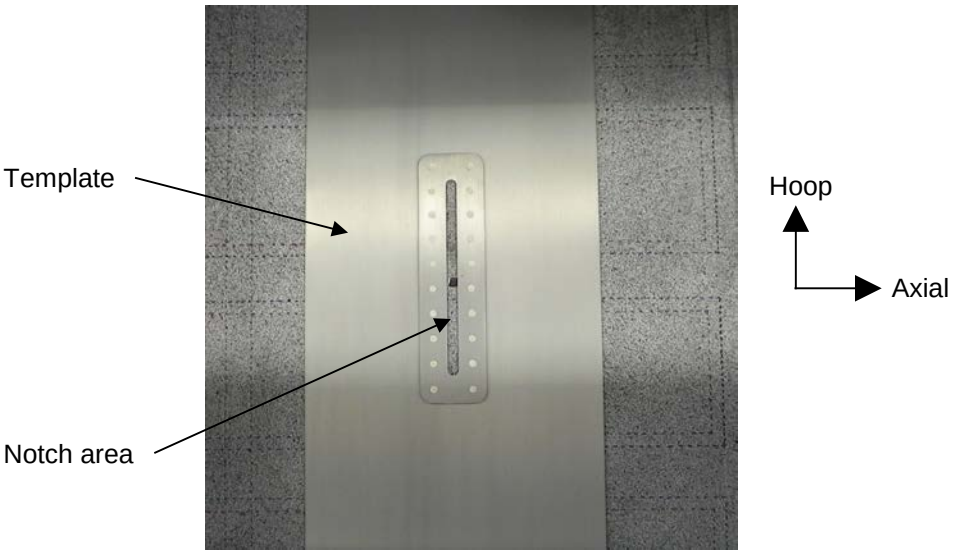

Figure D-2. Notch Machining Template

(a) (b)

Figure D-3. Notch Machining Process: (a) Drilling Start Hole and (b) Machining Notch

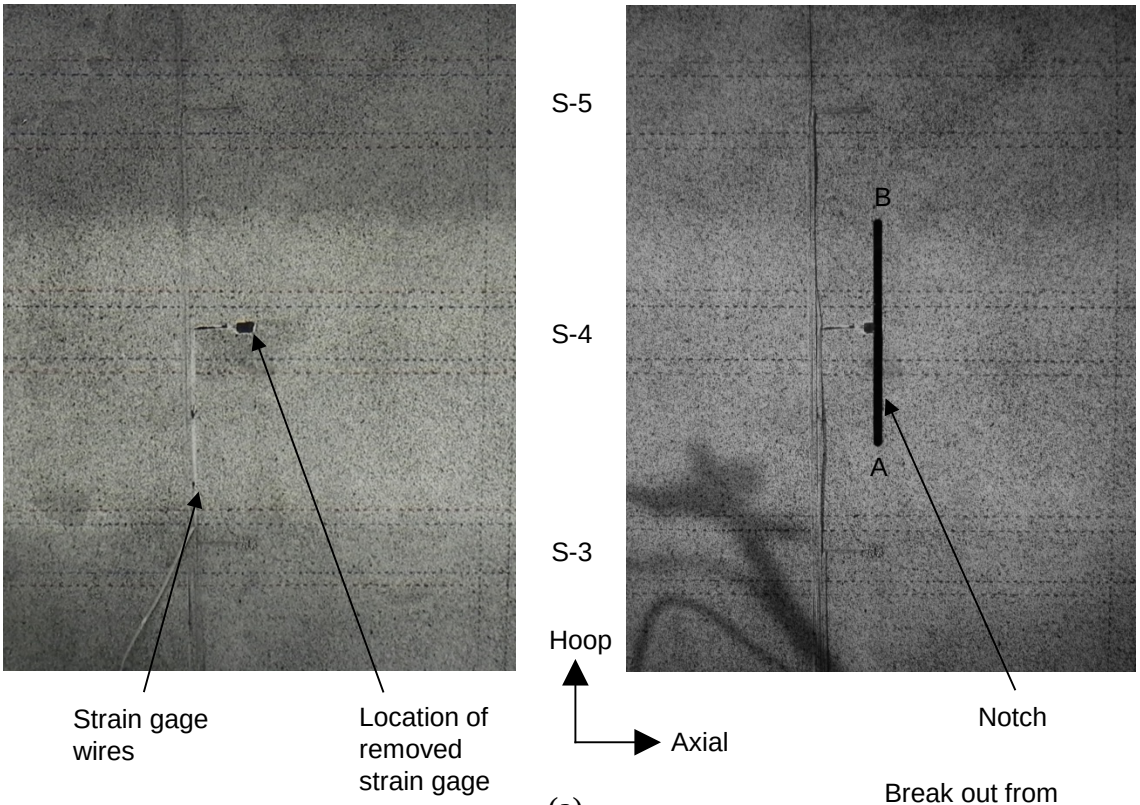

(a)

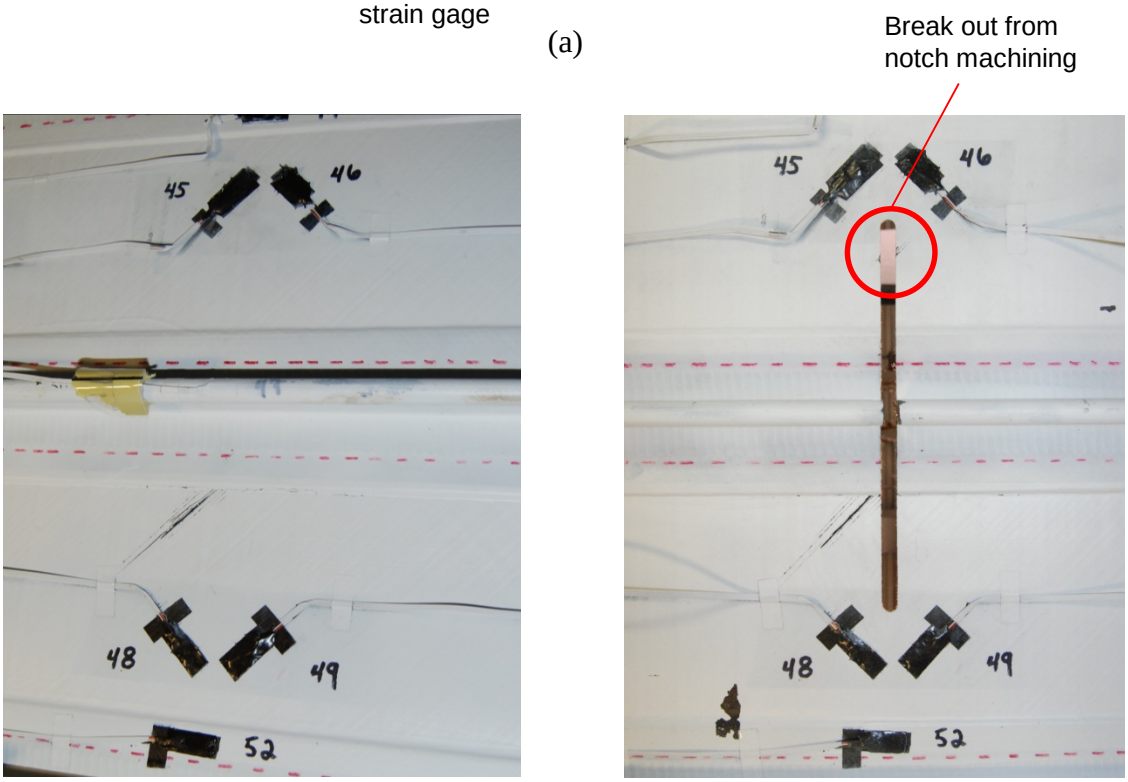

(b)

Figure D-4. Before and After Photos of the Notched Region: (a) Exterior Photos and (b) Interior Photos

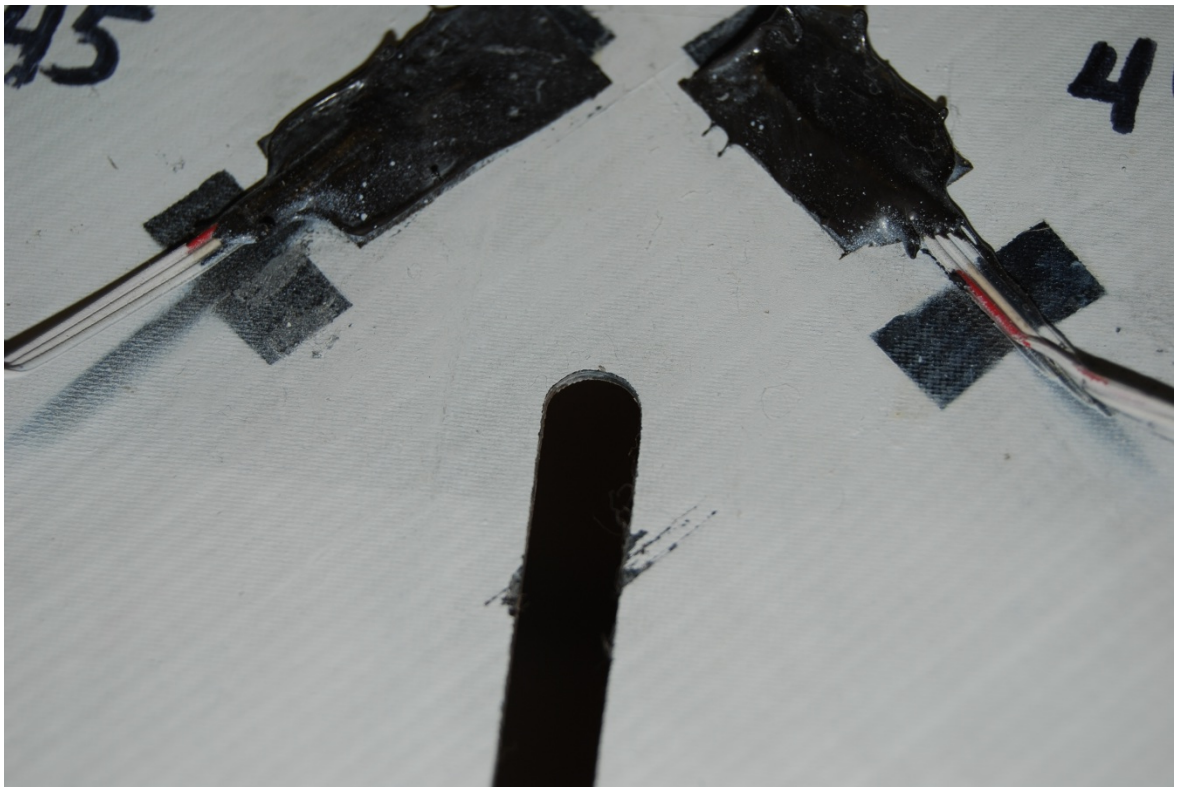

Figure D-5. Detailed View of Break Out That Occurred During Notch Machining

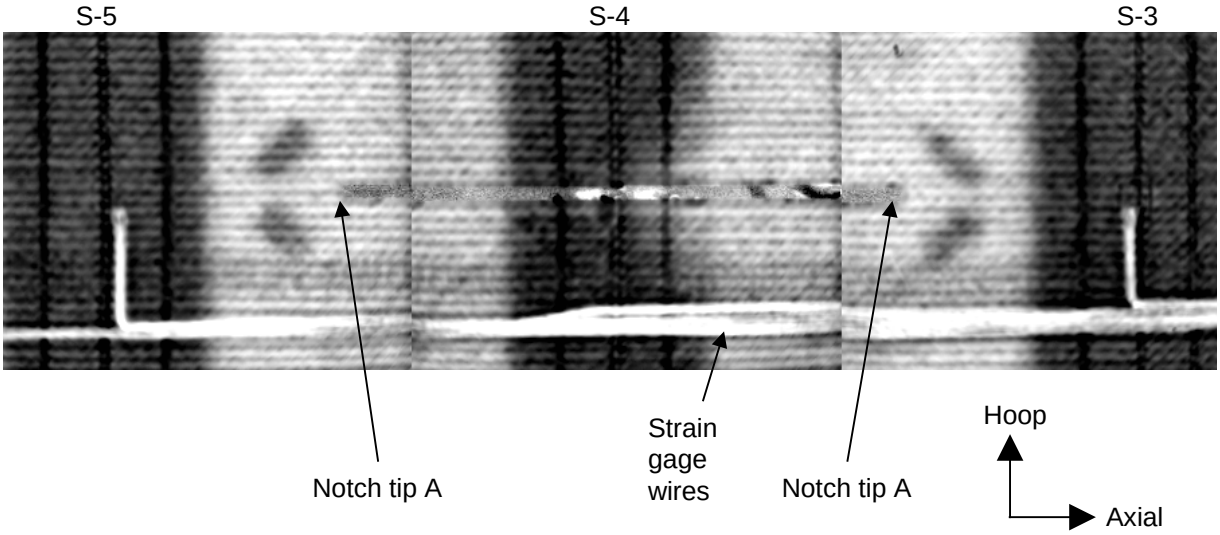

Figure D-6. Flash Thermography Results After Notch Machining (1D, t=1.2s)

APPENDIX E—LOADER, STRAIN, AND DISPLACEMENT DATA

E.1 LOADER, STRAIN, AND DISPLACEMENT DATA.

A load history of the panel is provided in table E-1. The maximum applied loads for axial, hoop, frame, and pressure are provided on a per-loader basis. Additional checkout tests were performed at low load levels and are not listed in table E-1.

Table E-1. Test Load History With Loads Specified for a Single Actuator

	Load Condition	Maximum Applied Loads			
		Axial [lbf]	Hoop [lbf]	Frame [lbf]	Pressure [psi]
Phase I	Axial	32,473	0	0	0
	Combined	36,436	11,423	2,390	9.2
	Pressure	5,270	15,192	3,178	12.2
Phase II	Limit Axial	32,473	0	0	0
	Limit Pressure	5,270	15,192	3,178	12.2
	Limit Combined	36,436	11,423	2,390	9.2
	Ultimate Pressure	7,925	22,844	4,780	18.4
	Ultimate Axial	48,710	0	0	0
	Ultimate Combined	54,654	17,134	3,584	13.8
Phase III	Final	67,000	13,136	2,748	10.6

The load cells, strain gages, and linear variable differential transformers (LVDTs) were used to acquire data at 10 Hz throughout each loading; this data are provided in this appendix. The location of each gage is available in appendix A. The strain and LVDT data were reduced by zeroing at point immediately before the first non-zero load command was sent.

The load data are provided for each actuator and reported in foot-pound force (lbf) for all but pressure, which is reported in pounds per square inch (psi). Each actuator is numbered in figure E-1. The tabulated load data that follows reference these numbers. The frame loaders are also denoted with an “R” or “H,” indicating radial or hoop directions, respectively. Insufficient data acquisition channels were available to measure load in both hoop and radial directions at every frame end.

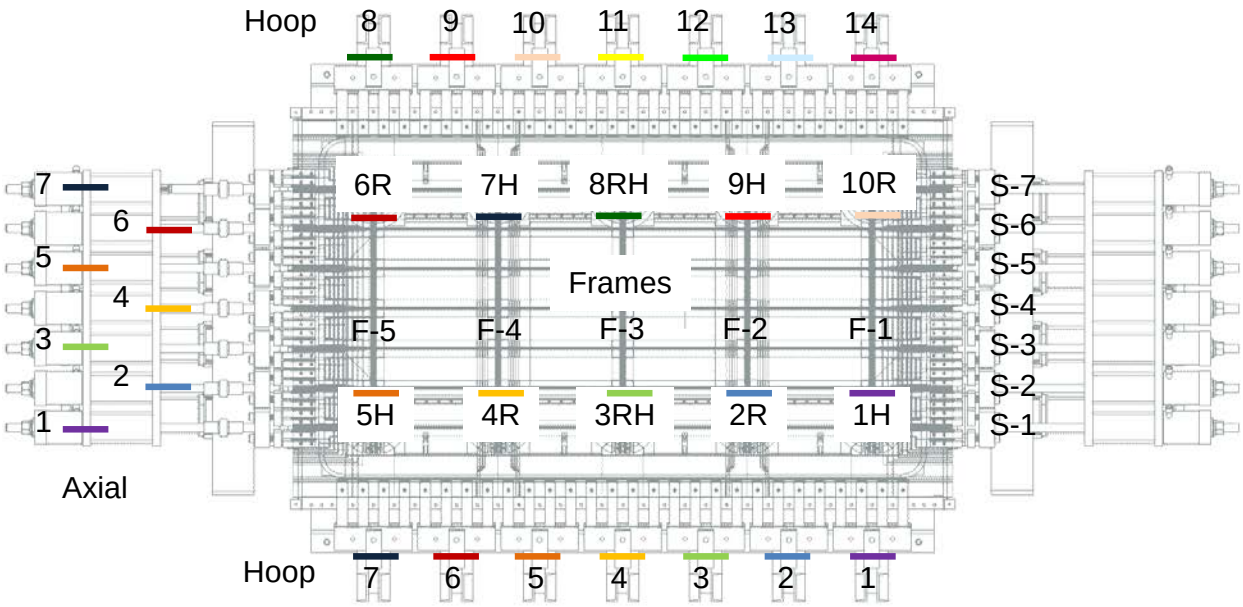

Figure E-1. Location and Numbering of Load Actuators

The data are provided in tabulated form for 10% load increments for each load case (see tables E-2 through E-28). Because of the voluminous amount of data, data reduction was automated with a MATLAB script. Complications in the data reduction scheme arose from data acquisition by two independent systems: HBM and VXI [19]. The general data reduction procedure is summarized into the following steps:

1. Read data from HBM and VXI files
2. Map raw strain, displacement, load (target, command, and feedback) into structure
3. Zero and shift the strain and displacement data
4. Identify and store data at 10% load increments

The MATLAB source code for each of these steps is available in Code Listings 1 through 4. Steps one and two were accomplished in a relatively straightforward manner and, thus, no detailed explanation is necessary. Step three provided some unique difficulties and, therefore, a detailed description of the procedure will be provided.

The purpose of step three was to synchronize the data from the two independent data-acquisition systems and zero the strain and displacement data at the start of loading. The HBM system acquired axial load from loader Axial-3 and pressure for the purpose of synchronizing to the VXI system. Channel Axial-3 was referred to as the driving channel for axial and combined load cases, and pressure was the driving channel for pressure load cases.

The load data from each driving channel (VXI and HBM) for the portion of data from the start of data acquisition to the point immediately before a non-zero target load was averaged and denoted as the “start average.” Loading was considered to begin at the first point that was greater than this mean value plus a predefined threshold; this point in time is referred to as the “start point.” For pressure-load cases, the threshold was 0.2 psi; for axial and combined-load cases, the

threshold was 300 pounds. Therefore, HBM and VXI system data were assigned independent start points. The strain and displacement data were zeroed using the start point as the reference.

The procedure is applied to the phase I axial data as an example. The VXI and HBM acquired axial load and the VXI axial target and axial command are shown plotted against time in figure E-2. The first non-zero load command occurred at 22.1 seconds. Averaging the VXI and HBM load data from time 0 to time 22.1, the results are -18.33 lbf and 9.43 lbf, respectively. Therefore, the respective load thresholds are 282 lbf (0.87% DLL) and 309 lbf (0.95% DLL), respectively. Setting the VXI and HBM start points at the instant when the load signals crossed their respective thresholds (noted in the figure), the resulting start points are 47.9 seconds and 59.4 seconds. At the start point, the time was shifted to zero and the strain and displacement data were zeroed.

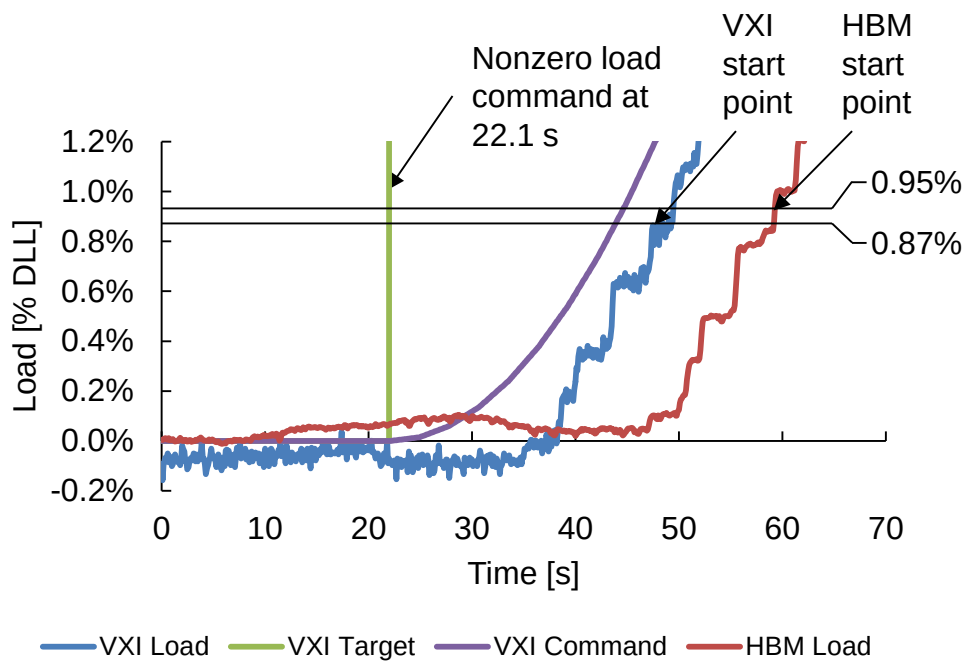

Figure E-2. Load Data Used for Zeroing Procedure in Phase I, Axial

Step four aimed to identify 10% load increment points and tabulate loader, strain, and displacement data for each increment. Past tests performed on the Full-Scale Aircraft Structural Test, Evaluation, and Research fixture used a stepped load application approach, where load was introduced in 10% increments and a hold between each increment was allowed to ensure equilibrium. However, in the PRSEUS tests, load was applied with no pauses in a haversine profile to prevent any potential damage propagation during a load hold. Therefore, an algorithm was used to identify the point at each load increment where the sum of the error in each loader was minimized. The procedure used was to first set a window on each load increment, identifying a set of possible times at which the sum of the loader errors might be smallest. For each point in the set, the sum was taken of the difference between the target load value and the actual load. The point with the minimum error was identified as the point for the load increment of interest and loader, strain, and displacement data were tabulated at this point. Data channels

from the HBM were synchronized to the VXI data by normalizing the maximum load recorded by the HBM to the max load recorded by the VXI system.

As an example, the procedure is applied for the first load increment (i.e., 10% DLL) of the Phase I axial only loading in the following. First, the window around the load increment is identified, as shown in figure E-3. The lower bound is identified as the first command load that is greater than the desired LS increment less 300 lbf, which, in this case, is 2,947 lbf. The upper bound is set as the first command load that is greater than the desired LS plus 500 lbf, which is 3747 lbf. The lower and upper bounds were found at times 93.6 and 100.9 seconds. The asymmetry in the window is required because the load lags the command. Within the window, the error (defined as absolute value of the difference between the desired LS increment and the current load) for each loader is summed. This sum is plotted in figure E-4. The time instant when this sum is minimized is used as the time instant for the LS.

Displacement data are provided with the following conventions on positive displacement. For axial displacement, overall extension of the panel was considered positive. For radial displacement, outward displacement of the panel was considered positive. The data are available in tables E-2 through E-28. These data were generated using MATLAB code provided in code listings 1-5.

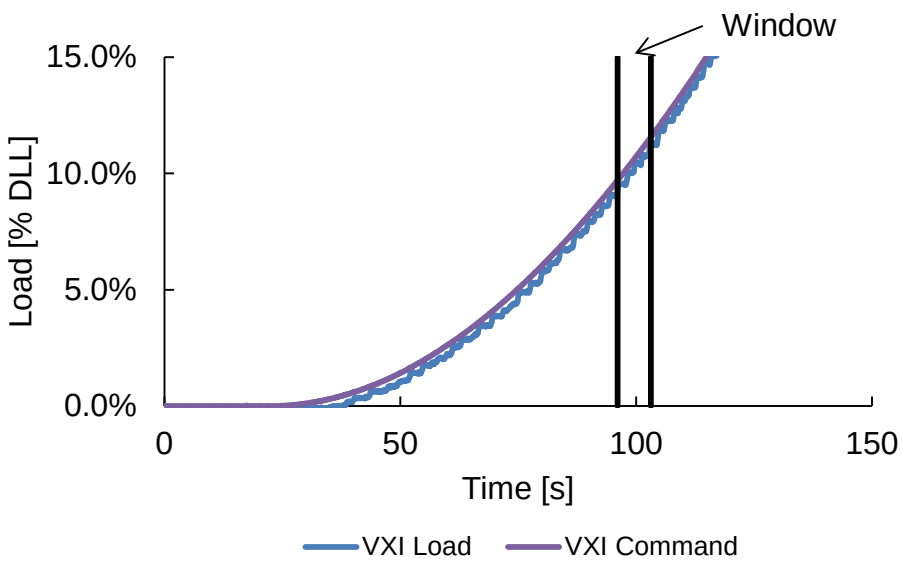

Figure E-3. Load and Command Data Near the First Load Step

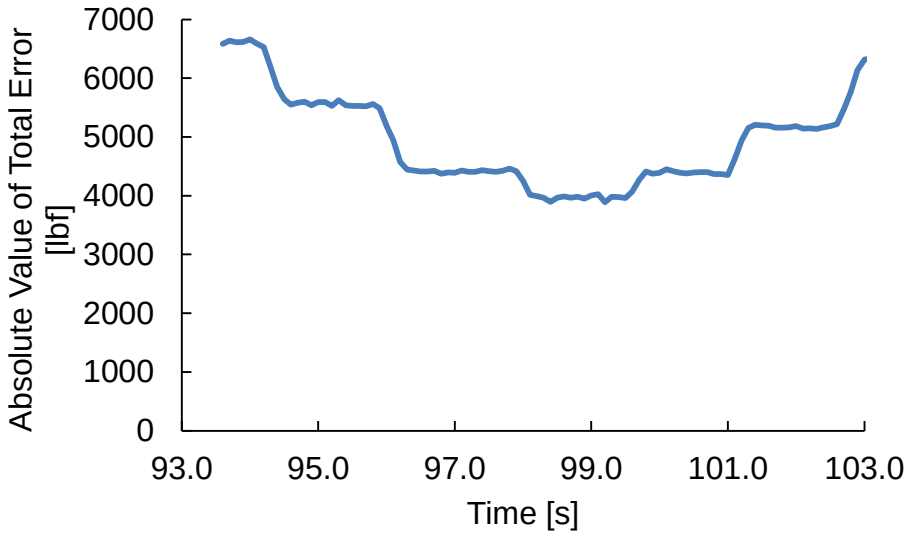

Figure E-4. Sum of Loader Error Near Load Step 1

Table E-2. Strain Data for Phase I, Axial [με]

Strain Gage No.	Load Magnitude [%Maximum Axial Load]									
	10%	20%	30%	40%	50%	60%	70%	80%	90%	100%
1	145	315	481	636	812	966	1123	1297	1466	1618
2	222	469	719	971	1213	1459	1703	1962	2205	2443
3	197	419	643	866	1081	1301	1520	1752	1970	2188
4	135	285	434	568	722	866	1006	1166	1320	1457
5	-90	-185	-282	-370	-473	-570	-656	-757	-866	-950
6	255	532	807	1080	1336	1603	1866	2142	2400	2657
7	273	572	870	1169	1442	1730	2016	2311	2585	2863
8	293	617	940	1266	1561	1874	2184	2503	2799	3099
9	273	577	880	1189	1466	1760	2053	2352	2628	2910
10	242	511	779	1059	1309	1574	1836	2106	2357	2609
11	-49	-94	-149	-194	-238	-292	-339	-386	-440	-487
12	-70	-142	-218	-286	-369	-447	-514	-595	-685	-750
13	-46	-88	-141	-187	-228	-283	-333	-381	-434	-485
14	234	491	752	1023	1262	1520	1776	2037	2279	2522
15	270	565	860	1161	1432	1720	2005	2299	2571	2848
16	280	582	884	1189	1467	1758	2046	2345	2623	2904
17	268	559	848	1136	1407	1686	1961	2252	2521	2790
18	235	490	744	991	1234	1479	1720	1979	2221	2458
19	-91	-184	-280	-366	-468	-563	-648	-748	-856	-939
20	137	294	446	582	743	886	1027	1190	1349	1486
21	208	434	660	884	1102	1322	1541	1775	1993	2213
22	205	428	653	877	1095	1316	1536	1768	1988	2199
23	146	316	481	637	804	963	1120	1291	1455	1603
24	-55	-107	-161	-206	-257	-307	-351	-400	-453	-493
25	-36	-69	-106	-142	-169	-207	-240	-271	-304	-337
26	341	716	1089	1462	1810	2166	2517	2884	3224	3559
27	332	699	1062	1424	1765	2112	2455	2813	3145	3477
28	175	371	567	784	968	1168	1369	1573	1760	1956
29	252	521	785	1047	1298	1552	1802	2067	2316	2555
30	256	525	788	1043	1293	1546	1792	2056	2307	2544

Table E-2. Strain Data for Phase I, Axial [με] (Continued)

Strain Gage No.	Load Magnitude [%Maximum Axial Load]									
	10%	20%	30%	40%	50%	60%	70%	80%	90%	100%
31	179	363	550	752	917	1122	1316	1514	1695	1885
32	326	673	1019	1363	1688	2017	2343	2686	3003	3265
33	-106	-221	-356	-490	-503	-609	-765	-838	-876	-1037
34	325	675	1020	1364	1691	2020	2349	2692	3010	3318
35	117	249	382	520	650	788	921	1055	1189	1324
36	119	252	384	520	649	787	920	1053	1189	1324
37	400	823	1219	1621	1978	2343	2699	3043	3376	3724
38	439	906	1342	1783	2173	2577	2970	3350	3718	4105
39	426	876	1298	1720	2095	2486	2862	3227	3582	3951
40	389	805	1197	1593	1946	2319	2675	3024	3363	3713
41	206	435	663	880	1107	1329	1547	1785	2014	2228
42	261	550	836	1131	1397	1677	1955	2242	2508	2776
43	228	480	732	980	1227	1475	1718	1981	2230	2471
44	259	546	833	1126	1392	1672	1952	2239	2507	2778
45	112	258	397	559	684	829	973	1110	1230	1366
46	114	235	348	465	561	664	769	868	960	1063
47	232	487	742	1000	1244	1496	1746	2012	2263	2507
48	124	257	383	509	624	741	860	976	1087	1206
49	132	292	445	618	753	911	1068	1215	1348	1498
50	252	528	802	1078	1333	1601	1866	2142	2400	2658
51	228	479	732	986	1232	1482	1728	1991	2240	2480
52	260	547	832	1122	1385	1664	1940	2225	2492	2760
53	213	450	689	926	1163	1397	1630	1879	2117	2342
54	118	251	384	526	657	798	937	1075	1214	1357
55	112	240	368	502	627	763	896	1029	1162	1299
56	-28	-56	-93	-127	-154	-197	-232	-266	-305	-339
57	12	20	33	41	43	56	68	76	87	105
58	-99	-233	-395	-562	-584	-758	-956	-1071	-1127	-1342
59	11	16	33	43	45	61	73	82	92	103
60	-26	-51	-84	-111	-138	-175	-207	-240	-279	-312

Table E-2. Strain Data for Phase I, Axial [με] (Continued)

Strain Gage No.	Load Magnitude [%Maximum Axial Load]									
	10%	20%	30%	40%	50%	60%	70%	80%	90%	100%
61	205	436	668	909	1132	1363	1591	1831	2057	2274
62	411	841	1244	1641	2011	2386	2747	3103	3452	3812
63	223	474	725	981	1222	1471	1719	1978	2223	2459
64	440	895	1322	1751	2135	2533	2915	3290	3654	4035
65	236	500	764	1027	1280	1539	1797	2069	2324	2573
66	353	724	1078	1443	1762	2101	2432	2751	3059	3380
67	240	505	765	1019	1274	1526	1777	2046	2301	2549
68	312	650	975	1317	1606	1920	2225	2515	2792	3079
69	217	451	679	890	1119	1334	1548	1785	2012	2227
70	-27	-54	-86	-114	-141	-174	-202	-232	-268	-296
71	-97	-178	-282	-427	-425	-545	-685	-763	-793	-969
72	-27	-54	-87	-114	-146	-181	-211	-245	-286	-315
73	153	322	493	664	830	1005	1177	1357	1533	1714
74	246	513	778	1036	1290	1542	1790	2047	2296	2538
75	244	507	769	1037	1288	1544	1796	2053	2299	2538
76	172	346	535	760	920	1125	1331	1516	1690	1879
77	-33	-62	-97	-132	-160	-198	-229	-257	-290	-318
78	4	3	7	13	10	18	23	23	24	30
79	4	8	14	25	21	32	38	36	37	42
80	-28	-57	-89	-120	-148	-182	-213	-242	-276	-307

Table E-3. Displacement Data for Phase I, Axial [inches]

LVDT No.	Load Magnitude [% Maximum Axial Load]									
	10%	20%	30%	40%	50%	60%	70%	80%	90%	100%
1	0.019	0.048	0.076	0.104	0.132	0.158	0.185	0.212	0.236	0.262
2	0.010	0.024	0.038	0.052	0.066	0.079	0.092	0.106	0.118	0.131
3	0.007	0.021	0.034	0.048	0.061	0.074	0.087	0.101	0.113	0.126
4	0.002	0.012	0.022	0.032	0.042	0.052	0.064	0.076	0.087	0.099
5	-0.001	0.004	0.011	0.016	0.022	0.028	0.036	0.045	0.053	0.061
6	0.007	0.017	0.027	0.048	0.042	0.053	0.070	0.075	0.072	0.090
7	0.011	0.024	0.038	0.065	0.062	0.078	0.099	0.109	0.108	0.128
8	0.006	0.013	0.021	0.042	0.036	0.047	0.063	0.068	0.064	0.081
9	0.006	0.016	0.026	0.046	0.041	0.053	0.069	0.074	0.072	0.088
10	0.012	0.025	0.038	0.063	0.061	0.075	0.095	0.103	0.103	0.122
11	0.005	0.011	0.018	0.037	0.032	0.042	0.056	0.062	0.059	0.074

Table E-4. Load Data for Phase I, Axial

	Load Magnitude [% Maximum Axial Load]									
	10%	20%	30%	40%	50%	60%	70%	80%	90%	100%
Axial - 1	3313	6553	9768	13024	16256	19456	22658	26000	29209	32279
Axial - 2	3315	6563	9825	13112	16389	19617	22819	26208	29436	32514
Axial - 3	3248	6505	9761	13037	16302	19526	22733	26124	29343	32469
Axial - 4	3197	6421	9656	12918	16160	19347	22555	25925	29149	32263
Axial - 5	3108	6348	9573	12840	16092	19296	22502	25864	29094	32192
Axial - 6	3204	6447	9701	12976	16251	19472	22665	26033	29260	32365
Axial - 7	3395	6607	9824	13082	16329	19531	22738	26068	29287	32402
Hoop - 1	177	270	243	304	428	357	406	495	475	510
Hoop - 2	44	8	-6	46	180	150	175	291	263	300
Hoop - 3	206	308	300	370	495	440	499	599	583	623
Hoop - 4	-2	65	-2	63	213	152	197	320	297	331
Hoop - 5	134	212	201	280	397	341	404	496	487	545
Hoop - 6	90	139	164	190	309	311	395	511	504	602
Hoop - 7	121	209	210	246	354	278	348	443	411	468
Hoop - 8	-1	79	50	93	209	151	188	267	267	304
Hoop - 9	-1	22	20	56	192	137	181	301	278	316
Hoop - 10	163	248	237	292	424	365	424	539	508	568
Hoop - 11	28	86	75	140	270	219	263	378	364	400
Hoop - 12	106	202	190	253	393	321	377	475	448	513
Hoop - 13	5	-3	5	27	136	107	136	238	238	260
Hoop - 14	8	74	74	118	183	147	198	257	220	301
Frame - 1H	552	557	565	578	514	560	558	556	584	540
Frame - 2R	-263	-193	-110	-48	-60	-33	43	58	56	146
Frame - 3H	283	264	264	207	209	192	159	141	156	111
Frame - 3R	-246	-199	-114	30	3	136	283	342	356	508
Frame - 4R	-121	-73	-31	-15	-23	-10	22	36	35	131
Frame - 5H	155	122	123	241	64	167	220	130	78	126
Frame - 6R	-323	-421	-480	-498	-653	-678	-690	-776	-880	-864
Frame - 7H	373	353	370	378	350	368	388	378	392	353
Frame - 8H	505	496	514	517	495	523	526	520	541	536
Frame - 8R	-154	-90	-16	25	10	77	145	181	187	315
Frame - 9H	419	395	428	428	414	446	462	442	463	414
Frame - 10R	-303	-341	-363	-310	-403	-382	-354	-386	-450	-412
Pressure	0.00	0.01	-0.02	0.06	-0.04	-0.06	0.03	0.04	-0.09	0.02

Table E-5. Strain Data for Phase I, Pressure [με]

Strain Gage No.	Load Magnitude [% Maximum Pressure]									
	10%	20%	30%	40%	50%	60%	70%	80%	90%	100%
1	-13	-16	6	8	27	40	55	75	92	115
2	23	65	101	151	180	223	249	279	309	338
3	20	56	85	120	143	184	208	232	262	284
4	0	4	20	15	26	44	60	72	91	107
5	98	247	351	512	619	723	816	909	1006	1089
6	35	91	128	180	213	259	284	317	345	374
7	46	112	149	218	256	306	332	366	396	423
8	53	127	166	248	289	344	373	407	441	469
9	50	118	157	237	276	330	359	392	425	451
10	38	93	128	201	239	290	320	352	385	411
11	36	122	209	305	391	474	557	638	724	808
12	110	275	395	575	695	816	920	1028	1137	1232
13	27	101	178	263	344	418	499	573	656	736
14	30	59	87	148	178	215	234	260	282	302
15	42	85	114	175	206	246	265	290	312	330
16	46	98	127	184	215	256	275	299	323	341
17	42	95	124	166	194	232	251	274	298	316
18	34	87	115	139	164	196	217	238	265	285
19	97	242	343	503	609	712	802	894	987	1070
20	-16	-28	-13	-45	-40	-22	-8	8	20	41
21	28	69	105	142	171	211	236	265	292	320
22	27	67	99	136	166	205	230	257	284	311
23	-11	-29	-17	-27	-13	6	24	40	56	73
24	35	95	145	222	273	323	369	419	466	513
25	16	57	101	146	195	242	291	336	386	434
26	59	151	224	328	387	473	525	584	645	698
27	53	138	203	292	347	431	482	536	595	645
28	18	55	78	110	135	174	193	214	240	255
29	14	32	53	67	86	108	121	136	147	163
30	8	18	33	29	41	65	75	90	101	115

Table E-5. Strain Data for Phase I, Pressure [με] (Continued)

Strain Gage No.	Load Magnitude [% Maximum Pressure]									
	10%	20%	30%	40%	50%	60%	70%	80%	90%	100%
31	35	74	97	122	135	180	207	227	243	262
32	64	154	224	311	372	447	496	552	603	654
33	-401	-831	-865	-1384	-1379	-1484	-1403	-1362	-1305	-1181
34	67	157	226	311	373	447	493	550	600	649
35	-11	-20	-32	-38	-49	-54	-65	-77	-84	-92
36	-6	-15	-22	-28	-42	-46	-57	-67	-76	-85
37	109	162	222	300	344	414	456	487	529	567
38	130	187	250	343	385	458	496	526	564	600
39	117	168	225	308	343	413	448	479	517	553
40	92	138	189	254	290	356	391	428	465	504
41	-9	-16	-16	-43	-48	-42	-41	-45	-39	-37
42	37	87	116	178	208	252	275	300	325	346
43	-4	-8	-8	-18	-21	-11	-13	-15	-13	-14
44	42	97	127	192	222	265	286	311	336	355
45	148	247	331	461	582	679	774	857	947	1043
46	137	207	318	422	494	601	678	752	819	888
47	-1	-2	2	0	1	11	10	8	8	9
48	107	161	272	364	420	522	593	664	730	794
49	124	219	277	381	492	572	649	718	790	870
50	33	79	106	153	180	217	234	259	281	301
51	-4	-13	-12	-15	-17	-8	-11	-11	-14	-12
52	40	96	127	188	217	260	279	307	331	351
53	-13	-32	-29	-40	-43	-37	-40	-37	-39	-35
54	-9	-17	-30	-37	-51	-57	-70	-84	-94	-104
55	-2	-2	-14	-20	-27	-32	-42	-52	-61	-68
56	30	103	183	249	325	396	472	543	621	697
57	9	14	16	9	8	5	2	7	9	9
58	-468	-874	-875	-1363	-1366	-1448	-1340	-1288	-1203	-1046
59	4	0	-7	-13	-19	-16	-21	-18	-23	-29
60	26	87	155	228	299	365	439	506	581	649

Table E-5. Strain Data for Phase I, Pressure [με] (Continued)

Strain Gage No.	Load Magnitude [% Maximum Pressure]									
	10%	20%	30%	40%	50%	60%	70%	80%	90%	100%
61	7	12	32	68	91	124	146	164	185	202
62	122	192	238	286	335	397	439	481	517	559
63	14	39	62	101	124	157	177	197	219	238
64	138	209	257	324	375	438	475	515	544	582
65	19	56	83	119	143	178	198	221	244	267
66	107	162	208	277	324	380	413	450	475	509
67	14	51	80	100	123	157	177	201	224	249
68	93	138	187	266	312	369	404	441	467	502
69	9	40	69	61	80	109	128	150	170	196
70	35	103	168	238	300	362	422	485	545	610
71	-428	-755	-765	-1218	-1243	-1329	-1246	-1208	-1122	-996
72	37	117	188	267	344	416	489	556	631	700
73	46	128	153	188	211	236	246	261	285	298
74	9	23	36	37	49	68	77	89	104	114
75	8	11	21	35	47	69	80	87	104	112
76	50	101	131	241	267	301	310	327	345	355
77	35	113	184	261	331	404	473	546	616	690
78	8	16	24	28	30	29	28	36	40	38
79	-3	-3	-3	-7	-2	1	9	5	18	15
80	9	38	70	102	137	170	208	241	278	314

Table E-6. Displacement Data for Phase I, Pressure [inches]

LVDT No.	Load Magnitude [% Maximum Pressure]									
	10%	20%	30%	40%	50%	60%	70%	80%	90%	100%
1	0.000	0.001	0.001	0.002	0.004	0.006	0.008	0.009	0.011	0.013
2	0.000	0.000	0.001	0.001	0.002	0.003	0.004	0.005	0.006	0.006
3	0.000	-0.002	-0.001	-0.001	-0.001	0.000	0.000	0.000	0.002	0.003
4	-0.003	-0.006	-0.007	-0.010	-0.011	-0.010	-0.012	-0.012	-0.011	-0.011
5	-0.004	-0.009	-0.009	-0.011	-0.013	-0.013	-0.015	-0.015	-0.015	-0.015
6	0.038	0.085	0.097	0.178	0.185	0.204	0.204	0.207	0.204	0.199
7	0.049	0.104	0.114	0.197	0.208	0.226	0.224	0.230	0.226	0.220
8	0.048	0.097	0.108	0.181	0.192	0.209	0.207	0.213	0.208	0.203
9	0.039	0.088	0.097	0.172	0.177	0.196	0.196	0.196	0.196	0.190
10	0.048	0.100	0.109	0.184	0.194	0.211	0.211	0.213	0.212	0.206
11	0.033	0.072	0.080	0.145	0.156	0.171	0.171	0.175	0.173	0.168

Table E-7. Load Data of Phase I, Pressure

Loader	Load Magnitude [% Maximum Pressure]									
	10%	20%	30%	40%	50%	60%	70%	80%	90%	100%
Axial - 1	524	1023	1578	2028	2528	3219	3690	4138	4694	5178
Axial - 2	480	987	1558	2016	2481	3194	3661	4127	4656	5181
Axial - 3	433	933	1499	1968	2499	3129	3613	4122	4656	5176
Axial - 4	361	876	1438	1897	2390	3054	3542	4021	4545	5058
Axial - 5	267	787	1363	1828	2348	2980	3448	3974	4498	5007
Axial - 6	373	887	1461	1909	2431	3082	3555	4068	4567	5057
Axial - 7	658	1216	1727	2208	2759	3313	3785	4336	4799	5251
Hoop - 1	1461	3035	4566	6085	7876	9142	10604	12278	13667	15178
Hoop - 2	1710	3070	4543	6092	7686	9114	10609	12140	13641	15150
Hoop - 3	1572	3047	4854	6103	7740	9153	10711	12129	13748	15165
Hoop - 4	1522	2986	4556	6154	7608	9162	10605	12121	13624	15195
Hoop - 5	1378	2852	4646	6186	7553	9218	10721	12124	13610	15220
Hoop - 6	1492	2964	4410	6049	7634	9068	10547	12223	13540	15098
Hoop - 7	1527	3087	4480	6188	7589	9158	10607	12081	13674	15210

Table E-7. Load Data of Phase I, Pressure (Continued)

Loader	Load Magnitude [% Maximum Pressure]									
	10%	20%	30%	40%	50%	60%	70%	80%	90%	100%
Hoop - 8	1544	3037	4502	6085	7617	9103	10650	12102	13686	15178
Hoop - 9	1484	3050	4510	5959	7643	9161	10772	12088	13695	15168
Hoop - 10	1475	3041	4546	6105	7639	9217	10662	12134	13714	15190
Hoop - 11	1550	3020	4522	6087	7596	9075	10655	12076	13662	15155
Hoop - 12	1637	3075	4601	6019	7554	9100	10693	12039	13691	15150
Hoop - 13	1572	3030	4531	6093	7582	9119	10630	12083	13682	15139
Hoop - 14	1544	3043	4499	6066	7581	9116	10706	12083	13636	15185
Frame - 1H	757	985	1163	1421	1714	2089	2362	2597	2912	3154
Frame - 2R	-661	-342	-337	55	75	178	137	157	142	101
Frame - 3H	539	814	1169	1387	1601	1936	2162	2578	2754	3009
Frame - 3R	-467	-269	-248	149	195	281	247	348	302	288
Frame - 4R	-458	-200	-187	14	54	132	112	160	148	100
Frame - 5H	512	762	892	1140	1496	1816	2199	2252	2754	2880
Frame - 6R	-505	-230	-192	101	144	203	182	199	204	165
Frame - 7H	604	946	1227	1484	1771	2026	2290	2605	2912	3122
Frame - 8H	671	991	1350	1619	1919	2200	2395	2800	3118	3378
Frame - 8R	-530	-204	-180	26	60	127	143	125	109	91
Frame - 9H	637	958	1248	1565	1842	2127	2331	2690	2965	3175
Frame - 10R	-462	-213	-179	97	134	247	262	269	292	275
Pressure	0.65	2.30	3.53	4.96	6.12	7.29	8.46	9.67	10.98	12.10

Table E-8. Strain Data for Phase I, Combined [με]

Strain Gage No.	Load Magnitude [% Maximum Axial Load]									
	10%	20%	30%	40%	50%	60%	70%	80%	90%	100%
1	98	303	492	685	867	1055	1234	1420	1602	1775
2	222	509	793	1071	1343	1627	1895	2175	2446	2708
3	186	442	694	942	1184	1439	1680	1933	2175	2413
4	71	254	424	597	762	936	1102	1275	1438	1605
5	680	657	550	432	325	216	105	-3	-103	-219
6	222	534	842	1143	1436	1742	2030	2329	2618	2898
7	251	584	917	1240	1556	1883	2191	2510	2820	3117
8	281	640	1001	1349	1690	2042	2375	2719	3055	3375
9	280	615	954	1279	1598	1929	2240	2563	2877	3177
10	274	575	875	1165	1449	1747	2027	2317	2600	2871
11	541	568	508	446	387	331	271	215	157	100
12	771	780	698	600	515	428	337	251	174	76
13	490	514	452	391	332	274	213	155	96	39
14	208	493	781	1064	1340	1627	1899	2182	2455	2720
15	209	530	861	1184	1499	1825	2134	2454	2765	3065
16	205	534	875	1205	1527	1860	2176	2502	2819	3123
17	179	498	825	1145	1455	1777	2082	2398	2704	2999
18	148	433	719	1000	1275	1560	1830	2110	2381	2645
19	668	645	541	424	318	211	101	-5	-103	-219
20	56	244	421	600	770	948	1116	1291	1456	1622
21	206	465	720	970	1215	1471	1714	1968	2214	2451
22	194	450	705	953	1198	1454	1695	1948	2193	2431
23	81	275	459	646	825	1010	1189	1372	1547	1720
24	334	315	255	190	132	74	16	-39	-91	-149
25	288	300	258	216	177	138	98	60	19	-16
26	454	889	1304	1701	2088	2489	2863	3253	3627	3982
27	417	842	1246	1636	2014	2407	2775	3157	3522	3875
28	182	383	599	807	1018	1242	1450	1670	1888	2094
29	107	401	698	996	1280	1576	1856	2145	2421	2693
30	75	370	666	961	1244	1539	1818	2108	2382	2657

Table E-8. Strain Data for Phase I, Combined [με] (Continued)

Strain Gage No.	Load Magnitude [% Maximum Axial Load]									
	10%	20%	30%	40%	50%	60%	70%	80%	90%	100%
31	140	356	563	771	979	1201	1413	1633	1836	2051
32	415	812	1190	1555	1911	2280	2628	2989	3337	3669
33	-427	-336	-512	-581	-710	-832	-952	-1087	-1294	-1343
34	406	807	1190	1558	1918	2295	2644	3008	3357	3694
35	-57	80	228	377	529	683	834	984	1143	1289
36	-58	79	228	378	531	685	837	988	1148	1294
37	383	817	1255	1666	2073	2474	2864	3245	3651	3999
38	386	863	1350	1806	2258	2703	3134	3556	4010	4394
39	345	809	1280	1721	2158	2589	3004	3411	3846	4220
40	328	762	1200	1614	2027	2435	2830	3217	3627	3988
41	-28	221	482	745	998	1263	1516	1777	2027	2279
42	220	535	857	1169	1474	1791	2090	2400	2701	2990
43	-6	262	553	842	1122	1416	1695	1984	2261	2537
44	217	531	855	1168	1474	1793	2094	2406	2711	3001
45	707	896	1055	1201	1350	1499	1641	1785	1936	2066
46	577	710	830	932	1043	1152	1259	1362	1478	1566
47	15	286	580	870	1154	1454	1736	2026	2308	2585
48	519	671	815	939	1071	1205	1334	1460	1598	1712
49	570	764	934	1095	1259	1424	1581	1735	1906	2044
50	177	480	790	1091	1386	1692	1981	2281	2573	2853
51	1	269	560	850	1131	1424	1704	1993	2272	2549
52	210	524	847	1159	1465	1782	2081	2392	2694	2983
53	-1	254	525	799	1063	1338	1601	1873	2134	2394
54	-72	64	216	368	525	684	843	1000	1169	1323
55	-45	84	225	369	517	668	819	968	1129	1276
56	461	500	457	414	372	333	290	250	207	165
57	-5	5	16	25	33	45	54	66	77	87
58	-359	-305	-546	-669	-857	-1028	-1197	-1375	-1630	-1708
59	-37	-25	-11	0	14	25	36	47	66	74
60	437	468	427	386	346	305	263	222	179	138

Table E-8. Strain Data for Phase I, Combined [με] (Continued)

Strain Gage No.	Load Magnitude [% Maximum Axial Load]									
	10%	20%	30%	40%	50%	60%	70%	80%	90%	100%
61	175	432	691	947	1196	1457	1704	1960	2207	2449
62	321	772	1222	1652	2076	2492	2898	3296	3719	4085
63	169	446	727	1004	1274	1557	1825	2104	2373	2637
64	345	818	1297	1750	2198	2637	3066	3486	3934	4321
65	169	462	758	1049	1333	1630	1911	2203	2486	2762
66	325	717	1113	1491	1868	2240	2604	2963	3341	3679
67	154	448	743	1033	1315	1610	1890	2182	2461	2735
68	348	705	1063	1405	1747	2085	2414	2735	3068	3374
69	115	378	638	898	1148	1409	1658	1915	2162	2404
70	393	419	384	346	310	276	238	203	166	129
71	-377	-277	-452	-522	-655	-777	-902	-1036	-1242	-1298
72	457	493	454	412	373	334	292	252	210	166
73	119	307	506	699	892	1095	1296	1496	1706	1904
74	71	363	661	959	1243	1535	1823	2106	2386	2661
75	78	366	663	959	1243	1534	1819	2101	2380	2657
76	191	368	571	769	969	1178	1385	1593	1808	2010
77	464	497	459	420	382	345	306	270	232	194
78	25	31	38	45	50	56	61	66	75	74
79	6	18	26	31	37	45	51	56	65	73
80	212	216	181	145	110	74	38	3	-34	-68

Table E-9. Displacement Data for Phase I, Combined [inches]

LVDT No.	Load Magnitude [% Maximum Axial Load]									
	10%	20%	30%	40%	50%	60%	70%	80%	90%	100%
1	0.008	0.037	0.068	0.100	0.131	0.162	0.192	0.221	0.258	0.277
2	0.004	0.018	0.034	0.050	0.066	0.081	0.096	0.110	0.129	0.138
3	0.000	0.014	0.029	0.045	0.060	0.075	0.090	0.104	0.123	0.132
4	-0.009	0.001	0.013	0.026	0.039	0.051	0.063	0.076	0.094	0.101
5	-0.011	-0.007	0.000	0.008	0.016	0.024	0.031	0.040	0.054	0.057
6	0.113	0.099	0.113	0.113	0.120	0.128	0.136	0.143	0.160	0.159
7	0.113	0.104	0.122	0.127	0.140	0.151	0.163	0.174	0.194	0.196
8	0.103	0.090	0.103	0.103	0.110	0.116	0.125	0.133	0.148	0.148
9	0.098	0.085	0.098	0.098	0.105	0.111	0.118	0.126	0.140	0.140
10	0.099	0.091	0.108	0.113	0.124	0.134	0.145	0.155	0.173	0.177
11	0.092	0.081	0.092	0.093	0.099	0.105	0.112	0.118	0.132	0.132

Table E-10. Load Data for Phase I, Combined

Loader	Load Magnitude [% Maximum Axial Load]									
	10%	20%	30%	40%	50%	60%	70%	80%	90%	100%
Axial - 1	3443	7295	10937	14631	18173	21876	25522	29158	32776	36331
Axial - 2	3420	7290	11003	14715	18301	22026	25700	29365	32996	36589
Axial - 3	3382	7254	10927	14631	18209	21923	25599	29291	32917	36520
Axial - 4	3291	7135	10830	14507	18046	21753	25400	29030	32678	36258
Axial - 5	3240	7089	10734	14432	17985	21678	25358	29005	32628	36220
Axial - 6	3314	7187	10890	14578	18142	21865	25541	29192	32810	36424
Axial - 7	3549	7348	10964	14644	18201	21887	25541	29166	32821	36385
Hoop - 1	9899	11423	11431	11400	11343	11400	11416	11408	11396	11454
Hoop - 2	9969	11421	11400	11379	11401	11413	11427	11424	11426	11425
Hoop - 3	9956	11392	11412	11429	11416	11405	11418	11437	11413	11316
Hoop - 4	9966	11418	11421	11394	11362	11412	11431	11430	11409	11436
Hoop - 5	9957	11393	11407	11400	11379	11425	11408	11450	11426	11395
Hoop - 6	9945	11401	11402	11442	11356	11442	11432	11416	11377	11417
Hoop - 7	9949	11419	11397	11411	11426	11393	11398	11432	11415	11406
Hoop - 8	9927	11409	11385	11428	11422	11405	11401	11404	11401	11439
Hoop - 9	9946	11455	11404	11363	11357	11406	11394	11423	11363	11444
Hoop - 10	9826	11398	11396	11431	11333	11430	11434	11436	11419	11450
Hoop - 11	9928	11409	11414	11416	11395	11400	11429	11424	11416	11432

Table E-10. Load Data for Phase I, Combined (Continued)

Loader	Load Magnitude [% Maximum Axial Load]									
	10%	20%	30%	40%	50%	60%	70%	80%	90%	100%
Hoop - 12	9940	11388	11386	11430	11402	11406	11403	11420	11395	11499
Hoop - 13	9925	11393	11464	11384	11363	11418	11459	11417	11400	11446
Hoop - 14	9889	11391	11396	11411	11339	11394	11449	11422	11398	11443
Frame - 1H	2175	2475	2469	2484	2488	2489	2470	2482	2546	2560
Frame - 2R	197	132	242	269	337	397	457	528	665	669
Frame - 3H	2045	2383	2400	2404	2411	2396	2367	2361	2394	2356
Frame - 3R	339	290	419	470	565	652	747	845	996	1032
Frame - 4R	207	126	233	256	331	389	456	524	649	653
Frame - 5H	1937	2237	2226	2177	2170	2183	2159	2175	2285	2349
Frame - 6R	202	48	8	-94	-154	-209	-262	-309	-302	-384
Frame - 7H	2222	2516	2568	2568	2631	2635	2623	2642	2686	2603
Frame - 8H	2343	2688	2721	2718	2736	2784	2751	2794	2821	2743
Frame - 8R	160	82	182	216	275	357	442	516	642	706
Frame - 9H	2273	2601	2630	2667	2693	2701	2689	2733	2781	2714
Frame - 10R	306	148	132	63	37	9	-16	-23	8	-31
Pressure	8.08	9.14	9.22	9.11	9.12	9.14	9.12	9.14	9.27	9.17

Table E-11. Strain Data for Phase II, Limit Axial [με]

Strain Gage No.	Load Magnitude [% Maximum Axial Load]									
	10%	20%	30%	40%	50%	60%	70%	80%	90%	100%
1	140	311	476	636	777	948	1118	1288	1454	1604
2	210	463	713	965	1219	1470	1714	1961	2204	2450
3	190	414	635	860	1086	1312	1530	1752	1970	2190
4	140	293	438	583	712	866	1020	1176	1328	1466
5	-102	-206	-306	-402	-467	-567	-672	-777	-880	-956
6	247	526	798	1075	1355	1624	1884	2147	2406	2670
7	260	561	859	1158	1466	1758	2039	2321	2594	2883
8	282	613	935	1264	1601	1918	2218	2524	2824	3138
9	261	570	872	1177	1491	1785	2064	2350	2630	2920
10	231	509	779	1051	1329	1592	1845	2102	2355	2614
11	-46	-99	-149	-201	-251	-303	-355	-409	-461	-511
12	-83	-166	-246	-322	-365	-444	-530	-617	-701	-756
13	-45	-95	-147	-200	-259	-313	-365	-419	-471	-530
14	226	493	754	1015	1277	1529	1773	2021	2263	2509
15	260	563	857	1153	1454	1741	2016	2296	2570	2851
16	268	577	878	1180	1488	1782	2063	2348	2627	2913
17	259	554	841	1131	1424	1708	1981	2259	2530	2806
18	227	484	734	987	1238	1490	1734	1982	2224	2466
19	-102	-205	-304	-399	-463	-561	-665	-769	-871	-945
20	147	305	455	605	735	894	1052	1209	1364	1502
21	209	440	664	889	1111	1339	1559	1782	2001	2217
22	196	421	642	868	1090	1317	1537	1758	1977	2192
23	151	320	485	652	793	962	1124	1291	1454	1598
24	-53	-108	-159	-208	-252	-301	-351	-402	-452	-494
25	-32	-71	-107	-143	-182	-216	-248	-282	-315	-352
26	321	701	1073	1445	1820	2183	2528	2876	3219	3563
27	315	684	1044	1407	1771	2127	2464	2806	3139	3477
28	162	362	563	763	983	1181	1366	1556	1748	1952
29	258	533	796	1058	1310	1569	1821	2076	2326	2568
30	264	539	799	1060	1306	1562	1813	2066	2314	2552

Table E-11. Strain Data for Phase II, Limit Axial [με] (Continued)

Strain Gage No.	Load Magnitude [% Maximum Axial Load]									
	10%	20%	30%	40%	50%	60%	70%	80%	90%	100%
31	189	384	575	779	989	1177	1356	1543	1727	1920
32	313	662	1000	1339	1675	2009	2328	2649	2963	3275
33	16	-60	-140	-248	-570	-670	-715	-780	-846	-1108
34	305	659	1000	1345	1688	2027	2349	2672	2991	3306
35	119	254	391	528	667	805	938	1089	1214	1353
36	120	254	390	527	667	805	939	1089	1216	1356
37	387	808	1212	1602	1999	2363	2706	3099	3397	3754
38	424	886	1332	1763	2205	2606	2984	3417	3746	4146
39	415	860	1290	1705	2129	2514	2877	3286	3608	3990
40	388	801	1204	1596	1995	2359	2705	3092	3404	3765
41	208	440	666	893	1106	1337	1565	1797	2024	2239
42	250	546	833	1123	1418	1698	1968	2241	2510	2784
43	226	485	737	991	1237	1493	1742	1995	2244	2487
44	248	541	827	1118	1416	1698	1968	2243	2513	2792
45	106	249	397	545	719	852	975	1113	1229	1380
46	102	212	320	431	558	659	753	867	945	1060
47	188	454	703	963	1201	1464	1715	1966	2220	2459
48	116	242	364	489	628	749	862	992	1096	1230
49	131	291	455	618	804	950	1086	1246	1363	1523
50	245	523	796	1073	1354	1624	1883	2147	2407	2672
51	225	485	739	995	1241	1497	1747	2001	2250	2493
52	250	541	827	1116	1413	1693	1962	2235	2503	2781
53	212	458	698	937	1161	1403	1640	1880	2118	2343
54	119	255	394	534	677	818	956	1112	1241	1388
55	114	242	374	508	645	779	911	1059	1184	1324
56	-27	-61	-97	-135	-171	-206	-242	-280	-318	-354
57	10	16	26	38	62	79	90	103	115	146
58	-15	-108	-235	-408	-827	-971	-1044	-1139	-1231	-1553
59	7	23	33	47	66	78	87	99	109	127
60	-27	-57	-88	-122	-156	-191	-226	-264	-300	-338

Table E-11. Strain Data for Phase II, Limit Axial [με] (Continued)

Strain Gage No.	Load Magnitude [% Maximum Axial Load]									
	10%	20%	30%	40%	50%	60%	70%	80%	90%	100%
61	202	444	678	914	1141	1372	1597	1825	2050	2268
62	403	827	1237	1633	2034	2409	2768	3172	3485	3852
63	218	475	727	982	1230	1481	1725	1972	2216	2455
64	426	879	1313	1734	2167	2559	2934	3357	3686	4077
65	232	500	762	1028	1289	1552	1808	2068	2323	2575
66	341	715	1076	1430	1797	2128	2444	2793	3082	3420
67	238	504	764	1025	1279	1542	1798	2057	2311	2560
68	304	647	980	1305	1643	1943	2229	2536	2806	3107
69	216	448	673	898	1115	1348	1576	1807	2032	2248
70	-28	-61	-93	-123	-154	-185	-218	-251	-284	-312
71	21	-39	-116	-235	-600	-701	-741	-799	-858	-1119
72	-29	-62	-95	-126	-150	-182	-218	-255	-293	-322
73	141	308	475	646	835	1008	1178	1356	1534	1730
74	246	522	787	1046	1306	1562	1812	2068	2316	2568
75	236	508	772	1035	1298	1552	1800	2054	2300	2552
76	148	335	523	717	934	1112	1284	1466	1646	1846
77	-29	-64	-97	-129	-164	-195	-225	-258	-290	-321
78	0	4	9	14	27	29	29	31	33	47
79	-1	5	8	14	28	28	27	30	34	46
80	-25	-57	-87	-119	-154	-185	-216	-249	-282	-317

Table E-12. Displacement Data for Phase II, Limit Axial [inches]

LVDT No.	Load Magnitude [% Maximum Axial Load]									
	10%	20%	30%	40%	50%	60%	70%	80%	90%	100%
1	0.020	0.049	0.077	0.106	0.134	0.161	0.188	0.227	0.241	0.266
2	0.010	0.024	0.038	0.053	0.067	0.081	0.094	0.114	0.121	0.133
3	0.008	0.022	0.036	0.049	0.063	0.076	0.089	0.109	0.115	0.128
4	0.003	0.014	0.025	0.035	0.045	0.055	0.066	0.086	0.089	0.101
5	-0.001	0.005	0.012	0.018	0.023	0.028	0.035	0.051	0.051	0.059
6	-0.009	-0.005	0.004	0.015	0.057	0.065	0.065	0.066	0.067	0.094
7	-0.006	0.002	0.016	0.034	0.082	0.093	0.095	0.099	0.104	0.134
8	-0.010	-0.009	-0.003	0.007	0.045	0.052	0.052	0.052	0.052	0.075
9	0.005	-0.003	0.015	0.019	0.040	0.043	0.059	0.061	0.048	0.072
10	-0.005	0.003	0.014	0.030	0.075	0.085	0.087	0.091	0.094	0.122
11	-0.009	-0.007	-0.001	0.009	0.046	0.052	0.050	0.051	0.051	0.071

Table E-13. Load Data for Phase II, Limit Axial

Loader	Load Magnitude [% Maximum Axial Load]									
	10%	20%	30%	40%	50%	60%	70%	80%	90%	100%
Axial - 1	3228	6513	9746	12973	16184	19442	22645	25945	29165	32399
Axial - 2	3283	6598	9865	13141	16372	19663	22906	26215	29461	32680
Axial - 3	3211	6496	9762	13016	16266	19554	22791	26124	29368	32596
Axial - 4	3266	6571	9799	13050	16246	19517	22727	26035	29240	32498
Axial - 5	3028	6333	9579	12803	16034	19319	22531	25832	29039	32267
Axial - 6	3147	6465	9718	12978	16207	19488	22742	26032	29227	32455
Axial - 7	3146	6399	9624	12853	16067	19356	22552	25869	29143	32466
Hoop - 1	20	0	25	-36	-45	-2	5	7	5	-9
Hoop - 2	8	8	24	-11	10	-29	21	3	-4	-13
Hoop - 3	-26	-42	52	-37	-78	5	27	17	-16	-2
Hoop - 4	6	-6	-4	-24	6	14	14	-3	-4	-10
Hoop - 5	-4	41	-29	19	-51	19	3	7	10	-13
Hoop - 6	-1	-42	-21	-3	-33	-4	55	95	137	295
Hoop - 7	9	43	77	138	156	168	182	213	229	274
Hoop - 8	12	-3	-10	5	12	5	-3	5	5	-3
Hoop - 9	-12	-10	-25	-1	-26	-5	11	-10	-9	-5

Table E-13. Load Data for Phase II, Limit Axial (Continued)

Loader	Load Magnitude [% Maximum Axial Load]									
	10%	20%	30%	40%	50%	60%	70%	80%	90%	100%
Hoop - 10	-20	3	1	-24	-15	20	4	-15	-4	3
Hoop - 11	-6	-11	-35	3	-33	-6	7	-4	-4	-1
Hoop - 12	-5	11	-7	-45	-16	-12	22	-5	4	-18
Hoop - 13	-10	-10	-54	4	-3	-3	19	-3	-3	-3
Hoop - 14	-16	5	-16	-9	27	5	-2	-2	5	-9
Frame - 1H	814	824	790	869	884	844	816	805	795	828
Frame - 2R	235	269	285	333	540	588	593	616	640	811
Frame - 3H	-20	29	-18	-21	-79	-93	-93	-90	-88	-124
Frame - 3R	206	254	353	475	789	861	888	932	976	1188
Frame - 4R	159	169	197	230	490	539	545	566	584	753
Frame - 5H	-427	-452	-495	-471	-205	-348	-486	-526	-529	-292
Frame - 6R	-19	-123	-204	-257	-133	-201	-303	-387	-461	-383
Frame - 7H	-132	-102	-52	-68	-85	-64	-45	-38	-34	-42
Frame - 8H	253	224	240	254	292	330	348	363	375	476
Frame - 8R	263	261	288	353	584	656	678	719	756	966
Frame - 9H	72	97	106	116	152	152	149	171	169	153
Frame - 10R	83	35	3	2	156	144	83	35	-6	91
Pressure	0.00	-0.03	-0.07	-0.09	0.06	0.08	0.05	0.00	-0.04	0.04

Table E-14. Strain Data for Phase II, Ultimate Axial [με]

Strain Gage No.	Load Magnitude [% Maximum Axial Load]									
	10%	20%	30%	40%	50%	60%	70%	80%	90%	100%
1	227	468	714	956	1197	1448	1688	1934	2166	2437
2	325	696	1073	1464	1818	2185	2545	2909	3248	3642
3	289	617	952	1301	1618	1948	2270	2598	2901	3249
4	206	421	638	858	1077	1305	1522	1746	1959	2207
5	-146	-295	-435	-557	-699	-849	-991	-1133	-1273	-1457

Table E-14. Strain Data for Phase II, Ultimate Axial [με] (Continued)

Strain Gage No.	Load Magnitude [% Maximum Axial Load]									
	10%	20%	30%	40%	50%	60%	70%	80%	90%	100%
6	361	770	1176	1601	1976	2368	2753	3136	3492	3924
7	396	843	1290	1760	2165	2590	3003	3417	3802	4256
8	425	909	1394	1903	2342	2799	3247	3691	4091	4609
9	396	848	1297	1770	2177	2602	3016	3431	3815	4268
10	354	758	1160	1582	1948	2331	2705	3079	3428	3831
11	-71	-147	-223	-301	-375	-453	-529	-607	-679	-766
12	-119	-238	-348	-438	-553	-674	-790	-905	-1020	-1174
13	-65	-139	-217	-298	-372	-449	-526	-604	-676	-762
14	354	738	1130	1534	1887	2256	2618	2980	3318	3708
15	398	835	1275	1734	2133	2550	2956	3366	3747	4181
16	405	851	1294	1759	2162	2585	2994	3408	3794	4229
17	388	817	1245	1693	2088	2499	2897	3299	3673	4098
18	340	715	1088	1478	1830	2196	2553	2911	3244	3625
19	-147	-294	-433	-553	-694	-841	-983	-1122	-1262	-1443
20	211	435	657	881	1107	1339	1557	1785	1999	2252
21	305	637	975	1325	1644	1977	2298	2625	2932	3293
22	297	624	962	1311	1628	1958	2278	2603	2916	3268
23	224	469	712	951	1188	1429	1662	1898	2114	2378
24	-75	-157	-230	-301	-373	-445	-515	-584	-646	-721
25	-51	-103	-156	-211	-257	-306	-356	-406	-447	-496
26	492	1044	1598	2169	2669	3187	3683	4182	4638	5173
27	478	1013	1553	2109	2600	3106	3595	4085	4520	5038
28	255	558	858	1176	1450	1737	2033	2315	2582	2901
29	369	766	1154	1555	1916	2294	2660	3023	3368	3771
30	369	762	1146	1540	1897	2273	2636	2998	3341	3741
31	249	540	829	1141	1401	1679	1958	2231	2486	2786
32	457	951	1453	1967	2424	2897	3350	3809	4230	4723
33	-5	-119	-300	-647	-768	-903	-1059	-1249	-1379	-1409
34	469	978	1495	2026	2493	2978	3446	3753	4148	4598
35	173	377	580	785	987	1193	1403	1609	1827	2027

Table E-14. Strain Data for Phase II, Ultimate Axial [με] (Continued)

Strain Gage No.	Load Magnitude [% Maximum Axial Load]									
	10%	20%	30%	40%	50%	60%	70%	80%	90%	100%
36	171	375	577	782	986	1192	1404	1612	1834	2035
37	545	1161	1733	2294	2816	3328	3846	4340	4887	5325
38	595	1274	1905	2529	3104	3670	4244	4790	5389	5871
39	577	1234	1841	2439	2991	3534	4084	4609	5185	5647
40	538	1154	1727	2292	2818	3337	3863	4366	4916	5376
41	310	646	983	1327	1654	1995	2326	2659	2975	3347
42	379	809	1238	1684	2075	2481	2878	3274	3644	4070
43	338	713	1089	1477	1835	2209	2574	2942	3287	3693
44	375	803	1232	1683	2075	2484	2885	3286	3659	4090
45	177	398	619	861	1055	1251	1448	1638	1847	2007
46	131	300	463	636	782	929	1086	1230	1388	1507
47	346	733	1103	1501	1852	2233	2597	2968	3310	3736
48	149	342	526	720	895	1071	1256	1430	1617	1769
49	205	448	687	943	1155	1366	1584	1790	2015	2190
50	362	770	1178	1605	1981	2373	2757	3141	3500	3917
51	339	715	1094	1483	1843	2218	2584	2954	3300	3706
52	375	801	1227	1676	2065	2471	2869	3268	3638	4069
53	324	677	1034	1397	1736	2091	2436	2785	3113	3501
54	172	380	587	799	1008	1221	1442	1659	1898	2106
55	164	361	559	761	961	1165	1377	1586	1813	2018
56	-44	-96	-150	-204	-255	-310	-364	-420	-474	-540
57	12	24	41	59	72	87	103	120	135	151
58	-59	-228	-487	-956	-1130	-1319	-1514	-1756	-1921	-1969
59	18	37	58	84	99	116	131	149	163	174
60	-38	-83	-131	-181	-232	-286	-340	-397	-451	-516
61	310	660	1012	1370	1696	2035	2365	2697	3008	3374
62	569	1189	1771	2345	2887	3421	3957	4470	5040	5501
63	333	707	1086	1476	1829	2196	2556	2916	3256	3653
64	598	1259	1877	2489	3057	3617	4182	4723	5307	5789
65	349	737	1132	1541	1910	2296	2673	3052	3406	3821

Table E-14. Strain Data for Phase II, Ultimate Axial [με] (Continued)

Strain Gage No.	Load Magnitude [% Maximum Axial Load]									
	10%	20%	30%	40%	50%	60%	70%	80%	90%	100%
66	483	1031	1551	2072	2554	3030	3515	3983	4487	4915
67	349	733	1121	1521	1889	2273	2646	3022	3374	3789
68	435	939	1420	1899	2334	2764	3200	3620	4050	4440
69	306	640	973	1317	1644	1985	2312	2646	2958	3325
70	-49	-95	-140	-184	-230	-278	-325	-372	-414	-473
71	13	-118	-290	-653	-772	-908	-1051	-1242	-1368	-1393
72	-43	-95	-142	-183	-234	-289	-343	-397	-453	-522
73	220	466	724	1003	1254	1523	1797	2066	2332	2624
74	363	759	1145	1538	1903	2279	2646	3011	3356	3743
75	358	753	1146	1539	1903	2274	2643	3005	3356	3740
76	231	513	814	1124	1381	1652	1944	2216	2476	2765
77	-43	-98	-149	-197	-243	-289	-338	-382	-424	-471
78	2	6	12	25	25	29	40	45	47	48
79	2	15	23	36	35	37	49	51	52	53
80	-43	-90	-137	-186	-231	-280	-328	-375	-418	-468

Table E-15. Displacement Data for Phase II, Ultimate Axial [inches]

LVDT No.	Load Magnitude [% Maximum Axial Load]									
	10%	20%	30%	40%	50%	60%	70%	80%	90%	100%
1	0.035	0.078	0.121	0.162	0.202	0.240	0.276	0.309	0.349	0.364
2	0.018	0.039	0.060	0.081	0.101	0.120	0.138	0.155	0.175	0.182
3	0.018	0.039	0.060	0.080	0.099	0.118	0.136	0.152	0.173	0.179
4	0.011	0.027	0.043	0.058	0.074	0.091	0.108	0.122	0.143	0.147
5	0.005	0.015	0.024	0.033	0.042	0.053	0.065	0.074	0.090	0.090
6	-0.006	0.004	0.023	0.060	0.067	0.073	0.082	0.095	0.101	0.095
7	0.000	0.017	0.042	0.088	0.099	0.111	0.124	0.142	0.151	0.147
8	-0.006	-0.001	0.014	0.048	0.055	0.061	0.066	0.078	0.083	0.076
9	-0.006	0.006	0.023	0.059	0.064	0.070	0.078	0.090	0.095	0.089
10	0.002	0.017	0.039	0.081	0.092	0.102	0.115	0.130	0.138	0.135
11	-0.004	0.003	0.018	0.051	0.056	0.061	0.067	0.077	0.081	0.074

Table E-16. Load Data for Phase II, Ultimate Axial

Loader	Load Magnitude [% Maximum Axial Load]									
	10%	20%	30%	40%	50%	60%	70%	80%	90%	100%
Axial - 1	5047	9850	14721	19656	24389	29232	34025	38873	43571	48645
Axial - 2	5376	10193	15123	20165	24882	29749	34568	39464	44183	49334
Axial - 3	5030	9835	14762	19777	24513	29411	34196	39149	43846	48965
Axial - 4	5714	10486	15378	20368	25034	29927	34741	39587	44287	49504
Axial - 5	4785	9581	14476	19438	24170	29043	33831	38728	43417	48580
Axial - 6	5442	10243	15171	20181	24914	29783	34594	39478	44184	49337
Axial - 7	5013	9768	14643	19581	24296	29174	33979	38803	43481	48648
Hoop - 1	177	15	11	57	84	108	113	117	142	128
Hoop - 2	288	320	385	457	494	508	548	546	573	553
Hoop - 3	92	-48	13	127	170	198	206	241	267	260
Hoop - 4	243	243	328	408	457	484	511	535	558	542
Hoop - 5	-41	-9	9	106	155	175	191	223	252	236
Hoop - 6	215	266	296	356	429	505	597	699	815	848
Hoop - 7	41	7	14	106	149	168	172	215	254	276
Hoop - 8	2	38	9	67	96	125	147	162	183	183
Hoop - 9	21	45	95	175	218	245	288	299	331	331
Hoop - 10	187	2	33	141	176	205	215	258	276	255
Hoop - 11	93	109	174	268	322	335	376	389	414	411
Hoop - 12	95	37	34	155	188	208	212	252	272	266
Hoop - 13	131	131	218	306	364	379	400	400	437	422
Hoop - 14	0	22	29	102	132	146	153	161	183	197
Frame - 1H	19	84	81	138	68	58	79	50	26	8
Frame - 2R	-33	4	78	265	313	369	440	539	601	578
Frame - 3H	298	237	230	198	199	191	190	177	175	187
Frame - 3R	-51	33	208	517	604	700	810	942	1028	1041
Frame - 4R	-34	-14	40	239	290	350	397	495	549	510
Frame - 5H	-2	177	165	289	125	19	172	109	27	-3
Frame - 6R	-229	-355	-420	-375	-476	-568	-630	-667	-735	-887
Frame - 7H	-62	-5	27	5	9	25	30	38	50	51
Frame - 8H	-15	14	34	11	18	29	32	50	65	65
Frame - 8R	25	35	130	326	384	454	532	638	705	704
Frame - 9H	40	7	53	84	101	111	116	128	140	92
Frame - 10R	-134	-167	-172	-73	-122	-158	-176	-183	-215	-308
Pressure	0.00	-0.06	-0.04	0.07	0.07	0.05	0.02	0.05	0.05	-0.05

Table E-17. Strain Data for Phase II, Limit Combined [με]

Strain Gage No.	Load Magnitude [% Maximum Axial Load]									
	10%	20%	30%	40%	50%	60%	70%	80%	90%	100%
1	77	275	460	649	837	1016	1201	1370	1559	1741
2	228	520	801	1080	1361	1630	1906	2159	2446	2711
3	204	462	711	959	1209	1450	1699	1925	2185	2424
4	66	243	409	579	747	916	1087	1242	1416	1581
5	717	709	602	484	376	264	156	48	-50	-163
6	253	569	873	1174	1481	1769	2064	2334	2641	2922
7	303	646	979	1306	1640	1950	2271	2561	2896	3198
8	364	739	1101	1453	1813	2149	2493	2808	3167	3499
9	314	657	991	1319	1652	1964	2285	2577	2912	3214
10	282	588	887	1180	1479	1759	2048	2312	2612	2886
11	521	548	489	430	370	316	257	199	142	83
12	813	840	755	659	573	480	394	304	229	135
13	471	492	431	372	311	254	195	136	77	17
14	209	501	787	1070	1358	1631	1909	2164	2454	2722
15	227	556	885	1209	1538	1848	2164	2454	2784	3087
16	231	568	906	1237	1574	1890	2213	2508	2845	3152
17	212	536	860	1179	1503	1810	2122	2408	2733	3031
18	187	474	756	1037	1321	1593	1870	2124	2411	2677
19	702	693	588	472	365	253	146	39	-58	-170
20	36	219	391	570	744	916	1091	1249	1423	1591
21	216	480	732	982	1236	1479	1730	1958	2219	2461
22	198	458	710	960	1214	1456	1706	1932	2193	2433
23	32	220	404	592	776	956	1139	1304	1489	1664
24	334	322	260	199	139	80	24	-30	-84	-140
25	280	288	247	207	165	128	90	51	12	-26
26	483	927	1336	1736	2137	2515	2901	3252	3650	4009
27	455	886	1284	1675	2066	2438	2818	3161	3550	3906
28	162	381	601	814	1036	1246	1464	1668	1899	2107
29	90	385	683	980	1277	1560	1847	2111	2404	2678
30	77	370	664	959	1253	1535	1821	2083	2373	2647
31	145	360	571	782	996	1207	1421	1617	1838	2040
32	439	845	1218	1585	1955	2304	2663	2986	3357	3642
33	-869	-916	-1076	-1152	-1326	-1390	-1515	-1630	-1852	-1952
34	425	832	1213	1584	1960	2314	2675	3002	3376	3717
35	-67	56	208	359	514	666	815	986	1126	1279

Table E-17. Strain Data for Phase II, Limit Combined [με] (Continued)

Strain Gage No.	Load Magnitude [% Maximum Axial Load]									
	10%	20%	30%	40%	50%	60%	70%	80%	90%	100%
36	-58	59	211	364	520	672	822	993	1134	1289
37	378	812	1252	1673	2089	2486	2872	3312	3647	4023
38	403	879	1368	1832	2294	2733	3159	3647	4019	4435
39	370	827	1297	1745	2191	2613	3024	3490	3852	4252
40	334	766	1205	1627	2046	2447	2838	3274	3624	4007
41	-29	214	472	734	994	1250	1508	1746	2009	2260
42	241	561	881	1195	1515	1814	2122	2403	2722	3014
43	-13	253	542	832	1123	1404	1689	1953	2246	2522
44	246	566	886	1201	1522	1823	2132	2416	2738	3032
45	669	899	1065	1220	1371	1514	1656	1821	1953	2088
46	589	751	868	978	1095	1199	1301	1434	1522	1622
47	-32	219	511	791	1080	1338	1629	1870	2169	2432
48	522	703	844	966	1105	1230	1356	1515	1627	1752
49	552	777	954	1119	1287	1446	1601	1779	1921	2069
50	212	521	826	1128	1435	1723	2020	2291	2599	2881
51	-16	251	541	832	1123	1405	1689	1954	2248	2525
52	238	559	878	1190	1510	1809	2116	2397	2718	3012
53	-25	229	498	772	1044	1309	1577	1825	2099	2362
54	-75	47	201	356	517	673	830	1009	1156	1319
55	-45	68	211	357	509	657	806	976	1118	1274
56	444	481	438	398	354	317	274	233	191	148
57	13	25	35	43	51	62	72	82	93	104
58	-784	-879	-1106	-1232	-1455	-1555	-1727	-1876	-2153	-2285
59	-14	0	11	19	30	36	49	57	75	85
60	420	453	412	373	330	292	251	208	166	122
61	134	395	653	910	1169	1418	1672	1904	2167	2411
62	362	807	1259	1692	2123	2538	2939	3388	3744	4136
63	162	442	721	1000	1281	1550	1825	2078	2364	2629
64	381	847	1329	1787	2245	2681	3104	3580	3957	4371
65	182	478	771	1063	1357	1639	1928	2193	2492	2771
66	337	724	1125	1508	1893	2260	2621	3017	3352	3706
67	169	466	756	1048	1341	1622	1910	2174	2470	2747
68	341	696	1060	1407	1756	2087	2411	2760	3067	3383
69	128	392	649	908	1168	1418	1673	1906	2166	2413
70	397	424	388	353	315	280	244	207	171	134

Table E-17. Strain Data for Phase II, Limit Combined [με] (Continued)

Strain Gage No.	Load Magnitude [% Maximum Axial Load]									
	10%	20%	30%	40%	50%	60%	70%	80%	90%	100%
71	-680	-724	-894	-975	-1160	-1224	-1351	-1464	-1685	-1786
72	453	485	446	405	363	323	282	239	201	156
73	201	396	591	783	980	1175	1373	1567	1780	1984
74	78	371	668	963	1258	1543	1827	2099	2388	2671
75	80	370	666	961	1255	1538	1819	2090	2379	2660
76	213	409	610	806	1013	1205	1404	1599	1818	2022
77	453	489	449	413	372	336	300	264	225	188
78	28	39	46	49	56	60	64	70	77	83
79	8	16	23	25	32	38	42	47	59	64
80	202	205	171	136	99	65	30	-5	-41	-77

Table E-18. Displacement Data for Phase II, Limit Combined [inches]

LVDT No.	Load Magnitude [% Maximum Axial Load]									
	10%	20%	30%	40%	50%	60%	70%	80%	90%	100%
1	0.010	0.040	0.071	0.103	0.135	0.165	0.195	0.237	0.253	0.281
2	0.005	0.020	0.036	0.052	0.068	0.083	0.098	0.119	0.127	0.140
3	-0.001	0.013	0.028	0.043	0.058	0.073	0.087	0.108	0.115	0.129
4	-0.008	0.002	0.014	0.027	0.039	0.052	0.064	0.085	0.089	0.101
5	-0.011	-0.007	0.000	0.007	0.015	0.022	0.030	0.045	0.046	0.054
6	0.154	0.157	0.170	0.174	0.187	0.190	0.197	0.204	0.221	0.226
7	0.160	0.169	0.187	0.196	0.215	0.221	0.232	0.244	0.265	0.274
8	0.141	0.145	0.156	0.158	0.171	0.173	0.180	0.185	0.201	0.206
9	0.141	0.143	0.154	0.157	0.169	0.172	0.178	0.185	0.200	0.205
10	0.138	0.145	0.162	0.170	0.187	0.193	0.204	0.214	0.234	0.243
11	0.133	0.136	0.146	0.149	0.160	0.163	0.168	0.174	0.188	0.193

Table E-19. Load Data for Phase II, Limit Combined

Loader	Load Magnitude [% Maximum Axial Load]									
	10%	20%	30%	40%	50%	60%	70%	80%	90%	100%
Axial - 1	3462	7380	11011	14678	18331	21895	25533	28988	32731	36399
Axial - 2	3422	7323	10999	14710	18408	22006	25651	29109	32923	36588
Axial - 3	3527	7418	11087	14773	18469	22070	25721	29190	32974	36659
Axial - 4	3378	7259	10896	14577	18230	21854	25431	28920	32727	36433
Axial - 5	3258	7149	10797	14462	18136	21683	25334	28789	32557	36231
Axial - 6	3108	7039	10684	14374	18069	21665	25326	28779	32575	36260
Axial - 7	3438	7295	10902	14561	18220	21771	25398	28873	32644	36340
Hoop - 1	9942	11429	11414	11397	11351	11396	11431	11350	11409	11452
Hoop - 2	9911	11443	11415	11410	11420	11422	11431	11401	11411	11433
Hoop - 3	9935	11426	11423	11435	11363	11409	11407	11345	11367	11415
Hoop - 4	9883	11416	11408	11428	11380	11461	11398	11388	11429	11406
Hoop - 5	9896	11432	11441	11420	11399	11380	11427	11391	11399	11411
Hoop - 6	10013	11334	11340	11463	11352	11440	11372	11340	11367	11432
Hoop - 7	9841	11468	11435	11406	11386	11367	11463	11442	11436	11418
Hoop - 8	9951	11406	11408	11441	11389	11421	11432	11424	11412	11443
Hoop - 9	9982	11482	11383	11381	11320	11362	11390	11373	11456	11406
Hoop - 10	9956	11366	11426	11458	11343	11395	11413	11384	11408	11417
Hoop - 11	9962	11415	11418	11427	11393	11414	11434	11386	11411	11427
Hoop - 12	9873	11461	11413	11445	11292	11447	11422	11370	11416	11382
Hoop - 13	9915	11413	11387	11419	11382	11370	11418	11373	11390	11428
Hoop - 14	9942	11453	11390	11378	11377	11409	11413	11368	11408	11424
Frame - 1H	1816	2143	2149	2098	2114	2093	2091	2088	2166	2140
Frame - 2R	310	357	453	484	595	605	670	731	881	926
Frame - 3H	1839	2170	2150	2128	2142	2082	2106	2056	2098	2073
Frame - 3R	425	516	633	693	813	853	942	1025	1173	1252
Frame - 4R	166	203	294	327	437	460	529	588	726	777
Frame - 5H	1646	1947	1969	1805	1845	1825	1774	1773	1985	1923
Frame - 6R	196	129	83	-15	-52	-143	-206	-263	-250	-306
Frame - 7H	1814	2217	2262	2237	2287	2230	2245	2238	2314	2302
Frame - 8H	2021	2449	2459	2423	2455	2406	2436	2426	2511	2527
Frame - 8R	286	274	349	405	494	543	600	680	792	863
Frame - 9H	1998	2390	2420	2388	2431	2385	2415	2420	2502	2492
Frame - 10R	337	288	280	228	218	170	147	139	168	141
Pressure	8.04	9.23	9.25	9.19	9.20	9.13	9.12	9.10	9.25	9.22

Table E-20. Strain Data for Phase II, Ultimate Combined [με]

Strain Gage No.	Load Magnitude [% Maximum Axial Load]									
	10%	20%	30%	40%	50%	60%	70%	80%	90%	100%
1	212	494	777	1045	1330	1590	1835	2107	2385	2669
2	369	790	1203	1610	2036	2421	2798	3195	3612	4025
3	316	689	1057	1417	1803	2150	2486	2846	3224	3604
4	157	406	664	904	1173	1413	1634	1887	2145	2402
5	689	535	363	206	33	-129	103	-59	-218	-390
6	370	831	1276	1715	2173	2584	2965	3384	3849	4291
7	418	924	1409	1888	2383	2827	3230	3737	4218	4758
8	495	1044	1566	2086	2616	3097	3549	4034	4545	5088
9	438	944	1427	1906	2399	2845	3248	3699	4176	4654
10	415	863	1292	1718	2160	2563	2940	3347	3774	4198
11	598	507	415	324	232	146	407	316	229	148
12	801	681	540	416	273	141	436	304	175	32
13	532	439	349	255	164	77	311	220	130	42
14	328	759	1179	1590	2023	2413	2764	3163	3580	3983
15	351	846	1323	1791	2281	2723	3102	3568	4043	4500
16	355	860	1346	1822	2318	2764	3141	3597	4075	4513
17	331	818	1289	1750	2232	2665	3038	3481	3943	4408
18	289	714	1130	1537	1965	2350	2698	3094	3504	3907
19	680	528	357	204	32	-127	100	-60	-217	-383
20	170	429	691	936	1205	1448	1664	1919	2177	2444
21	332	711	1084	1447	1835	2186	2526	2890	3277	3691
22	315	689	1060	1422	1807	2156	2497	2858	3233	3612
23	181	456	733	994	1277	1529	1758	2022	2292	2558
24	338	249	159	74	-15	-98	28	-57	-131	-229
25	317	257	197	137	77	20	159	101	50	-1
26	678	1291	1880	2450	3044	3572	4109	4640	5085	5535
27	636	1233	1809	2369	2954	3473	3998	4522	5070	5602
28	294	613	918	1241	1569	1871	2184	2495	2822	3160
29	236	684	1122	1548	1990	2390	2710	3119	3544	3968
30	212	655	1088	1507	1950	2349	2664	3078	3507	3936

Table E-20. Strain Data for Phase II, Ultimate Combined [με] (Continued)

Strain Gage No.	Load Magnitude [% Maximum Axial Load]									
	10%	20%	30%	40%	50%	60%	70%	80%	90%	100%
31	224	533	835	1144	1478	1778	2059	2369	2695	3010
32	595	1149	1685	2204	2750	3239	3730	4227	4749	5277
33	-225	-482	-591	-866	-996	-1161	-961	-1150	-1389	-1543
34	559	1097	1618	2122	2652	3130	3607	4092	4581	5042
35	-14	213	436	664	891	1121	1240	1468	1701	1935
36	-16	213	436	665	890	1120	1239	1470	1705	1939
37	546	1209	1823	2432	3009	3584	4064	4609	5157	5698
38	562	1299	1978	2654	3291	3925	4439	5043	5646	6242
39	529	1243	1898	2551	3165	3777	4264	4849	5437	6012
40	507	1170	1787	2402	2989	3572	4057	4619	5182	5725
41	95	480	871	1246	1649	2013	2286	2662	3049	3445
42	366	846	1308	1764	2236	2664	3035	3469	3924	4379
43	116	546	975	1392	1836	2238	2529	2942	3372	3808
44	359	841	1304	1764	2239	2669	3039	3476	3937	4397
45	825	1062	1279	1504	1719	1929	2388	2589	2797	3164
46	624	805	958	1132	1278	1435	1803	1951	2100	2228
47	125	555	982	1385	1844	2237	3178	3526	3925	4329
48	570	790	982	1192	1376	1570	1951	2140	2374	2554
49	677	937	1178	1424	1659	1890	2300	2514	2742	2988
50	324	784	1229	1669	2126	2539	2898	3320	3761	4190
51	121	551	981	1400	1844	2246	2536	2951	3382	3817
52	345	827	1291	1749	2223	2653	3020	3453	3912	4363
53	117	519	923	1313	1730	2110	2390	2782	3186	3598
54	-27	204	431	669	905	1148	1276	1521	1791	2048
55	-1	215	430	653	880	1111	1236	1470	1712	1947
56	499	435	373	309	246	186	429	362	298	229
57	1	20	35	49	68	84	106	124	146	163
58	-162	-534	-722	-1086	-1284	-1505	-1200	-1450	-1740	-1947
59	-32	-7	10	32	49	63	61	85	109	128
60	483	422	363	297	234	172	397	330	262	194

Table E-20. Strain Data for Phase II, Ultimate Combined [με] (Continued)

Strain Gage No.	Load Magnitude [% Maximum Axial Load]									
	10%	20%	30%	40%	50%	60%	70%	80%	90%	100%
61	294	677	1057	1427	1822	2177	2490	2855	3235	3616
62	526	1210	1844	2472	3075	3672	4185	4754	5326	5885
63	295	712	1124	1527	1955	2341	2680	3077	3490	3907
64	549	1273	1941	2606	3240	3870	4382	4985	5593	6212
65	306	744	1177	1600	2048	2452	2809	3224	3659	4095
66	492	1093	1653	2215	2756	3296	3746	4271	4802	5381
67	295	732	1163	1584	2029	2431	2789	3201	3633	4065
68	496	1041	1549	2058	2546	3030	3444	3913	4386	4829
69	251	637	1020	1389	1784	2139	2459	2826	3207	3585
70	428	375	322	267	212	159	361	306	242	176
71	-201	-459	-564	-832	-969	-1137	-882	-1083	-1302	-1468
72	491	436	375	317	251	189	407	335	271	192
73	208	496	781	1082	1386	1683	1974	2275	2585	2907
74	218	661	1096	1527	1962	2370	2682	3091	3509	3936
75	214	655	1088	1519	1951	2359	2673	3080	3482	3923
76	229	531	831	1149	1467	1771	2061	2369	2682	3010
77	501	446	393	335	275	220	454	393	345	271
78	30	40	46	56	63	70	89	96	104	110
79	13	24	30	42	51	60	81	93	103	115
80	229	177	126	73	19	-33	68	15	-33	-85

Table E-21. Displacement Data for Phase II, Ultimate Combined [inches]

LVDT No.	Load Magnitude [% Maximum Axial Load]									
	10%	20%	30%	40%	50%	60%	70%	80%	90%	100%
1	0.023	0.070	0.117	0.163	0.208	0.253	0.290	0.335	0.380	0.428
2	0.011	0.035	0.058	0.082	0.104	0.126	0.145	0.167	0.190	0.214
3	0.010	0.034	0.057	0.080	0.102	0.124	0.142	0.164	0.186	0.210
4	-0.001	0.018	0.037	0.055	0.075	0.094	0.111	0.131	0.152	0.174
5	-0.006	0.005	0.016	0.027	0.039	0.052	0.065	0.078	0.094	0.112
6	0.082	0.101	0.103	0.124	0.129	0.138	0.134	0.145	0.157	0.165
7	0.087	0.114	0.124	0.151	0.161	0.177	0.176	0.190	0.207	0.218
8	0.074	0.089	0.090	0.107	0.113	0.121	0.118	0.128	0.138	0.146
9	0.075	0.092	0.095	0.114	0.117	0.125	0.124	0.132	0.144	0.150
10	0.077	0.101	0.109	0.134	0.143	0.156	0.157	0.170	0.185	0.196
11	0.070	0.085	0.086	0.101	0.103	0.111	0.109	0.118	0.127	0.132

Table E-22. Load Data for Phase II, Ultimate Combined

Loader	Load Magnitude [% Maximum Axial Load]									
	10%	20%	30%	40%	50%	60%	70%	80%	90%	100%
Axial - 1	5556	10986	16387	21794	27350	32605	38079	43482	48914	54482
Axial - 2	5692	11154	16612	22089	27658	32981	38479	43954	49419	55045
Axial - 3	5427	10869	16319	21787	27370	32693	38234	43688	49167	54794
Axial - 4	5805	11197	16611	22032	27593	32867	38393	43858	49339	55003
Axial - 5	5405	10809	16242	21664	27227	32533	38015	43472	48928	54550
Axial - 6	5558	10991	16437	21889	27453	32788	38268	43751	49193	54801
Axial - 7	5415	10791	16172	21582	27146	32417	37904	43339	48784	54390
Hoop - 1	11355	11383	11400	11316	11417	11397	17134	17180	16978	17154
Hoop - 2	11412	11426	11431	11374	11446	11439	17043	16987	17100	17134
Hoop - 3	11392	11417	11458	11367	11337	11368	17177	17125	17061	17151
Hoop - 4	11423	11413	11340	11406	11338	11421	17124	17133	17146	17115
Hoop - 5	11434	11415	11429	11435	11420	11406	17144	17081	17137	17106
Hoop - 6	11446	11347	11389	11376	11429	11446	17039	17244	17162	17167
Hoop - 7	11277	11415	11487	11492	11384	11327	17270	16950	17020	17125
Hoop - 8	11403	11408	11421	11417	11417	11432	17140	17125	17114	17130

Table E-22. Load Data for Phase II, Ultimate Combined (Continued)

Loader	Load Magnitude [% Maximum Axial Load]									
	10%	20%	30%	40%	50%	60%	70%	80%	90%	100%
Hoop - 9	11299	11365	11356	11435	11406	11306	17176	17040	17135	17136
Hoop - 10	11506	11461	11446	11400	11329	11535	17098	17062	17045	17124
Hoop - 11	11464	11423	11408	11346	11328	11402	17114	17116	17090	17151
Hoop - 12	11314	11210	11369	11394	11474	11227	17192	17104	17007	17116
Hoop - 13	11401	11384	11449	11328	11357	11430	17007	17291	17033	17143
Hoop - 14	11389	11481	11436	11403	11337	11484	17189	17079	17105	17164
Frame - 1H	2100	2126	2104	2164	2096	2091	3146	3137	3204	3162
Frame - 2R	185	346	390	572	607	691	718	824	954	1029
Frame - 3H	2388	2430	2434	2442	2428	2405	3396	3468	3511	3519
Frame - 3R	330	495	581	764	866	987	1135	1238	1369	1459
Frame - 4R	125	284	327	482	537	613	632	736	855	918
Frame - 5H	2216	2298	2160	2240	2191	2216	3344	3419	3516	3522
Frame - 6R	141	75	-68	-111	-224	-293	-320	-361	-399	-457
Frame - 7H	2273	2397	2387	2449	2484	2438	3397	3492	3606	3617
Frame - 8H	2277	2412	2417	2414	2439	2435	3568	3658	3790	3800
Frame - 8R	173	305	361	532	597	713	866	938	1043	1125
Frame - 9H	2200	2324	2307	2359	2372	2370	3332	3404	3564	3575
Frame - 10R	252	208	113	143	68	32	76	52	57	16
Pressure	9.16	9.25	9.14	9.26	9.14	9.13	13.75	13.77	13.86	13.86

Table E-23. Strain Data for Phase II, Limit Pressure [με]

Strain Gage No.	Load Magnitude [% Maximum Pressure]									
	10%	20%	30%	40%	50%	60%	70%	80%	90%	100%
1	2	1	-4	11	35	55	74	100	119	134
2	27	63	123	158	186	210	242	277	299	333
3	24	57	113	143	167	188	216	247	266	297
4	4	9	-5	11	35	53	67	86	102	115
5	96	234	422	529	608	695	790	884	974	1069
6	29	77	147	181	213	236	274	306	330	360
7	35	93	195	235	267	291	331	364	387	420
8	41	110	237	286	324	353	399	441	469	512
9	36	95	211	252	284	309	346	378	400	434
10	32	77	175	217	248	274	309	340	361	396
11	55	141	227	315	397	480	565	649	729	814
12	107	262	472	594	686	784	893	999	1101	1209
13	48	119	201	277	353	433	511	591	669	749
14	19	47	127	155	175	191	218	246	262	286
15	27	64	153	185	204	218	244	268	283	306
16	31	74	159	192	213	227	253	277	291	315
17	28	71	136	167	191	206	230	255	269	292
18	23	66	105	133	159	177	201	227	247	270
19	93	228	415	518	597	682	777	867	955	1048
20	1	3	-31	-17	6	22	38	58	72	84
21	27	63	112	146	174	195	227	260	282	311
22	23	53	100	131	159	180	210	242	265	294
23	4	-18	-42	-29	-7	14	28	50	65	80
24	33	91	169	224	267	312	362	410	455	503
25	28	70	111	158	206	254	302	351	398	447
26	61	144	276	347	403	452	516	582	628	693
27	56	134	259	325	378	426	485	549	592	654
28	20	42	100	125	140	157	183	198	208	242
29	5	15	24	38	63	74	94	109	118	130
30	-1	11	11	22	47	58	77	91	101	111

Table E-23. Strain Data for Phase II, Limit Pressure [με] (Continued)

Strain Gage No.	Load Magnitude [% Maximum Pressure]									
	10%	20%	30%	40%	50%	60%	70%	80%	90%	100%
31	17	59	87	111	122	128	152	172	179	204
32	56	133	246	312	366	409	468	528	572	627
33	-196	-529	-1325	-1376	-1191	-1063	-1015	-916	-803	-779
34	55	128	245	305	360	401	461	516	560	612
35	-19	-29	-32	-41	-50	-61	-71	-80	-93	-97
36	-15	-23	-26	-35	-45	-56	-65	-75	-88	-93
37	63	135	250	300	333	375	412	450	479	532
38	71	153	289	336	365	407	443	478	504	555
39	63	136	258	301	330	371	405	438	464	514
40	55	113	205	246	283	323	359	396	425	473
41	-6	-17	-46	-47	-40	-39	-39	-34	-34	-32
42	26	68	158	191	217	236	264	289	304	332
43	-3	-13	-16	-15	-13	-16	-17	-15	-20	-22
44	28	75	169	201	224	241	269	293	307	334
45	124	236	390	485	562	654	728	820	904	999
46	112	217	341	426	493	571	650	717	785	860
47	6	4	7	14	581	657	664	645	661	640
48	91	181	285	360	424	497	570	633	697	767
49	96	196	336	416	480	556	620	693	764	843
50	24	63	133	161	185	201	230	255	272	295
51	-5	-17	-16	-15	-16	-22	-22	-20	-26	-25
52	28	74	161	192	214	231	260	284	299	324
53	-10	-26	-38	-39	-38	-41	-39	-33	-35	-35
54	-20	-29	-30	-40	-53	-67	-78	-90	-104	-110
55	-12	-17	-15	-23	-32	-42	-50	-59	-69	-73
56	49	124	179	256	331	409	484	561	635	711
57	4	12	6	6	10	8	12	17	21	16
58	-237	-561	-1348	-1389	-1183	-1018	-960	-853	-728	-671
59	-4	-3	3	-7	-7	-15	-16	-15	-16	-19
60	44	105	175	245	315	388	457	529	600	672

Table E-23. Strain Data for Phase II, Limit Pressure [με] (Continued)

Strain Gage No.	Load Magnitude [% Maximum Pressure]									
	10%	20%	30%	40%	50%	60%	70%	80%	90%	100%
61	14	14	55	80	103	120	142	163	176	197
62	70	150	220	271	311	352	391	433	471	522
63	14	32	82	107	128	146	170	194	208	231
64	81	160	265	317	344	382	416	452	483	530
65	17	47	96	121	145	163	190	218	235	260
66	69	129	235	282	303	338	369	401	427	470
67	17	47	75	101	127	146	175	204	222	247
68	65	117	230	275	298	333	367	401	430	472
69	17	44	40	65	90	109	135	162	181	201
70	46	115	184	245	306	370	433	496	557	618
71	-233	-472	-1208	-1270	-1089	-939	-878	-769	-650	-600
72	50	123	208	283	351	426	494	566	635	708
73	27	93	163	184	198	209	227	250	266	287
74	10	22	25	41	57	68	80	95	103	115
75	5	8	29	43	57	66	78	91	98	111
76	24	57	170	184	185	181	208	228	239	261
77	43	121	194	271	342	416	490	565	632	701
78	9	21	22	26	28	29	34	39	43	42
79	-1	-1	3	3	7	7	7	9	15	22
80	19	49	75	110	145	182	218	254	289	325

Table E-24. Displacement Data for Phase II, Limit Pressure [inches]

LVDT No.	Load Magnitude [% Maximum Pressure]									
	10%	20%	30%	40%	50%	60%	70%	80%	90%	100%
1	0.000	0.000	0.001	0.002	0.004	0.005	0.007	0.009	0.010	0.012
2	0.000	0.000	0.000	0.001	0.002	0.002	0.003	0.004	0.005	0.006
3	0.000	-0.002	-0.004	-0.004	-0.003	-0.003	-0.002	-0.001	-0.001	0.000
4	0.000	-0.004	-0.010	-0.012	-0.011	-0.011	-0.011	-0.010	-0.010	-0.009
5	-0.001	-0.005	-0.012	-0.014	-0.014	-0.015	-0.015	-0.014	-0.015	-0.015
6	0.021	0.064	0.186	0.199	0.183	0.174	0.175	0.169	0.161	0.165
7	0.024	0.067	0.192	0.207	0.191	0.182	0.183	0.178	0.171	0.173
8	0.023	0.062	0.174	0.188	0.175	0.166	0.167	0.162	0.156	0.157
9	0.020	0.058	0.169	0.183	0.169	0.163	0.162	0.155	0.147	0.152
10	0.018	0.052	0.164	0.178	0.164	0.158	0.157	0.152	0.144	0.147
11	0.021	0.057	0.164	0.178	0.166	0.158	0.158	0.153	0.146	0.148

Table E-25. Load Data for Phase II, Limit Pressure

Loader	Load Magnitude [% Maximum Pressure]									
	10%	20%	30%	40%	50%	60%	70%	80%	90%	100%
Axial - 1	478	946	1486	2019	2559	3000	3554	4139	4568	5115
Axial - 2	467	922	1450	2024	2541	3005	3576	4161	4580	5107
Axial - 3	612	1094	1610	2155	2680	3163	3692	4300	4758	5283
Axial - 4	389	850	1339	1932	2447	2931	3491	4062	4503	5002
Axial - 5	570	1030	1560	2092	2643	3101	3639	4254	4695	5215
Axial - 6	348	800	1245	1794	2323	2796	3343	3931	4395	4890
Axial - 7	740	1195	1824	2287	2823	3269	3803	4396	4885	5321
Hoop - 1	1706	2983	4608	6071	7601	9085	10590	12204	13848	15163
Hoop - 2	1634	3052	4609	6152	7604	9179	10634	12199	13851	15195
Hoop - 3	1603	3053	4628	6186	7577	9156	10447	12163	13757	15204
Hoop - 4	1586	3262	4483	6106	7610	9060	10664	12242	13599	15208
Hoop - 5	1662	3178	4731	6116	7591	9157	10810	12318	13802	15192
Hoop - 6	1532	3005	4549	6066	7636	9189	10649	12305	13698	15204
Hoop - 7	1472	3039	4573	6093	7550	9073	10700	12278	13697	15179
Hoop - 8	1513	3038	4555	6018	7586	9102	10624	12213	13701	15212
Hoop - 9	1534	2986	4570	6069	7542	9241	10663	12197	13660	15205
Hoop - 10	1613	2996	4593	6072	7603	9160	10615	12207	13686	15251
Hoop - 11	1566	3032	4613	6165	7625	9109	10663	12205	13696	15227
Hoop - 12	1598	3007	4540	6042	7613	9146	10555	12168	13688	15187
Hoop - 13	1608	3039	4541	6165	7588	9171	10650	12232	13641	15174
Hoop - 14	1600	3043	4580	6092	7608	9100	10584	12128	13673	15174
Frame - 1H	267	576	867	1051	1408	1662	2004	2312	2563	2829
Frame - 2R	-315	-68	503	556	452	368	407	378	311	329
Frame - 3H	257	638	808	1002	1376	1563	1944	2281	2592	2844
Frame - 3R	-229	-30	525	584	513	438	510	505	472	471
Frame - 4R	-286	-84	321	406	306	238	249	228	179	176
Frame - 5H	-138	210	796	959	1265	1400	1721	1993	2337	2692
Frame - 6R	-421	-200	294	343	279	215	214	204	172	191
Frame - 7H	282	630	851	1125	1437	1680	2023	2391	2660	2860
Frame - 8H	400	742	981	1280	1634	1856	2253	2608	2960	3172
Frame - 8R	-306	-44	377	417	335	300	281	265	236	273
Frame - 9H	461	743	999	1262	1595	1823	2167	2500	2785	2961
Frame - 10R	-241	-48	413	473	411	384	399	372	330	395
Pressure	0.91	2.27	3.72	4.95	6.18	7.23	8.51	9.81	11.01	12.24

Table E-26. Strain Data for Phase II, Ultimate Pressure [με]

Strain Gage No.	Load Magnitude [% Maximum Pressure]									
	10%	20%	30%	40%	50%	60%	70%	80%	90%	100%
1	-3	13	26	60	92	124	144	184	214	240
2	68	122	165	219	254	310	359	397	449	492
3	59	111	150	198	226	276	320	349	395	434
4	-24	-6	5	34	57	86	102	135	158	181
5	196	372	543	682	804	946	1106	1217	1355	1492
6	70	128	178	236	268	325	373	407	459	499
7	95	153	213	277	313	374	425	456	512	552
8	129	213	284	355	398	469	538	576	646	700
9	119	196	254	313	347	405	459	487	544	583
10	103	180	234	290	327	381	432	463	515	553
11	95	228	358	486	609	737	870	984	1110	1247
12	218	419	612	771	911	1073	1254	1383	1542	1698
13	81	196	314	432	551	669	792	905	1022	1145
14	85	130	172	215	240	281	319	343	385	416
15	93	148	193	236	254	296	334	350	392	419
16	328	832	-2414	8962	10996	6281	4511	-178	-2043	-1142
17	70	122	162	207	227	268	305	322	362	390
18	43	83	117	160	185	228	265	291	333	365
19	192	366	532	668	788	927	1083	1192	1327	1461
20	-37	-10	0	28	53	81	94	128	151	170
21	56	115	159	207	241	290	334	367	414	455
22	50	101	143	189	223	272	317	349	396	437
23	-24	2	17	45	73	99	118	152	177	201
24	75	163	245	314	379	452	529	592	662	733
25	41	113	187	258	329	401	476	543	615	684
26	147	263	359	464	533	639	737	803	900	980
27	136	248	340	439	502	602	694	757	847	924
28	82	143	179	215	238	271	311	317	365	394
29	12	38	52	81	106	128	143	166	190	207
30	1	23	39	69	87	110	125	142	166	183
31	28	75	118	152	169	201	240	246	284	314
32	126	237	328	416	480	569	653	712	794	866
33	-781	-992	-1106	-1011	-778	-708	-711	-407	-366	-265
34	126	234	323	412	475	565	651	707	790	864

Table E-26. Strain Data for Phase II, Ultimate Pressure [με] (Continued)

Strain Gage No.	Load Magnitude [% Maximum Pressure]									
	10%	20%	30%	40%	50%	60%	70%	80%	90%	100%
35	-10	-27	-44	-53	-69	-84	-100	-119	-127	-145
36	-6	-24	-40	-51	-68	-92	-109	-127	-136	-154
37	176	246	313	387	439	499	561	597	670	712
38	196	266	335	403	443	488	541	575	649	699
39	170	234	299	369	412	468	519	551	620	664
40	122	185	249	323	375	434	491	530	600	643
41	-32	-38	-50	-42	-42	-34	-38	-31	-21	-17
42	93	155	197	244	269	314	354	376	421	451
43	-6	-4	-14	-9	-17	-11	-16	-20	-14	-16
44	97	157	200	246	268	314	356	374	418	445
45	185	353	490	645	787	938	1111	1223	1366	1484
46	218	320	447	555	655	764	865	970	1089	1202
47	11	15	10	16	6	12	6	-2	7	5
48	175	270	391	494	593	701	807	904	1012	1116
49	155	288	398	523	633	747	861	946	1066	1163
50	70	117	155	200	223	268	305	328	371	401
51	3	3	-8	-4	-12	-8	-13	-17	-12	-16
52	88	140	183	229	250	297	336	355	400	428
53	-10	-15	-25	-20	-21	-15	-20	-14	-6	-5
54	-4	-26	-44	-58	-77	-95	-112	-135	-146	-168
55	-4	-17	-32	-38	-53	-67	-84	-103	-111	-130
56	69	182	291	405	518	632	748	858	971	1088
57	4	1	3	5	5	9	13	15	13	15
58	-768	-984	-1104	-963	-675	-564	-549	-178	-109	43
59	5	-6	-2	-10	-18	-24	-19	-17	-24	-22
60	72	175	278	385	492	597	708	810	919	1024
61	42	92	121	158	182	218	247	273	307	332
62	121	181	250	329	387	451	515	559	637	686
63	51	94	123	162	186	226	257	282	322	350
64	168	236	308	379	424	482	539	567	638	675
65	51	92	124	167	194	238	272	301	344	375
66	160	221	286	348	387	439	490	516	577	611
67	32	72	102	146	175	221	254	286	329	363
68	164	223	290	353	396	450	502	533	596	633
69	-2	37	64	103	131	172	202	233	272	303

Table E-26. Strain Data for Phase II, Ultimate Pressure [με] (Continued)

Strain Gage No.	Load Magnitude [% Maximum Pressure]									
	10%	20%	30%	40%	50%	60%	70%	80%	90%	100%
70	77	172	266	359	450	545	641	725	814	908
71	-713	-970	-1107	-973	-710	-611	-606	-257	-184	-46
72	87	204	311	420	521	629	744	843	941	1047
73	58	80	103	137	156	192	231	246	285	319
74	10	30	40	70	82	106	120	139	162	177
75	20	35	47	75	87	109	125	139	164	178
76	135	146	187	214	222	253	298	297	337	375
77	76	194	306	414	519	628	728	840	943	1045
78	13	14	20	25	27	33	38	48	51	57
79	1	-7	1	8	11	13	28	25	34	43
80	29	80	133	185	240	292	346	400	454	509

Table E-27. Displacement Data for Phase II, Ultimate Pressure [inches]

LVDT No.	Load Magnitude [% Maximum Pressure]									
	10%	20%	30%	40%	50%	60%	70%	80%	90%	100%
1	0.002	0.004	0.006	0.009	0.012	0.015	0.018	0.021	0.024	0.026
2	0.001	0.002	0.003	0.005	0.006	0.007	0.009	0.010	0.012	0.013
3	-0.002	-0.003	-0.002	-0.001	0.001	0.002	0.004	0.005	0.007	0.008
4	-0.008	-0.010	-0.010	-0.010	-0.008	-0.008	-0.006	-0.005	-0.003	-0.002
5	-0.007	-0.010	-0.010	-0.012	-0.011	-0.011	-0.011	-0.010	-0.009	-0.008
6	0.115	0.154	0.176	0.173	0.153	0.152	0.161	0.134	0.137	0.131
7	0.119	0.161	0.185	0.183	0.163	0.163	0.171	0.143	0.146	0.138
8	0.104	0.144	0.168	0.165	0.146	0.145	0.155	0.127	0.128	0.121
9	0.109	0.160	0.170	0.147	0.142	0.144	0.159	0.109	0.134	0.112
10	0.101	0.141	0.162	0.159	0.141	0.141	0.149	0.121	0.125	0.118
11	0.101	0.140	0.163	0.158	0.142	0.141	0.149	0.123	0.125	0.119

Table E-28. Load Data for Phase II, Ultimate Pressure

	Load Magnitude [% Maximum Pressure]									
	10%	20%	30%	40%	50%	60%	70%	80%	90%	100%
Axial - 1	926	1759	2513	3393	4071	4953	5704	6396	7303	8038
Axial - 2	970	1825	2560	3438	4132	4999	5760	6503	7354	8132
Axial - 3	890	1752	2496	3373	4087	4947	5700	6456	7301	8086
Axial - 4	914	1778	2503	3374	4075	4937	5690	6474	7307	8057
Axial - 5	591	1442	2160	3046	3740	4608	5364	6127	6967	7736
Axial - 6	724	1578	2289	3164	3852	4731	5502	6262	7116	7869
Axial - 7	963	1758	2453	3312	3939	4815	5620	6403	7200	7953
Hoop - 1	2283	4632	6879	9220	11304	13706	15970	18331	20508	22847
Hoop - 2	2246	4514	6795	9125	11324	13701	16005	18316	20605	22814
Hoop - 3	2337	4451	6918	9053	11409	13558	15921	18128	20464	22738
Hoop - 4	2136	4609	6886	9257	11406	13703	16054	18237	20535	22875
Hoop - 5	2180	4607	6800	9118	11345	13816	15988	18428	20552	22862
Hoop - 6	2291	4474	6828	9169	11454	13617	15982	18348	20541	22811
Hoop - 7	2245	4564	6865	9179	11332	13718	15834	18240	20553	22835
Hoop - 8	2314	4536	6816	9163	11431	13679	16007	18253	20588	22864
Hoop - 9	2096	4521	6809	9084	11312	13692	15926	18253	20559	22858
Hoop - 10	2177	4618	6694	9220	11491	13715	16152	18344	20568	22798
Hoop - 11	2299	4531	6877	9098	11428	13661	16008	18249	20545	22867
Hoop - 12	2297	4646	6887	9259	11364	13689	15956	18227	20522	22911
Hoop - 13	2236	4550	6863	9157	11283	13696	16022	18243	20509	22812
Hoop - 14	2215	4514	7019	9180	11402	13640	15974	18253	20564	22853
Frame - 1H	534	778	1273	1739	2172	2545	3098	3437	3848	4346
Frame - 2R	109	284	396	381	238	242	308	139	164	167
Frame - 3H	483	858	1394	1857	2319	2737	3243	3846	4162	4632
Frame - 3R	143	327	475	497	388	418	475	342	360	323
Frame - 4R	53	273	415	368	227	222	279	81	107	81
Frame - 5H	615	761	1321	1883	2275	2623	3321	3544	4034	4587
Frame - 6R	127	235	335	313	235	234	317	169	198	213
Frame - 7H	399	782	1268	1661	2126	2572	2984	3508	3886	4342
Frame - 8H	383	744	1279	1728	2159	2683	3239	3724	4099	4612
Frame - 8R	86	252	363	366	227	217	289	78	131	112
Frame - 9H	393	786	1273	1765	2182	2657	3024	3503	3793	4207
Frame - 10R	154	355	455	473	411	404	493	337	400	413
Pressure	1.61	3.56	5.56	7.43	9.11	10.95	12.96	14.71	16.60	18.46

E.2 CODE LISTING 1: WRAPPER FUNCTION FOR STEPS 1, 2, AND 3.

```
function [ structure ] = processRawData( vxiFile, hbmFile, loadCaseProp )
%readRawData creates two arrays of data from raw data files
%   Inputs:
%       vxiFile - string that specifies VXI file name
%       hbmFile - string that specifies HBM file name
%
%       %%%%%%%%%%%%%%%%%%%%%%%%%%%%%%%%%%%%%%%%%%%%%
%       % Must have only one worksheet               %
%       %%%%%%%%%%%%%%%%%%%%%%%%%%%%%%%%%%%%%%%%%%%%%
%
%       loadCaseName - array containing strings describing file
%           format [phase, appAxial, appP, runDate, runStartTime,
loadCaseName]
%           phase: 'Phase1', 'Phase2', 'Phase3'
%           appAxial: target axial load
%           appP: target pressure
%           runDate: load case run date YYMMDD, e.g.  '11_09_15' = (Sept 9,
%           2011)
%           runTime: load case run time 24hr, e.g.  '14_15' = (2:15PM)
%           loadCaseName: 'pressure', 'axial', 'combined'

% Load data files
vxiData = xlsread(vxiFile);
hbmData = xlsread(hbmFile);

% Delete header information
vxiData = deleteNaNRows(vxiData);
hbmData = deleteNaNRows(hbmData);

% Bring data into a structure
structure = populateDataComplete(vxiData,hbmData);

% Parse loadCaseProp array
structure.meta.phase = cell2mat(loadCaseProp(1));
structure.meta.appAxial = cell2mat(loadCaseProp(2));
structure.meta.appP = cell2mat(loadCaseProp(3));
structure.meta.timeStamp = cell2mat(loadCaseProp(4));
structure.meta.loadCaseName = cell2mat(loadCaseProp(5));
structure.meta.loadMag = cell2mat(loadCaseProp(6));
structure.meta.loadMagP = cell2mat(loadCaseProp(7));
structure.meta.loadMagAxial = cell2mat(loadCaseProp(8));
structure.meta.processedTimeStamp = cell2mat(loadCaseProp(9));

% Zero SG + LVDT
structure = zeroData(structure);

% Build file name
filename =
[structure.meta.phase,'_',structure.meta.loadCaseName,'_',structure.meta.load
Mag];
% Save structure as .mat
disp('Saving structure')
```

```
save([filename,'.mat'], 'structure')
% Save as excel file
disp('Saving data in excel format')
saveStructToExcel(structure,filename)

sprintf('Data processing complete, saved as: %s',filename)
disp('-----------------------------------------------------')


end
```

E.3 CODE LISTING 2: FUNCTION TO BUILD A DATA STRUCTURE.

```
function [ structure ] = populateDataComplete(vxiData,hbmData )
%populateDataComplete adds all data to the test data structure
%   Inputs:
%       vxiData - array with vxi data from the circular buffer
%       hbmData - array with hbm data (headers must be removed)
%   Outputs:
%       structure - structure containing all data
%       structure.full - data sampled at full rate
%

% Create data structure without down sampling
structure.full = dataMap();
% fnType is a cell array of fieldnames at the type level
fnType = fieldnames(structure.full);
% Loop through each type category: AD8,AD7,AD4,fuse,LVDT,SG
for indexType = 1:length(fnType)
    fnTypeCurrent = fnType{indexType};
    % fnNumber is a cell array of fieldnames at the number level
    fnNumber = fieldnames(structure.full.(fnType{indexType}));

    % Loop through each type number: e.g.  AD8_1, AD8_2, ...
    for indexNumber = 1:length(fnNumber)
        fnNumberCurrent = fnNumber{indexNumber};

        if isfield(structure.full.(fnTypeCurrent).(fnNumberCurrent),'system')
            if
strcmp(structure.full.(fnTypeCurrent).(fnNumberCurrent).system,'vxi')
                data = vxiData;
            else
                data = hbmData;
            end
        end

        % Handle axial, hoop, frame, and pressure
        if isfield(structure.full.(fnTypeCurrent).(fnNumberCurrent),'tar')
            structure.full.(fnTypeCurrent).(fnNumberCurrent).tar =
data(:,structure.full.(fnTypeCurrent).(fnNumberCurrent).arrayIndex(1));
            structure.full.(fnTypeCurrent).(fnNumberCurrent).cmd =
data(:,structure.full.(fnTypeCurrent).(fnNumberCurrent).arrayIndex(2));
            structure.full.(fnTypeCurrent).(fnNumberCurrent).value =
data(:,structure.full.(fnTypeCurrent).(fnNumberCurrent).arrayIndex(3));

        % Handle SG + LVDT
        else
            structure.full.(fnTypeCurrent).(fnNumberCurrent).value =
data(:,structure.full.(fnTypeCurrent).(fnNumberCurrent).arrayIndex(1));
        end
     end

end
end
```

E.4 Code Listing 3: Function That Builds Skeleton of Data Structure With Mapping to Raw Data Files.

```
function [ dataStruct ] = dataMap( )
%vxiDataMap creates a structure which maps channel labels to array index
%   arrayIndex = [tar, cmd, value]

% Axial Loaders
dataStruct.AD8.AD8_1 = struct('arrayIndex',[8,58,22], 'system','vxi',
'tar',[], 'cmd',[], 'value',[], 'label','Axial Load', 'units','lbs');
dataStruct.AD8.AD8_2 = struct('arrayIndex',[9,59,23], 'system','vxi',
'tar',[], 'cmd',[], 'value',[], 'label','Axial Load', 'units','lbs');
dataStruct.AD8.AD8_3 = struct('arrayIndex',[10,60,24], 'system','vxi',
'tar',[], 'cmd',[], 'value',[], 'label','Axial Load', 'units','lbs');
dataStruct.AD8.AD8_4 = struct('arrayIndex',[11,61,25], 'system','vxi',
'tar',[], 'cmd',[], 'value',[], 'label','Axial Load', 'units','lbs');
dataStruct.AD8.AD8_5 = struct('arrayIndex',[12,62,26], 'system','vxi',
'tar',[], 'cmd',[], 'value',[], 'label','Axial Load', 'units','lbs');
dataStruct.AD8.AD8_6 = struct('arrayIndex',[13,63,27], 'system','vxi',
'tar',[], 'cmd',[], 'value',[], 'label','Axial Load', 'units','lbs');
dataStruct.AD8.AD8_7 = struct('arrayIndex',[14,64,28], 'system','vxi',
'tar',[], 'cmd',[], 'value',[], 'label','Axial Load', 'units','lbs');
dataStruct.AD8.AD8_3_hbm = struct('arrayIndex',8, 'system','hbm', 'value',[],
'label','Axial Load', 'units','lbs');

% Hoop Loaders
dataStruct.AD7.AD7_1 = struct('arrayIndex',[95,160,118], 'system','vxi',
'tar',[], 'cmd',[], 'value',[], 'label','Hoop Load', 'units','lbs');
dataStruct.AD7.AD7_2 = struct('arrayIndex',[96,161,119], 'system','vxi',
'tar',[], 'cmd',[], 'value',[], 'label','Hoop Load', 'units','lbs');
dataStruct.AD7.AD7_3 = struct('arrayIndex',[97,162,120], 'system','vxi',
'tar',[], 'cmd',[], 'value',[], 'label','Hoop Load', 'units','lbs');
dataStruct.AD7.AD7_4 = struct('arrayIndex',[98,163,121], 'system','vxi',
'tar',[], 'cmd',[], 'value',[], 'label','Hoop Load', 'units','lbs');
dataStruct.AD7.AD7_5 = struct('arrayIndex',[99,164,122], 'system','vxi',
'tar',[], 'cmd',[], 'value',[], 'label','Hoop Load', 'units','lbs');
dataStruct.AD7.AD7_6 = struct('arrayIndex',[100,165,123], 'system','vxi',
'tar',[], 'cmd',[], 'value',[], 'label','Hoop Load', 'units','lbs');
dataStruct.AD7.AD7_7 = struct('arrayIndex',[101,166,124], 'system','vxi',
'tar',[], 'cmd',[], 'value',[], 'label','Hoop Load', 'units','lbs');
dataStruct.AD7.AD7_8 = struct('arrayIndex',[188,251,209], 'system','vxi',
'tar',[], 'cmd',[], 'value',[], 'label','Hoop Load', 'units','lbs');
dataStruct.AD7.AD7_9 = struct('arrayIndex',[189,252,210], 'system','vxi',
'tar',[], 'cmd',[], 'value',[], 'label','Hoop Load', 'units','lbs');
dataStruct.AD7.AD7_10 = struct('arrayIndex',[190,253,211], 'system','vxi',
'tar',[], 'cmd',[], 'value',[], 'label','Hoop Load', 'units','lbs');
dataStruct.AD7.AD7_11 = struct('arrayIndex',[191,254,212], 'system','vxi',
'tar',[], 'cmd',[], 'value',[], 'label','Hoop Load', 'units','lbs');
dataStruct.AD7.AD7_12 = struct('arrayIndex',[192,255,213], 'system','vxi',
'tar',[], 'cmd',[], 'value',[], 'label','Hoop Load', 'units','lbs');
dataStruct.AD7.AD7_13 = struct('arrayIndex',[193,256,214], 'system','vxi',
'tar',[], 'cmd',[], 'value',[], 'label','Hoop Load', 'units','lbs');
dataStruct.AD7.AD7_14 = struct('arrayIndex',[194,257,215], 'system','vxi',
'tar',[], 'cmd',[], 'value',[], 'label','Hoop Load', 'units','lbs');
```

```
% Frame Loaders
dataStruct.AD4.AD4_1H = struct('arrayIndex',[89,154,142], 'system','vxi',
'tar',[], 'cmd',[], 'value',[], 'type','hoop', 'label','Hoop Frame Load',
'units','lbs');
dataStruct.AD4.AD4_2R = struct('arrayIndex',[90,155,143], 'system','vxi',
'tar',[], 'cmd',[], 'value',[], 'type','radial', 'label','Radial Frame Load',
'units','lbs');
dataStruct.AD4.AD4_3H = struct('arrayIndex',[91,156,144], 'system','vxi',
'tar',[], 'cmd',[], 'value',[], 'type','hoop', 'label','Hoop Frame Load',
'units','lbs');
dataStruct.AD4.AD4_3R = struct('arrayIndex',[91,156,145], 'system','vxi',
'tar',[], 'cmd',[], 'value',[], 'type','radial', 'label','Radial Frame Load',
'units','lbs');
dataStruct.AD4.AD4_4R = struct('arrayIndex',[93,158,146], 'system','vxi',
'tar',[], 'cmd',[], 'value',[], 'type','radial', 'label','Radial Frame Load',
'units','lbs');
dataStruct.AD4.AD4_5H = struct('arrayIndex',[94,159,147], 'system','vxi',
'tar',[], 'cmd',[], 'value',[], 'type','hoop', 'label','Hoop Frame Load',
'units','lbs');
dataStruct.AD4.AD4_6R = struct('arrayIndex',[182,245,233], 'system','vxi',
'tar',[], 'cmd',[], 'value',[], 'type','radial', 'label','Radial Frame Load',
'units','lbs');
dataStruct.AD4.AD4_7H = struct('arrayIndex',[183,246,234], 'system','vxi',
'tar',[], 'cmd',[], 'value',[], 'type','hoop', 'label','Hoop Frame Load',
'units','lbs');
dataStruct.AD4.AD4_8H = struct('arrayIndex',[185,248,236], 'system','vxi',
'tar',[], 'cmd',[], 'value',[], 'type','hoop', 'label','Hoop Frame Load',
'units','lbs');
dataStruct.AD4.AD4_8R = struct('arrayIndex',[185,248,235], 'system','vxi',
'tar',[], 'cmd',[], 'value',[], 'type','radial', 'label','Radial Frame Load',
'units','lbs');
dataStruct.AD4.AD4_9H = struct('arrayIndex',[186,249,237], 'system','vxi',
'tar',[], 'cmd',[], 'value',[], 'type','hoop', 'label','Hoop Frame Load',
'units','lbs');
dataStruct.AD4.AD4_10R = struct('arrayIndex',[187,250,238], 'system','vxi',
'tar',[], 'cmd',[], 'value',[], 'type','radial', 'label','Radial Frame Load',
'units','lbs');

% Pressure
dataStruct.fuse.p = struct('arrayIndex',[18,68,30], 'system','vxi', 'tar',[],
'cmd',[], 'value',[], 'label','Internal Pressure', 'units','psi');
dataStruct.fuse.p_hbm = struct('arrayIndex',9, 'system','hbm', 'value',[],
'label','Internal Pressure', 'units','psi');

% LVDTs
% HBM
dataStruct.LVDT.LVDT_1 = struct('arrayIndex',2, 'system','hbm', 'value', [],
'label','Axial Displacement', 'units','in');
dataStruct.LVDT.LVDT_2 = struct('arrayIndex',3, 'system','hbm', 'value', [],
'label','Axial Displacement', 'units','in');
dataStruct.LVDT.LVDT_3 = struct('arrayIndex',4, 'system','hbm', 'value', [],
'label','Axial Displacement', 'units','in');
dataStruct.LVDT.LVDT_4 = struct('arrayIndex',7, 'system','hbm', 'value', [],
'label','Axial Displacement', 'units','in');
dataStruct.LVDT.LVDT_5 = struct('arrayIndex',6, 'system','hbm', 'value', [],
'label','Axial Displacement', 'units','in');
```

```
% VXI
dataStruct.LVDT.LVDT_6 = struct('arrayIndex',326, 'system','vxi', 'value',
[], 'label','Radial Displacement', 'units','in');
dataStruct.LVDT.LVDT_7 = struct('arrayIndex',327, 'system','vxi', 'value',
[], 'label','Radial Displacement', 'units','in');
dataStruct.LVDT.LVDT_8 = struct('arrayIndex',328, 'system','vxi', 'value',
[], 'label','Radial Displacement', 'units','in');
dataStruct.LVDT.LVDT_9 = struct('arrayIndex',329, 'system','vxi', 'value',
[], 'label','Radial Displacement', 'units','in');
dataStruct.LVDT.LVDT_10 = struct('arrayIndex',330, 'system','vxi', 'value',
[], 'label','Radial Displacement', 'units','in');
dataStruct.LVDT.LVDT_11 = struct('arrayIndex',223, 'system','vxi', 'value',
[], 'label','Radial Displacement', 'units','in');
dataStruct.LVDT.LVDT_12 = struct('arrayIndex',224, 'system','vxi', 'value',
[], 'label','Hoop Displacement', 'units','in');
dataStruct.LVDT.LVDT_13 = struct('arrayIndex',133, 'system','vxi', 'value',
[], 'label','Hoop Displacement', 'units','in');


% SGs
% HBM
dataStruct.SG.SG_35 = struct('arrayIndex',18, 'system','hbm', 'value', [],
'label','Axial Strain', 'units','\mu\epsilon');
dataStruct.SG.SG_36 = struct('arrayIndex',19, 'system','hbm', 'value', [],
'label','Axial Strain', 'units','\mu\epsilon');
dataStruct.SG.SG_37 = struct('arrayIndex',20, 'system','hbm', 'value', [],
'label','Axial Strain', 'units','\mu\epsilon');
dataStruct.SG.SG_38 = struct('arrayIndex',21, 'system','hbm', 'value', [],
'label','Axial Strain', 'units','\mu\epsilon');
dataStruct.SG.SG_39 = struct('arrayIndex',22, 'system','hbm', 'value', [],
'label','Axial Strain', 'units','\mu\epsilon');
dataStruct.SG.SG_40 = struct('arrayIndex',23, 'system','hbm', 'value', [],
'label','Axial Strain', 'units','\mu\epsilon');
dataStruct.SG.SG_45 = struct('arrayIndex',24, 'system','hbm', 'value', [],
'label','45° Strain', 'units','\mu\epsilon');
dataStruct.SG.SG_46 = struct('arrayIndex',25, 'system','hbm', 'value', [],
'label','45° Strain', 'units','\mu\epsilon');
dataStruct.SG.SG_48 = struct('arrayIndex',29, 'system','hbm', 'value', [],
'label','45° Strain', 'units','\mu\epsilon');
dataStruct.SG.SG_49 = struct('arrayIndex',34, 'system','hbm', 'value', [],
'label','45° Strain', 'units','\mu\epsilon');
dataStruct.SG.SG_54 = struct('arrayIndex',27, 'system','hbm', 'value', [],
'label','Axial Strain', 'units','\mu\epsilon');
dataStruct.SG.SG_55 = struct('arrayIndex',28, 'system','hbm', 'value', [],
'label','Axial Strain', 'units','\mu\epsilon');
dataStruct.SG.SG_62 = struct('arrayIndex',33, 'system','hbm', 'value', [],
'label','Axial Strain', 'units','\mu\epsilon');
dataStruct.SG.SG_64 = struct('arrayIndex',30, 'system','hbm', 'value', [],
'label','Axial Strain', 'units','\mu\epsilon');
dataStruct.SG.SG_66 = struct('arrayIndex',31, 'system','hbm', 'value', [],
'label','Axial Strain', 'units','\mu\epsilon');
dataStruct.SG.SG_68 = struct('arrayIndex',32, 'system','hbm', 'value', [],
'label','Axial Strain', 'units','\mu\epsilon');
% VXI
dataStruct.SG.SG_1 = struct('arrayIndex',270, 'system','vxi', 'value', [],
'label','Axial Strain', 'units','\mu\epsilon');
```

```
dataStruct.SG.SG_2 = struct('arrayIndex',271, 'system','vxi', 'value', [],
'label','Axial Strain', 'units','\mu\epsilon');
dataStruct.SG.SG_3 = struct('arrayIndex',272, 'system','vxi', 'value', [],
'label','Axial Strain', 'units','\mu\epsilon');
dataStruct.SG.SG_4 = struct('arrayIndex',273, 'system','vxi', 'value', [],
'label','Axial Strain', 'units','\mu\epsilon');
dataStruct.SG.SG_5 = struct('arrayIndex',274, 'system','vxi', 'value', [],
'label','Hoop Strain', 'units','\mu\epsilon');
dataStruct.SG.SG_6 = struct('arrayIndex',275, 'system','vxi', 'value', [],
'label','Axial Strain', 'units','\mu\epsilon');
dataStruct.SG.SG_7 = struct('arrayIndex',276, 'system','vxi', 'value', [],
'label','Axial Strain', 'units','\mu\epsilon');
dataStruct.SG.SG_8 = struct('arrayIndex',277, 'system','vxi', 'value', [],
'label','Axial Strain', 'units','\mu\epsilon');
dataStruct.SG.SG_9 = struct('arrayIndex',278, 'system','vxi', 'value', [],
'label','Axial Strain', 'units','\mu\epsilon');
dataStruct.SG.SG_10 = struct('arrayIndex',279, 'system','vxi', 'value', [],
'label','Axial Strain', 'units','\mu\epsilon');
dataStruct.SG.SG_11 = struct('arrayIndex',280, 'system','vxi', 'value', [],
'label','Hoop Strain', 'units','\mu\epsilon');
dataStruct.SG.SG_12 = struct('arrayIndex',281, 'system','vxi', 'value', [],
'label','Hoop Strain', 'units','\mu\epsilon');
dataStruct.SG.SG_13 = struct('arrayIndex',282, 'system','vxi', 'value', [],
'label','Hoop Strain', 'units','\mu\epsilon');
dataStruct.SG.SG_14 = struct('arrayIndex',283, 'system','vxi', 'value', [],
'label','Axial Strain', 'units','\mu\epsilon');
dataStruct.SG.SG_15 = struct('arrayIndex',284, 'system','vxi', 'value', [],
'label','Axial Strain', 'units','\mu\epsilon');
dataStruct.SG.SG_16 = struct('arrayIndex',285, 'system','vxi', 'value', [],
'label','Axial Strain', 'units','\mu\epsilon');
dataStruct.SG.SG_17 = struct('arrayIndex',286, 'system','vxi', 'value', [],
'label','Axial Strain', 'units','\mu\epsilon');
dataStruct.SG.SG_18 = struct('arrayIndex',287, 'system','vxi', 'value', [],
'label','Axial Strain', 'units','\mu\epsilon');
dataStruct.SG.SG_19 = struct('arrayIndex',288, 'system','vxi', 'value', [],
'label','Hoop Strain', 'units','\mu\epsilon');
dataStruct.SG.SG_20 = struct('arrayIndex',289, 'system','vxi', 'value', [],
'label','Axial Strain', 'units','\mu\epsilon');
dataStruct.SG.SG_21 = struct('arrayIndex',290, 'system','vxi', 'value', [],
'label','Axial Strain', 'units','\mu\epsilon');
dataStruct.SG.SG_22 = struct('arrayIndex',291, 'system','vxi', 'value', [],
'label','Axial Strain', 'units','\mu\epsilon');
dataStruct.SG.SG_23 = struct('arrayIndex',292, 'system','vxi', 'value', [],
'label','Axial Strain', 'units','\mu\epsilon');
dataStruct.SG.SG_24 = struct('arrayIndex',293, 'system','vxi', 'value', [],
'label','Hoop Strain', 'units','\mu\epsilon');
dataStruct.SG.SG_25 = struct('arrayIndex',294, 'system','vxi', 'value', [],
'label','Hoop Strain', 'units','\mu\epsilon');
dataStruct.SG.SG_26 = struct('arrayIndex',295, 'system','vxi', 'value', [],
'label','Axial Strain', 'units','\mu\epsilon');
dataStruct.SG.SG_27 = struct('arrayIndex',296, 'system','vxi', 'value', [],
'label','Axial Strain', 'units','\mu\epsilon');
dataStruct.SG.SG_28 = struct('arrayIndex',297, 'system','vxi', 'value', [],
'label','Axial Strain', 'units','\mu\epsilon');
dataStruct.SG.SG_29 = struct('arrayIndex',298, 'system','vxi', 'value', [],
'label','Axial Strain', 'units','\mu\epsilon');
```

```
dataStruct.SG.SG_30 = struct('arrayIndex',299, 'system','vxi', 'value', [],
'label','Axial Strain', 'units','\mu\epsilon');
dataStruct.SG.SG_31 = struct('arrayIndex',300, 'system','vxi', 'value', [],
'label','Axial Strain', 'units','\mu\epsilon');
dataStruct.SG.SG_32 = struct('arrayIndex',301, 'system','vxi', 'value', [],
'label','Axial Strain', 'units','\mu\epsilon');
dataStruct.SG.SG_33 = struct('arrayIndex',302, 'system','vxi', 'value', [],
'label','Hoop Strain', 'units','\mu\epsilon');
dataStruct.SG.SG_34 = struct('arrayIndex',303, 'system','vxi', 'value', [],
'label','Axial Strain', 'units','\mu\epsilon');
dataStruct.SG.SG_41 = struct('arrayIndex',304, 'system','vxi', 'value', [],
'label','Axial Strain', 'units','\mu\epsilon');
dataStruct.SG.SG_42 = struct('arrayIndex',305, 'system','vxi', 'value', [],
'label','Axial Strain', 'units','\mu\epsilon');
dataStruct.SG.SG_43 = struct('arrayIndex',306, 'system','vxi', 'value', [],
'label','Axial Strain', 'units','\mu\epsilon');
dataStruct.SG.SG_44 = struct('arrayIndex',307, 'system','vxi', 'value', [],
'label','Axial Strain', 'units','\mu\epsilon');
dataStruct.SG.SG_47 = struct('arrayIndex',308, 'system','vxi', 'value', [],
'label','Axial Strain', 'units','\mu\epsilon');
dataStruct.SG.SG_50 = struct('arrayIndex',309, 'system','vxi', 'value', [],
'label','Axial Strain', 'units','\mu\epsilon');
dataStruct.SG.SG_51 = struct('arrayIndex',310, 'system','vxi', 'value', [],
'label','Axial Strain', 'units','\mu\epsilon');
dataStruct.SG.SG_52 = struct('arrayIndex',311, 'system','vxi', 'value', [],
'label','Axial Strain', 'units','\mu\epsilon');
dataStruct.SG.SG_53 = struct('arrayIndex',312, 'system','vxi', 'value', [],
'label','Axial Strain', 'units','\mu\epsilon');
dataStruct.SG.SG_56 = struct('arrayIndex',313, 'system','vxi', 'value', [],
'label','Hoop Strain', 'units','\mu\epsilon');
dataStruct.SG.SG_57 = struct('arrayIndex',314, 'system','vxi', 'value', [],
'label','Hoop Strain', 'units','\mu\epsilon');
dataStruct.SG.SG_58 = struct('arrayIndex',315, 'system','vxi', 'value', [],
'label','Axial Strain', 'units','\mu\epsilon');
dataStruct.SG.SG_59 = struct('arrayIndex',316, 'system','vxi', 'value', [],
'label','Hoop Strain', 'units','\mu\epsilon');
dataStruct.SG.SG_60 = struct('arrayIndex',317, 'system','vxi', 'value', [],
'label','Hoop Strain', 'units','\mu\epsilon');
dataStruct.SG.SG_61 = struct('arrayIndex',318, 'system','vxi', 'value', [],
'label','Axial Strain', 'units','\mu\epsilon');
dataStruct.SG.SG_63 = struct('arrayIndex',319, 'system','vxi', 'value', [],
'label','Axial Strain', 'units','\mu\epsilon');
dataStruct.SG.SG_65 = struct('arrayIndex',320, 'system','vxi', 'value', [],
'label','Axial Strain', 'units','\mu\epsilon');
dataStruct.SG.SG_67 = struct('arrayIndex',321, 'system','vxi', 'value', [],
'label','Axial Strain', 'units','\mu\epsilon');
dataStruct.SG.SG_69 = struct('arrayIndex',322, 'system','vxi', 'value', [],
'label','Axial Strain', 'units','\mu\epsilon');
dataStruct.SG.SG_70 = struct('arrayIndex',323, 'system','vxi', 'value', [],
'label','Hoop Strain', 'units','\mu\epsilon');
dataStruct.SG.SG_71 = struct('arrayIndex',324, 'system','vxi', 'value', [],
'label','Hoop Strain', 'units','\mu\epsilon');
dataStruct.SG.SG_72 = struct('arrayIndex',325, 'system','vxi', 'value', [],
'label','Hoop Strain', 'units','\mu\epsilon');
dataStruct.SG.SG_73 = struct('arrayIndex',33, 'system','vxi', 'value', [],
'label','Axial Strain', 'units','\mu\epsilon');
```

```
dataStruct.SG.SG_74 = struct('arrayIndex',34, 'system','vxi', 'value', [],
'label','Axial Strain', 'units','\mu\epsilon');
dataStruct.SG.SG_75 = struct('arrayIndex',35, 'system','vxi', 'value', [],
'label','Axial Strain', 'units','\mu\epsilon');
dataStruct.SG.SG_76 = struct('arrayIndex',36, 'system','vxi', 'value', [],
'label','Axial Strain', 'units','\mu\epsilon');
dataStruct.SG.SG_77 = struct('arrayIndex',37, 'system','vxi', 'value', [],
'label','Hoop Strain', 'units','\mu\epsilon');
dataStruct.SG.SG_78 = struct('arrayIndex',216, 'system','vxi', 'value', [],
'label','Hoop Strain', 'units','\mu\epsilon');
dataStruct.SG.SG_79 = struct('arrayIndex',240, 'system','vxi', 'value', [],
'label','Hoop Strain', 'units','\mu\epsilon');
dataStruct.SG.SG_80 = struct('arrayIndex',125, 'system','vxi', 'value', [],
'label','Hoop Strain', 'units','\mu\epsilon');

end
```

E.5 CODE LISTING 4: FUNCTION THAT ZEROS STRAIN AND DISPLACEMENT DATA (STEPS 2 AND 3).

```
function [ zeroredStructure ] = zeroData( structure )
%zeroData creates a data structure with requested data zeroed
%   Creates a copy of the input structure and changes fields to
%   zero data.  Uses a minimum load threshold to throw out low-load level
%   data.
%
%   Inputs:
%       structure - data structure from processRawData


% Parameters
defaultAxialThreshold = 300;
defaultPressureThreshold = 0.2;
axialThresholdMax = 600;                        %Triggers error
pressureThresholdMax = 0.4;                     %Triggers error


% Find when loading begins
% This is a huge pain in the ass
% Assumptions:
%   1.  Loading doesn't start until load cells read above threshold
%   2.  Assume

% Finds index where tar becomes non-zero
axialTarStartIndex = find(structure.full.AD8.AD8_3.tar,1);
pressureTarStartIndex = find(structure.full.fuse.p.tar,1);

% Finds average of noise before loading starts, then calculates the
% threshold
axialStartAvg = mean(structure.full.AD8.AD8_3.value(1:axialTarStartIndex));
pressureStartAvg =
mean(structure.full.fuse.p.value(1:pressureTarStartIndex));
axialThreshold = axialStartAvg + defaultAxialThreshold;
pressureThreshold = pressureStartAvg + defaultPressureThreshold;

if axialThreshold > axialThresholdMax || pressureThreshold >
pressureThresholdMax
    disp 'Error, loads start above default threshold'

end

% Find the index where loading begins
axialLoadStartIndex = find(structure.full.AD8.AD8_3.value>axialThreshold,1);
pressureLoadStartIndex =
find(structure.full.fuse.p.value>pressureThreshold,1);

% Handle HBM
axialLoadStartIndexHBM =
find(structure.full.AD8.AD8_3_hbm.value>axialThreshold,1);
pressureLoadStartIndexHBM =
find(structure.full.fuse.p_hbm.value>pressureThreshold,1);
```

```
% Handle case of different axial and pressure start points
if axialLoadStartIndex ~= pressureLoadStartIndex
    loadStartIndexVXI = min([axialLoadStartIndex, pressureLoadStartIndex]);
    loadStartIndexHBM = min([axialLoadStartIndexHBM,
pressureLoadStartIndexHBM]);
else
    loadStartIndexVXI = axialLoadStartIndex;
    loadStartIndexHBM = axialLoadStartIndexHBM;
end



% Loops through type (e.g.  AD8, AD4, ..)
fnType = fieldnames(structure.full);
for indexType = 1:length(fnType)
    fnTypeCurrent = fnType{indexType};
    fnNumber = fieldnames(structure.full.(fnTypeCurrent));

    % Delete load data before loading begins
    % Should be true for all loaders
    if ~ismember(fnTypeCurrent,{'SG','LVDT'})
        for indexNumber = 1:length(fnNumber)
            fnNumberCurrent = fnNumber{indexNumber};

            % Get proper load start index depending on system
            if
strcmp(structure.full.(fnTypeCurrent).(fnNumberCurrent).system,'vxi')
                loadStartIndex = loadStartIndexVXI;
            else
                loadStartIndex = loadStartIndexHBM;
            end

            % Loop through category
            fnCat =
fieldnames(structure.full.(fnTypeCurrent).(fnNumberCurrent));
            for indexCat = 1:length(fnCat)
                fnCatCurrent = fnCat{indexCat};

                if ismember(fnCatCurrent,{'tar','cmd','value'})
                    tempStruct =
structure.full.(fnTypeCurrent).(fnNumberCurrent).(fnCatCurrent);

                    % Create new field name with z infront
                    newCatName = ['z' fnCatCurrent];

                    % Only grab data starting after loadStartIndex and zero

structure.full.(fnTypeCurrent).(fnNumberCurrent).(newCatName) =
tempStruct(loadStartIndex:end) - tempStruct(loadStartIndex);


                end
            end
```

```
        end


    % Zero strain gages
    else
        % Loops through number (e.g.  AD8-1, AD8-2)
        for indexNumber = 1:length(fnNumber)
            fnNumberCurrent = fnNumber{indexNumber};

            % Get proper load start index depending on system
            if
strcmp(structure.full.(fnTypeCurrent).(fnNumberCurrent).system,'vxi')
                loadStartIndex = loadStartIndexVXI;
            else
                loadStartIndex = loadStartIndexHBM;
            end

            % Only consider the value field
            tempStruct =
structure.full.(fnTypeCurrent).(fnNumberCurrent).value;

            % Only grab data starting after loadStartIndex  and zero
            structure.full.(fnTypeCurrent).(fnNumberCurrent).zvalue =
tempStruct(loadStartIndex:end) - tempStruct(loadStartIndex);
        end
    end

    % Account for rigid body motion (should only occur once)
    % Also change sign of LVDT
    if strcmp(fnTypeCurrent,'LVDT')
        % Calculate rbm
        rbm =
(structure.full.LVDT.LVDT_1.zvalue/2)+structure.full.LVDT.LVDT_2.zvalue;
        structure.full.(fnTypeCurrent).rbm.value = rbm;
        structure.full.(fnTypeCurrent).rbm.arrayIndex = '';
        structure.full.(fnTypeCurrent).rbm.system = '';

        % Loop through LVDT_2 thru LVDT_4
        LVDT_rbm = {'LVDT_2', 'LVDT_3', 'LVDT_4', 'LVDT_5'};
        for index = 1:4
            structure.full.(fnTypeCurrent).(LVDT_rbm{index}).zvalue = rbm -
structure.full.(fnTypeCurrent).(LVDT_rbm{index}).zvalue;
        end

        LVDT_changeSign =
{'LVDT_6','LVDT_7','LVDT_8','LVDT_9','LVDT_10','LVDT_11','LVDT_12','LVDT_13'}
;
        for index = 1:length(LVDT_changeSign)
            structure.full.(fnTypeCurrent).(LVDT_changeSign{index}).value =
structure.full.(fnTypeCurrent).(LVDT_changeSign{index}).value * -1;
            structure.full.(fnTypeCurrent).(LVDT_changeSign{index}).zvalue =
structure.full.(fnTypeCurrent).(LVDT_changeSign{index}).zvalue * -1;
        end
    end
end
```

```
zeroredStructure = structure;

end
```

E-6. Code Listing 5: Function That Tabulates Data At Each Load Step.

```
% File to create appendix material for FAA report
clear all;

% ----------------------------------------------------------------
% OPTIONS

% The file that contains the data we are operating on
file = 'Phase 2_pressure_ultimate.mat';

% The load steps we want tabulated data for
loadSteps = 0.1*[1 2 3 4 5 6 7 8 9 10];

% The error allowed in lbs for the risidual of the sum of all loaders from
% the target load step
loadStepTolerance = 100;

% ----------------------------------------------------------------
% CONSTANTS
loaders = {'AD8', 'AD7', 'AD4', 'fuse'};

% ----------------------------------------------------------------
load(file)

% Modify the structure "Structure" to include the specific data we want to
% tabulate

% Deal with some naming problems
if exist('dataStructure','var')
    Structure = dataStructure;
end

% Initailization
loadStepRowNumberVXI = zeros(1,length(loadSteps));
loadStepRowNumberHBM = zeros(1,length(loadSteps));

tempDataStructure = Structure;

% Find row where the loaders are closet to equilibrium
% Loop through each loadstep we need data for
for loadStep=1:length(loadSteps)

    % Set the target load for this load step
    driver = Structure.full.AD8.AD8_4;
    targetDriverLoad = loadSteps(loadStep)*Structure.meta.appAxial;
    if strcmp(Structure.meta.loadCaseName, 'pressure')
        driver = Structure.full.fuse.p;
        targetDriverLoad = loadSteps(loadStep)*Structure.meta.appP;
```

```
    loadStepTolerance = 0.1;
    disp 'driver is pressure'
end

% Get the specific target loads
targetPressureLoad = loadSteps(loadStep)*Structure.meta.appP;
targetAxialLoad = loadSteps(loadStep)*Structure.meta.appAxial;
targetHoopLoad = loadSteps(loadStep)*max(Structure.full.AD7.AD7_1.cmd);
targetFrameLoad = loadSteps(loadStep)*max(Structure.full.AD4.AD4_1H.cmd);

% Loop through the applied loads until we reach the start row which
% is defined as the first row were the cmd is steptar-2*tol
% Goal is to get a window on the target load rows
startRow = 0;
startTarget = targetDriverLoad-3*loadStepTolerance;
for i=1:length(driver.cmd)
    if driver.cmd(i) > startTarget
        startRow = i;
        break;
    end
end
if startRow == 0
    error 'Could not identify start row';
end

% Same thing but for end row
if loadStep ~= 10
    endRow = 0;
    endTarget = targetDriverLoad+5*loadStepTolerance;
    for i=startRow:length(driver.cmd)
        if driver.cmd(i)> endTarget
            endRow = i;
            break;
        end
    end
    if endRow == 0
        error 'Could not identify end row';
    end
else
    endRow = startRow+200;
    if(length(driver.cmd) < endRow)
        endRow = length(driver.cmd);
    end
end

% Goal is compute residual for each time instance, i
residual = zeros(endRow-startRow+1,1);

% Loop through each loader type
for typeIndex = 1:length(loaders)
    fnTypeCurrent = loaders{typeIndex};

    % Apply proper target load
    loadtarget = 0;
    % Frame loaders  (skip radial links)
    if strcmp(fnTypeCurrent, 'AD4')
```

```
            loadtarget = targetFrameLoad;
        elseif strcmp(fnTypeCurrent, 'AD7')
            loadtarget = targetHoopLoad;
        elseif strcmp(fnTypeCurrent, 'AD8')
            loadtarget = targetAxialLoad;
        elseif strcmp(fnTypeCurrent, 'fuse')
            loadtarget = targetPressureLoad;
        else
            % Just in case
            continue
        end


        % Loop through each loader number
        fnNumber = fieldnames(Structure.full.(fnTypeCurrent));
        for numberIndex = 1:length(fnNumber)
            fnNumberCurrent = fnNumber{numberIndex};
            loader = Structure.full.(fnTypeCurrent).(fnNumberCurrent);

            % Skip hbm load data and radial links
            if ~strcmp(loader.system,'hbm') && ~strcmp(fnNumberCurrent(end),
'R')

                % Loop through each time instance, i in the window, for
                % this loader
                for i=startRow:endRow
                    resIdx = i-startRow+1;

                    % Add the error on this loader to the residual
                    err = abs(loader.value(i) - loadtarget);
                    residual(resIdx) = residual(resIdx) + err;
                end
            end
        end
    end

    % Grab the time instance that minimizes the residual
    [value, index] = min(residual);

    % Get the row number
    loadStepRowNumberVXI(loadStep) = index - 1 + startRow;

    % Step 2: Find the corresponding row numbers for HBM
    % Normalizes the HBM load so it corresponds with VXI
    % Sets an upper bound to keep unloading from causing problems
    driverhbm = 'AD8_3_hbm';
    driverhbmcat = 'AD8';
    if strcmp(Structure.meta.loadCaseName, 'pressure')
        driverhbm = 'p_hbm';
        driverhbmcat = 'fuse';
    end
    % Upper bound, only compute once
    if loadStep == 1
        % Normalize load
        maxHBMload = max(Structure.full.(driverhbmcat).(driverhbm).value);
```

```
        % Get upper bound
        hbmMaxRes = abs(Structure.full.(driverhbmcat).(driverhbm).value -
maxHBMload);
        [~, MaxLoadIndex] = min(hbmMaxRes);
    end
    hbmRes = abs(Structure.full.(driverhbmcat).(driverhbm).value -
loadSteps(loadStep)*maxHBMload);
    [~, loadStepRowNumberHBM(loadStep)] = min(hbmRes(1:MaxLoadIndex+1000));

    % Offset for zvalue shift
    offsetHBM = length(Structure.full.SG.SG_35.value) -
length(Structure.full.SG.SG_35.zvalue);
    offsetVXI = length(Structure.full.SG.SG_1.value) -
length(Structure.full.SG.SG_1.zvalue);

    % Step 3: Build an array with all the data from selected rows
    % Loop through each data type
    dataTypes = {'SG', 'LVDT'};
    for typeIndex = 1:length(dataTypes)
        fnTypeCurrent = dataTypes{typeIndex};

        % Loop through each number
        fnNumber = fieldnames(Structure.full.(fnTypeCurrent));
        for numberIndex = 1:length(fnNumber)
            fnNumberCurrent = fnNumber{numberIndex};

            % Ignore the rbm (rigid body motion) structure
            if ~strcmp(fnNumberCurrent, 'rbm')
                device =  Structure.full.(fnTypeCurrent).(fnNumberCurrent);

                % Use the proper system (hbm vs vxi)
                if strcmp(device.system, 'hbm')
                    index = loadStepRowNumberHBM(loadStep)-offsetHBM;
                else
                    index = loadStepRowNumberVXI(loadStep)-offsetVXI;
                end

                % Get the tabulated data value for the load step
                tempValue = device.zvalue(index);

                % Create the tabulated data in mat

tempDataStructure.full.(fnTypeCurrent).(fnNumberCurrent).tabulatedData(loadSt
ep) =  tempValue;
            end
        end

    end

    % Get the loader data into tabulated form
    % Loop through each number
    for typeIndex = 1:length(loaders)
        fnTypeCurrent = loaders{typeIndex};
        fnNumber = fieldnames(Structure.full.(fnTypeCurrent));
```

```
        for numberIndex = 1:length(fnNumber)
            fnNumberCurrent = fnNumber{numberIndex};

            % ignore hbm channels
            nameSplit = regexp(fnNumberCurrent,'_','split');
            if ~strcmp(nameSplit(end), 'hbm')

                % Temporary
                device =  Structure.full.(fnTypeCurrent).(fnNumberCurrent);

                % Index of load;
                index = loadStepRowNumberVXI(loadStep);

tempDataStructure.full.(fnTypeCurrent).(fnNumberCurrent).tabulatedData(loadSt
ep) = device.value(index);
            end
        end
    end
end

% Step 4: Store the data to excel
dataToWrite = cell(94,11,3);
sgCounter = 1;
lvdtCounter = 1;
% Labels across the top
dataToWrite(1,2:end,1) = {0.1 0.2 0.3 0.4 0.5 0.6 0.7 0.8 0.9 1};
dataToWrite(1,2:end,2) = {0.1 0.2 0.3 0.4 0.5 0.6 0.7 0.8 0.9 1};
dataToWrite(1,2:end,3) = {0.1 0.2 0.3 0.4 0.5 0.6 0.7 0.8 0.9 1};

% Loop through each data type
dataTypes = {'SG', 'LVDT'};
for typeIndex = 1:length(dataTypes)
    fnTypeCurrent = dataTypes{typeIndex};

    % Loop through each number
    fnNumber = fieldnames(Structure.full.(fnTypeCurrent));
    for numberIndex = 1:length(fnNumber)
        fnNumberCurrent = fnNumber{numberIndex};

        % Ignore the rbm (rigid body motion) structure
        if ~strcmp(fnNumberCurrent, 'rbm')

            if strcmp(fnTypeCurrent,'SG')
                worksheet = 1;
                sgCounter = sgCounter + 1;
                curRow = sgCounter;
            else
                worksheet = 2;
                lvdtCounter = lvdtCounter + 1;
                curRow = lvdtCounter;
            end

            % Get the device number
            fnNumSplit = regexp(fnNumberCurrent,'_','split');
```

```
            % Add label in first column
            dataToWrite{curRow,1,worksheet} = fnNumSplit{2};

            % Append to array
            dataToWrite(curRow,2:end,worksheet) =
num2cell(tempDataStructure.full.(fnTypeCurrent).(fnNumberCurrent).tabulatedDa
ta);
        end
    end
end

% Loop through each loader
loadCounter = 1;
for typeIndex = 1:length(loaders)
    fnTypeCurrent = loaders{typeIndex};

    % Loop through each number
    fnNumber = fieldnames(Structure.full.(fnTypeCurrent));
    for numberIndex = 1:length(fnNumber)
        fnNumberCurrent = fnNumber{numberIndex};

        % Skip hbm
        nameSplit = regexp(fnNumberCurrent,'_','split');
        if ~strcmp(nameSplit(end),'hbm')

            % Increment
            loadCounter = loadCounter + 1;

            % Write row label
            if strcmp(nameSplit(1),'AD8')
                rowName = ['Axial - ' nameSplit{2}];
            elseif strcmp(nameSplit(1),'AD7')
                rowName = ['Hoop - ' nameSplit{2}];
            elseif strcmp(nameSplit(1),'AD4')
                rowName = ['Frame - ' nameSplit{2}];
            elseif strcmp(nameSplit(1),'p')
                rowName = 'Pressure';
            else
                error 'Unexpected data'
            end

            dataToWrite{loadCounter,1,3} = rowName;

            % Store the data
            dataToWrite(loadCounter,2:end,3) =
num2cell(tempDataStructure.full.(fnTypeCurrent).(fnNumberCurrent).tabulatedDa
ta);
        end
    end
end

% Store excel sheet
name = regexp(file,'\.','split');
xlsname = strcat(name{1}, '.xls');
xlswrite(xlsname, dataToWrite(:,:,1), 'SG')
```

```
xlswrite(xlsname, dataToWrite(:,:,2), 'LVDT')
xlswrite(xlsname, dataToWrite(:,:,3), 'Loaders')
```

APPENDIX F—DIGITAL IMAGE CORRELATION DATA

During the three test phases, digital image correlation (DIC) snapshots were captured for the two-bay region between F-2 and F-3 and S-3 and S-5. This appendix shows selected results for each test. The white regions are areas where results could not be computed because of interference from leaking water or strain gage wires.

The data reduction was performed such that virtual gauge length in DIC was similar to the strain gauge size used (0.125 to 0.25 inches). A facet size of 19 was used with a step size of 8 and computation size of 3. The image scale was estimated using the notch width and was typically about 0.015 inches per pixel.

Load data were recorded using the two analog data inputs on the DIC system. Calibration of the loads was performed at low load levels. While reducing the DIC data, some error was identified in the loads recorded by the DIC, and therefore using the maximum load point as a reference, the load was recalibrated in post processing to reduce the error.

Results are provided in the remainder of this appendix. Phase I results of axial strain fringe patterns for the combined load case are shown in figure F-1. These results indicate a uniform strain distribution in the test section from low loads through combined limit load.

Phase II axial strain results are shown in figure F-2 for the axial only load condition. Fringe patterns of the axial strain distribution are shown for three load levels with corresponding section plots on the right for three sections. These results show the development of a local strain concentration at the BVID location, which become evident once load reaches 100% DLL.

Phase III axial strain fringe patterns are shown in figure F-3 for six load levels during LS-2. The location of the adjacent stringer flange edge and first stitch row are highlighted with red and blue dashed lines. While results ahead of notch tip A were disrupted by leaking water, notch tip B shows the formation of the expected kidney shaped strain concentration as load increases. Strain gradients ahead of the notch tip in Phase III were examined in detail. Plots of strain along 0°, 45°, and 90° sections, at approximately 10% load increments up to visible damage formation are provided in figures F-4 through F-6. Extrapolating the axial strain along the 0 direction section plot at 70% DLL shows that the axial strain at the notch tip approached the material failure strain at the load level where damage formation was observed on the exterior surface.

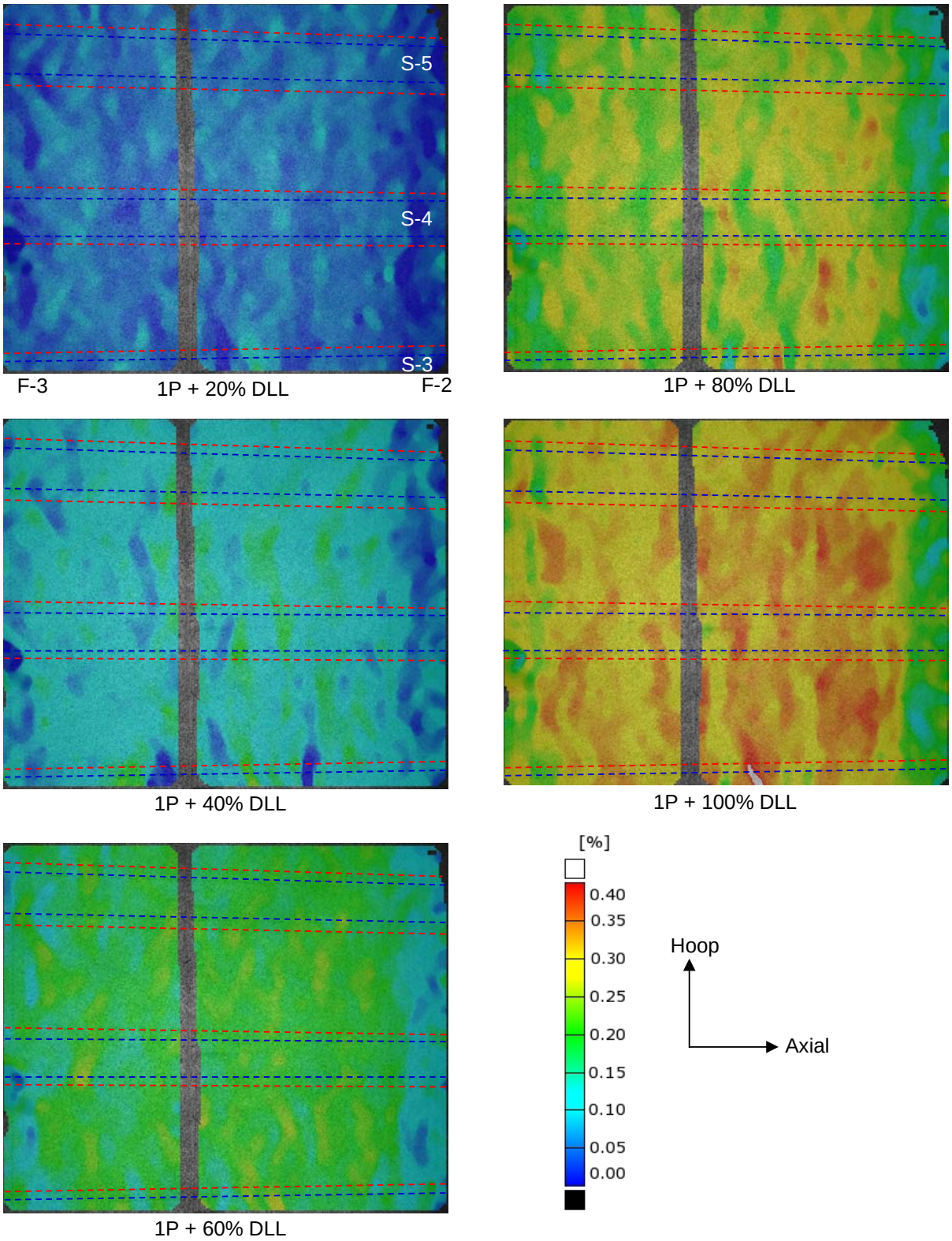

Figure F-1. Phase I, Combined Load, Axial Strain

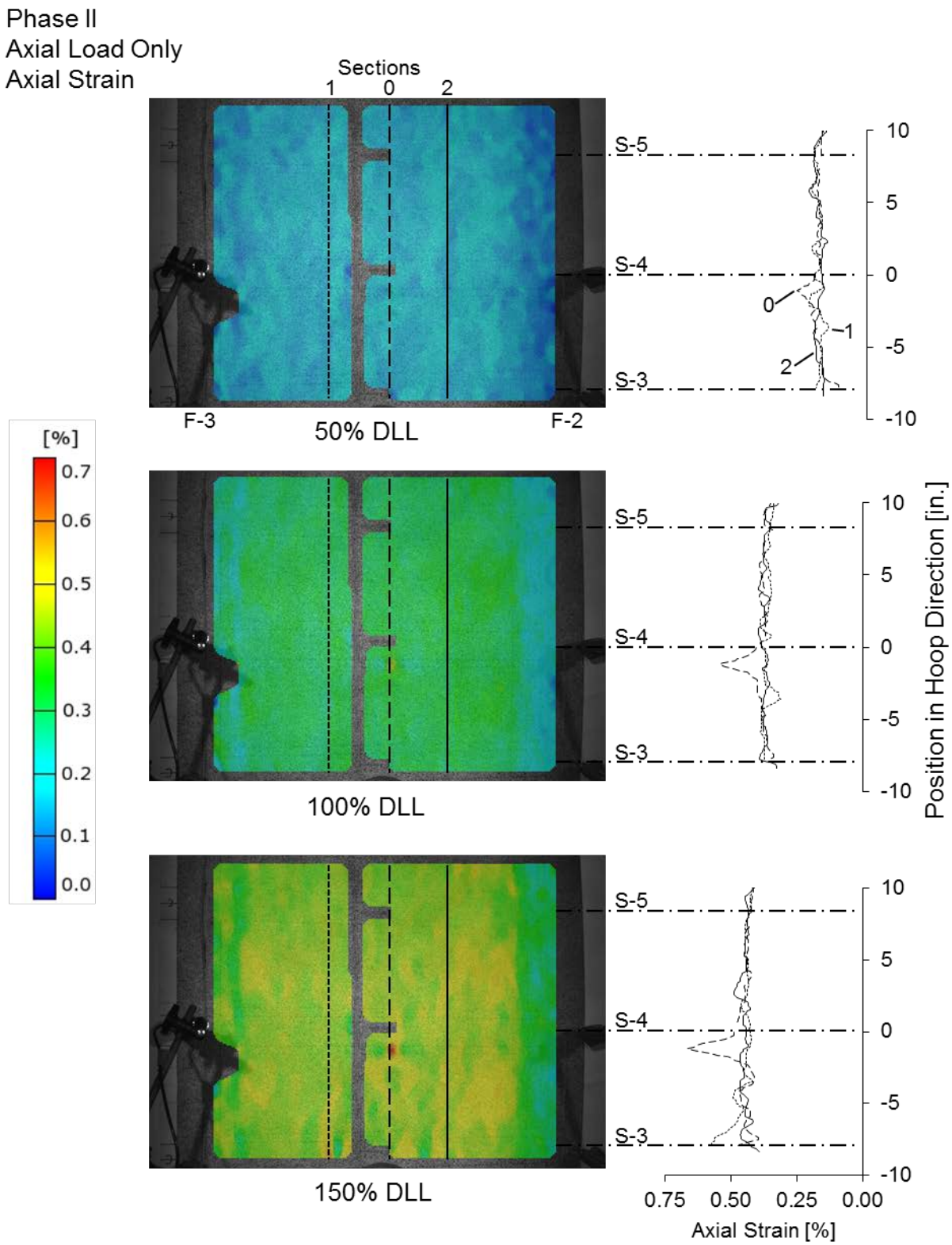

Figure F-2. Phase II, Axial Load Only, Axial Strain at Three Load Levels

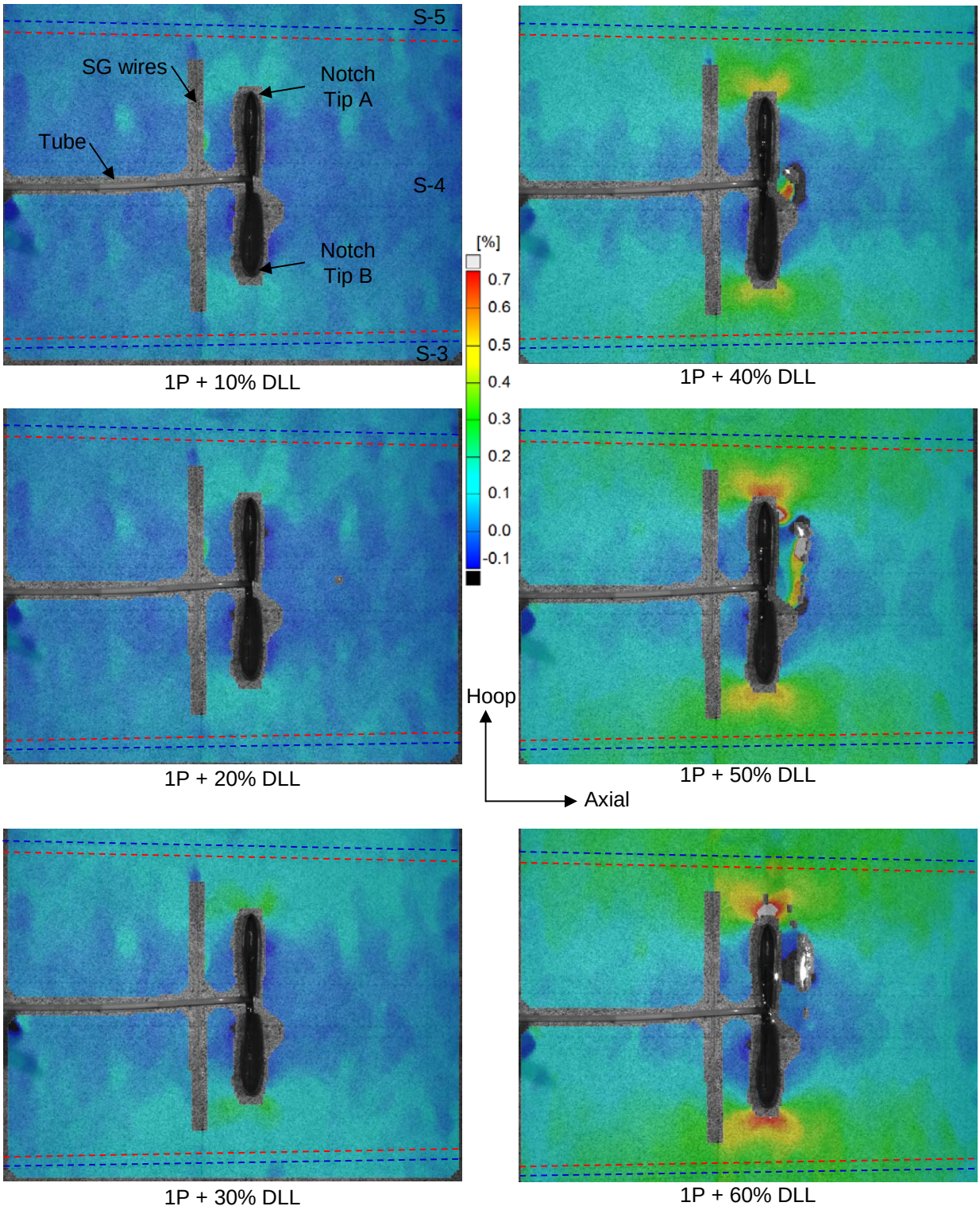

Figure F-3. Phase III, LS-2, Axial Strain Evolution up to Visible Damage Formation

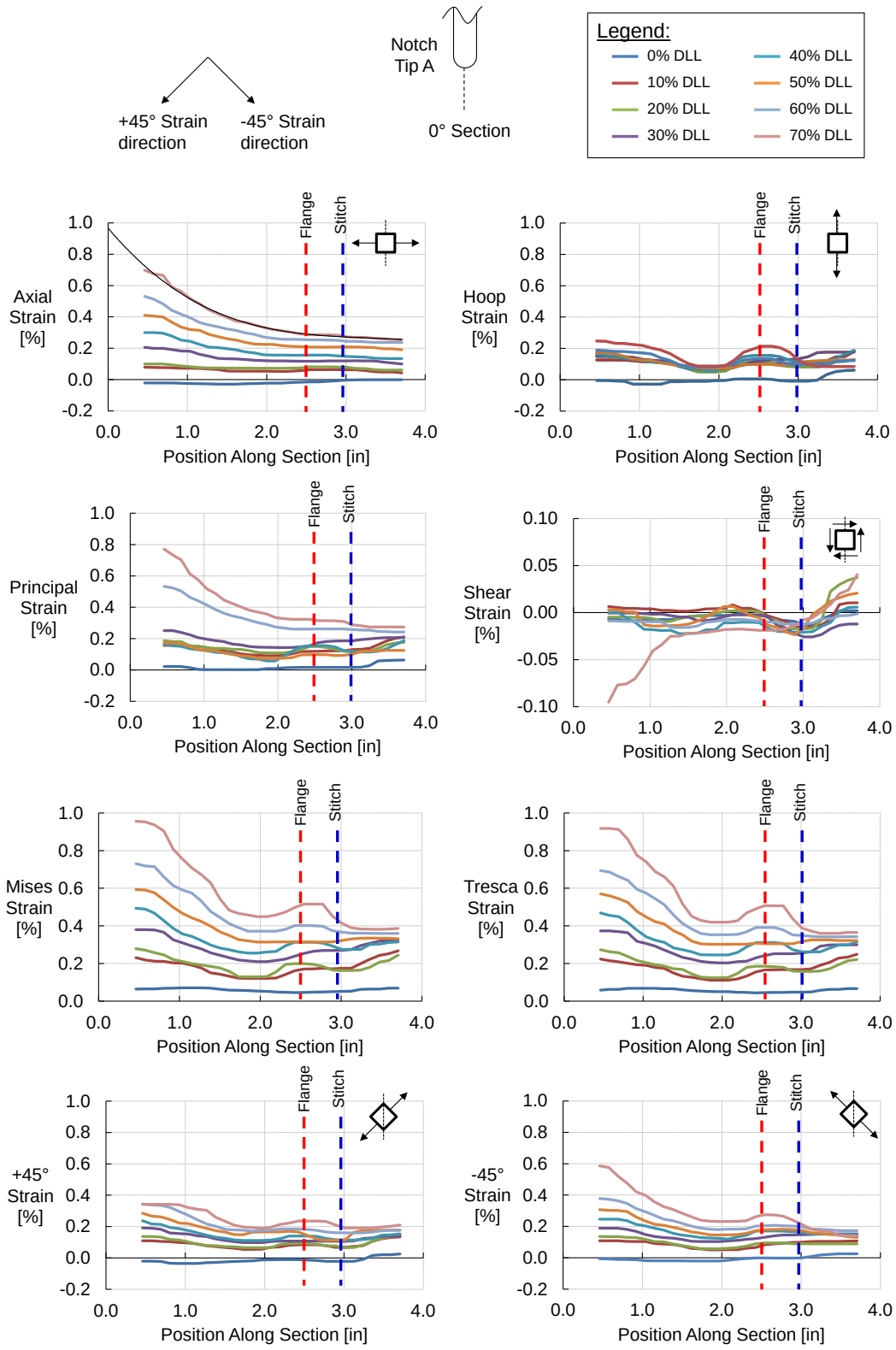

Figure F-4. Notch Tip Strains Along a Hoop Direction (0°) Section

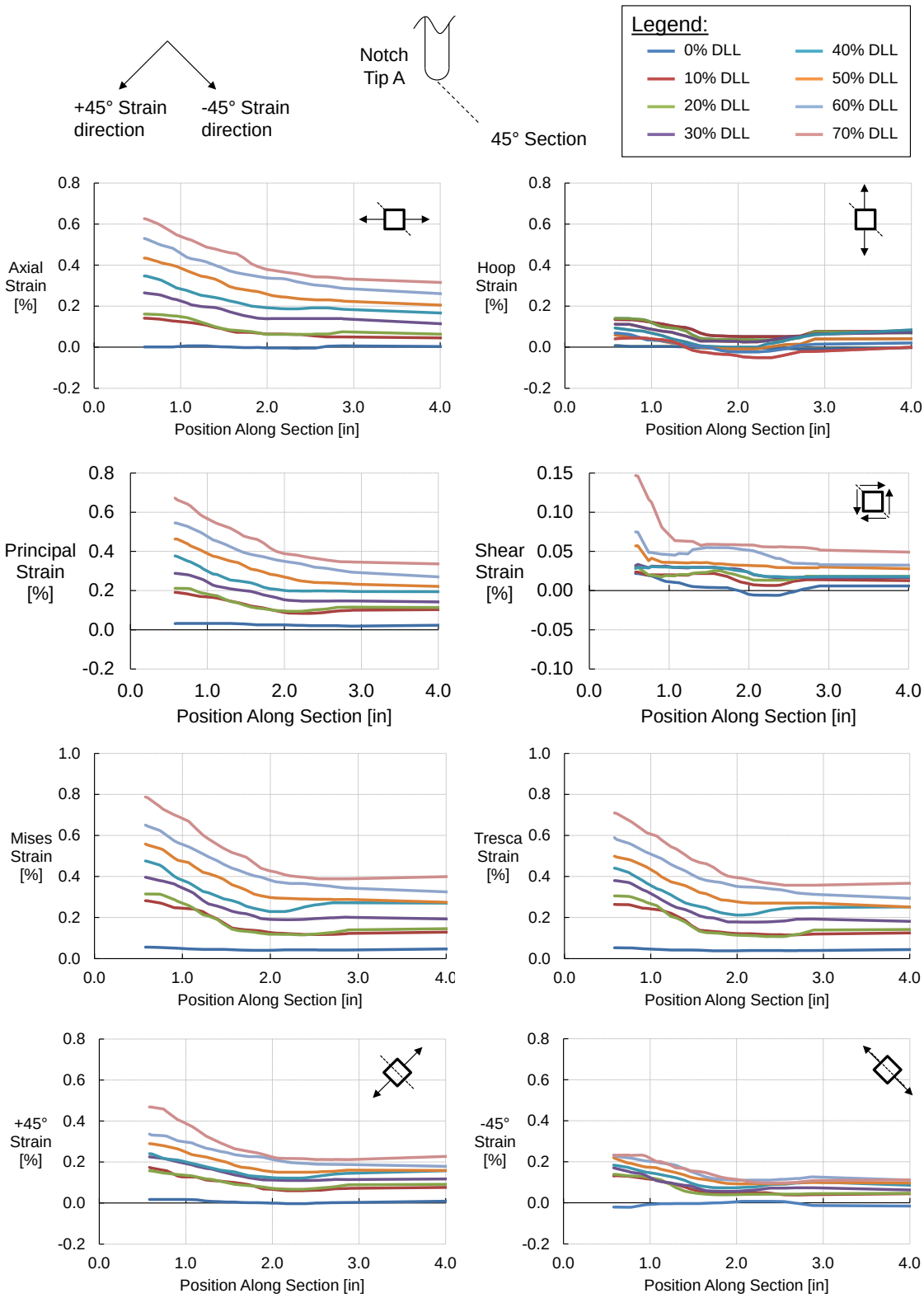

Figure F-5. Notch Tip Strains Along a 45°-Direction Section

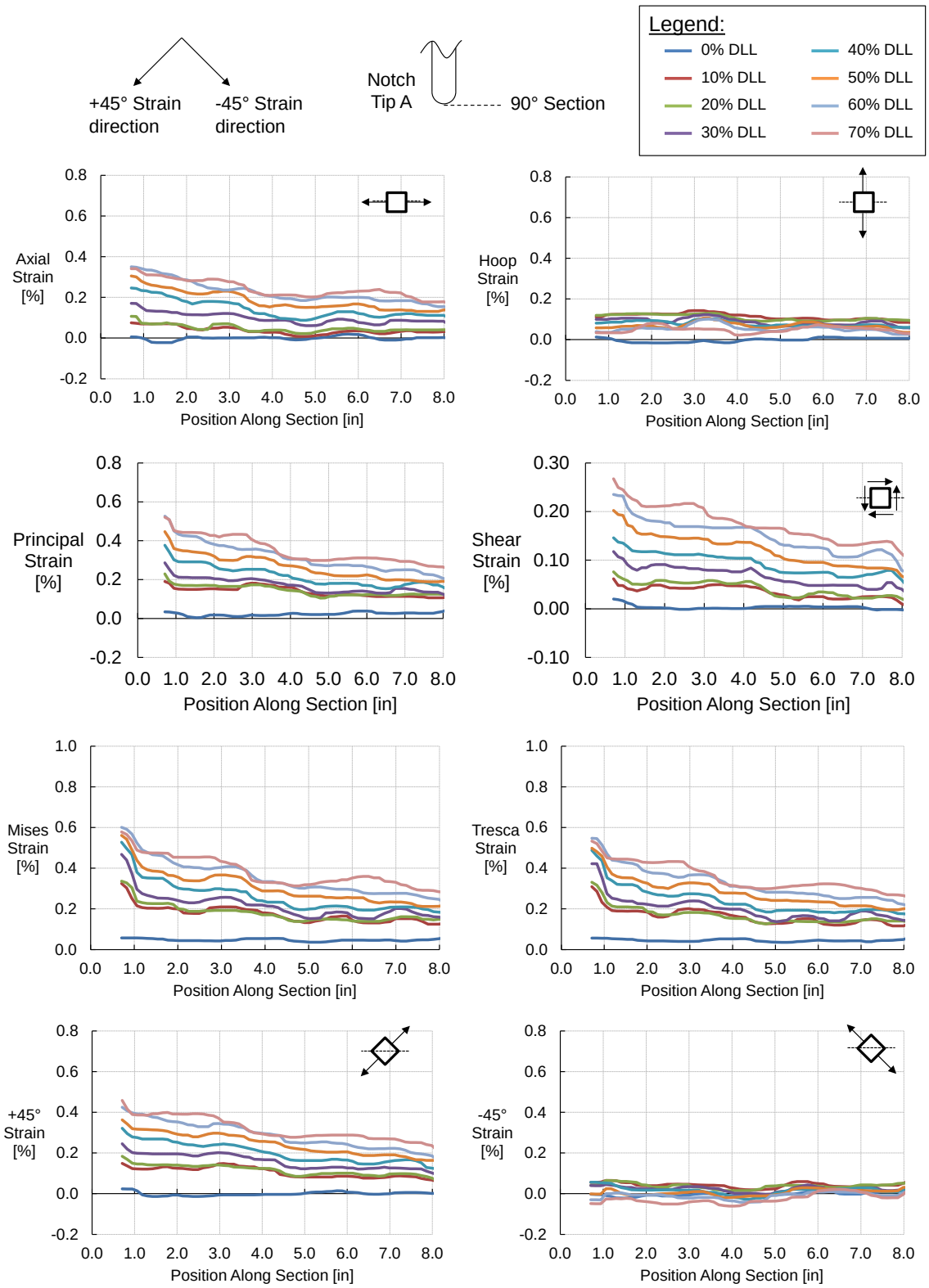

Figure F-6. Notch Tip Strains Along an Axial Direction (90°) Section

APPENDIX G—VISUAL MONITORING RESULTS

Throughout the test program, visual monitoring and inspections were conducted to identify damage formation and measure damage propagation. Still images, frames from video captures, and measurements made from the images are provided in this appendix. In all images captured during loading, the load magnitude is provided with the image. Note that no visual damage observations were made during Phase I, and therefore no images are provided.

Photographs from Phase II are shown prior to impact, after the first impact, after the second impact, and after all loadings were applied in figures G-1 through G-4. Measurements of the extent of visible damage are tabulated in table G-1 for the hoop and axial directions.

Table G-1. Measurements of Damage Extent During Phase II (units are inches)

Condition	Exterior		Interior	
	Hoop Direction	Axial Direction	Hoop Direction	Axial Direction
Baseline	-	-	-	-
After 1st impact	-	-	1.5	1.56
After 2nd impact	0.16	0.38	1.88	1.75
After loading	0.16	0.38	1.88	1.75

Photographs of Phase III damage formation and propagation are shown in figures G-5 through G-50. The exterior and interior camera images are shown in figures G-5 though G-32 and G-33 through G-50, respectively. The load when the exterior images were captured and the measurements of damage extent are provided in table G-2 up to the point where damage progressed out of the field of view. All of these exterior images are oriented such that the upper notch tip is notch tip B. The damage length was measured using two methods: (1) the length of the farthest most damage projected in the hoop direction and (2) the length of the path of the farthest most damage (excludes damage propagating directly in the hoop direction). Likewise, the interior image loads and damage extent are summarized in tables G-3 and G-4 for notch tip A and notch B, respectively. Interior images showing damage progression are only available for load step (LS) two.

Table G-2. Summary of Exterior Images and Damage Measurements During Phase III

Axial Load [% DLL]	Pressure [psi]	Figure No.	Damage in hoop direction		Damage path	
			Notch Tip A [in]	Notch Tip B [in]	Notch Tip A [in]	Notch Tip B [in]
0%	0	G-5	-	-	-	-
8%	7.35	G-6	-	-	-	-
12%	10.2	G-7	-	-	-	-
29%	9.2	G-8	-	-	-	-
41%	9.2	G-9	-	-	-	-
56%	9.2	G-10	-	-	-	-
70%	9.2	G-11	0.23	0.53	0.33	0.75
84%	9.2	G-12	0.60	0.75	0.85	1.07
88%	9.2	G-13	0.84	0.97	1.19	1.37
94%	9.2	G-14	1.18	1.44	1.67	2.04
100%	9.2	G-15	1.38	1.47	1.96	2.09
100%	0	G-16	1.38	1.47	1.96	2.09
100%	9.2	G-17	1.38	1.47	1.96	2.09
105%	9.2	G-18	2.00	1.73	2.82	2.45
110%	9.2	G-19	2.03	1.73	2.88	2.44
116%	9.2	G-20	2.35	1.73	3.33	2.45
121%	9.2	G-21	2.37	1.73	3.35	2.44
124%	9.2	G-22	2.38	2.63	3.36	3.72
134%	9.2	G-23	2.38	2.63	3.36	3.72
148%	9.2	G-24	4.00	2.94	5.66	4.16
163%	9.2	G-25	4.38	2.99	6.20	4.22

Table G-3. Summary of Interior Images and Damage Measurements During Phase III, LS-2, for Notch Tip A

Axial Load [%DLL]	Figure No.	Damage in hoop direction [in]	Damage path [in]
61%	G-33	0.6	0.88
66%	G-34	0.6	0.88
75%	G-35	0.6	0.88
80%	G-36	0.6	0.88
90%	G-37	1.8	2.47
95%	G-38	1.8	2.47
100%	G-39	1.8	2.47

Table G-4. Summary of Interior Images and Damage Measurements During Phase III, LS-2, for Notch Tip B

Axial Load [%DLL]	Figure No.	Damage in hoop direction [in]	Damage path [in]
54%	G-40	0.1	0.14
55%	G-41	0.4	0.53
63%	G-42	0.4	0.53
67%	G-43	0.6	0.88
74%	G-44	0.6	0.88
82%	G-45	0.6	0.88
83%	G-46	0.6	0.88
84%	G-47	1.5	2.12
88%	G-48	1.5	2.12
97%	Figure G-49	1.8	2.47
99%	G-50	1.8	2.47

(a) Exterior

(b) Interior

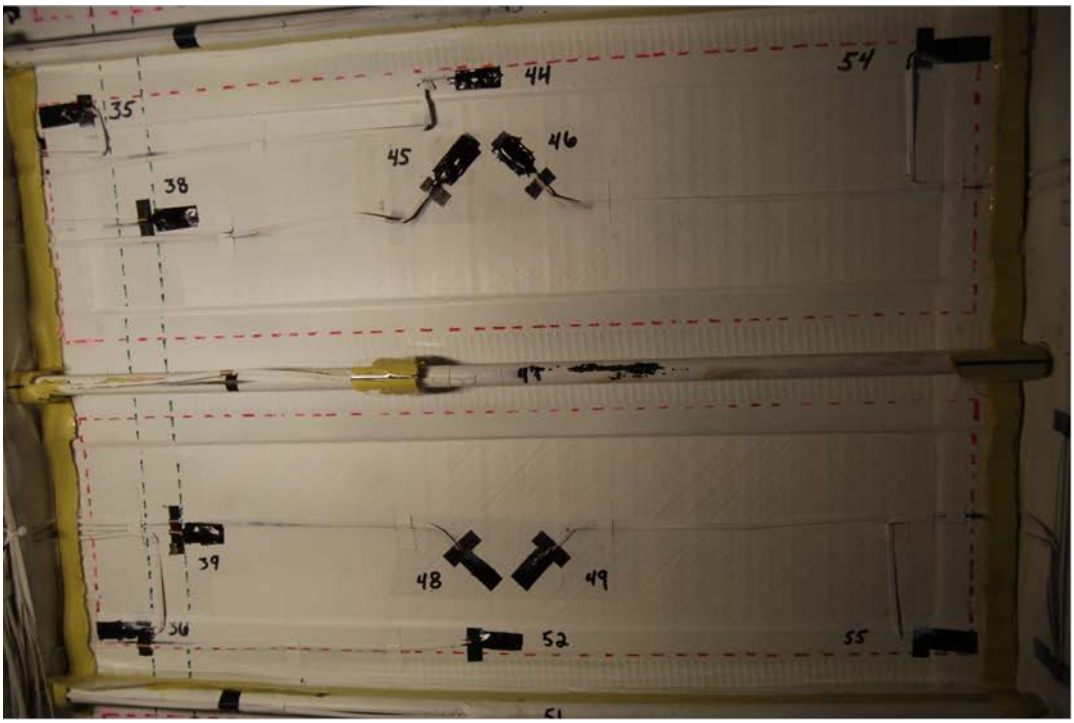

Figure G-1. Phase II, Baseline

(a) Exterior

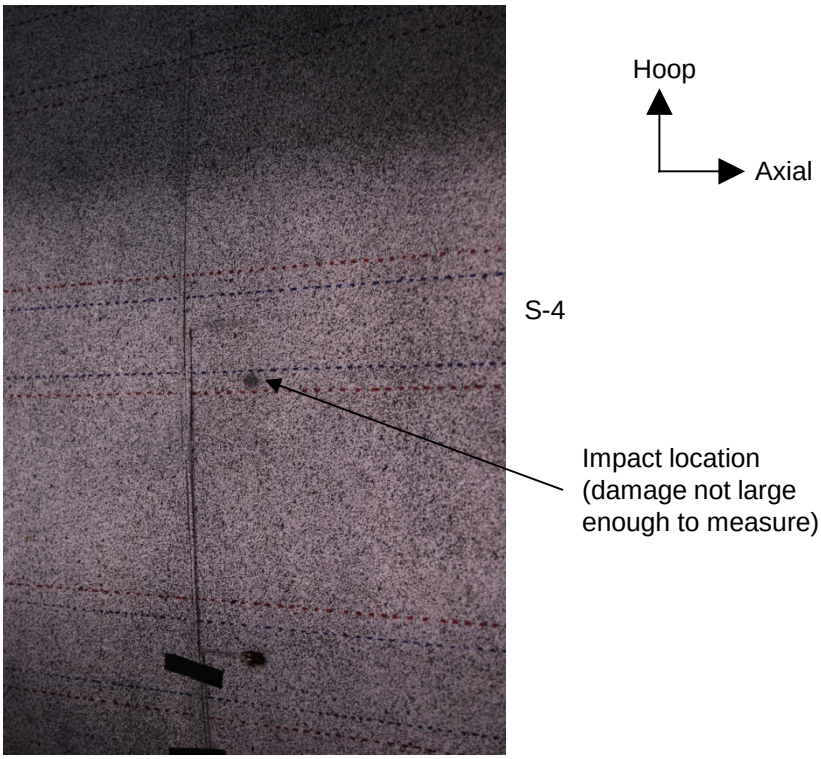

(b) Interior

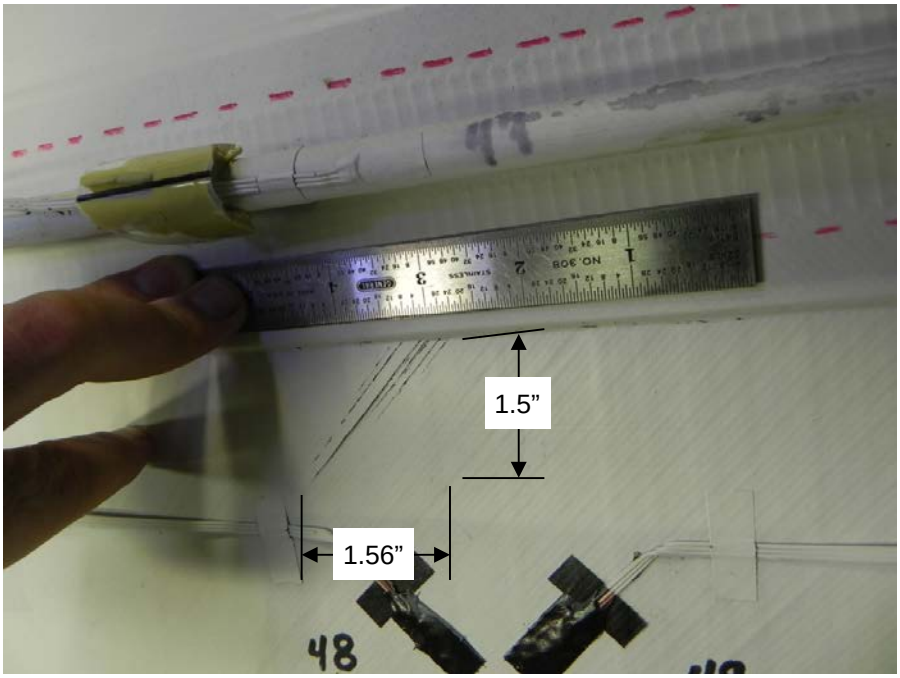

Figure G-2. Phase II, After First Impact

(a) Exterior

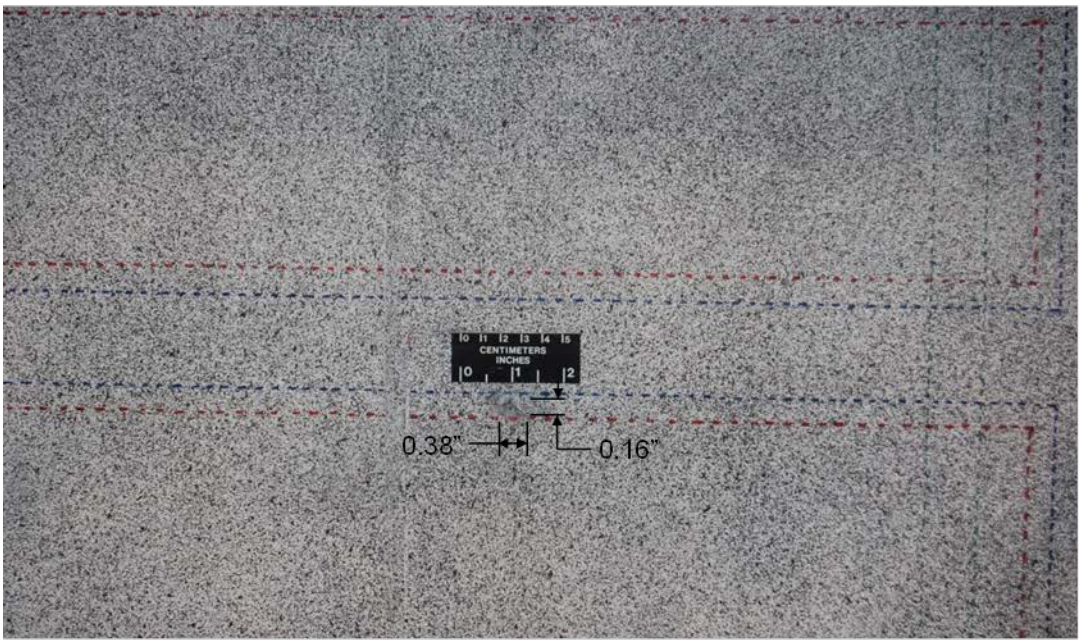

(a) Interior

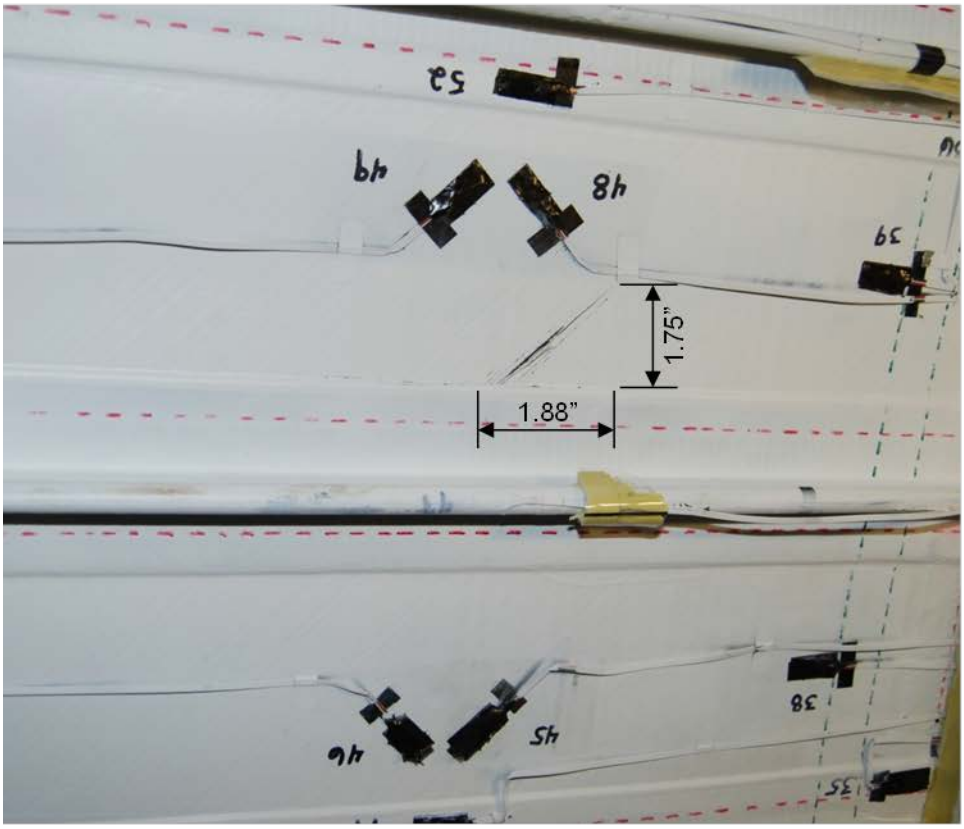

Figure G-3. Phase II, After Second Impact

(a) Exterior

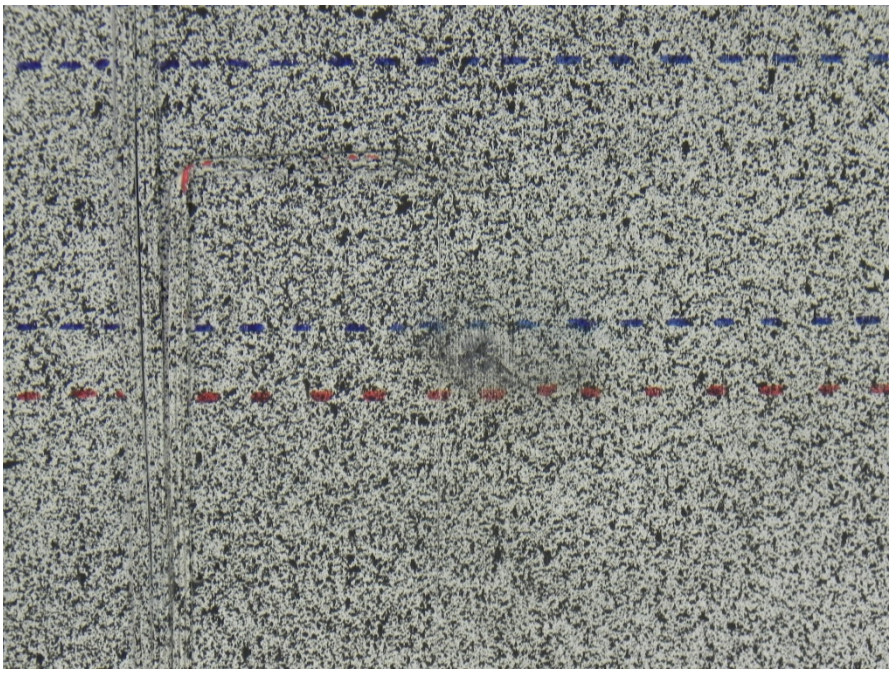

(b) Interior

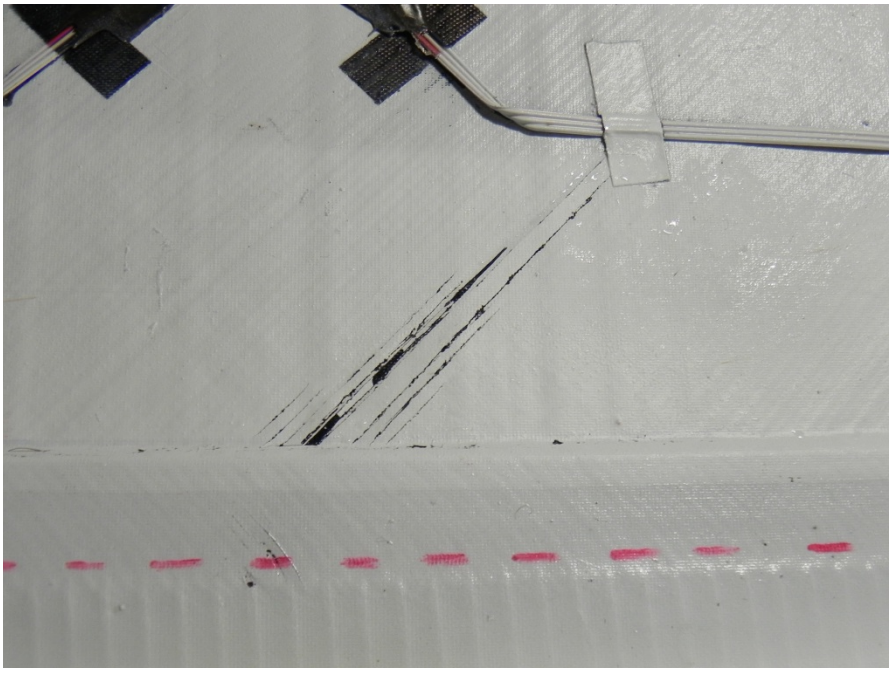

Figure G-4. Phase II, After All Loadings

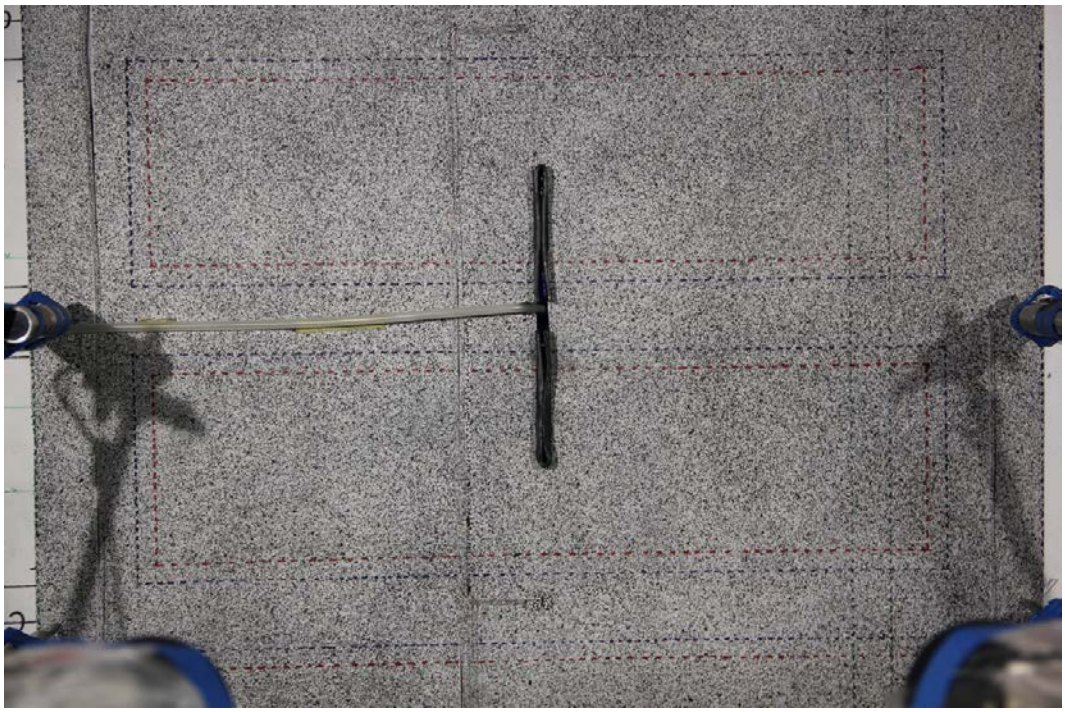

Figure G-5. Phase III Exterior, Baseline

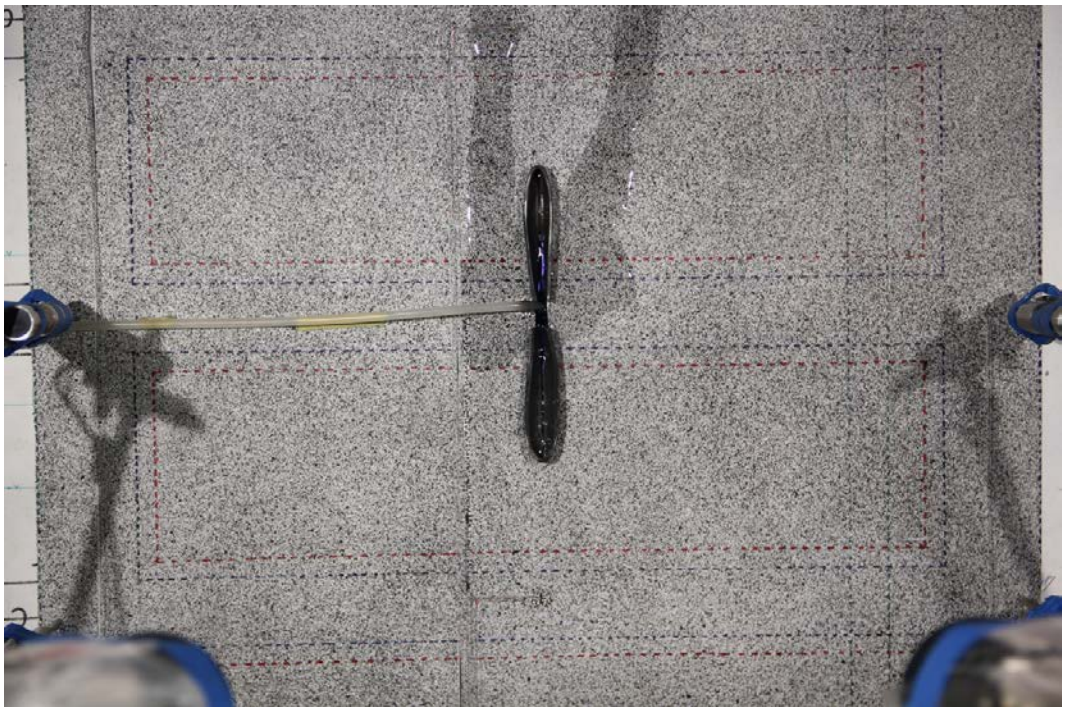

Figure G-6. Phase III Exterior, LS-1, Pressure 7.35 psi

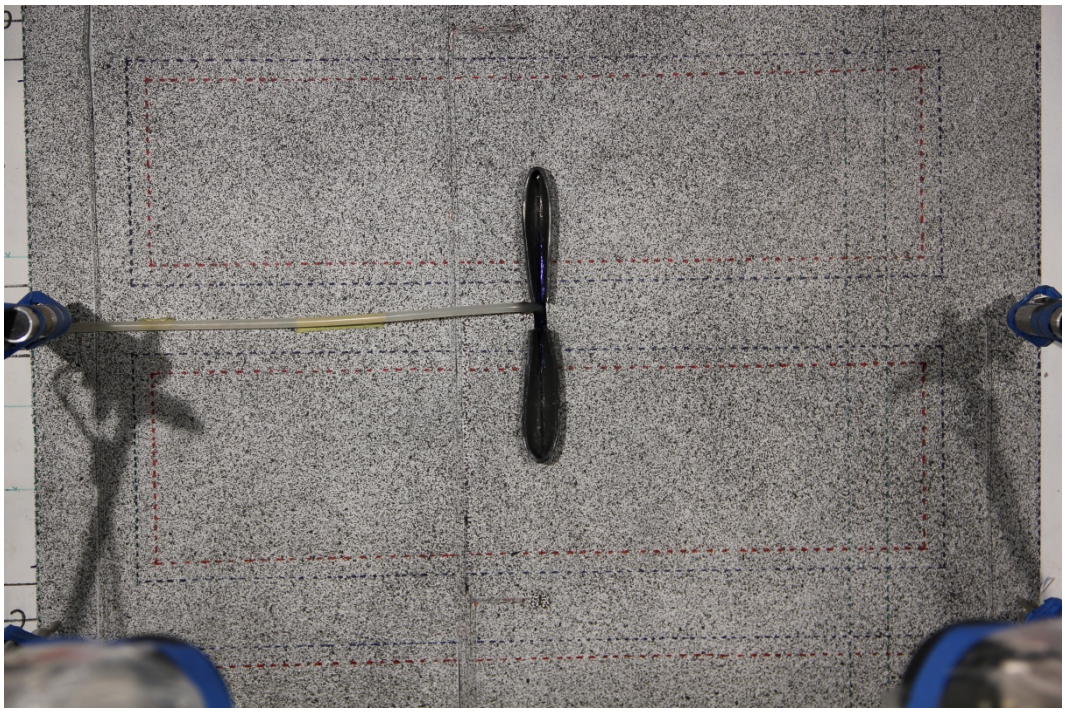

Figure G-7. Phase III Exterior, LS-1, Pressure 10.2 psi

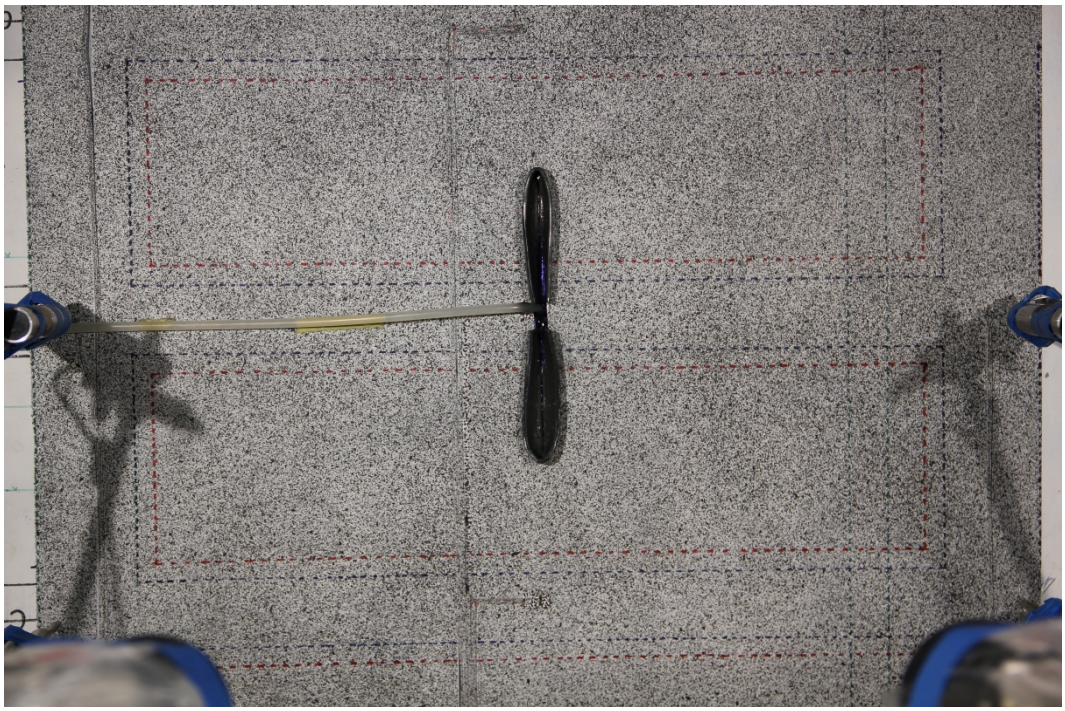

Figure G-8. Phase III Exterior, LS-2, Axial Load 29% DLL

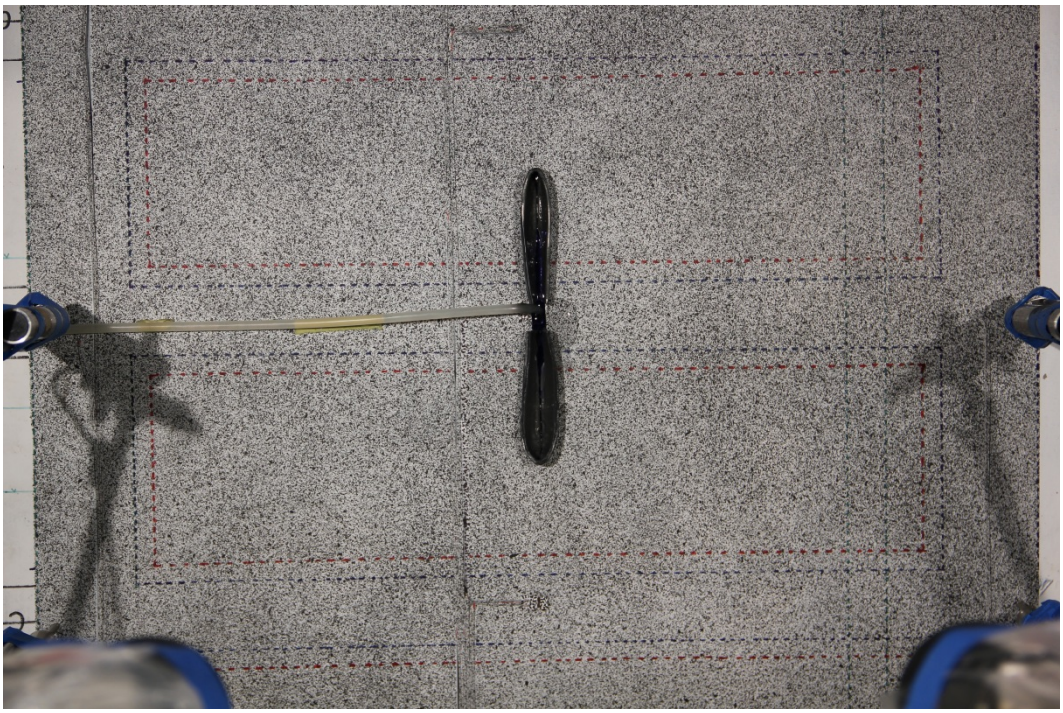

Figure G-9. Phase III Exterior, LS-2, Axial Load 41% DLL

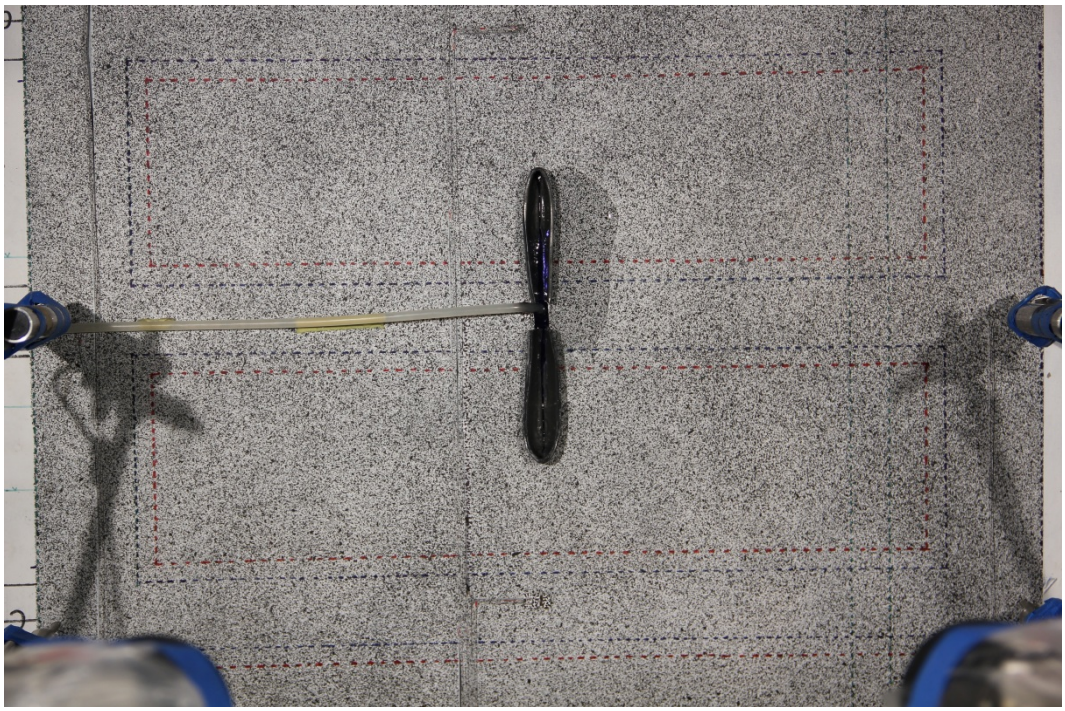

Figure G-10. Phase III Exterior, LS-2, Axial Load 56% DLL

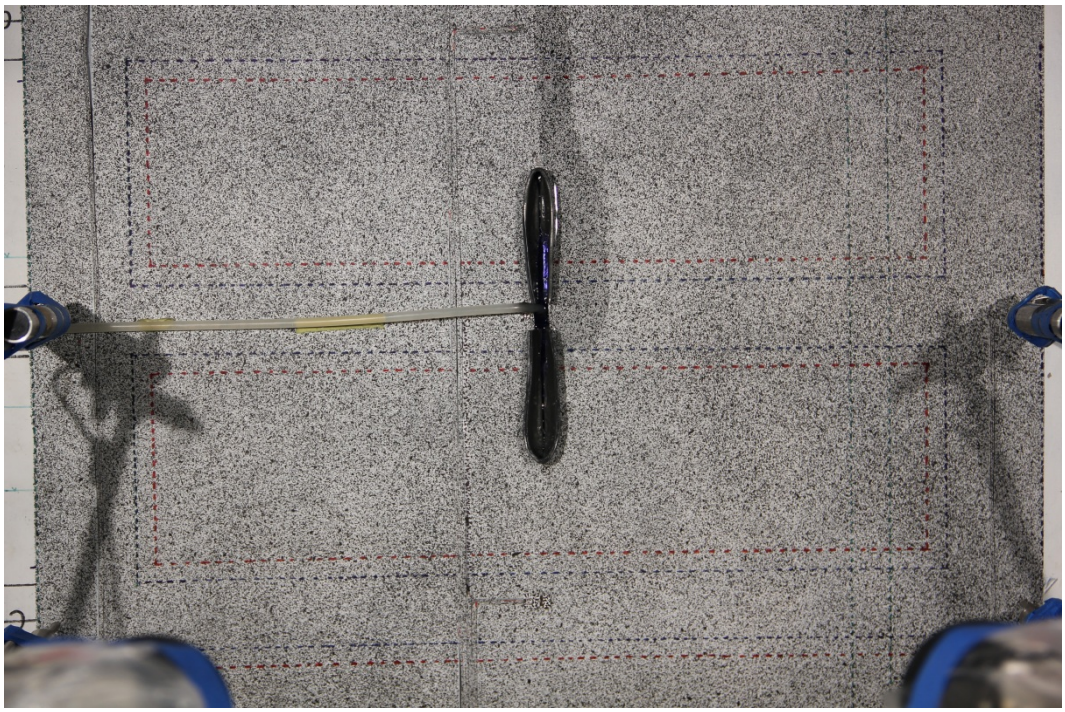

Figure G-11. Phase III Exterior, LS-2, Axial Load 70% DLL

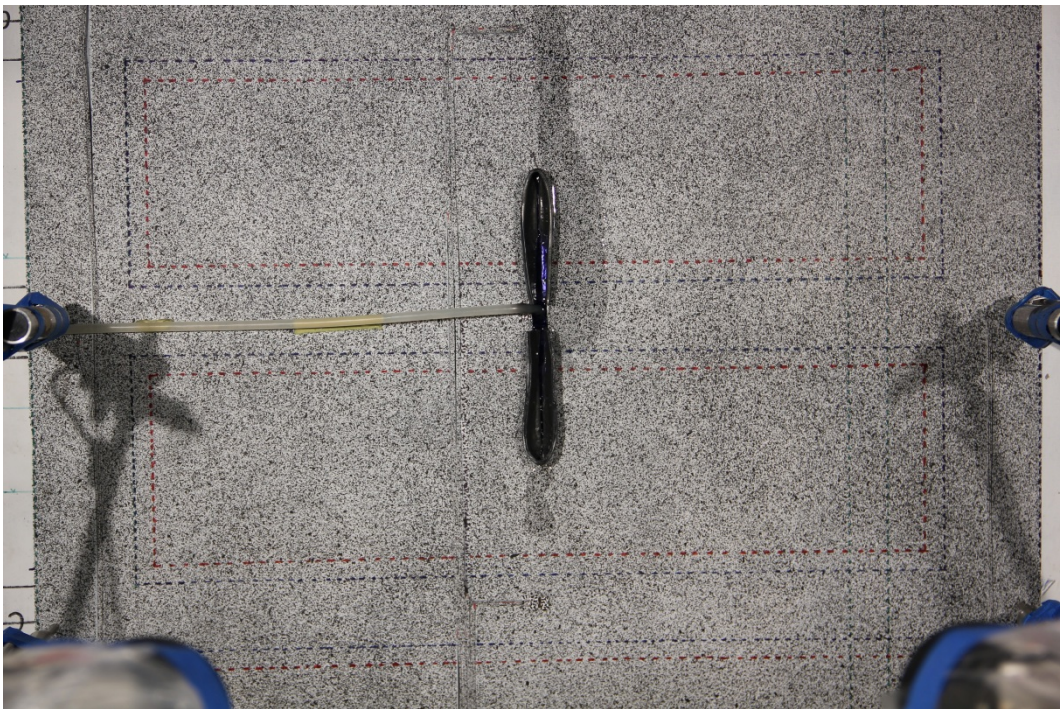

Figure G-12. Phase III Exterior, LS-2, Axial Load 84% DLL

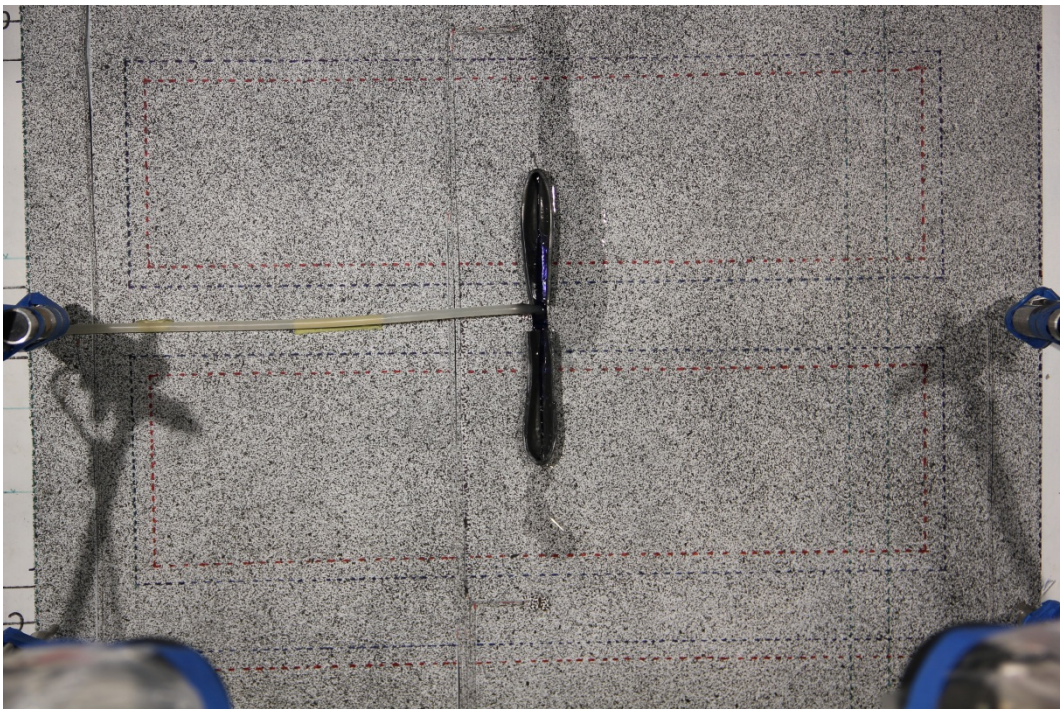

Figure G-13. Phase III Exterior, LS-2, Axial Load 88% DLL

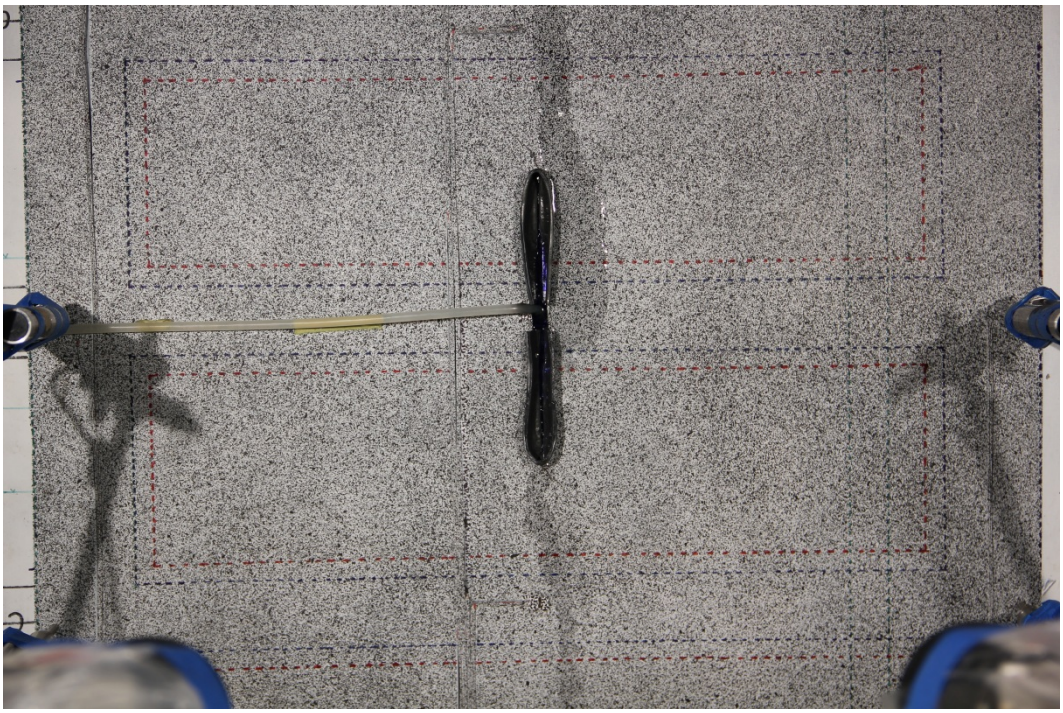

Figure G-14. Phase III Exterior, LS-2, Axial Load 94% DLL

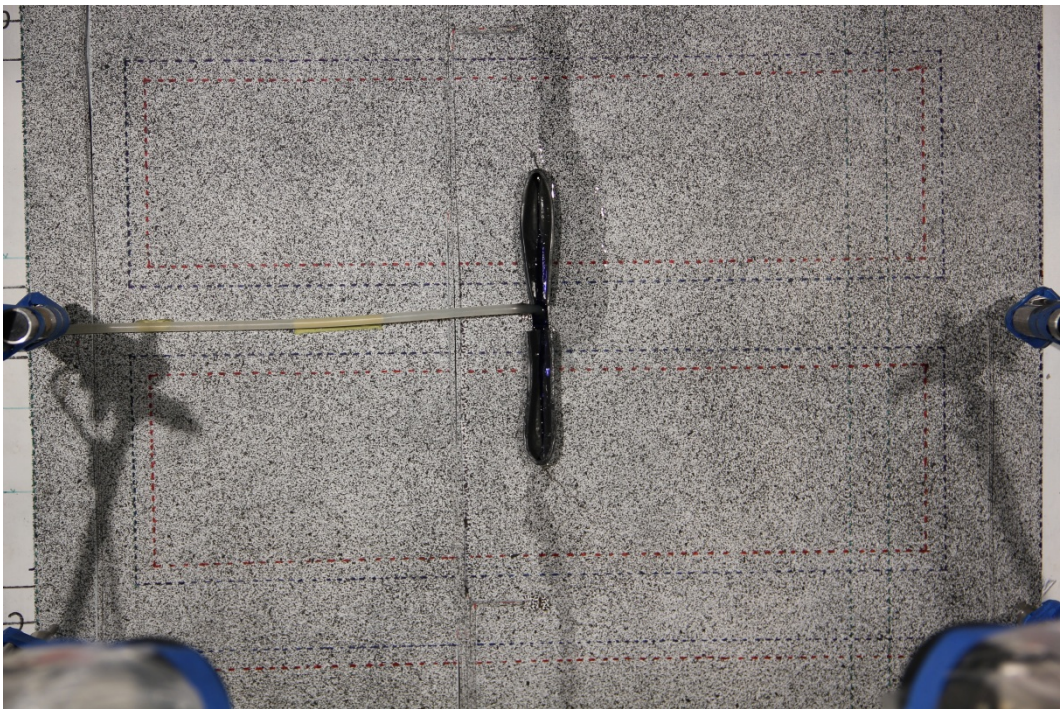

Figure G-15. Phase III Exterior, LS-2, Axial Load 100% DLL

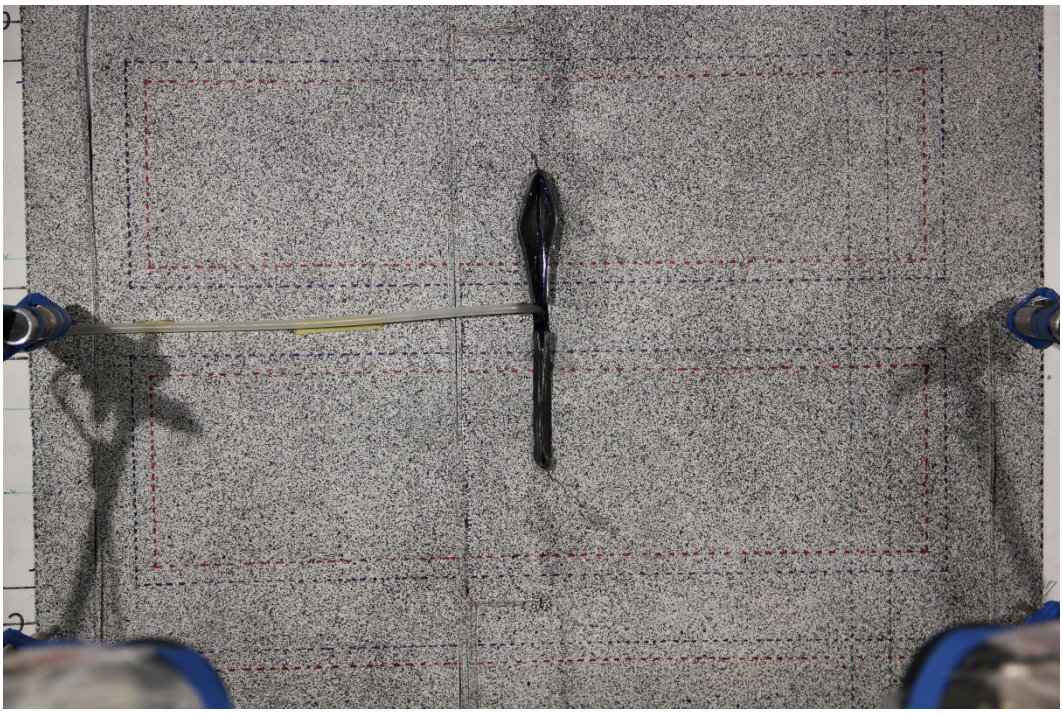

Figure G-16. Phase III Exterior, LS-3, Pressure 0 psi, Axial Load 100% DLL

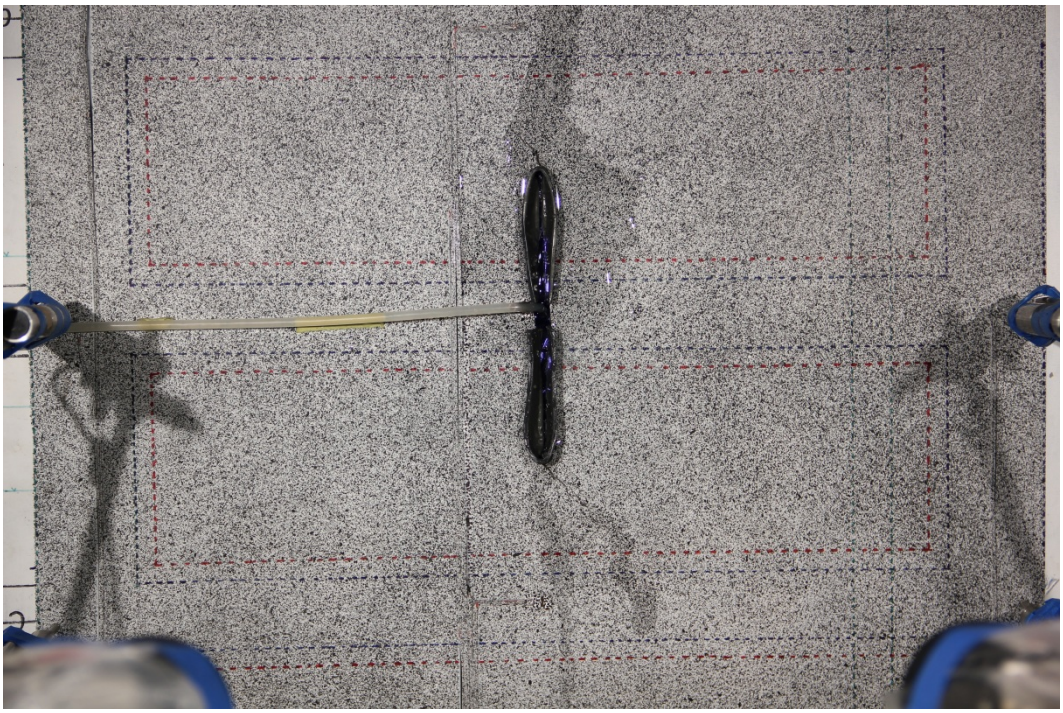

Figure G-17. Phase III Exterior, LS-4, Pressure 9.2 psi, Axial Load 100% DLL

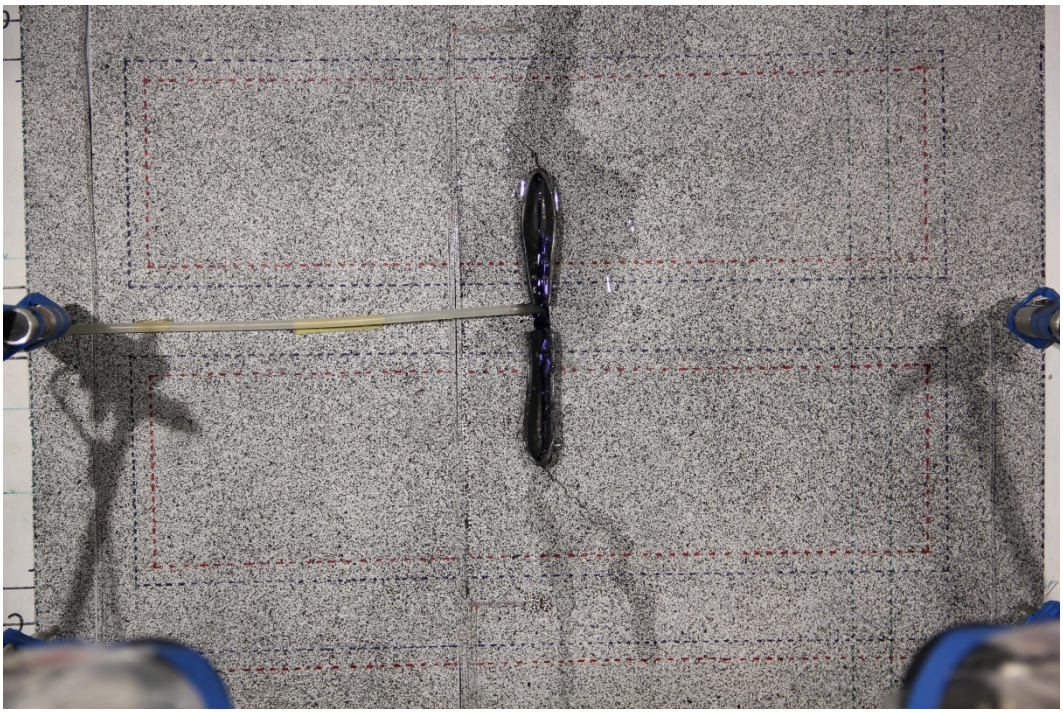

Figure G-18. Phase III Exterior, LS-5, Axial Load 105% DLL

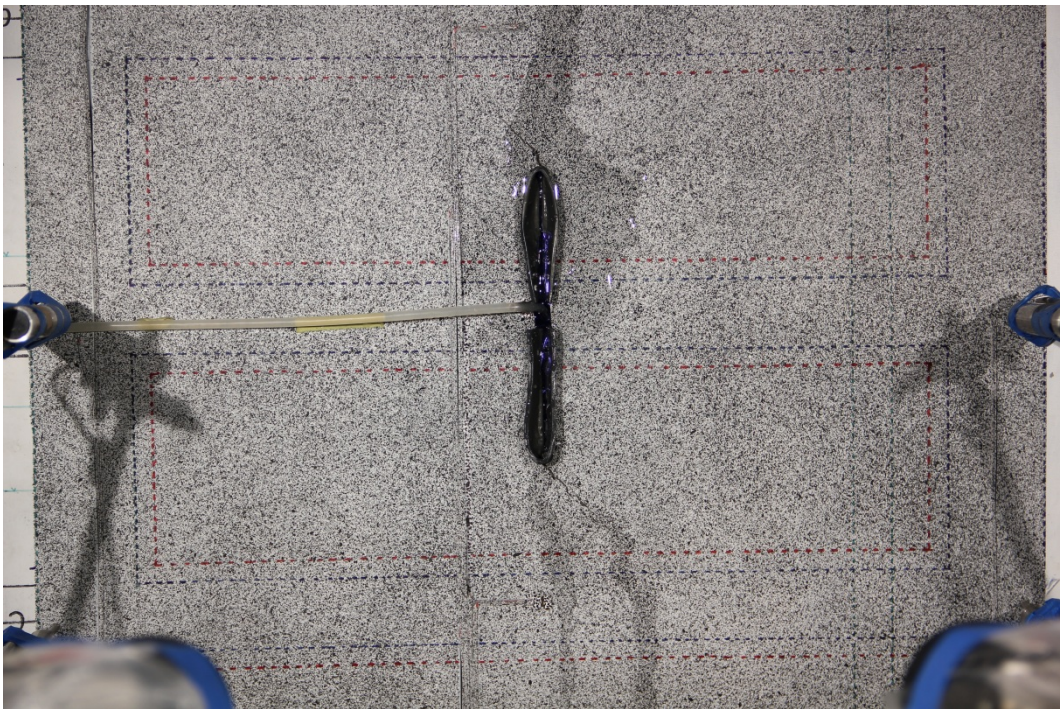

Figure G-19. Phase III Exterior, LS-5, Axial Load 110% DLL

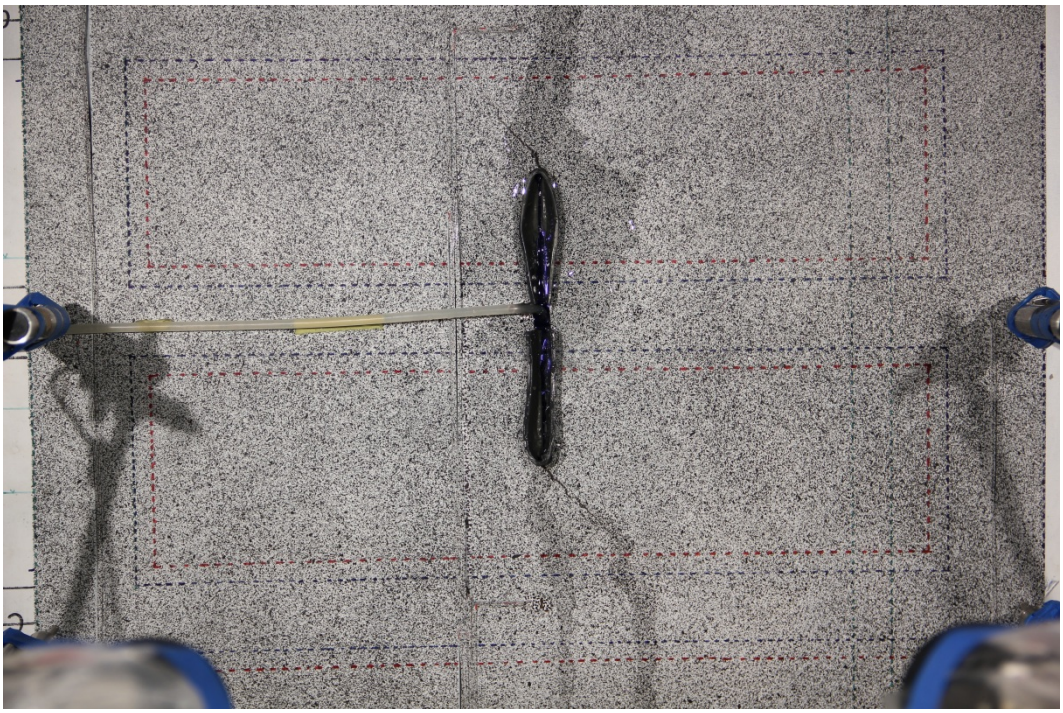

Figure G-20. Phase III Exterior, LS-5, Axial Load 116% DLL

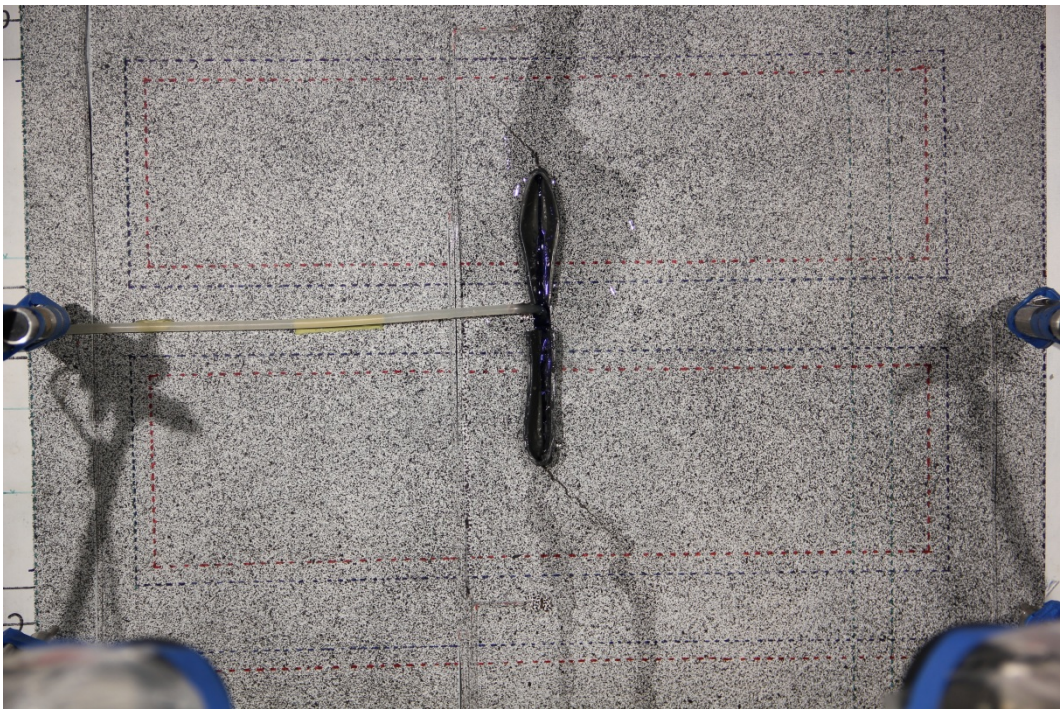

Figure G-21. Phase III Exterior, LS-5, Axial Load 121% DLL

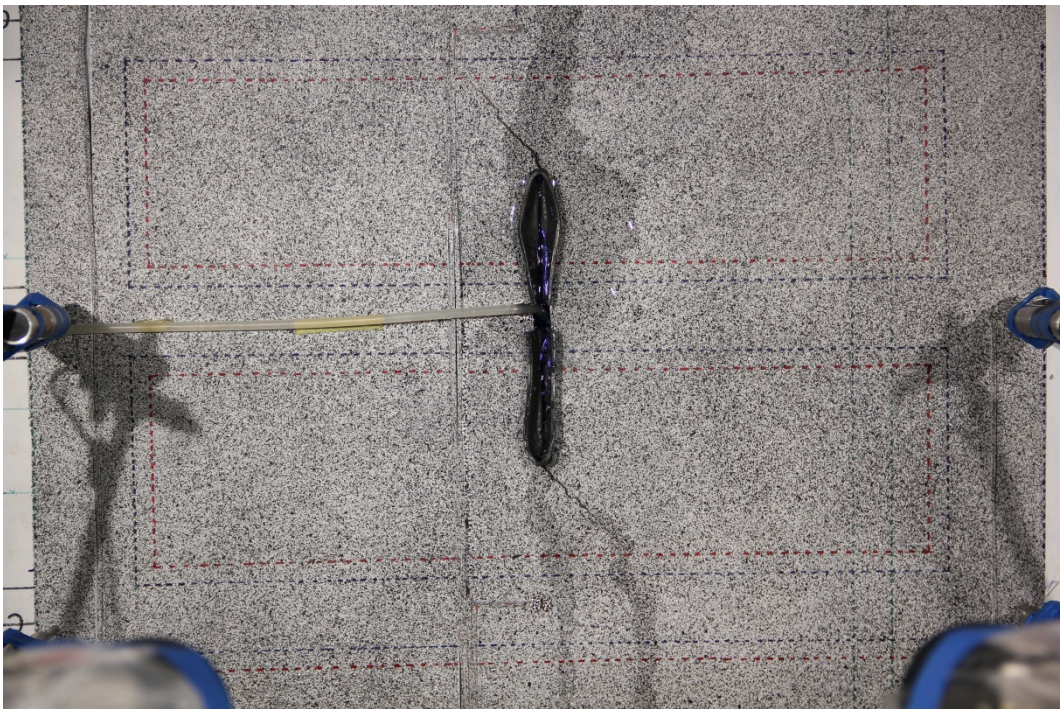

Figure G-22. Phase III Exterior, LS-5, Axial Load 124% DLL

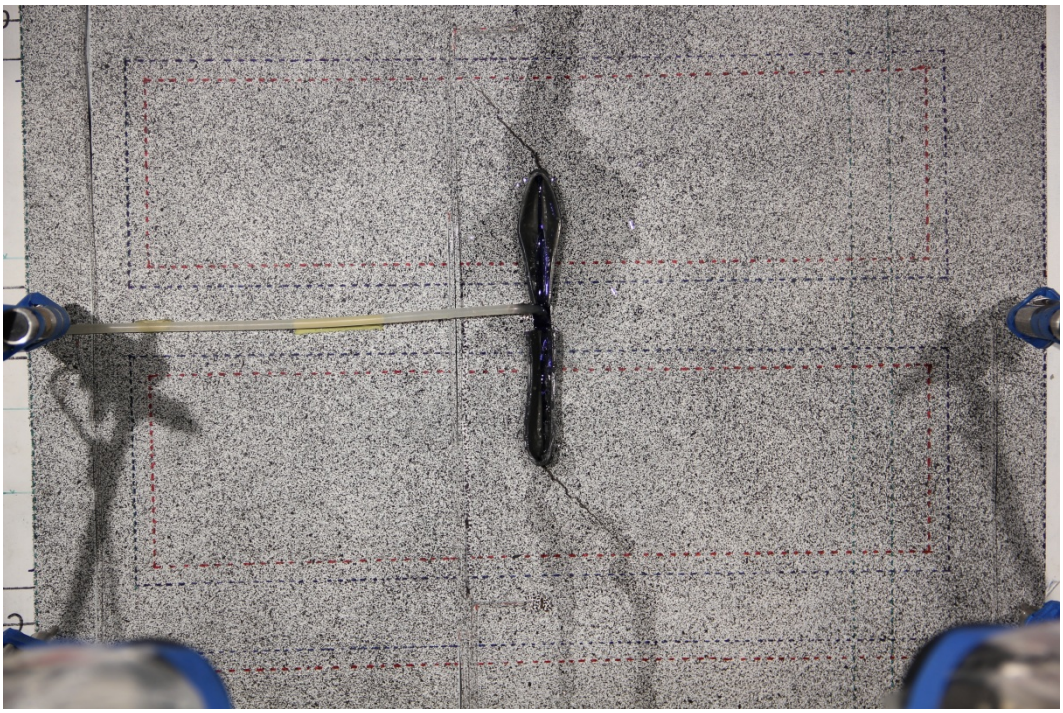

Figure G-23. Phase III Exterior, LS-5, Axial Load 134% DLL

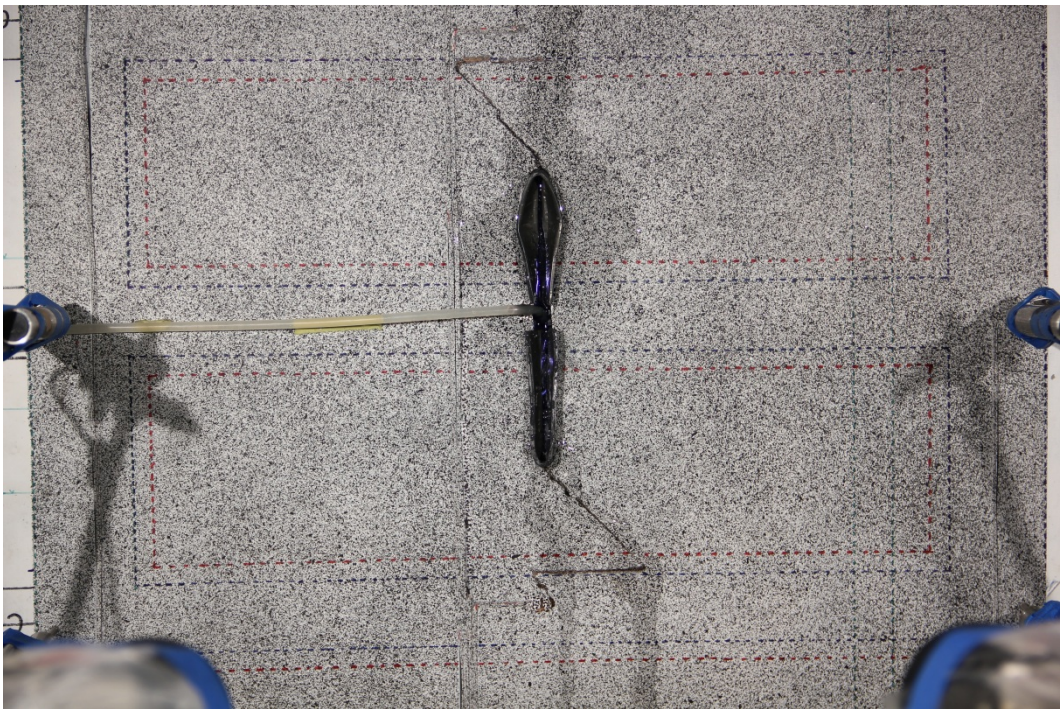

Figure G-24. Phase III Exterior, LS-5, Axial Load 148% DLL

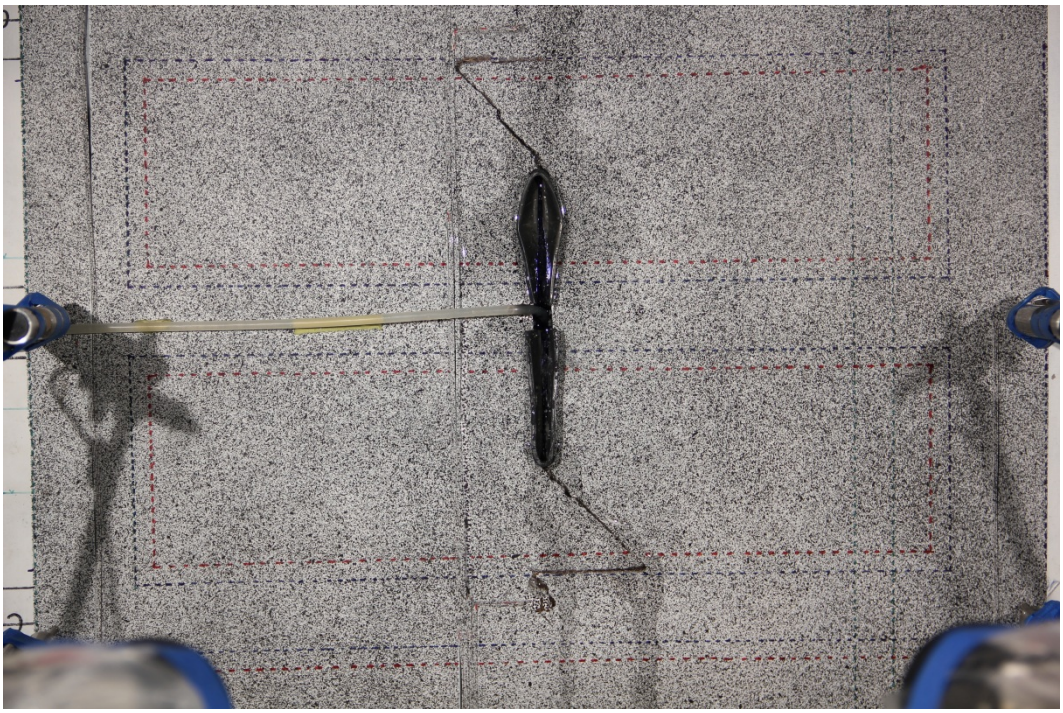

Figure G-25. Phase III Exterior, LS-5, Axial Load 163% DLL

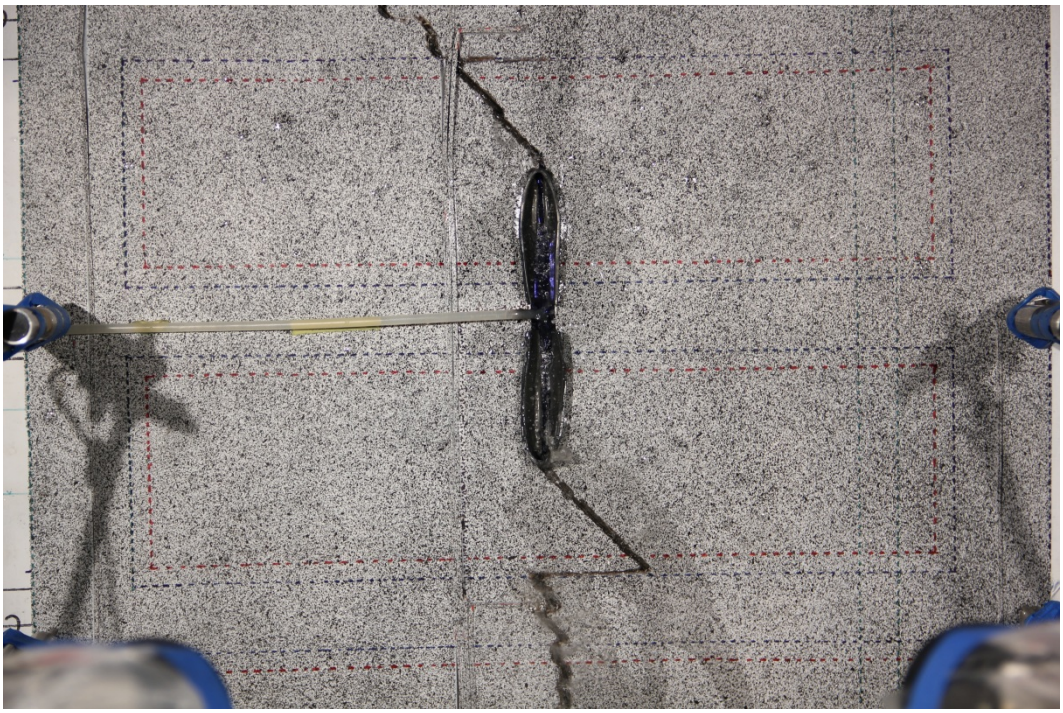

Figure G-26. Phase III Exterior, LS-5, Axial Load 157% DLL

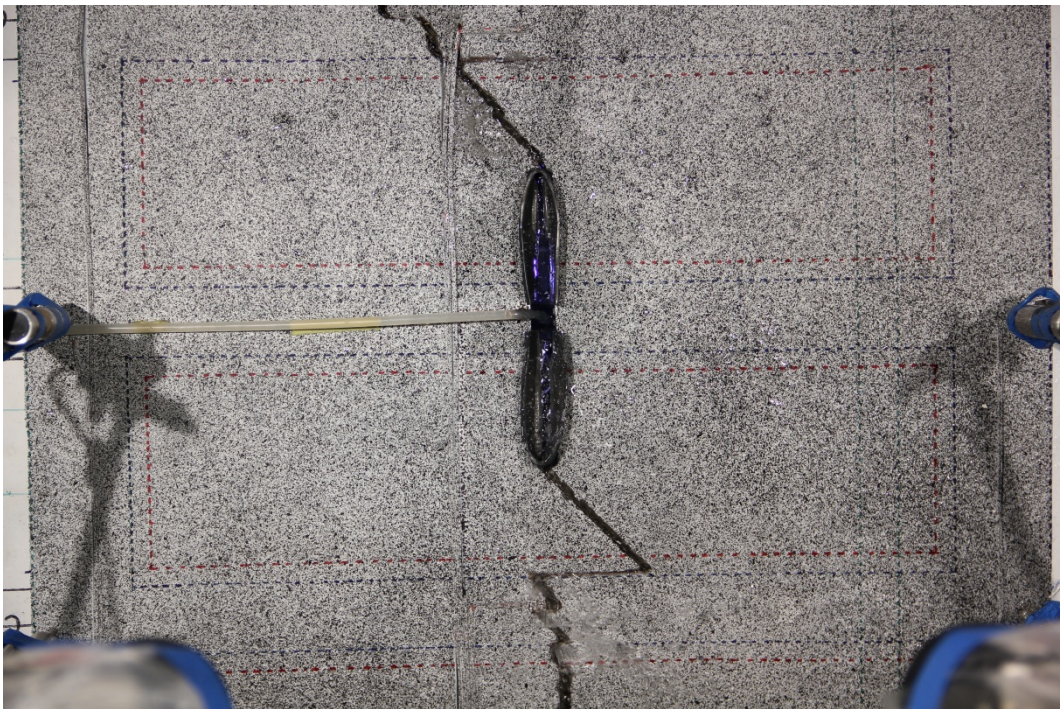

Figure G-27. Phase III Exterior, LS-5, Axial Load 163% DLL

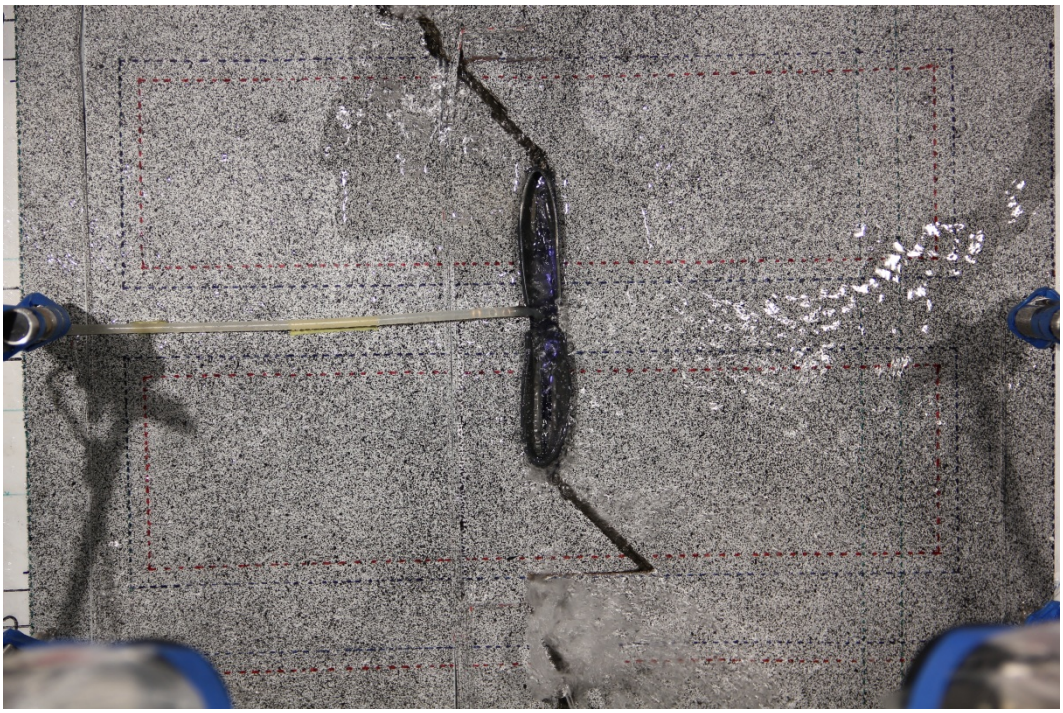

Figure G-28. Phase III Exterior, LS-5, Axial Load 165% DLL

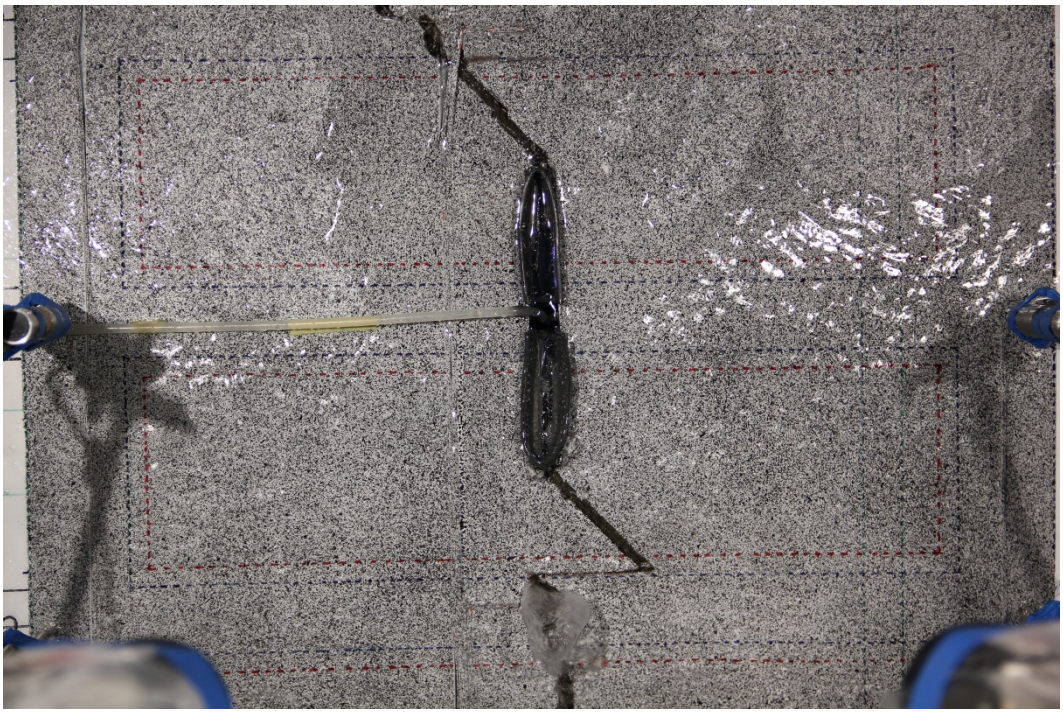

Figure G-29. Phase III Exterior, LS-5, Axial Load 173% DLL

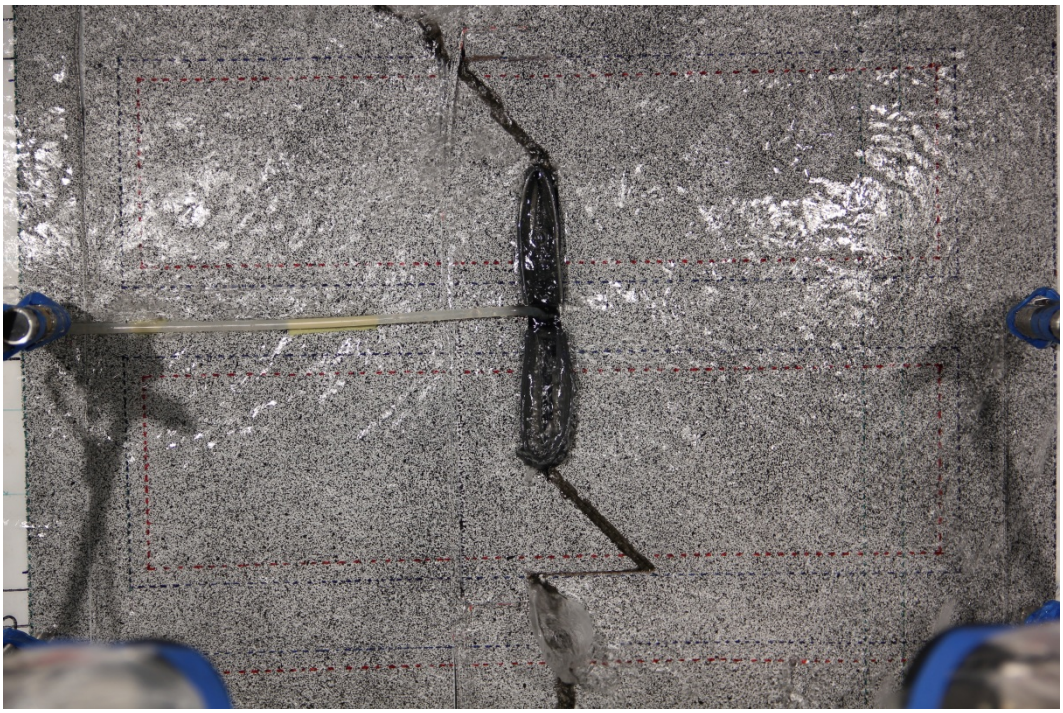

Figure G-30. Phase III Exterior, LS-5, Axial Load 179% DLL

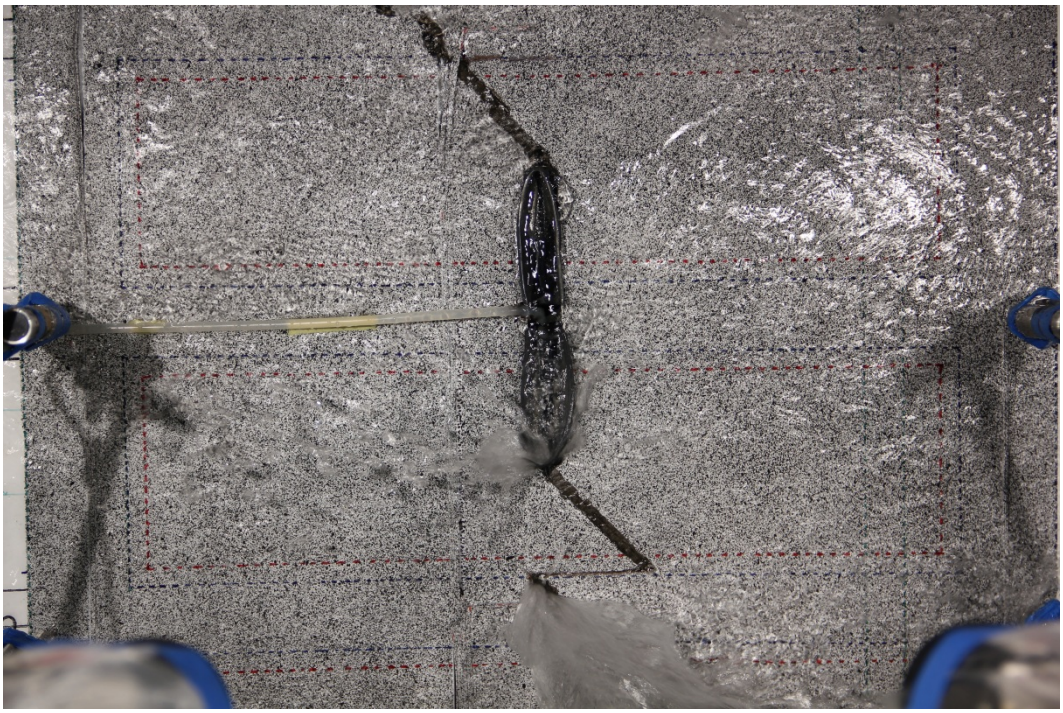

Figure G-31. Phase III Exterior, LS-5, Axial Load 184% DLL

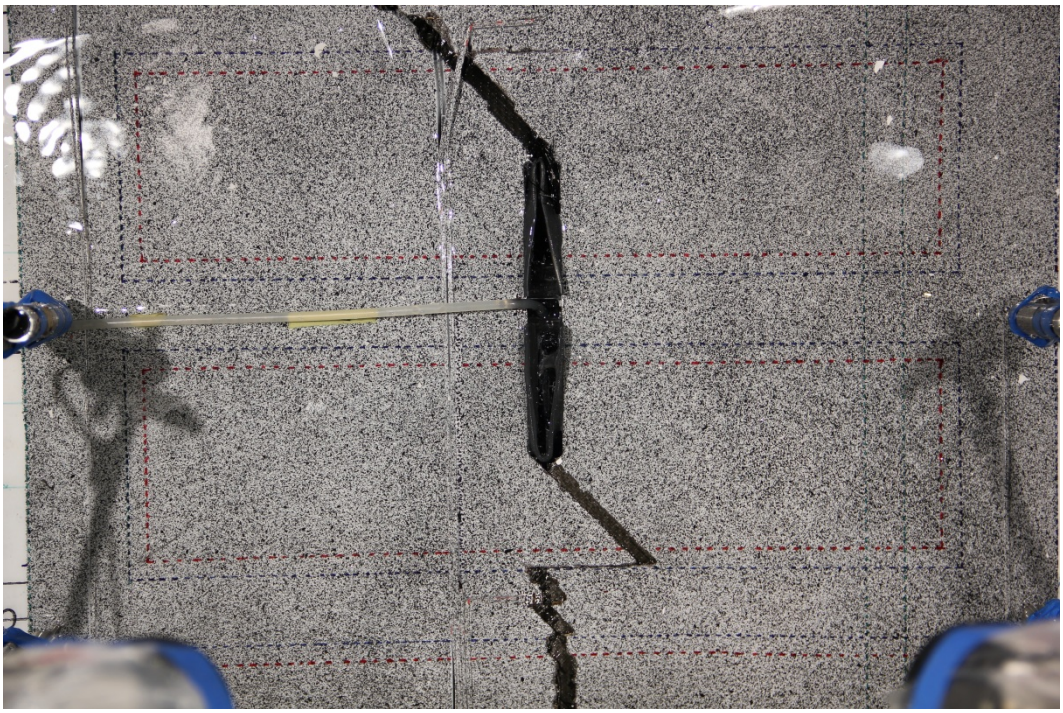

Figure G-32. Phase III Exterior, Post Failure

Figure G-33. Phase III Interior, Notch Tip A, LS-2, Axial Load 61% DLL

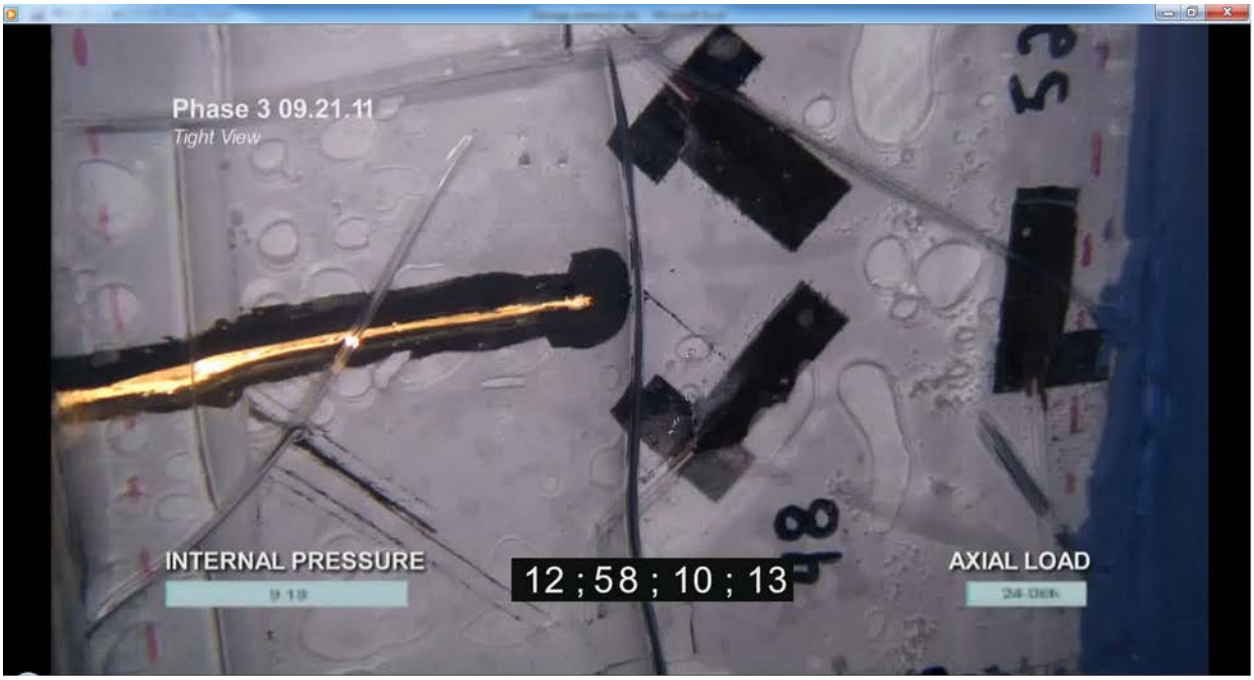

Figure G-34. Phase III Interior, Notch Tip A, LS-2, Axial Load 67% DLL

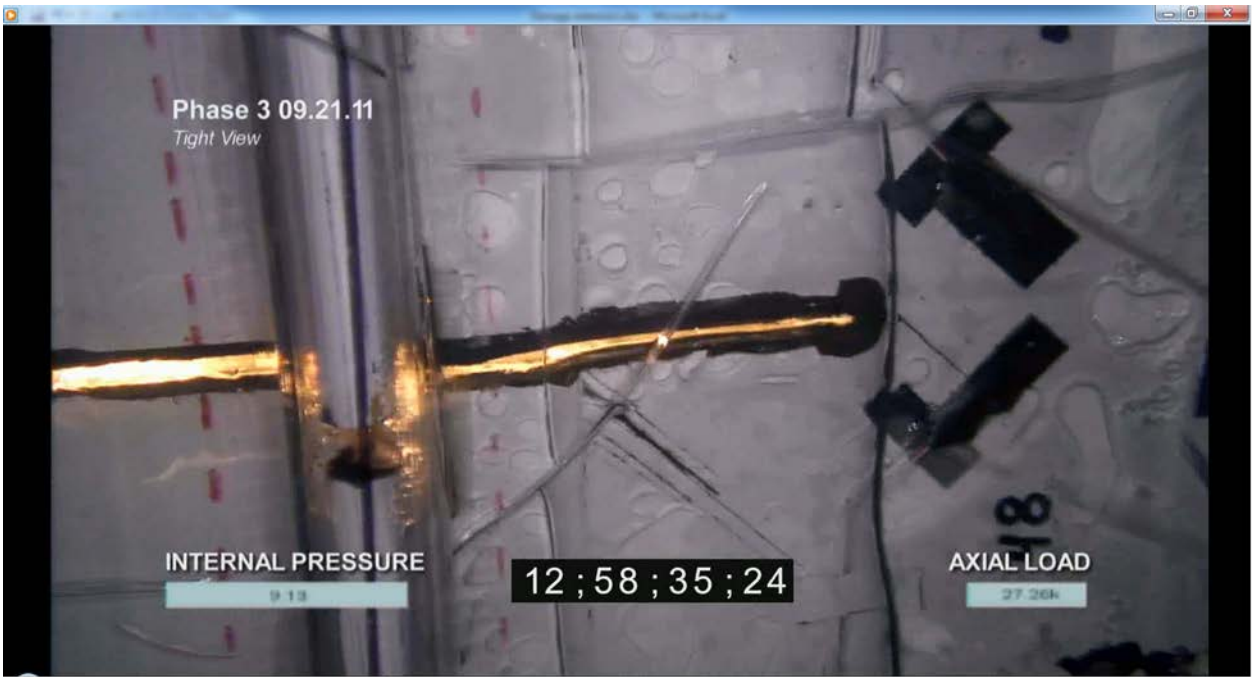

Figure G-35. Phase III Interior, Notch Tip A, LS-2, Axial Load 75% DLL

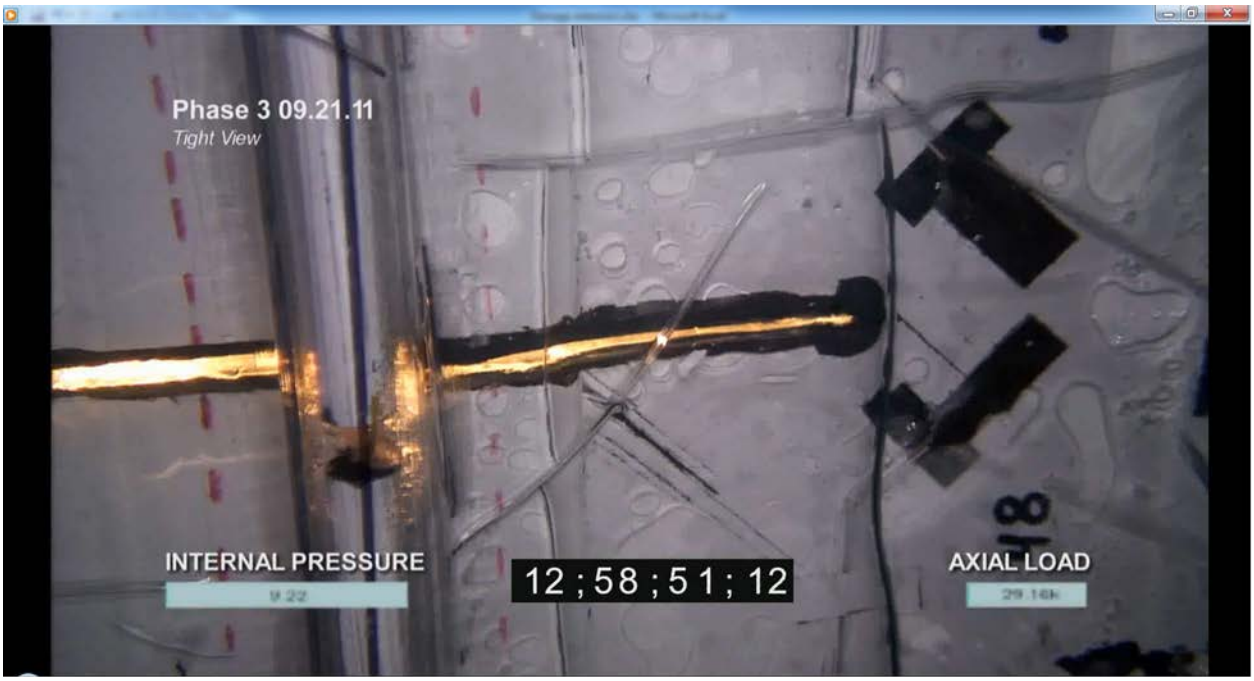

Figure G-36. Phase III Interior, Notch Tip A, LS-2, Axial Load 80% DLL

Figure G-37. Phase III Interior, Notch Tip A, LS-2, Axial Load 90% DLL

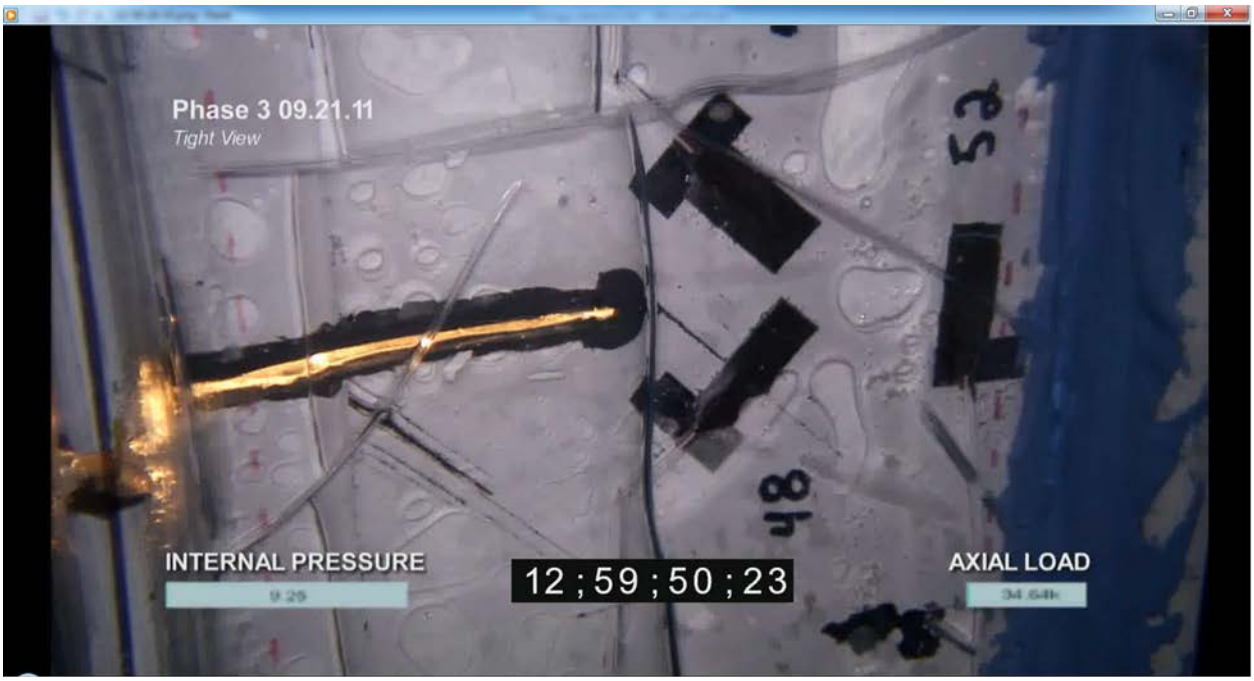

Figure G-38. Phase III Interior, Notch Tip A, LS-2, Axial Load 95% DLL

Figure G-39. Phase III Interior, Notch Tip A, LS-2, Axial Load 100% DLL

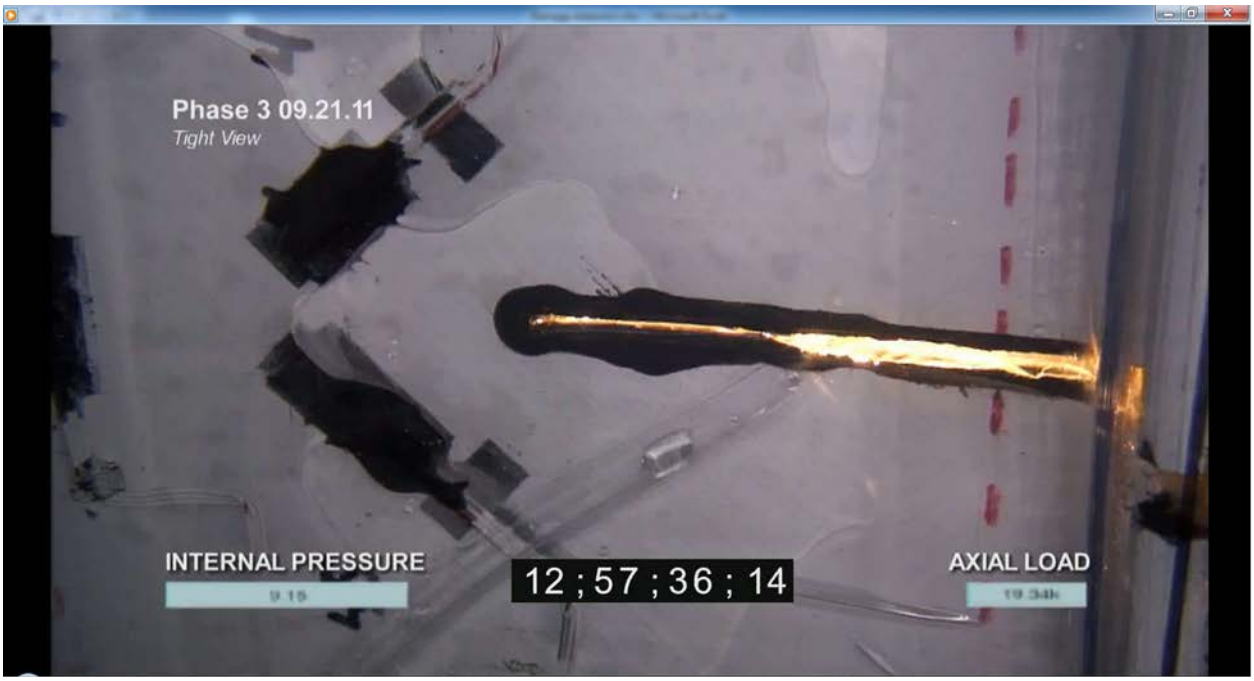

Figure G-40. Phase III Interior, Notch Tip B, LS-2, Axial Load 54% DLL

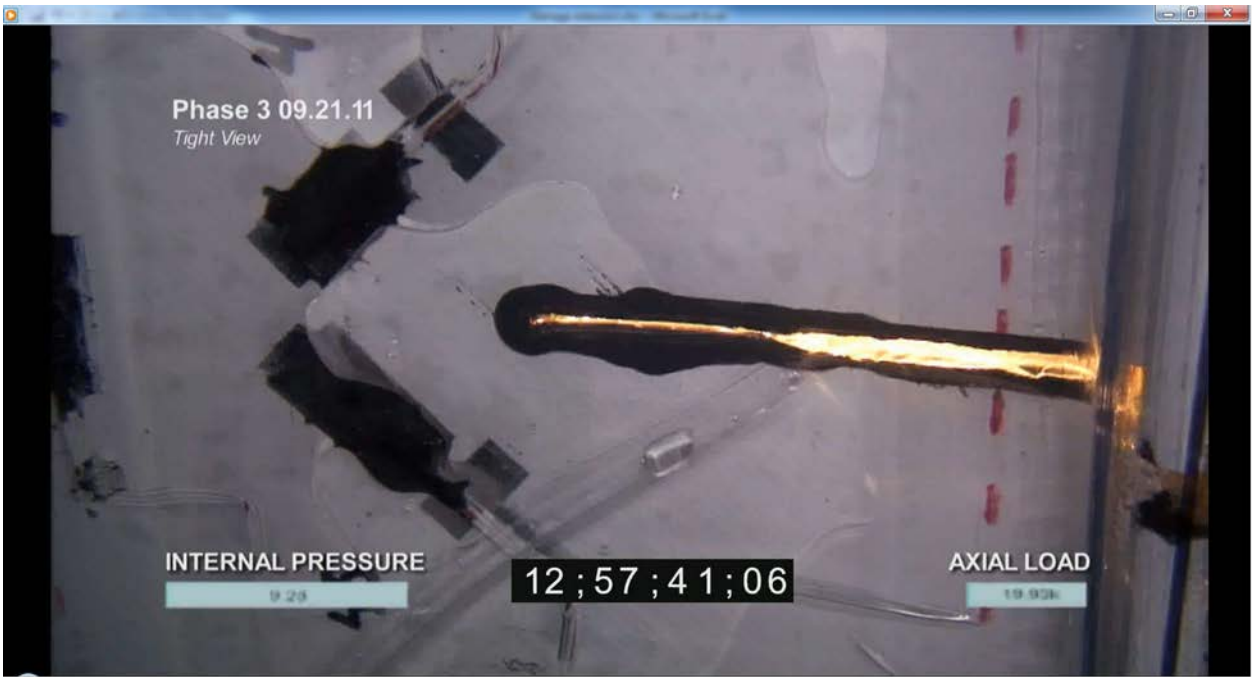

Figure G-41. Phase III Interior, Notch Tip B, LS-2, Axial Load 55% DLL

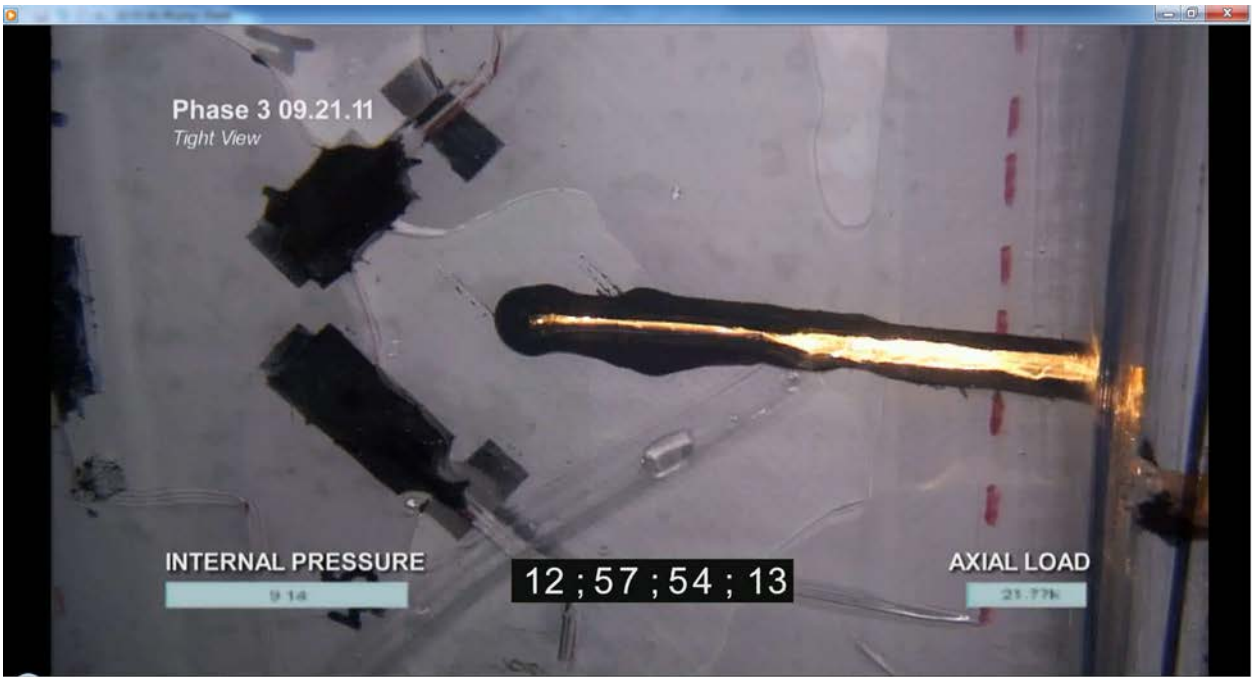

Figure G-42. Phase III Interior, Notch Tip B, LS-2, Axial Load 63% DLL

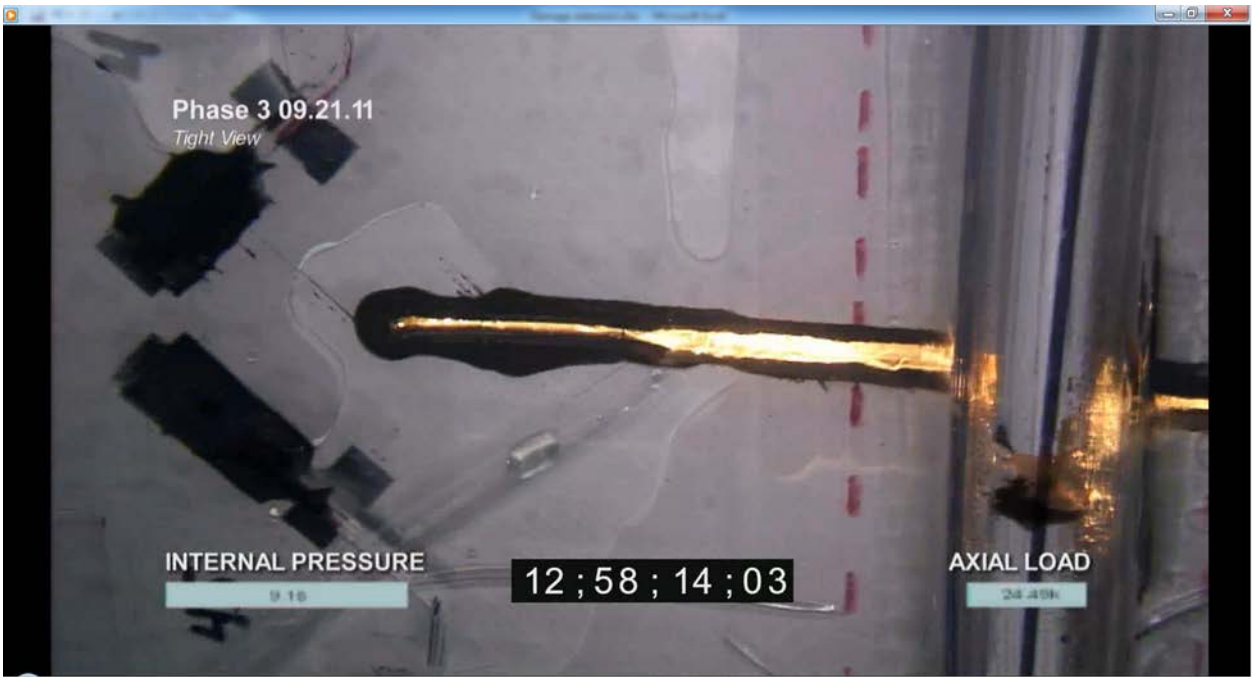

Figure G-43. Phase III Interior, Notch Tip B, LS-2, Axial Load 67% DLL

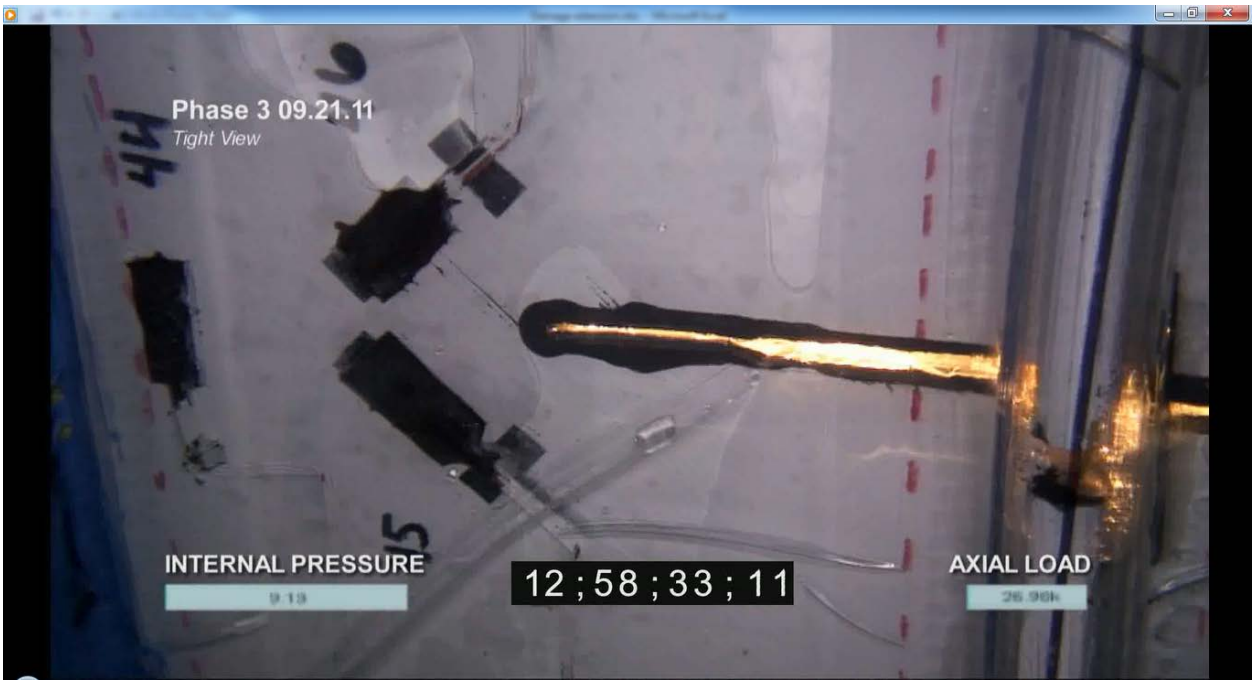

Figure G-44. Phase III Interior, Notch Tip B, LS-2, Axial Load 74% DLL

Figure G-45. Phase III Interior, Notch Tip B, LS-2, Axial Load 82% DLL

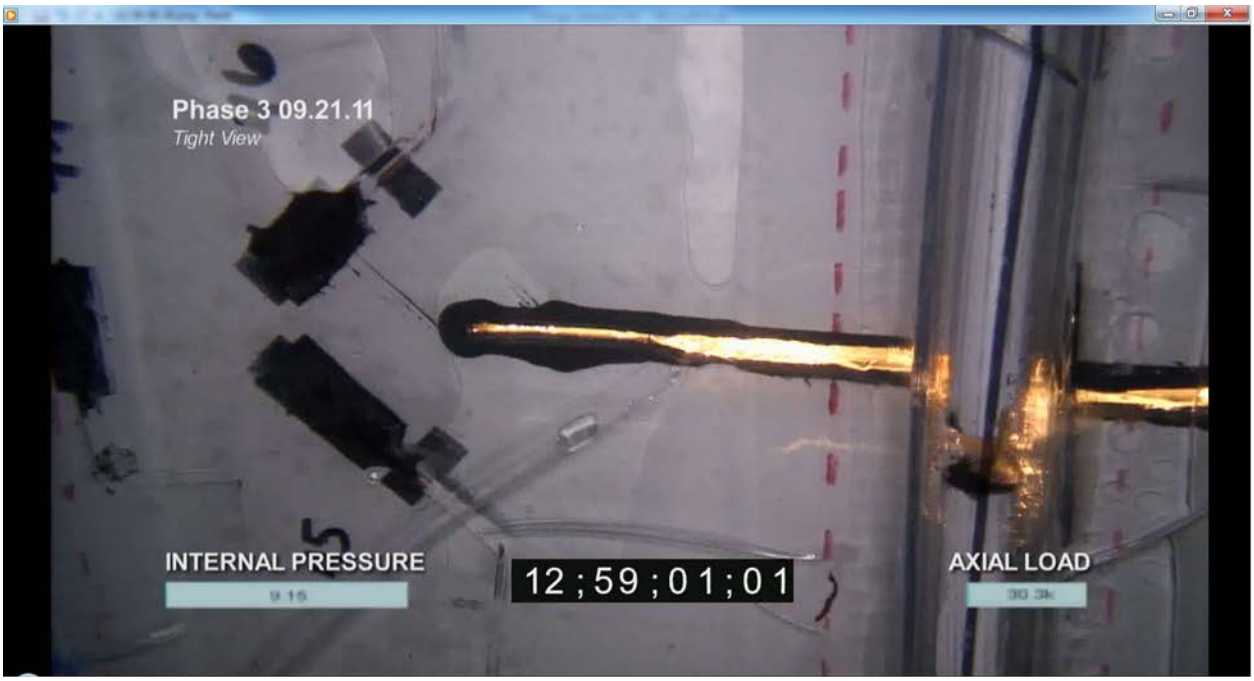

Figure G-46. Phase III Interior, Notch Tip B, LS-2, Axial Load 83% DLL

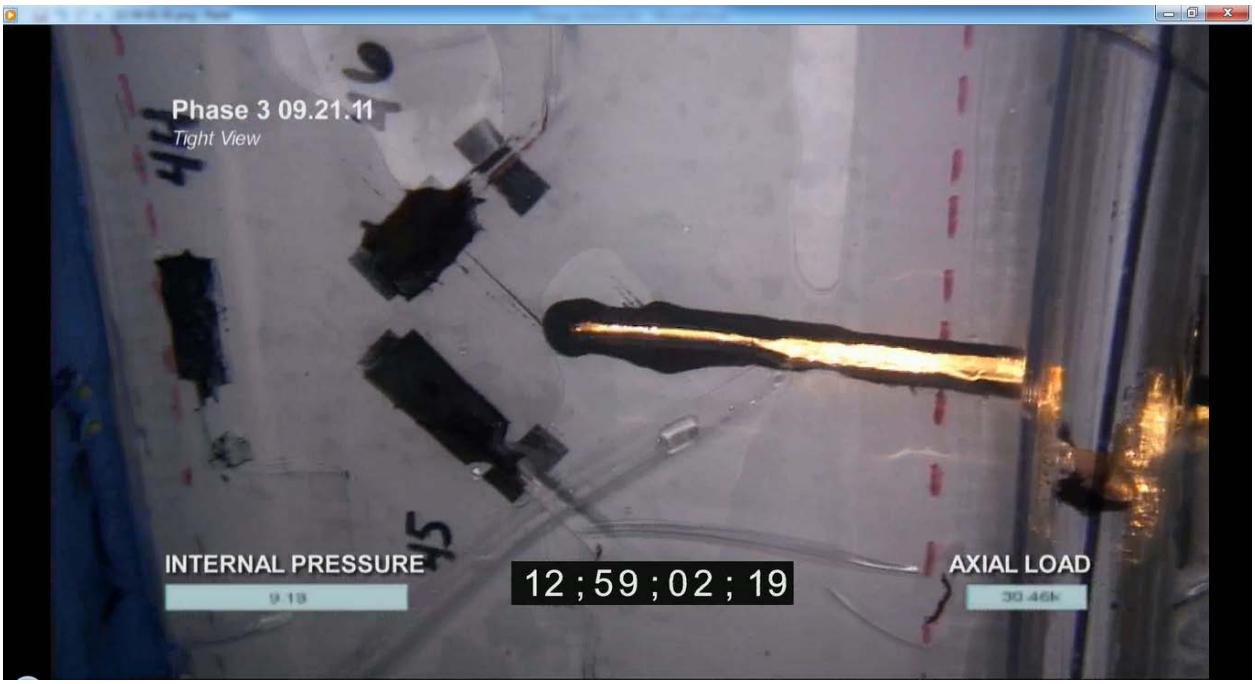

Figure G-47. Phase III Interior, Notch Tip B, LS-2, Axial Load 84% DLL

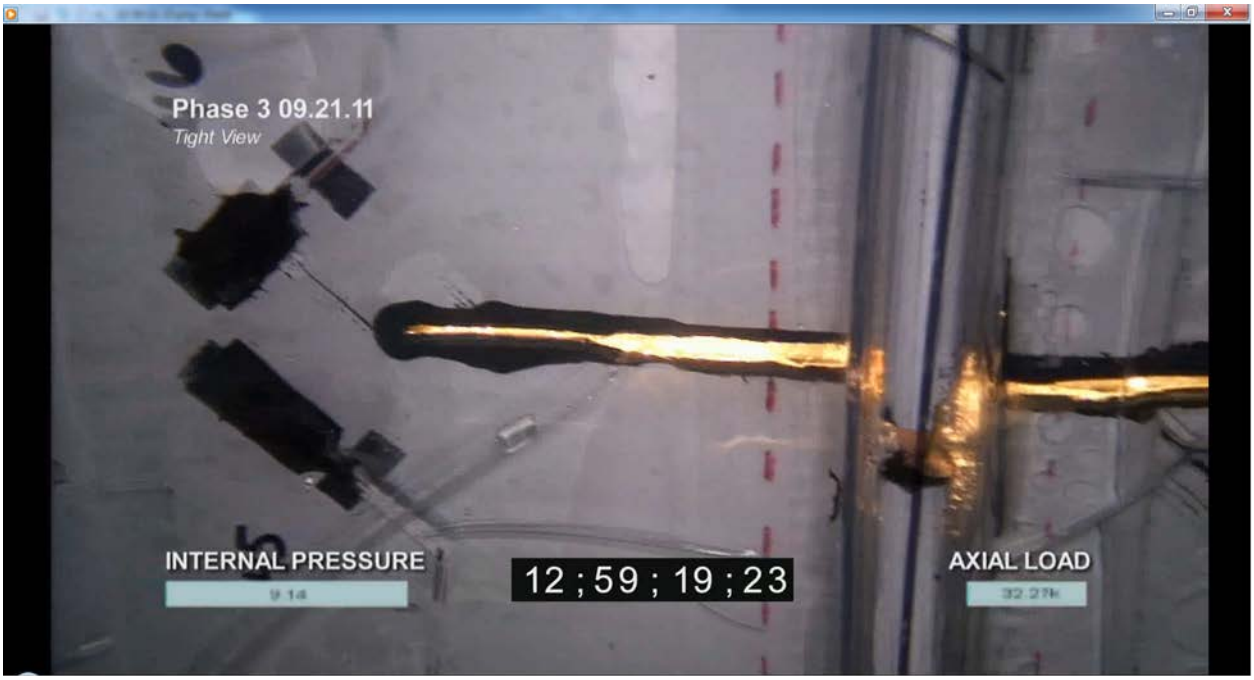

Figure G-48. Phase III Interior, Notch Tip B, LS-2, Axial Load 88% DLL

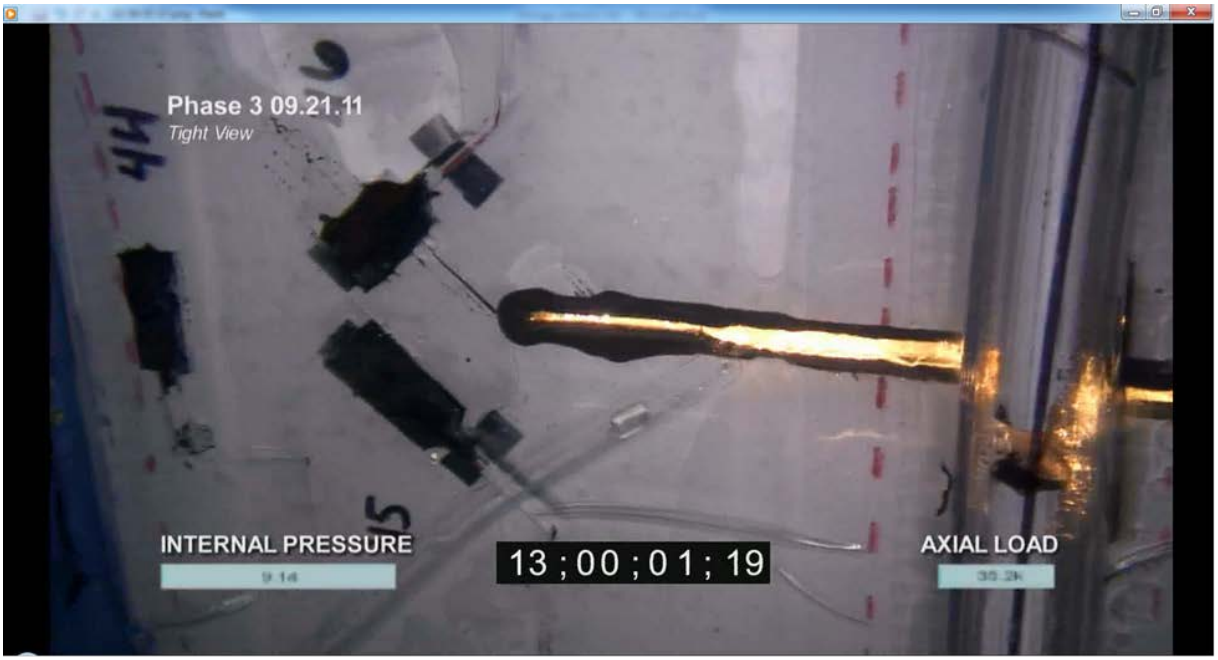

Figure G-49. Phase III Interior, Notch Tip B, LS-2, Axial Load 97% DLL

Figure G-50. Phase III Interior, Notch Tip B, LS-2, Axial Load 100% DLL